

CFD-BASED IMPELLER AND SEAL ROTORDYNAMIC FORCES

A Dissertation

by

FARZAM MORTAZAVI

Submitted to the Office of Graduate and Professional Studies of
Texas A&M University
in partial fulfillment of the requirements for the degree of

DOCTOR OF PHILOSOPHY

Chair of Committee, Alan B. Palazzolo
Committee Members, Diego Donzis
Sevan Goenezen
Dorrin Jarrahbashi
Head of Department, Andreas A. Polycarpou

December 2018

Major Subject: Mechanical Engineering

Copyright 2018 Farzam Mortazavi

ABSTRACT

Eccentrically operating turbomachinery components such as impellers and seals are subject to flow induced forces known as rotordynamic forces. Rotordynamic forces can be detrimental to the machine stability and longevity. Therefore, industrial guidelines, such as American Petroleum Institute level II stability criteria, require provision of advanced computational methods to predict the rotordynamic forces of impellers and seals. Current study aims to introduce Computational Fluid Dynamics (CFD) based methodologies with fewer restrictions compared to prior studies. Such generality encompass transient approaches as opposed to quasi-steady; asymmetric features such as primary flow paths, diffusers and volutes; open impellers compared to the classical case of closed impellers; multi-frequency modeling versus single-frequency approach; interaction with rotating stall; and dimensionless rotordynamic forces applicable to a spectrum of specific speed families. The evolution of CFD-based rotordynamic models in this work is initiated with a quasi-steady groove-on-rotor liquid annular seal case, followed by a transient single-frequency prediction of volute and diffuser rotordynamic forces, and further extended by a phase-modulated multi-frequency method applied to open impellers. All cases are validated against experimental data. The contribution of primary flow path, diffuser and volutes are found to be substantial despite the earlier belief that the majority of impeller rotordynamic forces stem from the front leakage path. Finally, a detailed discussion on the physical origins of fluctuations (bumps and dips) appearing on impeller impedances under partload operation is delivered.

In parallel, a CFD code has been developed in FORTRAN to model turbulent liquid annular seal flows as a long term goal to produce a CFD-based seal rotordynamic model. The Finite Difference Method (FDM) code utilizes McCormack (MCK) scheme along with the Pseudo-Compressibility Method (PCM) to solve Reynolds Averaged Navier-Stokes (RANS) equations in cylindrical coordinates. It was found that combination of MCK and PCM could successfully handle a diverse set of problems while accommodating high performance features such as collocated non-uniform grid, multigrid and parallel computing.

DEDICATION

Dedicated to my parents, Saeid and Mojdeh, who never stopped believing in me.

ACKNOWLEDGEMENTS

I would like to thank my committee chair, Dr. Palazzolo, who gave me the wonderful opportunity to research on the intriguing field of impeller rotordynamics. His patience, guidance and constant encouragement made this work possible.

I am grateful to my committee member, Dr. Donzis, who shared his insight with my numerous CFD questions. I am thankful to my committee members, Dr. Goenezen and Dr. Jarrahbashi, for their support and serving as my committee on such a short notice.

I am very grateful to Dr. Moore of Southwest Research Institute for his support and educating me on the subject of impeller rotordynamics. My appreciation also goes to Dr. Tsujimoto and Dr. Childs, for providing me with indispensable research data and sharing their knowledge with me. I am also thankful to Mr. Mueller of CFturbo for providing us with turbomachinery design tools. I am grateful to Dr. Eunseok Kim and Mr. Moreland who facilitated my research progress in the early days.

My gratitude also goes to my friends and colleagues and the department faculty and staff for making my time at Texas A&M University a great experience. I would like to specially say thanks to my colleagues at VCEL, to Behzad my true friend who provided me with a second home, to Samira and Mehrshad for their support, and to Farnaz for her endless love and support. Finally, thanks to my mother and father for their inspiration each and every day through my Ph.D.

CONTRIBUTORS AND FUNDING SOURCES

Contributors

This work was supervised by a dissertation committee consisting of Professor Palazzolo and Professor Goenezen and Professor Jarrahbasahi of the Department of Mechanical Engineering and Professor Donzis of the Department of Aerospace Engineering.

The experimental data used in Chapter II (seal study) was provided by Mr. James Moreland and Dr. Dara Childs. The data are available in Mr. Moreland's dissertation from Texas A&M University. The experimental data used in Chapter III (volute study) were taken from Dr. Belgacem Jaroux's (Jery) dissertation from CalTech. The geometry depicted in Chapter IV (open impeller study) was provided by Dr. Yoshinobu Tsujimoto and Dr. Hironori Horiguchi from Osaka University and the experimental data were published in 1999 in an article listed in the ASME Journal of Fluids Engineering.

All other work for the dissertation was completed by the student, under the advisement of Professor Palazzolo of the Department of Mechanical Engineering.

Funding Sources

The funding for this project was provided by the Turbomachinery Research Consortium (TRC) at Texas A&M University.

NOMENCLATURE

A	Area, m ²
A^+	Asymptotic constant near the wall
B	Groove depth, m
\hat{B}	Stretch factor parameter
\mathbb{B}	Constant in law of the wall
b_2	Blade outlet width, m
c, C	Cross-coupled and direct damping coefficients, Ns/m
c, \mathcal{C}	Dimensionless cross-coupled and direct damping coefficients
CFL	Courant–Friedrichs–Lewy number; (in 1D $u\Delta t/\Delta x$)
C_{eff}	Effective damping, Ns/m
C_f	Skin friction coefficient; $\left(\frac{\tau_w}{1/2\rho U_\infty^2}\right)$
C_{ij}	Damping coefficient, Ns/m
C_p	Pressure coefficient; $\left(\frac{p-p_{ref}}{1/2\rho U_2^2}\right)$
C_r	Radial clearance, m
C_δ	Mesh deformation exponent
d	Gap A axial length, m
\mathcal{d}	Defect in nonlinear multigrid
D	Diameter, m
D_H	Hydraulic diameter, m
e	Eccentricity, m

\mathbf{E}	Flux vectors in r direction in MacCormack scheme
E_h	H-ellipticity factor
f	Dimensional force, N
f	Source term in nonlinear multigrid
F	Dimensionless force
\overline{F}	Dimensionless forces at zero frequency ratio
\mathbf{F}	Flux vectors in θ direction in MacCormack scheme
f_s	Serial fraction
F_1, F_2	First and second blending functions in BSL and SST models
g	Gravitational acceleration, m/s^2
G	Pressure gradient, N/m^3
\mathbf{G}	Flux vectors in z direction in MacCormack scheme
h	Film thickness, m
H	Pump head, m
\mathbf{H}	Source term vector in MacCormack scheme
III	Heaviside step function
H_{ij}	Dynamic stiffness coefficient, N/m
H_r	Hendrick's seal mixing length constant
I	Turbulence intensity
II	Interpolator operator (restriction and prolongation)
k	Turbulence specific kinetic energy, m^2/s^2
k, K	Cross-coupled and direct stiffness coefficients, N/m

k, \mathcal{K}	Dimensionless cross-coupled and direct stiffness coefficients
K_{ij}	Stiffness coefficient, N/m
l	Turbulent length scale, m
L	Length, m
\mathbb{L}	Linear operator
l_i	Lagrange polynomials
L_M	Inertial length of impeller
$L_2(\phi)$	Second norm of the residual
m, M	Cross-coupled and direct added mass coefficient, kg
\mathcal{m}, \mathcal{M}	Dimensionless cross-coupled and direct added mass coef.
M_{ij}	Virtual mass coefficient, kg
n	Number of grooves
N	Number of nodes
\mathbb{N}	Nonlinear operator
p	Pressure, Pa
p_{in}, p_{out}	Supply and discharge pressure, Pa
P_k	Turbulence production term, m^2/s^3
Q	Flow rate, m^3/s
\hat{q}^m	Empirical convergence factor of order m
r	Radial position, m
R	Rotor radius, m
\mathbb{R}	Residual

Re	Reynolds number; (uL/ν)
Re_T	Turbulence Reynolds number; $(k^{1/2}l/\nu)$
ROT	Switch function for rotating frame
r_2	Impeller discharge radius, m
s	Stretch function
S	Speed-up
\mathcal{S}	Source term
S_R	Roughness scale
\bar{S}_{ij}	Shear rate tensor, 1/s
ss	Double sided stretch function
t	Time, s
t_{ij}	Viscous shear stress tensor, Pa
T	Temperature, $^{\circ}C$
\mathbb{T}	Torque, Nm
t_b	Blade thickness (uniform), m
u	Velocity, m/s
\mathbb{u}	Uncorrected velocity, m/s
u_{τ}	Shear velocity, m/s
\mathbf{U}	Unknown vector, rotational (linear) velocity vector, m/s
\mathbf{v}	Correction velocity, m/s
\mathbf{V}	Absolute (stationary frame) velocity, m/s
v_{θ}	Swirl velocity, m/s

\forall	Cell volume, m ³
w	Defect velocity, m/s
\mathbf{W}	Relative (rotating frame) velocity vector, m/s
W_0	Mean velocity, m/s
x_i	Cartesian coordinate
y^+	Solver Yplus; $\left(\frac{y}{\nu} \sqrt{\frac{\tau_w}{\rho}}\right)$
y	Distance from the wall, m
z	Axial position, m
Z	Number of blades

Greek Symbols

α	Under-relaxation factor
β	Blade angle, °
$\hat{\beta}$	Pseudo compressibility factor, m ² /s ²
β^*	Constant in k - ω model
δ	Mesh displacement, m
Δ	Spacing, amplitude
δ_{ij}	Kronecker delta
Δp	Pressure drop from inlet to outlet, kPa
ε	Roughness, m
ϵ	Eccentricity ratio; (e/C_r)

	Also turbulence specific dissipation, m^2/s^3
ϵ_Δ	Shift in algebraic grid stretching method
η	Efficiency; $\left(\frac{\rho g H Q}{T \omega}\right)$
ϕ	Variable, Also discharge flow coefficient; $\left(\frac{Q}{\pi \omega r_2 D_2 b_2}\right)$
ϕ/ϕ_d	Relative flow rate
φ	Phase angle; Projection angle, rad
γ	Intermittency, also
$\hat{\gamma}$	Constant in k - ω model
Γ_δ	Mesh stiffness, N/m
κ	Constant in law of the wall
λ	Friction factor
μ	Dynamic Viscosity, kg/ms
ν	Kinematic viscosity, m^2/s
ν_t	Eddy viscosity, m^2/s
ω	Rotational speed, rad/s Also turbulence specific dissipation rate, 1/s
Ω	Whirl rotational speed, rad/s
ω_s	Specific speed (metric); $\left(\frac{\omega Q^{\frac{1}{2}}}{(gH)^{\frac{3}{4}}}\right)$
Π	Power coefficient; $\left(\frac{T \omega}{\rho r_2^5 \omega^3}\right)$

ψ	Head coefficient; $\left(\frac{gH}{r_2^2 \omega^2}\right)$
ρ	Density, kg/m ³
ϱ	Stretch factor
τ	Shear stress, Pa
τ_{ij}	Total shear stress tensor, Pa
τ_{ij}^*	Reynolds stress tensor, Pa
θ	Circumferential location
σ_k, σ_ω	Constants in BSL and SST models
ξ	Parametric variable
ζ	Vorticity, 1/s

Subscripts

0	Stationary radial thrust component, Suction
1	Inlet
2	Discharge (outlet)
3	Diffuser
4	Volute
b	Blade
Cir	Circular volute
Conc	Concentric, non-whirling solution
d	Design flow

Dif	Diffuser
Exp	Experiment
<i>fsh</i>	Front shroud
<i>g</i>	Groove
<i>h</i>	Hub
<i>i</i>	In the i^{th} direction, Also at the i^{th} node
Imp	Impeller
∞	Free stream
<i>l</i>	Land; leakage
<i>log</i>	In logarithmic layer
<i>n, t</i>	In normal and tangential direction in the whirling frame
Off	Off-centered spinning
<i>p</i>	Node adjacent to the wall
QS	Quasi-steady model
Rad	Radius based volute
Rec	Rectangular volute
Rnd	Round asymmetric volute
<i>s</i>	Seal
Trn	Transient model
Trp	Trapezoidal volute
θ	In circumferential direction; Denoting momentum thickness
<i>sh</i>	Shroud

v	Diffuser vane
vis	In viscous sublayer
Vol	Volute
w	Wall
x, y	In x and y direction in the stationary frame

Superscript

*	Corrector step
c	Coarse
f	Fine
h, H	Grid size levels
m	At the m^{th} time step
+	Normalized wall quantity
' , ' , '''	Multigrid intermediate values

Abbreviations

API	American Petroleum Institute
AR	Aspect Ratio
ASME	American Society of Mechanical Engineers
BEP	Best Efficiency Point
BC	Boundary Condition

BSL	Baseline
CAD	Computer Aided Design
CFD	Computational Fluid Dynamics
CS	Correction Storage
DOE	Department of Energy
FAS	Full Approximation Storage
FDM	Finite Difference Method
FFT	Fast Fourier Transform
FR	Frequency ratio; (Ω/ω)
FTCS	Forward-Time Central-Space
FVM	Finite Volume Method
FW	Full Weighting
HW	Half Weighting
GS	Gauss-Seidel (iteration method)
LES	Large Eddy Simulation
LHS	Left Hand Side
McCk	MacCormack method
MCK	Mass, damping and stiffness model
MDAO	Multi-Disciplinary Analysis and Optimization
MG	Multigrid
MPI	Message Passing Interface
NS	Navier-Stokes
OSR	Outlet Swirl Ratio, of the seal; ($v_{\theta,out}/R\omega$)

PCC	Pressure Compatibility Condition
PCM	Pseudo Compressibility Method
PDE	Partial Differential Equation
PPE	Pressure Poisson Equation
PSR	Pre-Swirl Ratio, of the seal; $(v_{\theta,in}/R\omega)$
RANS	Reynolds-Averaged Navier-Stokes
RHS	Right Hand Side
RMS	Root Mean Square
RSM	Reynolds Stress Model
SIMPLE	Semi-Implicit Pressure Linked Equations
SOR	Successive Over-Relaxation
SSGR	Smooth Stator-Grooved Rotor
SSME	Space Shuttle Main Engine
SST	Shear Stress Transport
TE	Truncation Error
TRC	Turbomachinery Research Consortium
WFR	Whirl frequency ratio; $(C/k\omega)$

TABLE OF CONTENTS

	Page
ABSTRACT	ii
DEDICATION	iv
ACKNOWLEDGEMENTS	v
CONTRIBUTORS AND FUNDING SOURCES.....	vi
NOMENCLATURE.....	vii
TABLE OF CONTENTS	xviii
LIST OF FIGURES.....	xxiii
LIST OF TABLES	xxxv
1. INTRODUCTION.....	1
1.1. Problem Statement and Motivation.....	1
1.2. Background	3
1.2.1. Turbomachinery	3
1.2.2. Impeller and Seal Types	6
1.2.3. CFD	9
1.2.4. Whirling Motion.....	10
1.2.5. Rotordynamic Forces and Rotordynamic Instability.....	12
1.3. Literature Review.....	20
1.3.1. Experimental Studies.....	20
1.3.1.1. Seals	20
1.3.1.2. Impellers.....	22
1.3.2. Theoretical Studies	26
1.3.2.1. Bulk-Flow theory	26
1.3.2.2. Potential flow theory	28
1.3.2.3. Actuator disk theory.....	32
1.3.3. CFD Studies	33
1.3.3.1. 2D perturbation CFD models	33
1.3.3.2. 3D quasi-steady models	33
1.3.3.3. Hybrid CFD Bulk-Flow model	36
1.3.3.4. 3D transient models.....	36
1.4. Objectives.....	37

1.5. Novelties and Contributions.....	38
2. ROTORDYNAMIC FORCES OF A ROTOR-GROOVED LIQUID ANNULAR SEAL: A QUASI-STEADY CFD-BASED APPROACH	40
2.1. Introduction	40
2.2. Methodology	44
2.3. Numerical Modeling	47
2.3.1. Computational Domains.....	47
2.3.2. Grid Quality and Convergence.....	50
2.3.3. Boundary Conditions and Solver Settings.....	54
2.4. Results	55
2.5. Conclusion.....	70
3. ROTORDYNAMIC FORCES OF VOLUTES AND DIFFUSERS: A TRANSIENT CFD APPROACH.....	72
3.1. Introduction	72
3.2. Design Parameters and Dimensions.....	77
3.3. Numerical Methodology	81
3.3.1. Computational Domains.....	81
3.3.2. CFD Set-up.....	83
3.3.3. Mesh Deformation.....	83
3.3.4. Force Extraction Method.....	87
3.3.5. Shroud, Diffuser and Volute Force Extraction.....	92
3.3.6. Model Error	95
3.3.7. Grid Independency	98
3.4. Results and Discussion.....	102
3.4.1. Validation	102
3.4.2. Volute and Diffuser Rotordynamic Forces	105
3.4.3. Impact of Clearance, Gap A and Spin Speed	110
3.5. Conclusion.....	114
4. OPEN IMPELLER ROTORDYNAMIC FORCES: A TRANSIENT MULTI-FREQUENCY CFD APPROACH.....	116
4.1. Introduction	116
4.2. Geometry and Dimensions	118
4.3. Numerical Methodology	121
4.3.1. CFD Set-up.....	121
4.3.2. Computational Domains.....	121
4.3.3. Transient Analysis.....	122
4.3.4. Grid Independency	129
4.4. Results and Discussion.....	130
4.4.1. Validation	130
4.4.2. Rotating Stall.....	134

4.4.3. Specific Speed Effect	137
4.4.4. Bumps and Dips in Closed Impellers	150
4.5. Conclusion.....	154
5. STANDALONE CFD CODE FOR LIQUID ANNULAR SEALS	157
5.1. Introduction	157
5.2. Governing Equations.....	158
5.2.1. Momentum and Continuity Equations	158
5.2.2. Rotating Frame	160
5.2.3. Turbulence Modeling	161
5.2.3.1. Wilcox $k-\omega$	162
5.2.3.2. Menter's BSL	166
5.2.3.3. Menter's SST.....	171
5.2.3.4. Production Limiter	172
5.2.3.5. Wilcox Low-Re version of $k-\omega$	172
5.3. Pseudo-Compressibility Method.....	174
5.4. MacCormack Scheme	175
5.4.1. 2D Cartesian Version	178
5.4.2. 3D Cylindrical Version	181
5.5. SIMPLE Method	187
5.6. Stability	190
5.7. Non-uniform Discretization	192
5.7.1. Bulk of Fluid	192
5.7.2. Boundary Conditions.....	194
5.7.3. Algebraic Grid Spacing Formulation	197
5.7.3.1. An alternative algebraic method.....	199
5.7.3.2. A hybrid approach.....	200
5.7.3.3. Comparison of algorithms.....	200
5.7.3.4. 2D and 3D non-uniform mesh generation.....	203
5.8. Boundary Conditions	205
5.8.1. Wall	205
5.8.2. Roughness Treatment.....	206
5.8.3. Inlet.....	207
5.8.4. Outlet.....	208
5.8.5. Symmetry	209
5.8.6. Periodic.....	209
5.8.7. Interface.....	211
5.9. Wall-Function.....	212
5.9.1. Wall-Function Implementation	215
5.9.2. Wall Roughness Modeling for Wall-Functions.....	216
5.9.3. Connecting Log-layer to the Wall.....	217
5.9.4. Automatic Wall-Functions	217
5.9.5. Swirling Flow Wall-Functions	219
5.10. Multigrid.....	224

5.10.1. Ellipticity	224
5.10.2. A Comparison of Elliptic Solvers	224
5.10.3. Parallelizability vs Smoothing	225
5.10.4. H-Ellipticity Measure	226
5.10.5. Transfer Operators	227
5.10.6. Cycles and Numerical Efficiency	229
5.10.7. Multigrid Solver	230
5.10.7.1. Linear 2D multigrid example	232
5.10.8. Nonlinear Multigrid	239
5.10.8.1. 1D nonlinear multigrid example	240
5.10.8.2. 2D nonlinear multigrid example	247
5.11. Pressure Compatibility Condition	248
5.11.1. Adaptation to Pseudo-Compressibility Method	250
5.12. Parallel Version	253
5.12.1. MPI	253
5.12.2. Speed-up Expectation	254
5.12.3. MPI Laminar Helical Flow	255
5.12.3.1. Overlap	257
5.12.3.2. Explicit BC and synchrony	258
5.12.3.3. Partition sizing	258
5.12.3.4. Results	259
5.12.4. MPI Turbulent Annular Seal	260
5.12.4.1. Collective operations	261
5.12.4.2. Two by two communications	262
5.12.4.3. Speed-up results	264
5.12.4.4. Load balancing	264
5.12.4.5. Extra wall load	266
5.12.4.6. Improving parallel performance	267
5.13. Validation	269
5.13.1. Cavity Flow in Cartesian Coordinate	269
5.13.2. Taylor-Couette Flow in Stationary Frame	271
5.13.3. Fully Developed Steady Helical Flow Inside an Annulus	273
5.13.4. Backward Facing Step Flow	278
5.13.5. Wall-function and Low-Re Predictions for Pipe Flow	282
5.13.6. Low Re Seal Leakage	285
5.13.7. High Re Seal Leakage	287
5.13.8. 3D Seal Leakage	292
5.14. Conclusion	296
6. CONCLUSION	297
6.1. Commercial CFD Approach	297
6.2. Standalone CFD Code	300
6.3. Future Work	300
6.3.1. Linear Stability Analysis for Bumps and Dips	300

6.3.2. Phase Averaging for Concurrent Frequencies	301
6.3.3. Modified Alford Force Model	301
6.3.4. Impeller Rotordynamic Forces in Reverse Operation	302
6.3.5. Potential Flow-Based Impeller Rotordynamic Forces	302
6.3.6. High Fidelity Turbulence Modeling	303
6.3.7. Novel 2D Axisymmetric Methods for Rotordynamic Forces ..	303
REFERENCES	304
APPENDIX A CFX SOLVER THEORY	328
A.1. Discretization of Governing Equations	328
A.2. High Resolution Scheme	330
A.3. Pressure-Velocity Coupling	331
A.4. Mesh Deformation	332
A.5. Eddy Viscosity Turbulence Modeling	332
A.6. Curvature Correction	333
A.7. Automatic Near Wall Treatment	334
A.8. Transition Modeling	335
APPENDIX B CFTURBO DESIGN PROCEDURE	337
APPENDIX C CFX SAMPLE SET-UP FILE FOR A WHIRLING OPEN IMPELLER	361
APPENDIX D MACCORMACK DISCRETIZATIONS FOR NON- UNIFORM GRID	374

LIST OF FIGURES

	Page
Figure 1. Schematic of some components of a turbomachine.....	4
Figure 2. Impeller classification as centrifugal, mixed and axial.....	7
Figure 3. Closed impeller versus open impeller.....	8
Figure 4. Some annular seal variations	8
Figure 5. Typical task procedure for a CFD solution.....	10
Figure 6. Schematic of an eccentric rotor with a circular whirling motion. The dimensions are exaggerated for illustration purposes.....	11
Figure 7. Impeller eccentric motion. (a) whirling motion (b) precession motion	12
Figure 8. Fluid induced rotordynamic force model.....	13
Figure 9. A typical impeller or seal impedance shape	14
Figure 10. Bernoulli effect causing a negative stiffness in blade to blade plane	15
Figure 11. Alford force caused by the asymmetric tip clearance efficiency causes a cross-coupled stiffness.....	16
Figure 12. Lomakin effect in the meridional plane forms a restoring normal force	17
Figure 13. Magnus effect due to interaction of impeller circulation and whirling velocity lifts the impeller.....	18
Figure 14. Self-excited rotordynamic instability by impellers and seal fluid induced forces	19
Figure 15. Test rig used to measure open impeller rotordynamic forces (reprinted from [66]).....	23
Figure 16. Bulk-Flow modeling for turbulent thin film flows	27
Figure 17. Sample potential flow impeller modeling (singularity method) by distribution of sources and vorticities	29

Figure 18. Typical frequency ratios that impeller and diffuser rotating stall may appear	31
Figure 19. Negative stiffness.....	41
Figure 20. Schematic of the seal and dimensions	43
Figure 21. Quasi-steady circular whirling motion in CFD modeling	45
Figure 22. Computational domains used for CFD simulation	49
Figure 23. Swirl injectors at radial injection configuration.....	49
Figure 24. Swirl injectors added to the model	50
Figure 25. Mesh inside each groove.....	51
Figure 26. Exploded view of the grid.....	51
Figure 27. Grid convergence.....	52
Figure 28. Suppressed back flow at inlet chamber and flow streamlines at inlet plenum	56
Figure 29. Flow reattachment in extension annulus.....	57
Figure 30. Pressure and swirl ratio variation at $r=50.9\text{ mm}$ in the inlet plenum, seal and outlet chamber.....	57
Figure 31. Leakage, pre-swirl and outlet swirl ratio versus frequency ratio.....	58
Figure 32. Dynamic stiffness $Re(H_{ii})$ variation versus excitation frequency (experimental data adapted from [49])	59
Figure 33. Dynamic stiffness $Re(H_{ij})$ variation versus excitation frequency (experimental data adapted from [49])	59
Figure 34. Dynamic stiffness $Im(H_{ii})$ variation versus excitation frequency (experimental data adapted from [49])	60
Figure 35. Dynamic stiffness $Im(H_{ij})$ variation versus excitation frequency (experimental data adapted from [49])	60
Figure 36. Normal and tangential forces acting on the rotor	64
Figure 37. Effect of rotor speed on leakage (experimental data adapted from [49]).....	65

Figure 38. Effect of Δp on leakage (experimental data adapted from [49]).....	66
Figure 39. Effect of roughness on leakage, PSR & OSR.....	67
Figure 40. Effect of roughness on normal and tangential impedances at $\Omega=0$	68
Figure 41. Several commercial CFD methods to model impeller rotordynamic forces.....	75
Figure 42. Schematic of Gap A configurations.....	77
Figure 43. Pump dimensions. (a) main dimensions (b) narrow versus wide clearance	79
Figure 44. Volute designs from CFturbo. (a) circular (b) radius based (c) rectangular (d) round asymmetric (e) trapezoidal.....	80
Figure 45. Exploded view of the computational domains.....	82
Figure 46. Mesh deformation boundary conditions. (a) blade to blade view (b) meridional view.....	85
Figure 47. Gradual mesh deformation and the lag in e_x (red curve)	86
Figure 48. Sample FFT of the dimensionless forces in the stationary frame at $\Omega/\omega=-0.6$	87
Figure 49. Zero frequency ratio force extraction	91
Figure 50. Shifted grid for the quasi-steady model.....	92
Figure 51. Axisymmetric nozzle added after the diffuser and the volute removed.....	93
Figure 52. Pressure monitor at diffuser throat marked with yellow crosses.....	94
Figure 53. Pressure pulsations at diffuser vanes indicate no sign of stall.....	94
Figure 54. Fictitious force due to the fixed axis of spin.....	96
Figure 55. Quasi-steady dimensionless normal and tangential forces with centered and off-centered spinning motion (eccentricity $e=1.26$ mm)	98
Figure 56. Grids used in the mesh independency study.....	99

Figure 57. Grid independency results. ψ is the head coefficient, η the efficiency and RMS_F shows the RMS of force value departure from the finest mesh values	101
Figure 58. Dimensionless dynamic forces from various grid densities	101
Figure 59. Experimental and numerical pump characteristics (experimental data adapted from [73]).....	102
Figure 60. Dimensionless normal and tangential forces, predictions versus experiments. QS and Trn correspond to quasi-steady and transient, respectively (experimental data adapted from [73])	104
Figure 61. The trapezoidal volute rotordynamic forces versus the impeller for the wide clearance configuration	105
Figure 62. Total dimensionless normal and tangential forces of the same impeller working with various volutes	106
Figure 63. Contributions of the impeller and various volutes to the total normal and tangential forces.....	107
Figure 64. Contributions of the diffuser and the volute to the total normal and tangential forces.....	109
Figure 65. The quasi steady model predictions follow the transient results closely for the narrow clearance configuration. Trapezoidal volute is included in both cases	110
Figure 66. Transient force predictions of the narrow versus wide clearance. Trapezoidal volute is included in both cases	111
Figure 67. Gap A influence on the dynamic forces.....	112
Figure 68. Independency of the dimensionless normal and tangential forces from the spin speed (experimental data adapted from [73]).....	113
Figure 69. The whirling open impeller and its rotordynamic forces.....	119
Figure 70. Meridional view of the open impellers for various specific speeds	120
Figure 71. Computational domains (a) impeller (b) Upstream and downstream components.....	122
Figure 72. Mesh quality after 4 whirling cycles for $\epsilon=0.5$. Note the folded (detached) cells at the upper side of the propeller in the temporal case.....	124

Figure 73. Mesh orthogonality angle well preserved with the complex periodic approach.....	125
Figure 74. Transient phase modulated multi-frequency modeling. (a) The orbit (b) The imposed phases at each frequency.....	127
Figure 75. Grid independency results for the open impeller.....	130
Figure 76. The open impeller head-flow characteristic in the pump mode (experimental data adapted from [66])	131
Figure 77. Predictions of CFD-based rotordynamic forces vs experiments (experimental data adapted from [66]) at multiple flow rates: (a) $\phi=0.185$ (b) $\phi=0.424$ (c) $\phi=0.330$ (d) $\phi=0.508$	132
Figure 78. Comparison of single frequency vs multi frequency results at $\phi=0.330$ (experimental data adapted from [66]).....	133
Figure 79. Sudden jump appearing at $\phi=0.285$, $\Omega/\omega=0.79$ in the original experimental study (adapted from [66])	134
Figure 80. Non-dimensional forces in the stationary and the whirling frames at $\phi=0.285$	135
Figure 81. Rotating stall appearing in CFD results. Co-rotating stall at the impeller eye at $\phi=0.285$, $\Omega/\omega=0.83$	136
Figure 82. $C_p=-0.15$ iso-surface showing the three lob tip vortex structure.....	137
Figure 83. Design and simulation characteristics of the investigated open impellers. Filled markers denote the design values and blank markets show the simulated values.....	139
Figure 84. Rotordynamic forces of the original and the scaled impeller for the same eccentricity ratio and flow coefficient.....	140
Figure 85. Effect of the specific speed on the rotordynamic forces of the open impellers. (a) normal forces (b) tangential forces.....	141
Figure 86. Off-flow rotordynamic forces for $\omega_s=0.3$. (a) normal forces (b) tangential forces.....	144
Figure 87. Off-flow rotordynamic forces for $\omega_s=0.6$. (a) normal forces (b) tangential forces.....	144
Figure 88. Off-flow rotordynamic forces for $\omega_s=0.9$. (a) normal forces (b) tangential forces.....	145

Figure 89. Off-flow rotordynamic forces for $\omega_s=1.2$. (a) normal forces (b) tangential forces	145
Figure 90. Off-flow rotordynamic forces for $\omega_s=1.8$. (a) normal forces (b) tangential forces	146
Figure 91. Phase averaging schematic	147
Figure 92. Stiffness values for $\omega_s=0.3$ versus the relative flow rate. \mathcal{K} is the dimensionless direct stiffness and \mathcal{K} is the dimensionless cross-coupled stiffness.....	148
Figure 93. New dimensionless format for rotordynamic forces for various specific	150
Figure 94. Isolated leakage path model ILPM for the impeller related flows	151
Figure 95. Comparison of rotordynamic forces for closed impeller, open impeller and ILPM. (a) normal forces (b) tangential forces	152
Figure 96. Bumps and dips in ILPM getting stronger as the inlet swirl velocity increases by a factor of 3. (a) normal forces (b) tangential forces	153
Figure 97. Concentric ILPM results showing a minuscule peak at $\Omega/\omega=0.2$ for the inflow swirl condition of $2V_\theta$	154
Figure 98. BSL blending function.....	170
Figure 99. Vorticity magnitude in BSL model.....	170
Figure 100. Staggered grid	177
Figure 101. FTCS method (a) Pressure field with staggered grid. (b) Pressure field with collocated grid. I and J shows the node number in x and y directions	178
Figure 102. Comparison of on-uniform distribution schemes	201
Figure 103. Aspect ratio distribution.....	202
Figure 104. Grid generation flow chart.....	204
Figure 105. Uniform grid	204
Figure 106. Non-uniform grid.....	205

Figure 107. Correct implementation of periodic boundary conditions	210
Figure 108. Steps to implement periodic boundary conditions.....	211
Figure 109. Bilinear interpolation	211
Figure 110. Wall-function implementation flow chart.....	216
Figure 111. Swirling wall-function	223
Figure 112. V and W cycles for 3 level multigrid.....	229
Figure 113. Restriction from fine grid to coarse grid.....	231
Figure 114. Prolongation from the coarse grid to fine	232
Figure 115. Left) original domain. Middle) Prolonged fine domain. Right) Restricted coarse domain	233
Figure 116. Revised 4 level multigrid V cycle.....	234
Figure 117. (a) Boundary conditions. (b) Exact solution.....	235
Figure 118. (a) Numerical multigrid solution (b) Exact solution.....	237
Figure 119. Multigrid converged residuals on (a) Coarse grid (b) Medium grid	237
Figure 120. Convergence history of multigrid versus single grid.....	239
Figure 121. FAS multigrid algorithm for 4 level V cycle.....	244
Figure 122. FAS solution converges on all levels (CS solution only converges on the fine grid).....	245
Figure 123. Accelerated convergence rate of McCk with FAS MG scheme	246
Figure 124. SIMPLE solution to cavity flow at Re=1000 on 65 by 65 grid, using pressure compatibility condition	250
Figure 125. Pressure fields at Re=100 for cavity flow with and without PCC	252
Figure 126. Continuity equation residual with and without PCC	252
Figure 127. Typical parallelizing steps using MPI	254
Figure 128. Boundary conditions for the laminar helical flow	256

Figure 129. Radial partitioning of the annular domain	256
Figure 130. Overlapping cells and passing boundary conditions.....	257
Figure 131. Speed-up achieved for helical flow with MPI parallel	259
Figure 132. MPI broadcast operation	261
Figure 133. MPI allreduce operation used to set the global time step	262
Figure 134. Two by two communication	263
Figure 135. Balancing the loads of the partitions.....	266
Figure 136. Speed-up improvement for the turbulent annular seal code after adding load balance.....	268
Figure 137. Communication time.....	269
Figure 138. a) $Re=1$ $\beta=0.1$. b) $Re=100$ $\beta=100$.c) $Re=1000$ $\beta=10$	270
Figure 139. Cavity flow $Re=100$,(a) Current CFD code, (b) Hirsch (adapted from [249]).....	270
Figure 140. Pressure distribution $Re=10$	271
Figure 141. Confined flow in cylindrical coordinate	272
Figure 142 . Secondary flows in an annular cavity with rotating outer wall at $Re_{\theta}=600$	272
Figure 143. Schematic of helical flow geometry	273
Figure 144. Change of frame.....	275
Figure 145. Helical flow, CFD vs exact solution	277
Figure 146. Helical flow pressure, CFD vs exact solution.....	277
Figure 147. Backward facing step, pressure field	279
Figure 148. Backward facing step, axial velocity field.....	280
Figure 149. Current code prediction vs literature (validation adapted from [254]).....	281
Figure 150. Pressure-pressure CFD solution of rotating BFS with $PSR=0.0$	282

Figure 151. Fully developed turbulent pipe flow boundary conditions	283
Figure 152. Velocity profile prediction of Low Re model, high Re with wall- function and power law	284
Figure 153. Velocity prediction of low Re and laminar versions of the code for a annular seal of Re=3037	286
Figure 154. Convergence plot at $\Delta p=6.89 \text{ MPa}$, $\omega=10200 \text{ rpm}$, Re=10300	288
Figure 155. Axial and circumferential velocity profiles at $\Delta p=6.89 \text{ MPa}$, $\omega=10200 \text{ rpm}$, $Re_z=9000$, $Re_\theta=5000$	288
Figure 156. Developing flow and computational grid at $\Delta p=6.89 \text{ MPa}$, $\omega=10200 \text{ rpm}$ and Re=10300	289
Figure 157. Pressure drop profile at $\Delta p=6.80 \text{ MPa}$, $\omega=10200 \text{ rpm}$ and Re=10300	290
Figure 158. Axial and circumferential velocity profiles at $\Delta p=4.14 \text{ MPa}$, 5.52 MPa , 6.89 MPa	291
Figure 159. Periodic BC schematic	292
Figure 160. Annular seal 3D mesh (non-uniform)	293
Figure 161. Velocity vectors inside the 3D laminar seal at Re=1075	294
Figure 162. Pressure drop in the 2π model seal. Note that the discontinuity in periodics disappear upon convergence	294
Figure 163. Element-based finite volume method, 2D representation	329
Figure 164. Select a pump project	337
Figure 165. Provide operational condition at BEP	337
Figure 166. Select to create a new impeller	338
Figure 167. Provide the main dimensions	339
Figure 168. Select meridional contour	339
Figure 169. Accept or modify the hub and shroud profiles	340
Figure 170. Add the hub and shroud thicknesses	341
Figure 171. Select blade properties	341

Figure 172. Set number of blades.....	342
Figure 173. Set the blade angles.....	342
Figure 174. Select blade meanlines icon.....	343
Figure 175. Design the meanlines.....	343
Figure 176. Select blade profiles.....	344
Figure 177. Input the desired blade thickness distribution.....	344
Figure 178. Select blade edges.....	345
Figure 179. Fillet and trim the leading and trailing edges of the blades.....	345
Figure 180. Select 3D model for inspection.....	346
Figure 181. The 3D view of the created impeller.....	346
Figure 182. Add extension to the impeller.....	347
Figure 183. Add another component after impeller.....	348
Figure 184. Set the diffuser dimensions.....	348
Figure 185. Set the diffuser vane properties.....	349
Figure 186. Define the meanline properties.....	350
Figure 187. Impeller and diffuser 3D view.....	351
Figure 188. Add a volute.....	351
Figure 189. Set inlet dimensions of the volute.....	352
Figure 190. Select the cross section step.....	352
Figure 191. Select the volute cross section shape.....	353
Figure 192. Select spiral areas.....	353
Figure 193. Set the area progression settings.....	354
Figure 194. Select diffuser.....	354
Figure 195. Add a diffuser to the volute.....	355

Figure 196. Select cutwater	355
Figure 197. Set the cutwater angular position	356
Figure 198. The 3D view of the impeller, diffuser and the volute	356
Figure 199. Go to the volute CFD setup	357
Figure 200. Add pipe extension	357
Figure 201. Add a new stator before the impeller	358
Figure 202. Define the suction pipe extent	359
Figure 203. Model with suction pipe	359
Figure 204. Go to export module	360
Figure 205. Export the CAD model	360
Figure 206. Apply turbo rotation for a full 360 degree model	361
Figure 207. Import the computational domains	362
Figure 208. Transient analysis settings	362
Figure 209. Select the mesh locations and the fluid type	363
Figure 210. Mesh deformation settings	364
Figure 211. Turbulence settings	365
Figure 212. Blade boundary conditions	366
Figure 213. Shroud boundary conditions	367
Figure 214. Interface location and frame settings	367
Figure 215. Interface connection settings	368
Figure 216. Internal interface settings	368
Figure 217. Interface mesh motion boundary condition	369
Figure 218. Solver settings	369
Figure 219. Define expressions	370

Figure 220. Array of frequencies and phases used in this case.....	371
Figure 221. Define output monitors	371
Figure 222. Single frequency complex displacement model	372
Figure 223. Periodic displacement BC on the blade and hub	373
Figure 224. Define whirling frequency	373

LIST OF TABLES

	Page
Table 1. Seal dimensions (adapted from [49])	44
Table 2. Sub-domain grid sizes	53
Table 3. Operational conditions (adapted from [49]).....	55
Table 4. Rotordynamic coefficients comparison (experimental data adapted from [49])	62
Table 5. Dimensions and operating conditions provided (adapted from [73].) The shroud thickness t_{sh} and the diffuser inlet width b_3 are found from inverse design using CFTurbo	78
Table 6. Grid size break-down	81
Table 7. Grid sizes selected for the grid independency study	98
Table 8. Force coefficient predictions (experimental data adapted from [73]).....	104
Table 9. Impeller and volute rotordynamic coefficients	108
Table 10. Comparison of impeller, diffuser and volute rotordynamic coefficients	109
Table 11. Impact of the clearance profile on the rotordynamic coefficients.....	111
Table 12. Impact of the Gap A on the rotordynamic coefficients.....	112
Table 13. The design parameters and the operating conditions of the validation impeller (adapted from [66])	119
Table 14. Design properties of the specific speed study impellers	120
Table 15. Grid sizes selected for grid independency study.....	129
Table 16. Scaled impellers' dimensionless groups	140
Table 17. Comparison of the open impeller rotordynamic force coefficients versus specific speed, for the same eccentricity ratio ($\epsilon=0.005$) at the design flow ($\phi/\phi_d=1$).....	142
Table 18. Assessment of various grid distributions	203

Table 19. Comparison of efficient elliptic solvers (adapted from [240]).....	225
Table 20. Smoothing vs parallelizability (adapted from [240])	226
Table 21. Speed-up achieved using 2D Multigrid.....	238
Table 22. FAS speed-up on 65 node grid.....	245
Table 23. FAS multigrid speed-up for cavity flow at Re=1000.....	248
Table 24. Speed-up and solution time data for the 256×64 grid	260
Table 25. Speed-up results for turbulent annular seal on a 64×64 grid with L ₂ (w _z)=10 ⁻⁴	264
Table 26. Improved speed-up results	267
Table 27. Boundary conditions for helical flow inside an annulus	276
Table 28. Boundary conditions for backward facing step.....	279
Table 29. Low Re results vs High Re <i>k-ω</i> with wall-functions	282
Table 30. Skin friction CFD versus Moody chart at Re=6500.....	284
Table 31. Plain annular seal dimensions and operational conditions.....	285
Table 32. Leakage and Re validation (experimental data adapted from [49])	285
Table 33. High Re plain annular seal dimensions and operational conditions (adapted from [50]).....	287
Table 34. Leakage rates vs pressure drop (experimental data adapted from [50])	290
Table 35. Leakage prediction results in 3D turbulent mode	295
Table 36. Computational cost of 2D and 3D modes for L ₂ (w _z)=10 ⁻⁵	295

1. INTRODUCTION

1.1. Problem Statement and Motivation

Turbomachinery industry relies on rotating equipment to produce power, convert energy and transfer energy in form of high pressure flow. As the technology advances and competition inclines, the turbomachinery industry pushes for denser and more economic power generation. To achieve the same level of power at smaller dimensions, the rotational speed of the machine has to rise which causes new technical and reliability issues.

A high speed machine faces larger imbalance forces, has to operate in between critical speeds, needs more effective sealing technology, has an increased chance of centrifugal and thermal growth and rubbing may occur, and finally is exposed to larger transient fluid-induced forces [1]. All of these mean that the machine should be able to endure larger vibration amplitudes or be able to damp them effectively, while operating on a stable condition. Many industrial reports and case studies indicate that this is not the case, and large size power plants or chemical plants has to be shut down due to unstable rotordynamic operation [2-4]. One of the famous cases is the Space Shuttle Main Engines (SSME) turbopump rotordynamic instability problem which incurred a cost of \$100 million in 6 months [5, 6]. Other well-known example is the rotordynamic instability problem of Ekofisk multi-stage gas injection compressor. During this instability occurrence, an estimated 100,000 barrels of oil was lost each day [7]. Such temporary down times incur heavy costs in terms of lost product and maintenance. The affected industries include but are not limited to: Oil & Gas, Power, Agriculture,

Petrochemical, Wastewater, Aviation, etc. For the pump industry alone, according to the United States Department of Energy (DOE) [8], pumping systems account for 20% of total energy usage in the world. Pumps on average hold 40% share of the total industrial energy consumption. About 40% of total life cycle cost of a pump stems from maintenance cost which is directly affected by the impeller and seal rotordynamic performance. Furthermore, the current research has been funded by 35 turbomachinery companies named as “Turbomachinery Research Consortium” (TRC) which explains the significance of this topic for the turbomachinery industry*.

Despite this fact, some components in a turbomachine have not been rigorously analyzed for their impact on the rotordynamic stability of the machine. This is partly due to the multi-disciplinary knowledge required to study the fluid-solid interaction forces. Some components have received more attention owing to their simpler geometrical analysis or simply larger share of rotordynamic contribution. Of such, one can name hydrodynamic bearings [9], shafts themselves [10, 11], and seals [1, 12], to the point that they are the primary subject of textbooks. On the other hand, components such as impellers and volutes do not easily lend themselves to analysis. As a result of which, there is a scarcity of available data for these components as well as a lack of physical understanding of the underlying physical mechanism in play [13].

Considering the new expectations from the rotor and the lack of knowledge on the rotordynamic behavior of components such as impellers, it is the role of the rotordynamist to adapt and develop tools for the safe operation of the rotor. The

* <https://turbolab.tamu.edu/trc/>

author's experience with industrial partners shows that many rotordynamists still use unreliable algebraic relations (such as Wachel formula [14]) to model impeller rotordynamics which simply denotes the lack of impeller models available to them. Accordingly, the American Petroleum Institute (API) has provisioned standard obligations to ensure the rotordynamic stability of the rotating machinery [15, 16]. On occasions when such guidelines fail to suppress instabilities, a level II stability analysis should be performed to accurately model the forces caused by the secondary components such as impellers. Such accurate analysis often falls under the category of Computational Fluid Dynamics (CFD) modeling. Moreover, the application of CFD in rotordynamics obviates the need for many costly experimental procedures and test rigs. An established model will eventually substitute experiments owing to its efficiency, accuracy and low cost. Throughout this work, the data have been validated against high quality experimental data whenever possible. Repeated validations will support the implementation of these models instead of time consuming expensive experiments.

In this section, an overview of the topic of impeller and seal rotordynamic forces is delivered. An introductory background further clarifies closely related areas such as turbomachinery, rotordynamics and CFD. The literature review of the topic is concluded with a discussion on the objectives and novelty of the current work.

1.2. Background

1.2.1. Turbomachinery

Turbomachines are types of a special class of machines that use rotation as a means to convert or transfer energy. These machines can retract energy such as turbines

or inject energy such as pumps and compressors. The rate of energy conversion is typically controlled by the rotational speed of the shaft. The shaft or the rotor connects various rotating equipment together and transfers the energy through rotation. This complex rotating system is composed of certain necessary components such as impellers, bearings, seals, gears and couplings, diffusers and volutes, dampers, etc. Some of the components involved in the current problem are demonstrated in Figure 1.

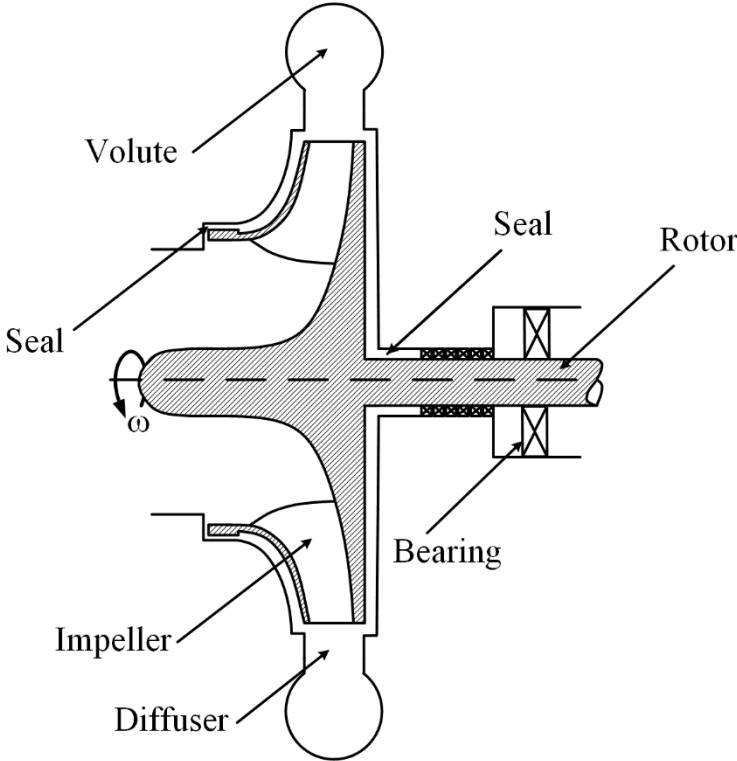


Figure 1. Schematic of some components of a turbomachine

In the heart of any turbomachine, there is an impeller which interacts with the fluid. The purpose of the impeller is to either to absorb power from the flow, or to

pressurize the flow (inject power) or to simply transfer the fluid by injecting momentum. For example, a turbo-pump impeller is either designed to deliver high values of head H (pressure in the form of column of water) which is typical of highly radial impellers, or to provide flow rate Q which is typical of highly axial impellers [17]. The rotating impeller at radius r has a linear velocity of $u = r\omega$. The suction pipe delivers some fluid to the impeller, as the fluid conveys through the impeller channel (r is rising), the velocity component in the stationary frame increases. Therefore, the fluid passing through the impeller picks up this speed and has a high content of kinematic energy. In other words, impeller is controlling the fluid level of energy through this kinematic condition. The higher the dimensions and rotational speed of the pump, the more power it uses. And so is larger the side effects such as axial and radial thrust due to the impeller pressure level [18].

Bearings are other types of rotating equipment which are present in any turbomachine in order to carry the dynamic and static loads caused by primary or secondary components connected to the shaft. Each component excites the rotor in certain way, and naturally the shaft has to go through these forced vibrations and critical speeds within safe operating margins [16]. Thus, dynamic forces caused by the impellers have to be handled in a reliable fashion by the bearings. The bearings themselves affect the mode shapes of the shaft and therefore play a key role in the ultimate dynamic fluid forces rising from shaft vibrations [19]. That said, in the current work certain types of pre-determined motions are imposed and the effects of bearings are not studied.

The pressurized fluid needs to be contained within the components of the machine. Leakage causes product loss, hazardous operation and reduced efficiency. Appropriate types of seals limit the leakage rate. The sealing is typically achieved by forming a very tight clearance in order of $100 - 200\mu m$ or larger between rotating and stationary parts. A tight film thickness means large pressure and velocity gradients. Therefore, any asymmetry in the seal clearance can lead to large fluid induced forces [20].

Finally, the high content of energy in the impeller has to be converted into potential energy. It is the role of diffusers and side channels (in multi-stage machines) to gradually expand the flow in order to convert velocity into pressure. A collector (also known as volute or spiral casing) collects the pressurized fluid and direct it into a discharge pipe. The volute's cross sectional area increases as it collects more fluid in order to keep the same level of pressure around the impeller. This way there is no side load acting on the impeller and the shaft [21].

1.2.2. Impeller and Seal Types

Impellers often have a 3D design. As the head and flow requirements of the impeller vary, the design parameters converge to certain classes of impeller shapes [22]. More specifically, the high head low flow impellers assume a centrifugal shape with an axial entry and radial exit. High flow low head impellers fall under the category of axial impellers with axial entry and exit. The intermediate levels of relative pressure-flow assume a mixed flow shape, marked by an axial entry, but a discharge which is in between radial and axial (See Figure 2). In the current work, the centrifugal type has

received the most attention due to its wider application and the 3D nature of the flow which is out of reach by 2D models.

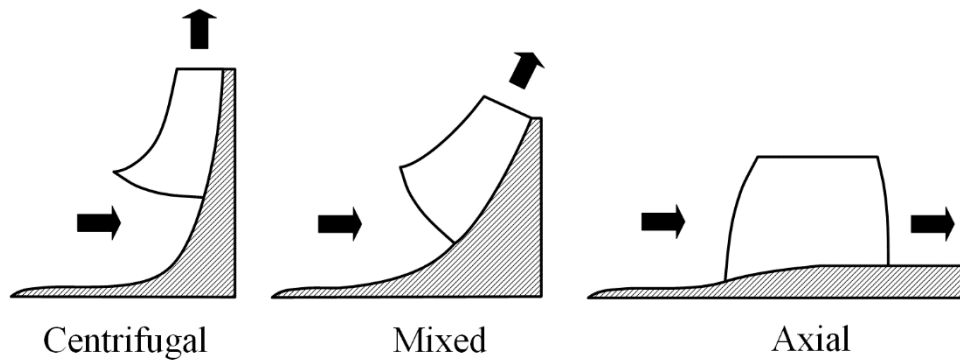


Figure 2. Impeller classification as centrifugal, mixed and axial

The impeller primary channel is enclosed by a hub (inner) and a shroud (outer) curve. Usually both curves represent solid rotating walls and a closed impeller is formed by the blades, hub and the shroud. Depending on the application, the shroud can be removed, in which case, an open impeller (also known as unshrouded impeller) will be resulted. Figure 3 compares a closed impeller to an open impeller. There are relatively smaller scenarios also present that both the hub and shroud are removed and the impeller is a fully open impeller [23]. In the current dissertation, an open impeller always refers to centrifugal unshrouded impellers.

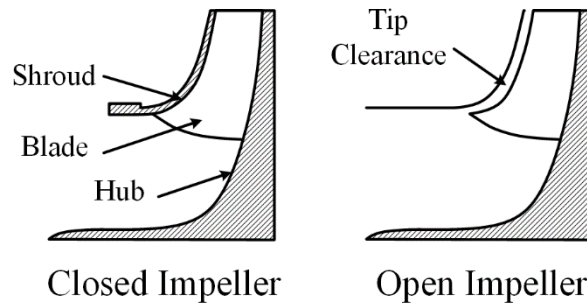


Figure 3. Closed impeller versus open impeller

Annular seals have relatively simpler designs. Liquid annular seals can be as simple as a plain annulus with a tight clearance. Sometimes grooves, spirals or knurlings are introduced on the surface of either the rotor side or the stator side to further increase the pressure drop and reduce the leakage rate [24]. Gas seals use other types of popular designs such as labyrinth seals which looks like a saw-tooth profile (basically more complex grooved version), and damper seals. Damper seals introduce a pattern of pockets (rectangular, hole-pattern, honeycomb, ...) to further introduce pressure drop and at the same time provide damping for the rotor [25]. Figure 4 shows some of these seal types. In this study, only liquid annular seals have been investigated.

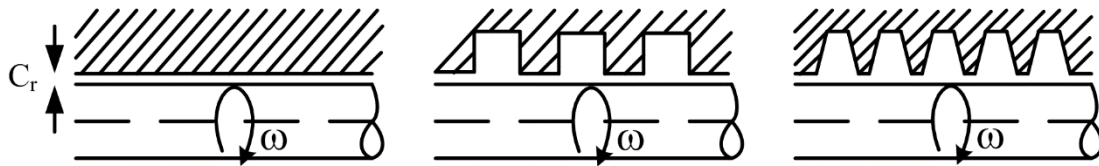


Figure 4. Some annular seal variations

1.2.3. CFD

With the advent of computers, it is possible to solve the governing equations of fluid motion, Navier-Stokes (NS) equations, in small computational cells or elements [26]. The overall domain of interest is then broken into these small elements to generate a mesh. Solution is obtained on a mesh and integral quantities are extracted to accurately estimate the operating conditions or forces acting on certain geometry. The approach is known as Computational Fluid Dynamics (CFD) and it involves numerical analysis, fluid dynamics, and knowledge of computer hardware and programming. Given to the wide range of applicability of CFD, its support for multiple physics, handling general geometries, and relying on less assumptions, industry is shifting from traditional simple models to full 3D transient CFD models. This movement also applies to both turbomachinery and rotordynamics. Current work relies on CFD to find solutions for the problem of impeller and seal rotordynamics.

A typical CFD solution in the current work consists of 4 major steps. The design step defines the geometry of the components. The geometry has to be discretized into elements which allows CFD to solve the governing equations at each element. Typically, finer grids result in more accurate predictions. The third step is therefore to set up the CFD problem with the appropriate boundary conditions. After the solution field is known, the data has to be post-processed for meaningful rotordynamic quantities such as rotordynamic forces. Figure 5 summarizes these steps and the typical software used in this dissertation to do each step.

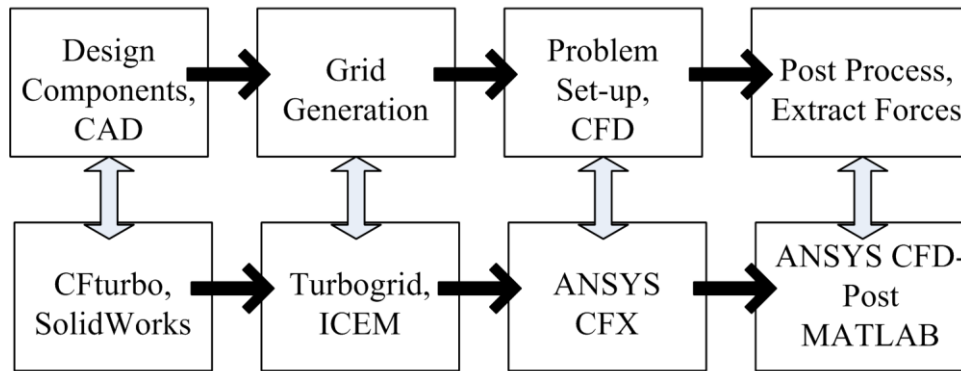


Figure 5. Typical task procedure for a CFD solution

1.2.4. Whirling Motion

Every shaft has certain amount of residual imbalance [27]. The components mounting on the shaft also cause some extra imbalance or excitation. For example, impeller and volute system always cause some hydraulic imbalance act on the shaft [28]. These internal and external excitations lead to the vibration of the shaft at the shaft speed or other frequencies. As a result, the shaft tends to operate eccentrically and it relies on an external damping system to limit these motions. The external damping has its own limitations and cannot serve as the sole remedy [1]. So the source of excitation has to be identified and controlled. Figure 6 shows a shaft with rotational speed (spin speed) of ω which is whirling in a circular orbit with eccentricity e and whirl speed of Ω .

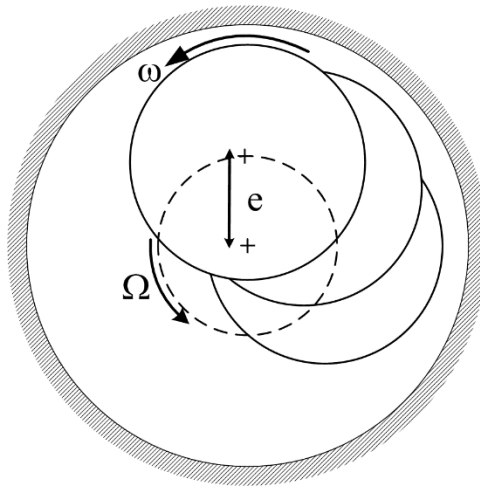


Figure 6. Schematic of an eccentric rotor with a circular whirling motion. The dimensions are exaggerated for illustration purposes

Thus, the shaft whirls around its bearings center. Depending on the shaft mode shape, this motion can be translational, conical or assume other shapes [19]. A typical industrial form of motion which occurs close to the first critical speed is the translation motion or the whirling motion. The whirling motion has no pitch angle associated with it [29]. In other words, a whirling impeller is not tilted, it is only eccentric. In the current study, all the motions are whirling types of motion. An overhung impeller with stiff bearings will not be accurately represented by a whirling motion; a precession motion is more applicable [30]. Figure 7 shows both motions.

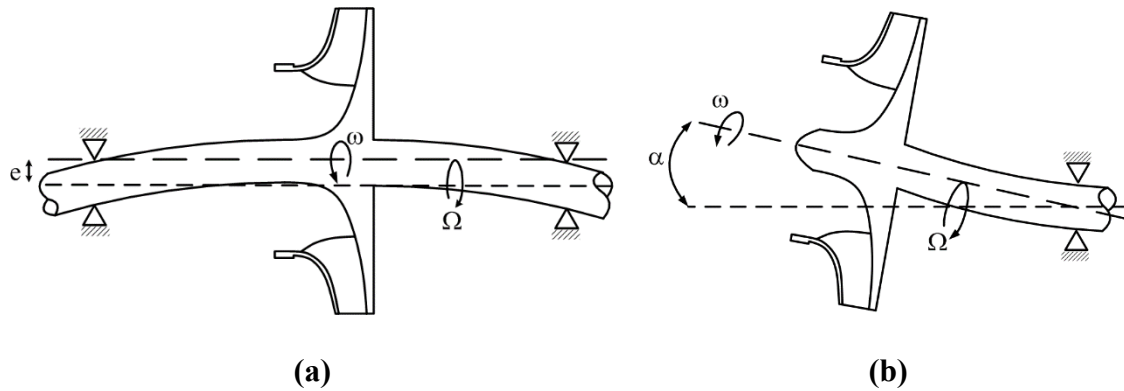


Figure 7. Impeller eccentric motion. (a) whirling motion (b) precession motion

In the current work, it is not desired to determine the root of the eccentric motion or eliminate it. It is assumed that the shaft has already entered such undesired phase due to various reasons, and the external damping has not been sufficient to suppress this motion. Under such circumstances, it is sought to investigate whether the impeller or seal rotordynamic forces cause an unstable motion or not. Next section further discusses these topics.

1.2.5. Rotordynamic Forces and Rotordynamic Instability

The eccentric motion of the shaft causes eccentric operation of components such as seals and impellers. For instance, an eccentric seal operation leads to an asymmetric distribution of seal clearance around the rotor. This in turn causes biased distribution of pressure and momentum around the rotor. As a result, a dynamic (transient) force appears that whirls around the rotor. This is called a rotordynamic force. Rotordynamic forces are usually simplified and modeled by a linear force model in industrial applications [31]. The linear model consists of stiffness, damping and mass both in direct (K, C, M) and cross-coupled (k, c, m) directions [32]. The whirling coordinate

frame has a component in the eccentricity direction F_N (normal component) and a component which is perpendicular to the eccentricity direction F_t (tangential component). The positive F_n is in the direction of eccentricity. The positive direction of F_t is determined by the spinning direction not the whirling direction [33], as it is shown in Figure 8.

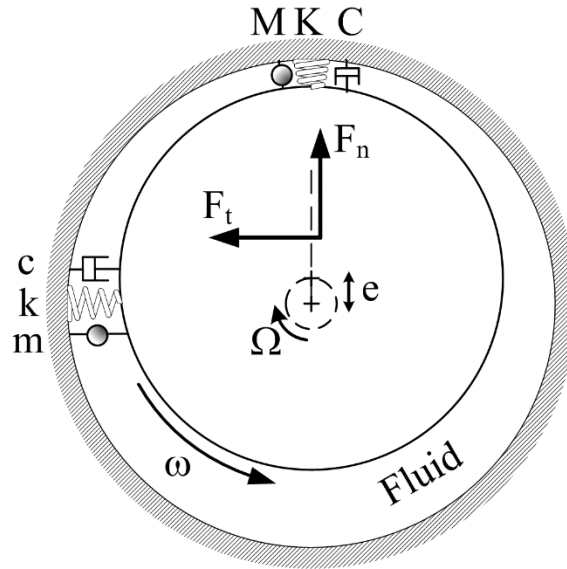


Figure 8. Fluid induced rotordynamic force model

The forces are related to the rotordynamic force coefficients through:

$$\frac{F_n}{e} = -K - c\Omega + M\Omega^2$$

$$\frac{F_t}{e} = k - C\Omega - m\Omega^2$$
(1)

The force divided by the eccentricity is often called impedance in the context of impeller and seal rotordynamics (although the classic definition of impedance is the force divided by the velocity) [34, 35]. As is illustrated in Figure 9, the rotordynamic forces are typically presented in graphs of impedance-frequency, with the horizontal axis set as the ratio of the whirl frequency to the spin frequency (shaft rotational speed) [36]. In practice, when doing CFD analysis the impedances are obtained and the coefficients are estimated from the forces through a curve fitting [37]. Rotordynamists prefer to work with these coefficients and input them in a vibration model for the rotor system.

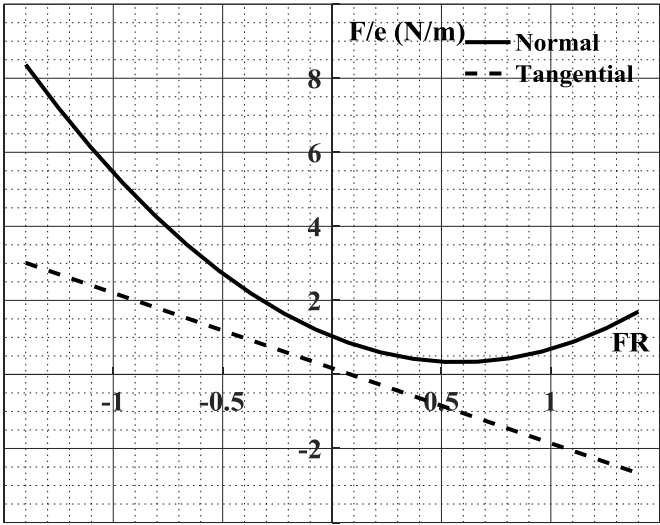


Figure 9. A typical impeller or seal impedance shape

Rotordynamic forces can be caused by various mechanisms in impellers and seals [1]. One can name the Bernoulli effect in an impeller with a wide front leakage

path profile where a non-uniform profile around the circumference causes a non-uniform pressure distribution which is proportional to e and appears as a negative direct stiffness term (See Figure 10). There are also acceleration and velocity dependent terms appearing due to the Bernoulli effect, meaning that this effect contributes to the added mass and cross-coupled damping as well, but the negative stiffness impact is the more unique and notable outcome [38].

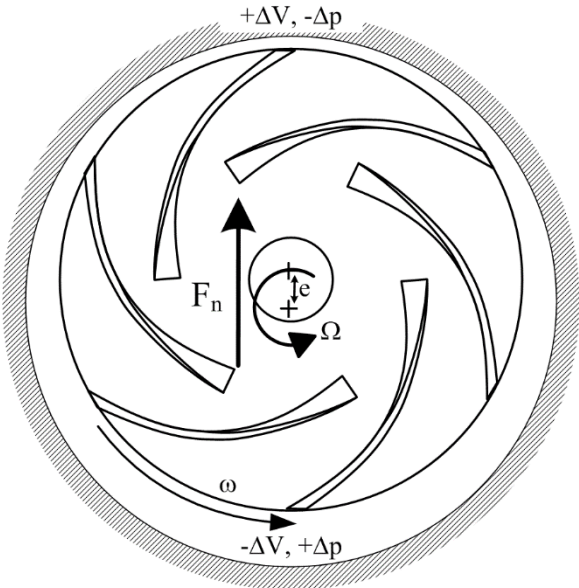


Figure 10. Bernoulli effect causing a negative stiffness in blade to blade plane

Other famous mechanism is the Thomas/Alford force [39, 40] where the non-uniform tip clearance in an axial impeller leads to a non-uniform tip clearance efficiency around the impeller and a net torque. Alford force is proportional to e and appears as a stiffness term (usually the cross-coupled term is important for the analyst). Classical definition

considers Alford force to be drive the forward whirl in turbines and the backward whirl in pumps, compressors and fans [41]. However, more recent studies show that the sign of cross-coupled stiffness k is not necessarily fixed for all flow rates and geometries [42, 43]. Figure 11 shows the Alford force for both modes.

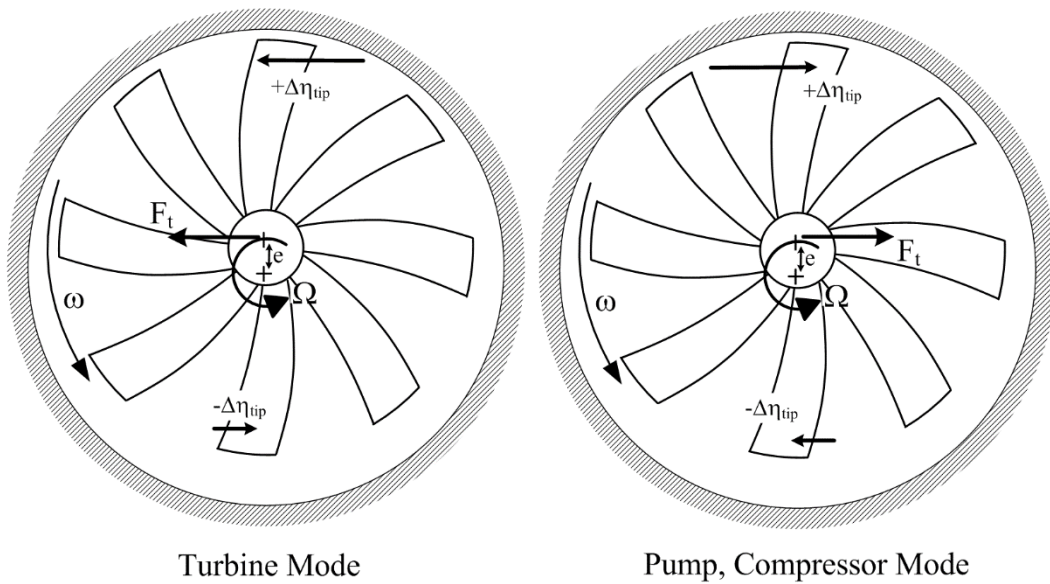


Figure 11. Alford force caused by the asymmetric tip clearance efficiency causes a cross-coupled stiffness

Seals or impellers with tight clearances are subject to another mechanism known as the Lomakin effect [20, 44] where the tighter clearance side has larger resistance and therefore has lower contraction loss coefficient, while the wider clearance side has smaller resistance and hence a larger contraction loss. This causes an imbalance in pressure distribution along the leakage path and a centering force appears [45].

Lomakin effect is proportional to e and appears as a positive direct stiffness according to Figure 12.

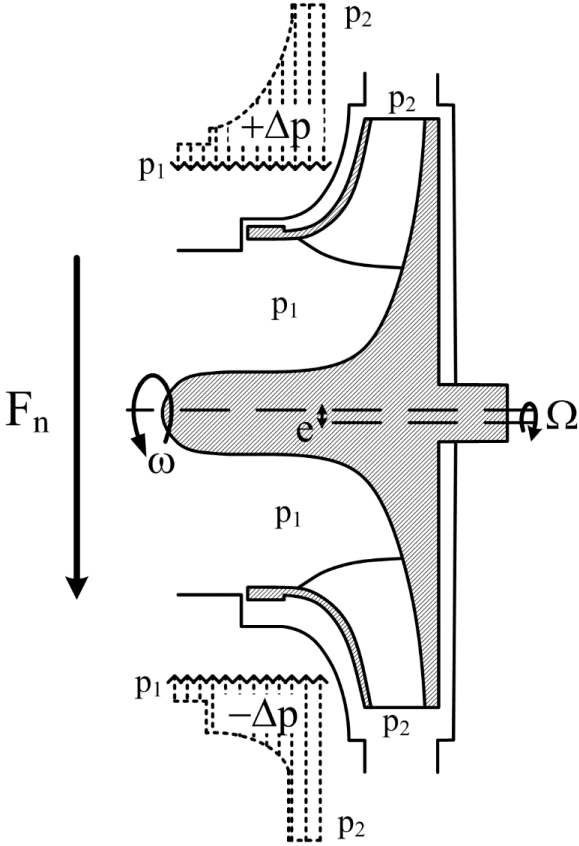


Figure 12. Lomakin effect in the meridional plane forms a restoring normal force

The volume of fluid inside a whirling impeller is subject to centrifugal forces due to the whirling motion. This force is proportional to $e\Omega^2$ and behaves as a positive added mass [46]. Impellers subject to a whirling motion also form a circulation multiplied by the whirling velocity which lifts the impeller towards the center. This is a Magnus effect

and it is proportional to $e\Omega$ and appears as a cross-coupled damping term [36]. The Magnus effect is shown in Figure 13.

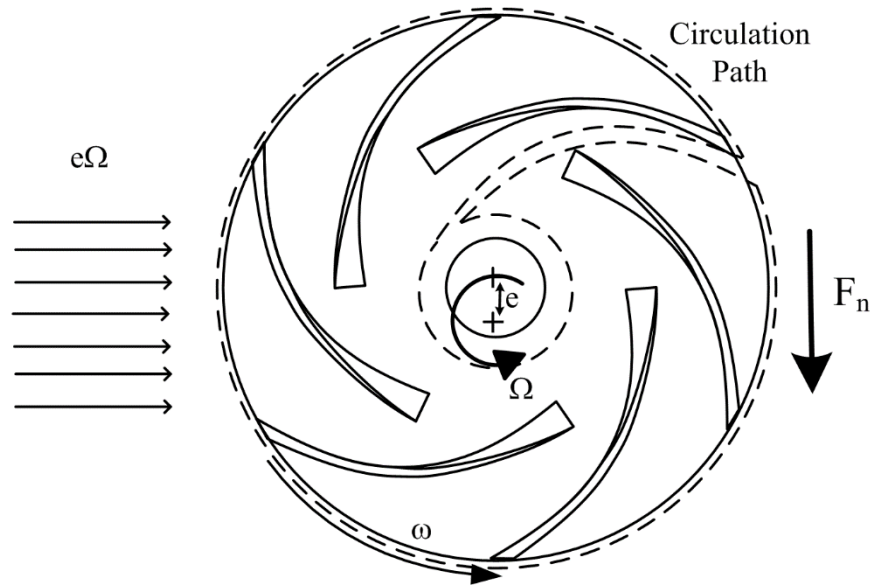


Figure 13. Magnus effect due to interaction of impeller circulation and whirling velocity lifts the impeller

The direct damping can be simply caused by the viscous losses due to the eccentric motion. It should be noted that there is always some level of cross-coupling present in the problem since the extremum pressure location does not generally align with the location of maximum or minimum eccentricity.

While the whirling motion itself can be destructive and it is a source of vibrations, the fluid-solid interaction between the rotating parts and the flow may result in more severe consequences. An unfortunate case would be the rotordynamic instability, where the fluid induced forces caused by the whirling motion keep feeding

energy to a critical speed [1]. As a result, the vibrations will grow by increasing the speed and finally the amplitudes are so large that the machine trips and stops operating. Impellers, seals and bearings are notorious components that have the potential to destabilize the machine [47]. Figure 14 shows a typical case of rotordynamic instability.

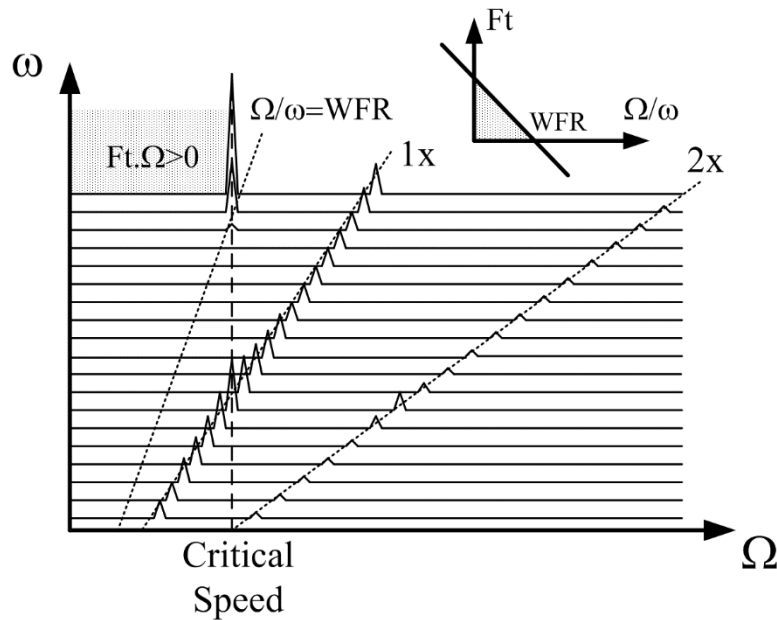


Figure 14. Self-excited rotordynamic instability by impellers and seal fluid induced forces

When the ratio of whirl frequency to spin frequency Ω/ω reaches certain onset speed of instability marked by the Whirl Frequency Ratio (WFR), the tangential forces are larger than the damping forces (The onset speed of instability can be pushed beyond the WFR by increasing external damping [47]). Rotordynamic forces get stronger with the increase in the size of eccentricity. Since the tangential force component has already

met the instability requirement $F_t \cdot \Omega > 0$, then a centrifugal force forms that further decenters the rotor. As a result F_t grows even larger with time or with the increase of frequency. this self-excited fluid induced instability continues till either rub occurs or the rotor reaches a limit cycle [47]. Note that external damping can delay the onset speed of instability but when the instability started, the damping cannot restrain the growth unlike a synchronous imbalance problem.

1.3. Literature Review

The literature in the area of impeller and seal rotordynamics is summarized in this section. The studies are divided into three major categories of experimental, theoretical and CFD works. Since this dissertation is focused on CFD-based methodologies, the theoretical and the experimental investigation are briefly addressed for the sake of brevity.

1.3.1. Experimental Studies

1.3.1.1. Seals

There is a fairly large amount of data and literature available for liquid and gas annular seal rotordynamic performance. The experimental campaigns have been long going on due to inaccuracy of theoretical models and limitations of early computational tools. Typically a shaker test rig applies certain vibration to the stator (instead of the rotor) in two orthogonal directions and the forces on the rotor are collected [48]. Due to the tight clearance, the pressure on both rotor and stator are almost equal and same forces will be resulted if the rotor would have been shaken. By doing a Fast Fourier

Transform (FFT), components of each frequency are extracted and the impedance can be plotted [49].

Various seal studies has been done on plain seals [50, 51] given to their wide usage, simple manufacturing and analysis, large rotordynamic coefficients including damping and direct stiffness. To improve the leakage characteristics of plain annular seals, grooved seals [52-55] became popular in pump industry. The manufacturing is still simpler than many other seals, and the rotordynamic characteristic can be improved by selection of an appropriate helical angle against the development of swirl inside the seal [56]. Labyrinth seals received equal attention for gas applications [57-59]. The seal provided satisfactory leakage reduction and could be slightly worn off during rubs without immediate need for replacement. However they showed large cross-coupled stiffness and low direct damping, therefore poor stability performance. A class of seals was later developed known as damper seals for gas applications which provide better stability characteristics in wider operation range [60]. Hole-pattern and honey-comb seals [57, 61, 62] and pocket damper seals [58] are among these studies. Villasmil et al. [24] further studied intentionally roughened and knurled surface seals to form a database of friction factors and rotordynamic characteristics to be used in Bulk-Flow codes or industrial applications.

Current topic of interest has shifted from single gas or liquid annular seal tests to multi-phase, bubbly, or supercritical seals [63-65] due to the subsea oil and gas applications as well as the rise of supercritical CO₂ power generation.

1.3.1.2. Impellers

In contrast to the vast number of measurements done for seal geometries, only a few experimental measurements have been done on impellers which either study pump impellers or axial gas impellers (compressor, steam turbine and stage gas turbine). Impellers are more difficult to design and manufacture, the Reynolds number is typically one to two order of magnitude larger, shaking does not apply, casing pressure is not reflective of rotor pressure, collecting and post processing data is more complex, and they are simply more costly to test. Also impeller forces in test operating conditions (lower rpms and pressure ratios) are typically smaller than seals which encourages the analyst for larger eccentricities. Large eccentricity means measurable forces with less uncertainty, but at the same time the applicability to real industrial cases reduces. Finite amplitude motions trigger nonlinear effect which may not be present in reality. Figure 15 shows a typical test rig used for measurement of whirling impeller rotordynamic forces.

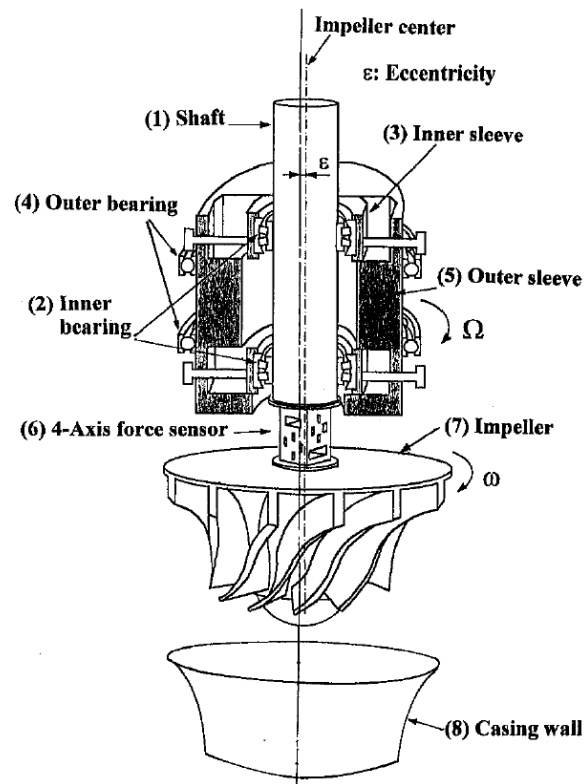


Figure 15. Test rig used to measure open impeller rotordynamic forces (reprinted from [66])

Primarily, Hergt and Kreiger [67] reported dynamic side loads (including tangential forces) in eccentric pump impellers. Shoji and Ohashi [46, 68] were among the first to test a centrifugal pump closed impeller with 2D geometry. In a series of publications they added vaneless and vaned diffusers as well as 3D impellers to their investigations [69]. The test rig uses two series of shafts and bearing sleeves to impose the circular whirl motion. It was confirmed that the impeller is destabilizing in a sub-synchronous forward whirl region which almost vanished when the impeller geometry is 2D without appreciable hub shroud length. Their study was continued with an almost similar test rig by the Caltech group for more impeller types [70, 71], volutes [72, 73],

front shroud leakage and swirl ratio [74-76], and inducers under cavitation operation [77]. To this date, these tests provide the major body of information available on impeller rotordynamic behavior. Also, the tests done with an isolated front shroud test rig indicated no bumps and dips, even with large swirl ratios [74]. At the same time, one independent study by Bolleter et al. [78] investigated the impeller impedances using a rocking arm test rig. Results suggested large destabilizing forces for the impellers marked by WFR values above 1.0. The test rig was not used again for impellers, other scholars suspect the test rig may have caused unwanted pitch motion and therefore larger forces [1].

The experimental campaign with pumps continued by Tsujimoto, Yoshida and their colleagues. They were the first to test a centrifugal whirling open impeller compressor as a pump [66]. In their study they noted large jumps appearing in impedances due to rotating stall. For the first time, they also measured destabilizing moments on the backshroud of a closed impeller [79] as well as an open impeller [29] under precession motion. Their inspections with the phase averaging method indicated a new mechanism where the whirling motion triggers an early rotating stall [80]. There has been no other report similar to this observation after that publication. The test rig has been recently upgraded with magnetic bearings for better impedance resolution [81]. Song et al. [82] recently identified a new instability class caused by a precession motion and back shroud moments in a Francis turbine. Childs and Muhammad [83] afterwards explained this instability by structural negative damping. Most recent measurement on impellers were done by Pace et al. [33] who used a chirping

(continuous spectrum) test rig to obtain the impeller impedances. They focused on cavitation instabilities in inducers [84] and identified similar bumps and dips at forward small frequency ratios. The inducers are type of open impellers and some of the bumps and dips were associated to the rotating tip leakage flow [85].

Lastly, there has been similar experimental efforts in axial compressors and turbines. Many of these studies are built upon the subject of Alford force and tip clearance excitation. Although, it is now clear that Alford force is not the only destabilizing mechanism in axial impellers (many other mechanisms are also present in centrifugal impellers) [66, 86]. Alford [87] and Thomas [41] independently identified this phenomena. They used a simple linear relation (modeled as a cross-coupled stiffness term) with a proportionality factor to relate the tangential forces to basic operational and geometrical parameters. Vance and Laudadio [40] tested a fan and showed that this factor is flow rate dependent, among other dependencies. Later Ehrich [43] shed further light on the topic and showed that the direction of whirl can change based on the flow rate for axial compressors. The experimental work for gas turbines were continued by Martinez-Sanchez et al. [86] and Song and Martinez-Sanchez [88]. They identified other mechanism in axial impellers which were not explained by the Alford formula. For example, the direct stiffness caused by the asymmetric pressure distribution has been neglected by the Alford model, similar to the significant damping effects. Similar effort has been made in axial compressors by Storace et al. [89] who showed that axial compressors can be excited for forward whirl by the Alford force even close to their design point. However, the majority of modern compressor designs

are excited for the backward whirl at design flow which fortunately contributes to stabilization of aircraft engines.

Despite the attention to axial turbines and compressors, centrifugal compressors and gas turbines lack experimental data to this date and the industry keeps relying on the data obtained for incompressible machines, theoretical models and simulations.

1.3.2. Theoretical Studies

1.3.2.1. Bulk-Flow theory

Many thin film turbulent flow applications show velocity profiles which are well-approximated with uniform profiles in the bulk region of the flow. The sharp gradients are limited to the regions very close to the walls, either in stationary wall or rotor-stator flows. This special class of flow satisfies the zero normal pressure gradient assumption $\partial p / \partial n = 0$ which allows the analyst to drop the radial velocity component. The case gets even more simplified for axisymmetric flows where there is no variation in θ direction. So it is only sufficient to solve for two velocity components and pressure along the streamline direction over a 1D grid. Viscous effects can be estimated by substituting empirical friction factor coefficient instead of shear stress terms. Therefore a concentric solution can be estimated for leakage and swirl distribution by solving a simplified form of continuity and momentum equations known as zeroth order Bulk-Flow equations. For the rotordynamic coefficients, a first order perturbed form of equations is solved and the dependency on time t and circumferential locations θ can be eliminated by assumption of first harmonics. Therefore, this approach is quick and can yield good approximations when the underlying assumptions apply. Turbulent journal

bearings, annular seals and some tight clearance impeller leakage passages (secondary paths) satisfy these assumptions and Bulk-Flow can be applied to these problems [1] (See Figure 16).

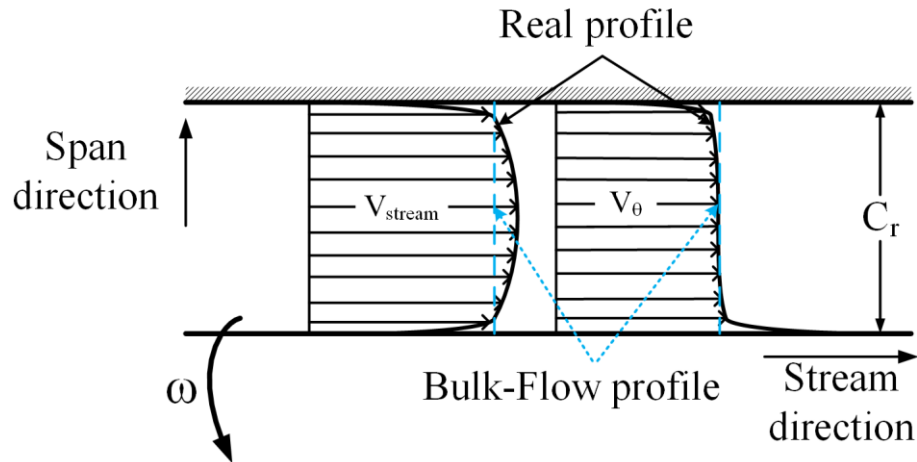


Figure 16. Bulk-Flow modeling for turbulent thin film flows

The Bulk-Flow model was first proposed by Hirsh [90] for turbulent lubricant films specifically bearings. He proposed to use a friction factor model which depends on Reynolds number, a multiplier and an exponent. The simplicity of such relation instead of modeling wall flows encouraged many other scholars to further develop this model. Childs [32, 91] adapted the model to annular seals and impeller leakage passages, followed by Palazzolo et al. [92]. San Andres [93] adapted the equations to turbulent bearing hybrid bearings with thermal effects. The model showed promising results especially for plain annular seals and the model could be readily extended to other more complex seal geometries by slightly modifying the friction factors and

coupling supplementary equations. Scharrer [94] introduced a new two control volume variation of Bulk-Flow to solve for labyrinth seal rotordynamic forces. Multiple control volumes allow calculating various clearance depths and sudden expansion losses. Nordmann and Weiser [95] extended this technique to three control volumes. Padavala and Palazzolo [37] and Venkataraman and Palazzolo [96] incorporated elastic deformations in the seal model. The impact of flow pressure on seal clearance profile is significant in high pressure applications. More recently San Andres [97] used mixture relations to adapt the Bulk-Flow model to bubbly plain annular seals.

Despite their mid-range success in 1980s to 2000s, Bulk-Flow models suffer from many major simplifications. For example they are heavily reliant on empirical data for boundary conditions, friction factors and loss coefficients, or they are inherently unable to handle flows with dominant separations and recirculation which occur in many industrial flows. Consequently, the development of this class of models has been slowed down in recent years.

1.3.2.2. Potential flow theory

Inviscid incompressible flow impellers can be modeled with 2D potential flow theory similar to the panel methods (surface singularity distributions) [98] which are very popular in airfoil calculations. This method is especially useful for modeling highly centrifugal 2D impellers. In this approach usually some projection plane of the impeller is selected and the streamline component of the flow and the tangential component are modeled using simple potential functions such as distributed sources and vorticities. Kutta condition [99], no-slip condition and impenetrable wall conditions are

used to solve the unknown distribution of vorticities which involves solving integro-differential equations. Since the method is 2D (span direction is not modelled) without viscous effects, the model can be solved very quickly. The other advantage is the insight about the various design parameters and their influence with the rotordynamic forces, so it can be used for optimization studies. Figure 17 shows a whirling 2D impeller along with the diffuser modeled by distribution of vorticities and flow sources.

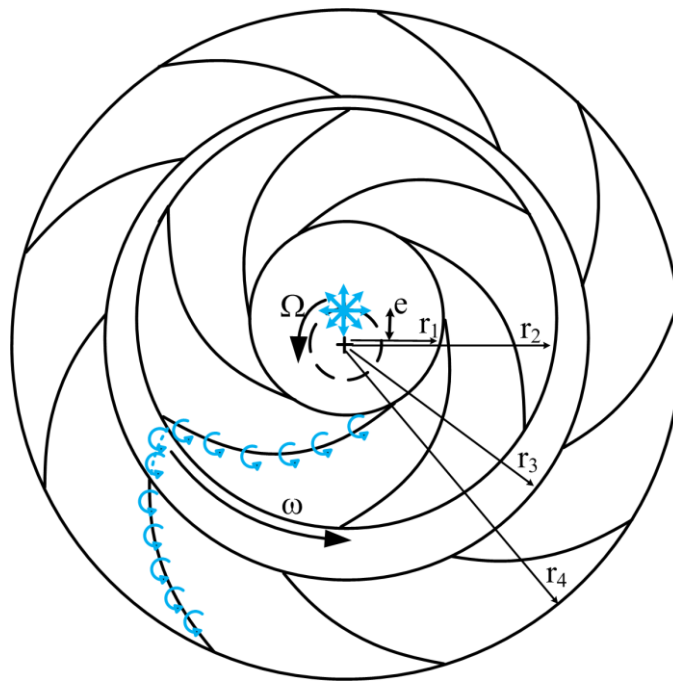


Figure 17. Sample potential flow impeller modeling (singularity method) by distribution of sources and vorticities

Csanady [100] proposed a method based on 2D potential flow theory to estimate the radial forces on a concentric impeller caused by a volute. Colding-Jorgensen [101] was the first to employ this method for prediction of whirling pump and compressor

(incompressible flow) impellers. Shoji and Ohashi [36] greatly developed this approach for centrifugal pump closed impellers, while Chamieh et al. [72] as well as Adkins and Brennen [102] did so for volute effects. Shoji and Ohashi proposed a quick and easy method to estimate the added mass due to whirling motion in the primary flow. The impeller model was one more time significantly improved by Tsujimoto et al. [103] considering the effects of volute in a single model. In their work, several important concepts were made clear: the quasi-steady model has considerable difference with transient results for impellers, the impeller model has skew-symmetry (6 rotordynamic coefficients are enough instead of 12), and the impeller model showed small bumps and dips. Tsujimoto et al. [104] in an independent publication investigated the impact of diffuser rotating stall on impeller impedances and the jump phenomena was observed in impeller impedances. In this work, they suggested a very simplified model for 2D impeller dimensionless impedances (primary flow):

$$F_t = \left(\frac{L_M}{r_2}\right) \left(1 - \frac{\Omega}{\omega}\right) \phi \quad (2)$$

$$F_N = \left(\frac{L_M}{r_2}\right) \left(1 - \frac{\Omega}{\omega}\right) \left(\psi - \frac{\Omega}{\omega}\right) \quad (3)$$

where ϕ is the impeller flow coefficient and ψ is the impeller head coefficient and L_M is the inertial length of the impeller defined as:

$$L_M = \int_{r_1}^{r_2} \frac{r_2}{r \sin^2 \beta} ds = \frac{r_2}{\sin^2 \beta} \log\left(\frac{r_2}{r_1}\right) \quad (4)$$

Here β is a fixed blade angle in simple log spiral design and s denotes the stream-wise coordinate. What is interesting about this relation is that it is dependent on operating conditions as well as frequency ratio and impeller major design parameters r_1, r_2 and β . The work on the effect of diffusers was continued by Yoshida et al. [105] and Tsujimoto et al. [106]. Their findings showed that diffuser rotating stall can be accurately predicted by 2D inviscid models. The number of cells and the rotation frequency were tabulated and graphed to identify potential chance of facing a stall during operation and to distinguish an impeller stall from a diffuser stall (See Figure 18).

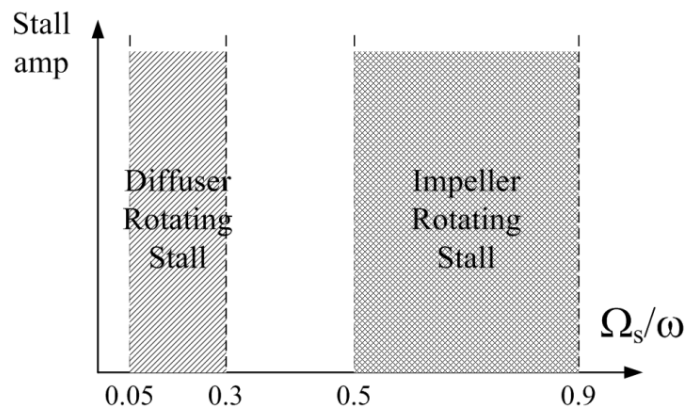


Figure 18. Typical frequency ratios that impeller and diffuser rotating stall may appear

Later, the approach was adapted to centrifugal open impellers with tip leakage loss modeling by Hiwata and Tsujimoto [107]. More recent adaptations were done by Semenov et al. [108] for cavitating inducers and the rotating choke phenomenon. There

has been no other major development in impeller potential flow solvers in the recent years, probably due to their limitations and advancements of CFD and turbulence modeling.

1.3.2.3. Actuator disk theory

Actuator disk models assume infinite number of blades with zero thickness so the flow will perfectly follow the blade profile without any blockage effect like a streamlining disk. The disk also is assumed to have zero thickness. The model is very popular in aerospace applications and therefore has been widely used for analysis of axial turbomachinery where the assumptions are more applicable. Although it can be upgraded with supplementary models to account for radial effects and viscous losses, in its simplest form the model neglects such effects. Due to the infinite blade assumption, there is no variation in θ direction which makes it very helpful for quick calculations. Therefore the actuator disk model is even more simplified than the potential flow and Bulk-Flow model.

Colding-Jorgensen [42] used the actuator disk model for prediction of axial compressor stability. He similar to Ehrich [43] concluded that the Alford factor change change sign depending on flow and geometrical parameters. Song et al. [109] applied the model to gas turbines to further investigate Alford force and other effects such as asymmetric pressure distribution in whirling axial impellers. Song and Cho [110] utilized actuator disk model with assumption if incompressibility and perturbation model for whirling stage compressors in order to inspect the effect of asymmetric clearance on the flow redistribution in the compressor. Similar efforts has been made by

Spakowski [111] and Ehrich et al. [112] to incorporate other rotordynamic effects (more advanced Alford force models) due to asymmetric clearance distributions in stage compressors and turbines. Recently the model was adapted by Song and Song [113] to centrifugal impeller front shroud forces and the stiffness results showed acceptable agreement with experiments.

1.3.3. CFD Studies

1.3.3.1. 2D perturbation CFD models

By the late 1980's and early 1990's, researchers started to implement reduced order CFD models to predict seal leakage flow and rotordynamic coefficients. Demko [114] utilized a Finite Difference Method (FDM) CFD code based on the Quadratic Upstream Interpolation for Convective Kinematics (QUICK) scheme to estimate an incompressible seal leakage flow. Later, he and his coworkers modeled seal using rotating frames. Dietzen and Nordmann [115] used a reduced order 2D axisymmetric perturbation based on FDM model to estimate a groove-on-stator seal rotordynamic force coefficients. More advanced 2D perturbation based CFD models were developed for other axisymmetric models by Arghir and his colleagues [116, 117] for more complex seal geometries. Rhode et al. [118] used FDM and the cavity-by-cavity simplifying assumption to model the flow inside a centered gas labyrinth seals while saving computation resources.

1.3.3.2. 3D quasi-steady models

Tam et al. [119] (shortly after also followed by Dietzen and Nordmann [120]) proposed a 3D FDM-based solution for seal rotordynamic forces. In this approach, the

dependence on time and the perturbation solution is avoided by changing the frame of the whirling seal problem. A general curvilinear coordinate was used in order to increase the eccentricity in the whirling simulations and extend the model to journal bearing flows. This approach is being widely used for axisymmetric seals nowadays. Hendricks et al. [121] used this method along with several eddy viscosity models to develop seal CFD solvers and study the secondary flows inside seals. Rhode et al. [122] also adapted their cavity-by-cavity FDM model to this 3D quasi-steady solution strategy in order to estimate labyrinth seal rotordynamic forces.

Impellers on the other hand, have been rarely studied by an independent CFD code for rotordynamic coefficients, perhaps due to the difficulties present in modeling the entire physics. Baskharone and Hensel [123] was among the few people who modeled the leakage passage of an impeller (impeller blades and primary passage were not modeled) for rotordynamic coefficients based on a Finite Element Method (FEM) quasi-steady 3D approach. Baskharone also used the code to investigate the effect of swirl brakes on the shroud forces and stability considerations [124]. Although the approach is useful to isolate the effects of shroud forces, the boundary conditions in this approach are not generally realistic and the method cannot be used regularly unless accurate measurements have been performed at the inlet and outlet sections.

It was about this point, which is close to early 2000's that development of independent CFD codes for seals and impellers came to a standstill. With the rapid advancements of commercial CFD solvers and the flexible options they offered for complex geometries and speed-up, researchers switched to these solvers. The 3D quasi-

steady model was first applied by Moore and Palazzolo [125] to a groove-on-stator seal under circular whirling motion. The results agreed well with the Bulk-Flow model predictions and experiments. Later the same authors applied this method to an eccentric impeller front shroud model [34]. In their study, the primary passage was centered assuming that the contributions to the impeller total rotordynamic forces were negligible. However, the presence of primary passage allowed setting better boundary conditions and specifically better swirl and loss conditions at the entrance of the secondary passage. Moore et al. [126] used this model again, this time to obtain rotordynamic coefficients of compressor impellers. The application of commercial CFD codes to various seal types has since continued by Untaroiu et al. [127-129], Ha and Choe [130], among others [131, 132]. The approach was also applied to impeller front shroud by Kim and Palazzolo [35] to inspect the presence of bumps and dips in the impeller impedances. They noticed that increasing inlet swirl will induce larger bumps in the curves, and modification of the casing profile will reduce the swirl and therefore suppress the bumps and dips. A second study by Kim and Palazzolo [133] introduced a general transfer function method to accommodate the impedances with the bumps and dips for stability calculations, in contrast to the second order mass, damping and stiffness approach. The results showed that bumps and dips have a destabilizing effect and they should be considered in the stability model. Kim and Palazzolo [30] further extended the quasi-steady approach to study the moments acting on the back shroud (rear shroud) of an impeller with precession motion. The precession motion has been rarely studied while the moments can be more destabilizing than the whirling motion.

Moreover, their model combined the effects of whirl and precession simultaneously and extracted the forces and moments by a 4by4 rotordynamic coefficient model.

1.3.3.3. Hybrid CFD Bulk-Flow model

More recently, a new Hybrid approach for seals has become more popular which combines zeroth order solution from 2D or 3D pie section CFD and Bulk-Flow first order solution. Since the mean velocities (including leakage rate) and the shear stresses in the Bulk-Flow model are input from CFD results without major simplifications, the Bulk-Flow predictions markedly improve. The Hybrid approach is much more efficient than a full 3D CFD study, especially for axisymmetric seals where a 2D CFD model is sufficient to complete the first phase of calculations. This approach was first used by Migliorini et al. [134, 135] and then followed by other researchers [129, 136]. All said, this approach has to be fine-tuned for each geometry. The viscous effects face difficulties in the locations of discontinuity and the Bulk-Flow approach is still unable to account for radial variations during the whirling motion.

1.3.3.4. 3D transient models

Until recently, the transient methods faced many problems due to large computational cost, difficult post processing and accommodating mesh motion during vibration. After complex mesh deformation methods were appended to commercial CFD packages, this approach was first applied to a gas seal by Chochua and Soulas [137] using a simple 1D rectilinear motion. The approach received attention after several years and the same methodology was applied to hole-pattern and honeycomb seals by Nielsen et al. [138]. Still 2D motions were troublesome to implement.

Eventually, the same seal was studied by Yan et al. [139] single frequency circular whirl motion (now 2D motion) and the results agreed well with the experiments. Li et al. [140] further improved the method by imposing multiple small amplitude frequencies simultaneously. Their study only combined forward whirl motions and adapted an elliptical orbit for pocket damper seals in order to extract full 2by2 matrix coefficients [140-142]. Despite the success of the transient model and its generality, it has not been applied to impellers so far (until current dissertation) given to the complexity of impeller design and appearance of negative volumes as well as high computational cost.

1.4. Objectives

Current dissertation seeks the following objectives:

- I. Provide rotordynamic force data for uninvestigated geometries such as groove-on-rotor seals, centrifugal open impellers, volutes and diffusers.
- II. Upgrade the CFD-based methodology from axisymmetric quasi-steady to non-axisymmetric transient.
- III. Enhance the accuracy of the CFD-based predictions by improving boundary conditions, grid quality, and turbulence modeling.
- IV. Perform parametric studies with respect to geometrical properties, operational conditions and modeling settings.
- V. Provide more general dimensionless rotordynamic force data for a large class of open impellers which can be tabulated or input into industrial codes.
- VI. Investigate more about the origins of bumps and dips in impeller impedances.

- VII. Deliver the basis for a standalone seal CFD code which improves the predictions compared to simpler Bulk-flow models and runs efficiently.

1.5. Novelties and Contributions

Following list discusses some of the contributions of the current dissertation. To the best of the author's knowledge, the named items find novelty, especially in the context of impeller and seal rotordynamic forces:

- CFD QS model has been applied to the groove-on-rotor liquid annular seal type. Decisive uncertain parameters such as swirl ratio, surface roughness, clearance size as well as inlet and outlet loss coefficients are further discussed and quantified.
- A CFD single-frequency transient model has been applied to obtain volute and diffuser rotordynamic force coefficients. This is the first time CFD is being used to model impeller rotordynamic forces along with its upstream and downstream non-axisymmetric components. The application of mesh deformation approach to impeller forces is unique to this study.
- A computationally-efficient CFD multi-frequency transient method has been applied to solve for open impeller rotordynamic forces. Centrifugal impellers have been long untouched in this subject due to the difficulties associated with the tip clearance mesh in the whirling model. The approach is further bolstered using a novel appendage of phase modulation technique to include more concurrent frequencies in a single simulation. It is only now with the power of CFD, after couple of decades, possible to more accurately quantify the contribution of impellers' primary and secondary path flows to total forces.

- A new dimensionless CFD-based approach has been presented to obtain a good approximation of dimensional open impeller rotordynamic forces. The affinity laws of turbomachinery and dimensionless groups such as specific speed, flow coefficient and eccentricity ratio allow application of these dimensionless data to a large class of open impellers without the need to model each single impeller.
- Origins of bumps and dips in impeller rotordynamic forces have been further analyzed. It has been verified that these fluctuations are real and they have a hydrodynamic instability nature. Strong jumps are attributed to the rotating stall in the primary flow path and the diffuser. Weaker bumps and dips have been identified and attributed to swirl dependent resonances inside the secondary flow path.
- A new CFD code has been developed for seal applications. The code combines the explicit MacCormack (McCk) scheme with Pseudo-Compressibility Method along with ω based family of turbulence models. The non-uniform discretized McCk showed promising speed-up potential when used in conjunction with the nonlinear Multigrid method and the MPI paralleled version. Furthermore, an explicit modification of Semi-Implicit Pressure Linked Equations (SIMPLE) method was appended to the McCk solver on a collocated grid.

2. ROTORDYNAMIC FORCES OF A ROTOR-GROOVED LIQUID ANNULAR SEAL: A QUASI-STEADY CFD-BASED APPROACH*

2.1. Introduction

High performance turbomachinery requires highly reliable seals to reduce losses associated with leakage passages. Counter-intuitively these complex seals may happen to be the main source of instability in rotating machinery. More specifically, circumferentially grooved liquid annular seals are frequently used in high performance machinery to ensure low leakage rates and protect from debris clogging the seal passage, given to their complex step-land geometry and superior pressure loss [1, 49]. However, this advantage comes at a price of reduced effective damping and severely smaller direct stiffness compared to plain liquid annular seals. A study by Marquette et al. [53] sheds light on deceptively low values of Whirl Frequency Ratio (WFR) in these class of seals while the effective damping is diminished. That said, the rotordynamic performance faces even more problems when the grooves are machined onto the rotor instead of stator or the so called Smooth Stator Grooved Rotor configuration (SSGR). Massey [2] reports a sub-synchronous instability in a multistage pump which employed long balance drum seal with SSGR configuration. The problem was eventually solved by changing the seal type. To further clarify the concept of negative stiffness, consider

* Reprinted in part with permission from “Prediction of Rotordynamic Performance of Smooth Stator-Grooved Rotor Liquid Annular Seals Utilizing Computational Fluid Dynamics,” by Mortazavi, F., and Palazzolo, A., 2018. *ASME J. Vib. Acoust.*, 140(3), pp. 031002-031002-031009., Copyright 2018 by ASME.

an off-centered grooved-rotor as is sketched in Figure 19. The centered rotor is shown with full lines and the eccentric rotor with dotted line. As fluid flows inside the seal, the side with smaller clearance has sharper entrance loss but milder friction loss. Since the major contributor to the loss is the entrance loss, therefore the net force will be in the direction of eccentricity and negative stiffness forms. In other words, while the Lomakin effect [44] tries to center the rotor, consecutive entrance losses leads to an off-centering force. In light of this argument, both versions of circumferentially grooved seals are prone to negative stiffness; however, the rotor-grooved class has an extended rotating surface which increases whirl frequency ratio f_ω and drops effective damping C_{eff} .

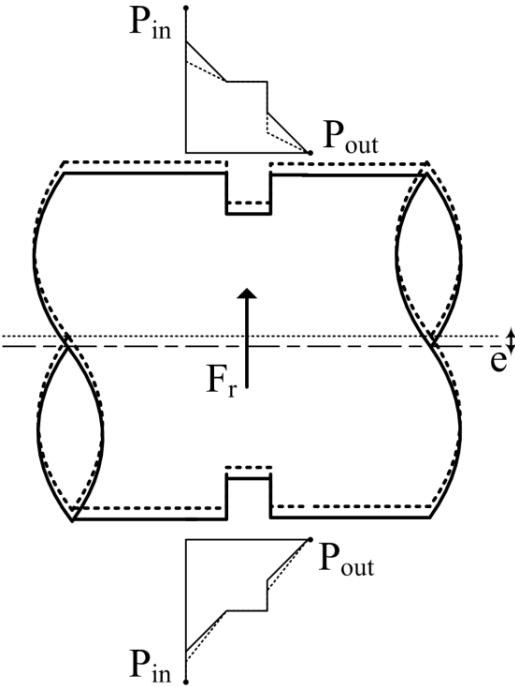


Figure 19. Negative stiffness

Most studies done so far discuss the groove-on-stator type which is more stable than SSGR. Iwatsubo and Sheng [54] developed a two-control-volume method to predict grooved seals performance. An extended three-control-volume version was introduced by Marquette and Childs [143] based on the well-known Bulk flow theory [90]. Bulk flow-based solutions are fast and physically reliable, yet they require a prior knowledge of friction factors and inlet-outlet loss coefficients which are not available in most cases. Also the theory only applies to certain type of flows where an almost uniform bulk profile is established. More recent studies tend to take advantage of rising computational power and well-developed CFD codes. Dietzen and Nordmann [115] were among the first to introduce a CFD solution to grooved seals by using a rotor fixed coordinate and perturbation analysis. Later they conducted a study using 3D CFD for simultaneously grooved rotor and stator seals [120] and concluded these seals cause outward radial forces and large tangential forces. Moore and Palazzolo [34, 125] introduced a convenient method to simulate circular whirling cases using CFD quasi-steady solution. This method has been adopted in the current rotordynamic study. Untaroiu et al. [144] used the similar technique in modelling a long aspect ratio circumferentially groove on stator seal with rounded profile. They modeled the upstream of seal inlet up to the outer radius of rear shroud to account for the Pre-Swirl Ratio (PSR) effects indirectly. Meng et al. [145] present a turbulence study on groove-on-rotor seal but their study is focused on velocity profiles and the nature of flow inside the seal. More recently, Kim and Ha [146] examined a GSSR seal using computational fluid dynamics and compared their results to experimental data with good agreement. A

KC model has been used and 2D flow results have been used as initial condition for full 3D simulation to expedite convergence.

Current study attempts to model a 15 step SSGR seal based on recent experiments done by Moreland and Childs [49, 55] in Texas A&M University on SSGR seals. A sketch of the seal schematic is shown in Figure 20 according to the geometry provided by Moreland and Childs [49]. Table 1 includes the information regarding the seal dimensions.

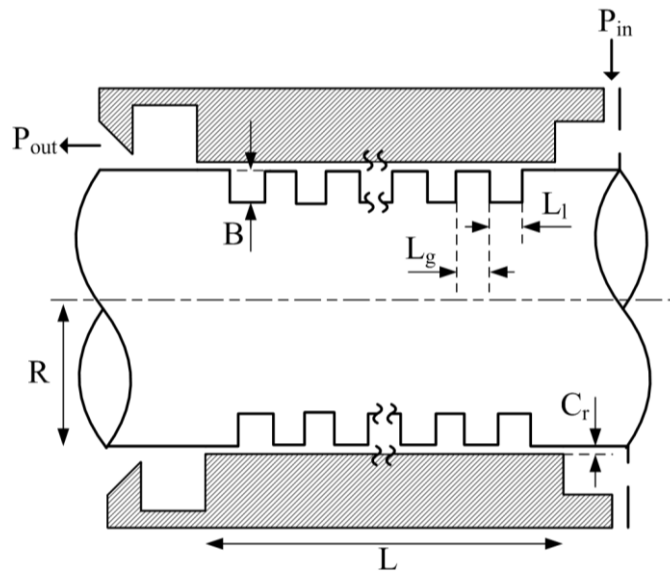


Figure 20. Schematic of the seal and dimensions

The experimental data have been obtained based on Glienicke's shake method [48]. However, this study imposes a circular whirling motion on the rotor instead of shaking the stator. A transient CFD study by Yan et al. [139] confirmed that results from a circular precession agree with the results obtained from shaking method. The

advantage of a circular whirl lies in the fact that it can be easily transformed into a time-independent rotating frame problem, and thereby reducing total computational time considerably. The details of the method used will be discussed in the Methodology section.

Table 1. Seal dimensions (adapted from [49])

n	L _l (mm)	L _g (mm)	B (mm)	C _r * (μm)	R (mm)	L (mm)
15	1.524	1.524	1.524	183.81	50.8	50.8

* Adjusted for thermal growth

Current CFD-based methodology allows for inexpensive and accurate modeling of circumferentially grooved seals characteristics. These characteristics are further scrutinized to investigate the destabilizing nature of SSGR seals compared to the plain annular seals. Additionally, this approach allows for accurate calculation of pre-swirl ratio (PSR) and outlet swirl ratio (OSR) which proves to be a challenging task in experimental studies. Finally, effects of surface roughness on leakage, stiffness values, PSR and OSR are presented.

2.2. Methodology

The quasi-steady modeling of circular whirling motion relies on a change of frame from stationary frame to the rotor fixed frame that rotates with speed of Ω about

the centered position. The stator speed should be set to $-\Omega$ and rotor speed should be set to $\omega - \Omega$ rotating about eccentric position [34, 35]. One can confirm the accuracy of these assumptions by reducing the boundary conditions back in stationary frame as shown in Eqs. (5) and (6):

$$@ r = R_{stator}, \quad v_{\theta} = R_{stator}(-\Omega + \Omega) = 0 \quad (5)$$

$$\begin{aligned} @ r = R_{rotor}, \quad v_{\theta} &= \vec{r}\Omega + \vec{R}_{rot}(\omega - \Omega) \\ &= (\vec{e} + \vec{R}_{rot})\Omega + \vec{R}_{rot}(\omega - \Omega) = \vec{R}_{rot}\omega + \vec{e}\Omega \end{aligned} \quad (6)$$

where \vec{e} is the eccentricity vector. Alternatively, the schematic provided in Figure 21 clearly illustrates the procedure of changing the problem from stationary frame to rotating frame.

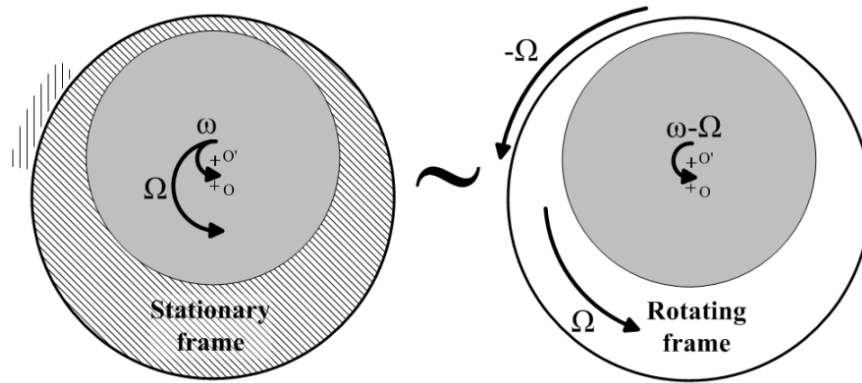


Figure 21. Quasi-steady circular whirling motion in CFD modeling

The experimental results from Moreland and Childs [49] provides the more general set of 12 rotordynamic coefficients K_{ij} , C_{ij} and M_{ij} corresponding to stiffness,

damping and virtual mass coefficients, respectively. The reaction force model for the seal is defined as:

$$\begin{aligned} \begin{bmatrix} F_x \\ F_y \end{bmatrix} &= \begin{bmatrix} K_{xx} & K_{xy} \\ K_{yx} & K_{yy} \end{bmatrix} \begin{pmatrix} \Delta x \\ \Delta y \end{pmatrix} + \begin{bmatrix} C_{xx} & C_{xy} \\ C_{yx} & C_{yy} \end{bmatrix} \begin{pmatrix} \Delta \dot{x} \\ \Delta \dot{y} \end{pmatrix} \\ &+ \begin{bmatrix} M_{xx} & M_{xy} \\ M_{yx} & M_{yy} \end{bmatrix} \begin{pmatrix} \Delta \ddot{x} \\ \Delta \ddot{y} \end{pmatrix} \end{aligned} \quad (7)$$

To find the equivalent coefficients from CFD simulations, the normal and tangential forces should be calculated in two distinct positions over a range of excitation frequencies Ω . To further elaborate on this, in accordance with the approach taken by Untaroiu et al. [127] the rotor whirls in a circular orbit about the centered position, described as:

$$\begin{cases} \Delta x = e \cos \Omega t \\ \Delta y = e \sin \Omega t \end{cases} \quad (8)$$

where e denotes the eccentricity and $\Omega > 0$ and $\Omega < 0$ corresponding to forward and backward whirl, respectively. Substituting back into the force model of Eq. (7):

$$\begin{aligned} - \begin{bmatrix} F_x \\ F_y \end{bmatrix} &= \begin{bmatrix} K_{xx} & K_{xy} \\ K_{yx} & K_{yy} \end{bmatrix} \begin{pmatrix} e \cos \Omega t \\ e \sin \Omega t \end{pmatrix} + \begin{bmatrix} C_{xx} & C_{xy} \\ C_{yx} & C_{yy} \end{bmatrix} \begin{pmatrix} -e\Omega \sin \Omega t \\ e\Omega \cos \Omega t \end{pmatrix} \\ &+ \begin{bmatrix} M_{xx} & M_{xy} \\ M_{yx} & M_{yy} \end{bmatrix} \begin{pmatrix} -e\Omega^2 \cos \Omega t \\ -e\Omega^2 \sin \Omega t \end{pmatrix} \end{aligned} \quad (9)$$

is obtained. If one sets $\Omega t = 0$,

$$\begin{aligned} - \begin{bmatrix} F_x \\ F_y \end{bmatrix} &= \begin{bmatrix} K_{xx} & K_{xy} \\ K_{yx} & K_{yy} \end{bmatrix} \begin{pmatrix} e \\ 0 \end{pmatrix} + \begin{bmatrix} C_{xx} & C_{xy} \\ C_{yx} & C_{yy} \end{bmatrix} \begin{pmatrix} 0 \\ e\Omega \end{pmatrix} \\ &+ \begin{bmatrix} M_{xx} & M_{xy} \\ M_{yx} & M_{yy} \end{bmatrix} \begin{pmatrix} -e\Omega^2 \\ 0 \end{pmatrix} \end{aligned} \quad (10)$$

In similar manner one more set of equations is found by setting $\Omega t = \pi/2$. Subsequently, four equations are available to be solved at multiple frequencies and extract the coefficients by second order least-square-fitting.

$$\left\{ \begin{array}{l} -\frac{F_{x,0}}{e} = K_{xx} + C_{xy}\Omega - M_{xx}\Omega^2 \\ -\frac{F_{y,0}}{e} = K_{yx} + C_{yy}\Omega - M_{yx}\Omega^2 \\ -\frac{F_{x,\frac{\pi}{2}}}{e} = K_{xy} - C_{xx}\Omega - M_{xy}\Omega^2 \\ -\frac{F_{y,\frac{\pi}{2}}}{e} = K_{yy} - C_{yx}\Omega - M_{yy}\Omega^2 \end{array} \right. \quad (11)$$

Since steady-state simulation is adopted, instead of $\Omega t = 0$ the rotor is shifted towards x coordinate and for $\Omega t = \pi/2$ the rotor is shifted towards y coordinate.

The dynamic stiffness coefficients will be used here to compare the CFD results to experimental measurements. According to Childs and Hale [147] the dynamic stiffness H_{ij} in complex form is defined as:

$$H_{ij} = (K_{ij} - \Omega^2 M_{ij}) + j(\Omega C_{ij}) \quad (12)$$

2.3. Numerical Modeling

2.3.1. Computational Domains

Computational Fluid Dynamics CFD was developed to deal with complex flows where other rough engineering estimations cannot provide us with satisfactory results.

Shortcomings of CFD solutions usually arise from inaccurate turbulence modeling, inaccurate boundary conditions, inappropriate grid resolution or wrong type of analysis. In order to judge CFD as a powerful tool to predict rotordynamic characteristics of a system, one should take excessive care in implementing the correct conditions.

To achieve a high fidelity model, a number of extra domains are included in computational domain as illustrated in Figure 22. The inlet and outlet chambers before and after the seal ensure correct modeling of pressure loss and recovery and the fast transition of flow swirl at inlet. These domains should not be dropped at any cost. Furthermore, the correct simulation of PSR requires the exact modeling of injection holes. In order to suppress the back flow at the injection holes, an orifice extension is integrated which supplies the inlet pressure p_{in} (See Figure 23 and Figure 24).

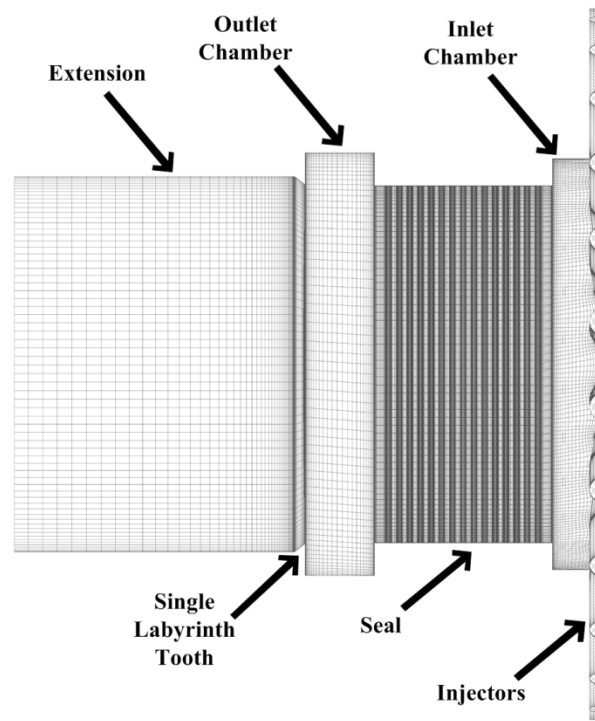


Figure 22. Computational domains used for CFD simulation

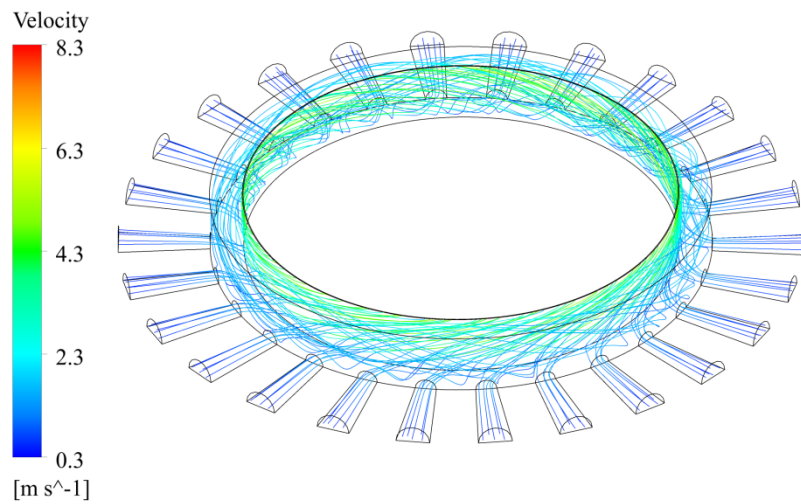


Figure 23. Swirl injectors at radial injection configuration

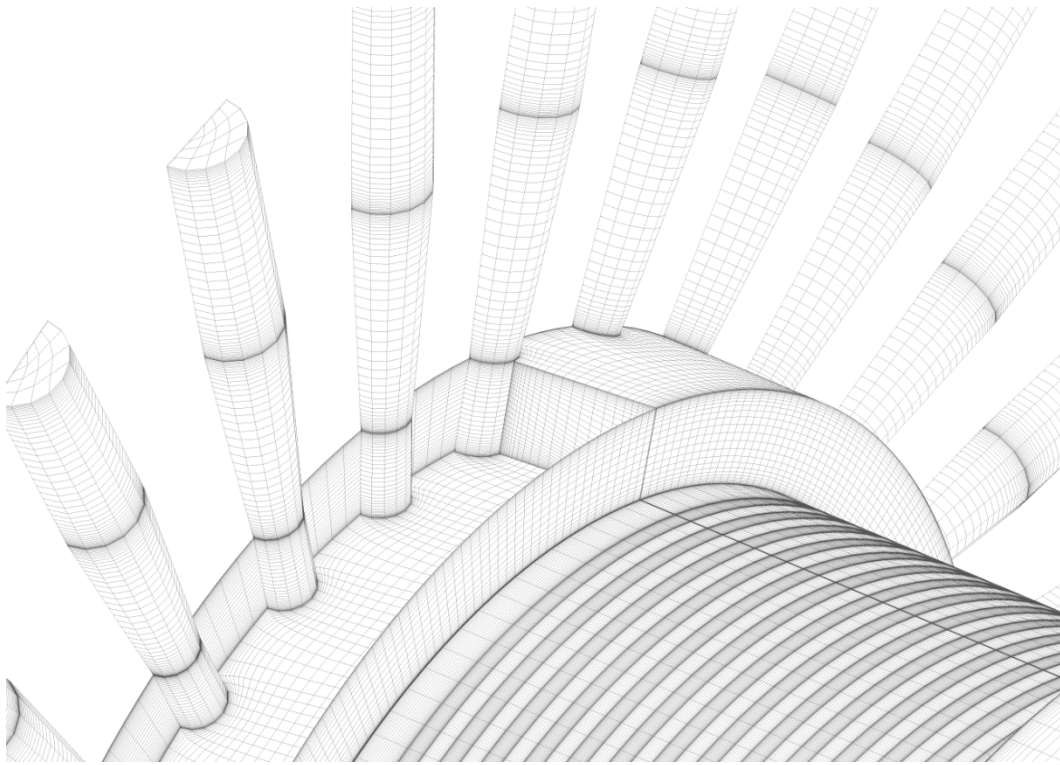


Figure 24. Swirl injectors added to the model

A single labyrinth tooth on stator is required to hold back-pressure at high frequencies and suppress suction at the outlet. Finally, an extension annular region is placed after the tooth to ensure the separated flow after the tooth is reattached and solution is not affected by reverse flow at the outlet. The extension domain is stationary with smooth walls and its contribution to total pressure loss is less than 0.5%.

2.3.2. Grid Quality and Convergence

Figure 25 shows a sample groove mesh and Figure 26 shows the exploded view of the grid. The y^+ value is below 5 through the entire mesh.

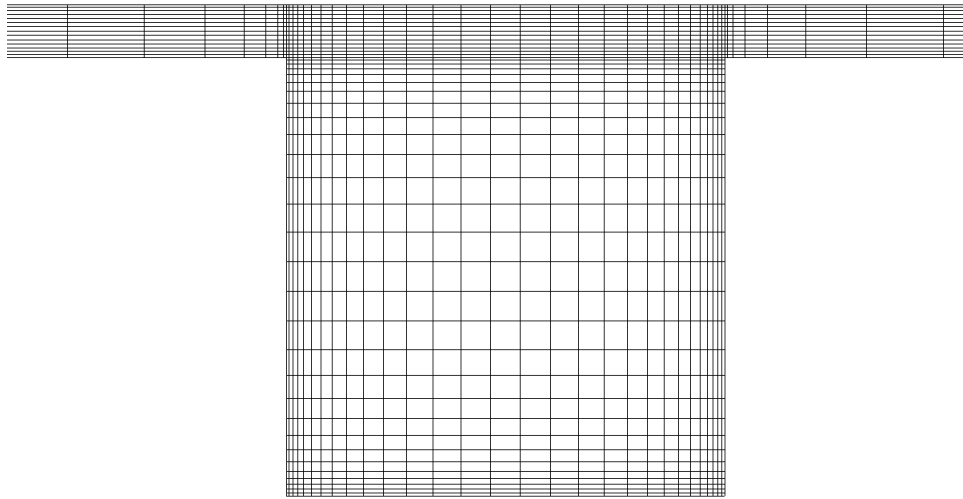


Figure 25. Mesh inside each groove

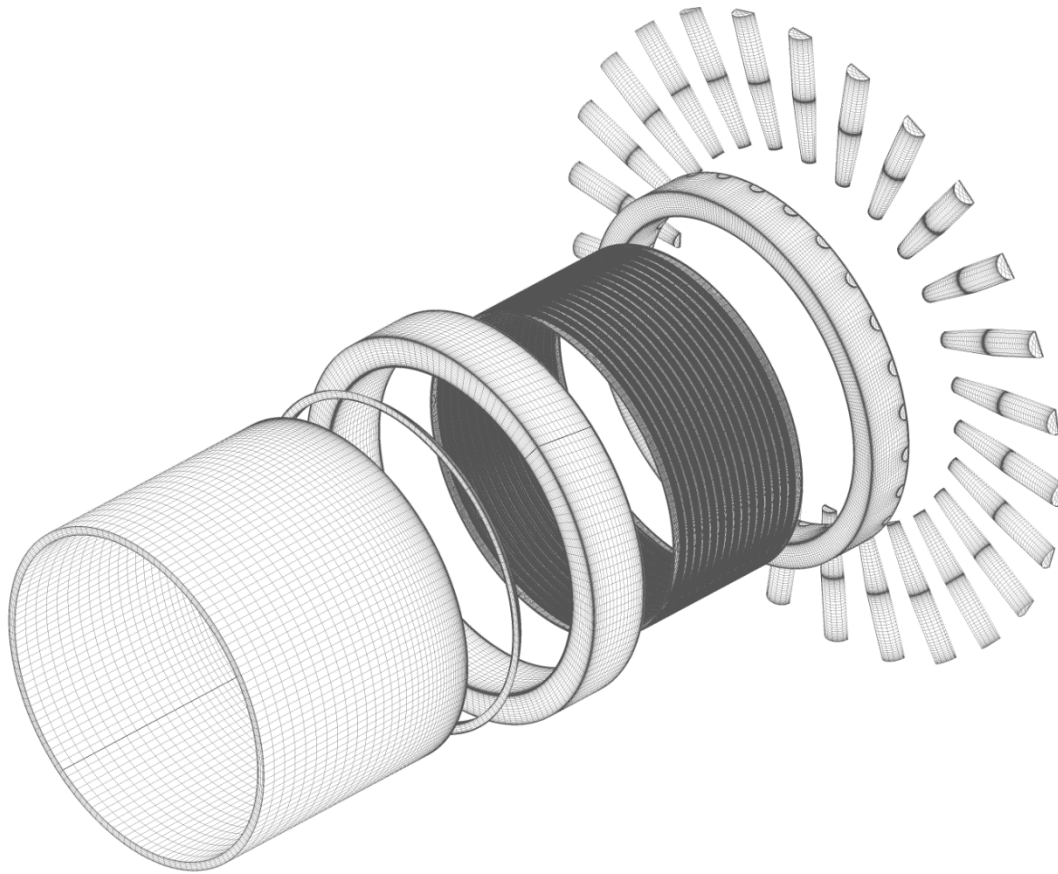


Figure 26. Exploded view of the grid

The grid only consists of structured hexahedral cells to enhance convergence quality and accuracy of results with minimum computational cost.

In order to rule out mesh density influence on simulation results, a grid independency study has been conducted. Five (5) distinct grids have been used (Figure 27). Five parameters of interest have been selected to conduct the study; Leakage which is expected to be less sensitive to grid resolution; F_x and F_y acting on the rotor section where seal is located in an eccentric position in alignment with x direction; and finally Outlet Swirl Ratio and Pre-Swirl Ratio which are strong functions of shear stress and grid refinement. The test point used for grid independency has the static eccentricity $e_x = 0.1C_r$, $\omega = 2000 \text{ rpm}$, $\Omega = 0 \text{ rpm}$, and $\Delta p = 207 \text{ kPa}$. The ratios of each grid size to the next has been tried to be kept constant (about 1.55-1.60).

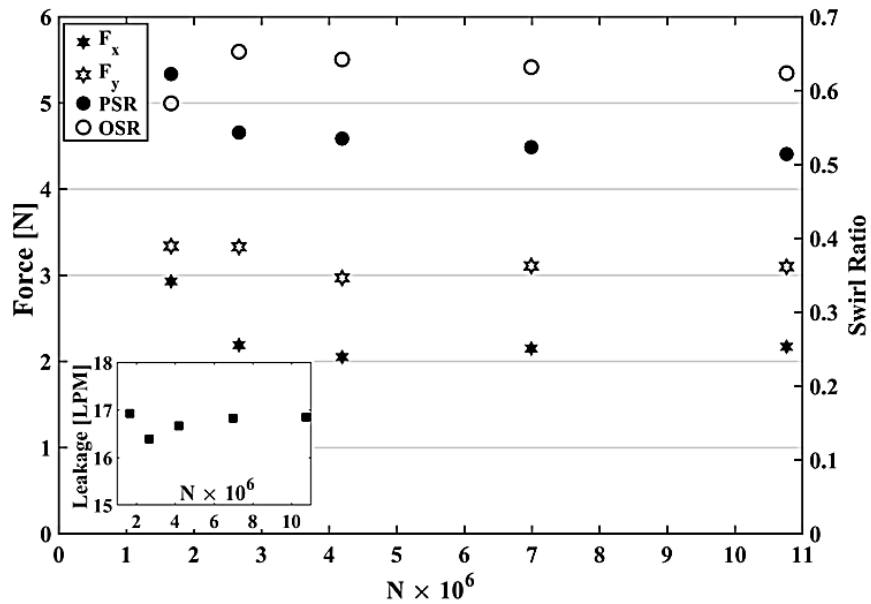


Figure 27. Grid convergence

In all cases, the distance of the first node from the wall is kept a constant small value to ensure y^+ value does not affect the conclusion from grid convergence results. Grid convergence results suggest that the medium grid is capable of producing accurate results with a more efficient grid compared to the finer configurations. The leakage results almost match the experimental data $\dot{Q}_{exp} = 16.86 \text{ LPM}$.

The final resolution of medium grid's sub-domains is given in Table 2. The significance of these data lies in the portion of computational and human effort required in preparing domains other than the domain of interest. These extra domains are required to fully replicate the experimental condition. Auxiliary domains use up to 25% of computational cells in this case.

Table 2. Sub-domain grid sizes

Domain	N
Injection	41,000
Inlet Chamber	474,000
Seal	3,299,000
Outlet Chamber	232,000
Single Tooth	56,000
Extension	94,000
Total	4,196,000

2.3.3. Boundary Conditions and Solver Settings

The commercial code ANSYS CFX 16.1 has been employed to solve the turbulent Navier-Stokes equations in rotating frame. The $k-\omega$ SST turbulence model with curvature correction term has been chosen [145, 148-151] in accordance with multiple studies in rotating machinery with internal flows [152, 153]. A detailed discussion of ANSYS CFX solver settings and theory is given in Appendix A.

A symmetry boundary condition has been implemented to only model half of the test section since the original test rig consists of two identical seals with a shared inlet plenum. The inlet and outlet static pressures are assigned and the leakage rate is calculated. This is the actual boundary conditions in the case of seals, not the “pressure-mass flow” counterpart. The frozen-rotor interface has been used to connect the domains. No-slip boundary condition is imposed on all walls. The clearance size is adjusted for thermal growth and a small roughness of $4\ \mu m$ is integrated into the wall model to get the best match for leakage rate. Of the utmost importance is to have meticulous readings of clearance and roughness because both parameters have a strong effect on rotordynamic coefficients and leakage rate [131]. In fact for certain leakage rate, there is a spectrum of clearances and roughness to converge to the same leakage rate. Table 3 lists the operational conditions and fluid properties.

Table 3. Operational conditions (adapted from [49])

p_{in}	p_{out}	ω	μ	ρ	T
(kPa)	(kPa)	(rpm)	(kg/ms)	(kg/m ³)	(°C)
207	0	2000	1.792×10^{-3}	774	46.1

2.4. Results

Figure 28 clarifies the need for including the injectors before inlet chamber. The pressure is barely lost before entering the seal; in fact, stagnation pressure due to jet of injected fluid causes a small rise in pressure which leads to back flow. Hence, the orifice type injectors ensure numerical stability. Figure 29 explains the necessity of an extension annulus after the tooth. The tooth itself suppresses back flow at high excitation frequencies.

Figure 30 depicts the trend of pressure and swirl ratio all the way from inlet chamber to the single tooth labyrinth. These data have been extracted from the plane of $r = 50.9 \text{ mm}$ which is almost the mid-plane inside the seal clearance. The pressure profile evidently resembles a linear pressure drop along the seal. This operating configuration has about 10% pressure loss at inlet and no pressure recovery at outlet. These data are especially helpful for calibrating a bulk-flow model for SSGR. Also the small pressure drop at single tooth asserts the fact that there is no suction at the outlet chamber. As regards to swirl ratio, several important observations can be made. First of all, the seal section of the rotor should not be flush with the inlet rotor radius since the

high swirl ratio close to the rotor surface supplies an inflow of high swirl ratio into the seal (*please note that $r = 50.9 \text{ mm}$ outside the seal is representative of an area very close to the rotating wall and has higher swirl ratios than average*). Instead, a groove or step should be placed before the seal inlet to take advantage of core flow's low swirl ratio. With current design, the seal cannot benefit from the radial injection low pre-swirl.

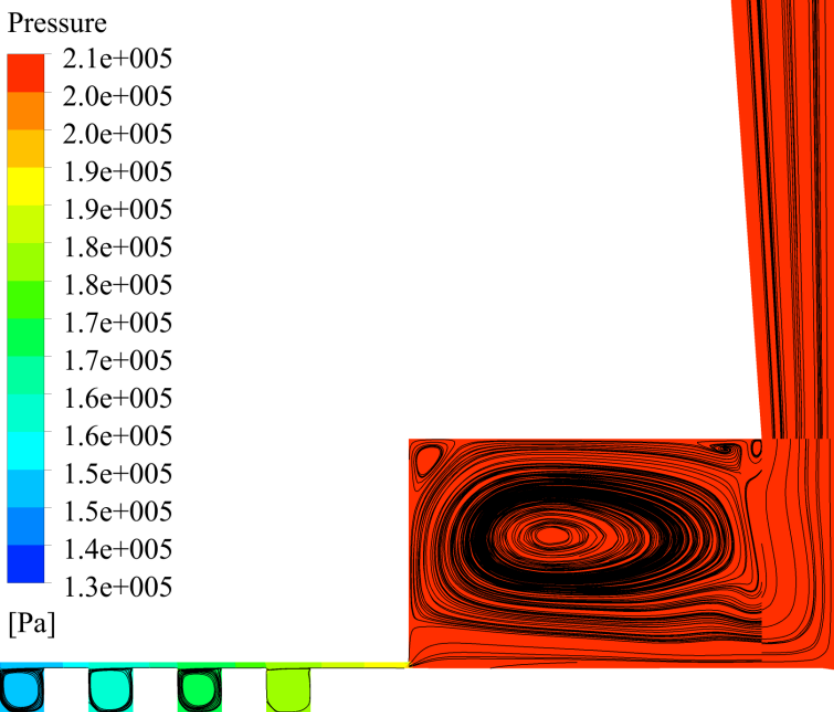


Figure 28. Suppressed back flow at inlet chamber and flow streamlines at inlet plenum

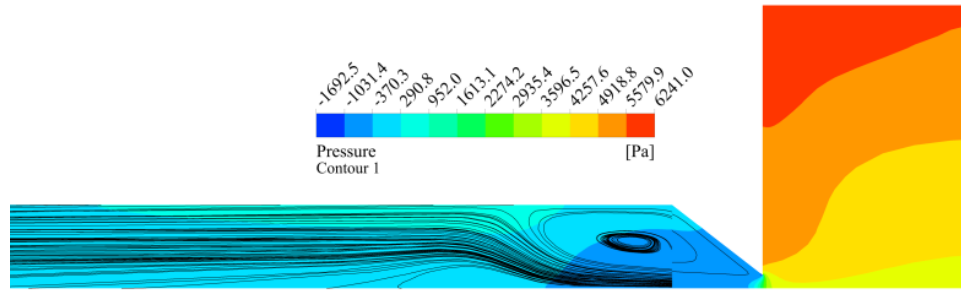


Figure 29. Flow reattachment in extension annulus

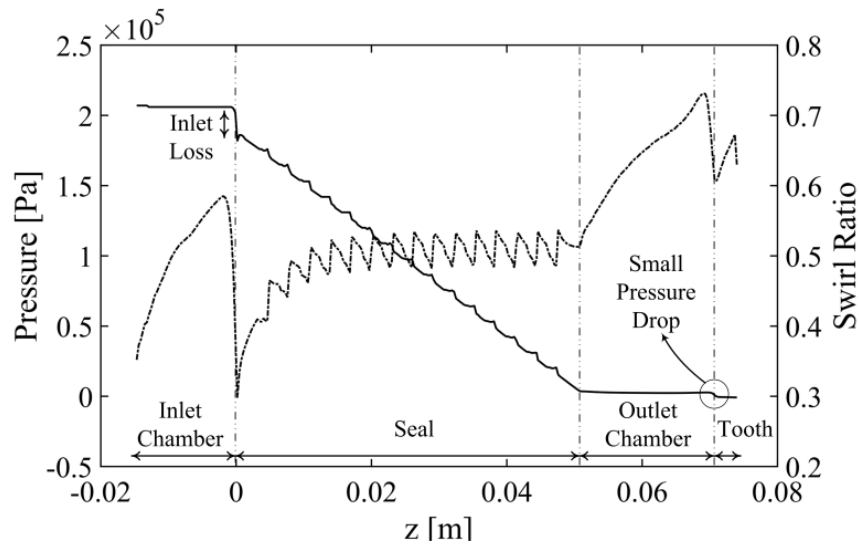


Figure 30. Pressure and swirl ratio variation at $r=50.9$ mm in the inlet plenum, seal and outlet chamber

In addition, the swirl ratio experiences a steep drop and is almost discontinuous right before any inlet section. Therefore, PSR cannot be measured accurately with conventional methods such as a pitot tube. Even at the outlet section, the OSR should be measured at multiple radii and then averaged to give the correct result, although it is not discontinuous like PSR. Finally, almost half way through the seal, the swirl ratio has reached its final value and there is no appreciable gain in swirl after this point.

In accordance to Figure 31 OSR shows a small sensitivity to the excitation frequency while PSR is larger for the backward whirl especially at lower frequency ratios (FR). The data in this figure refers to both forward and backward whirl. Leakage, however, shows more sensitivity to the FR. Referring to Figure 21, the shear rate continues to grow as Ω increases which results in an additional loss.

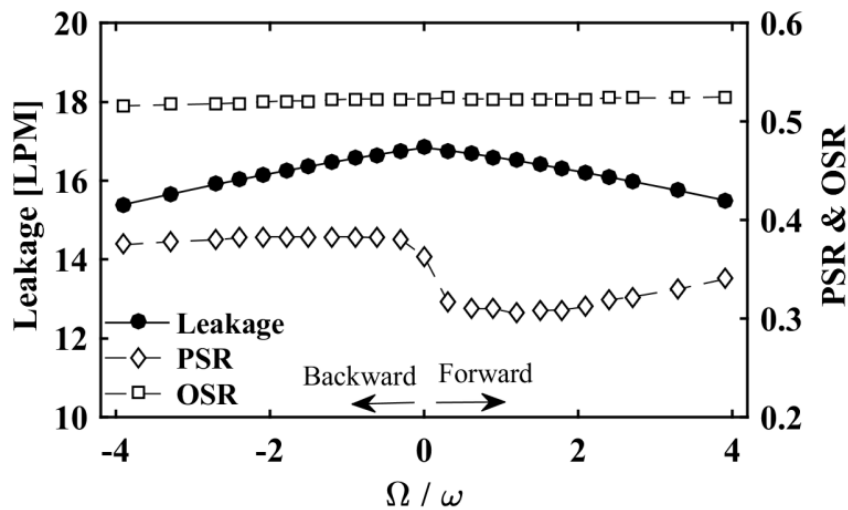


Figure 31. Leakage, pre-swirl and outlet swirl ratio versus frequency ratio

The pressure and shear stresses acting on the seal section of the seal are integrated to find F_x and F_y , the acting forces on the rotor. In experiments, these forces are measured on the stator. While the radial pressure gradient is small both set of forces are equivalent. CFD calculations verify the validity of this assumption. Next, these forces are used to find the dynamic stiffness coefficients. Figure 32- Figure 35 show how these coefficients vary against excitation frequency.

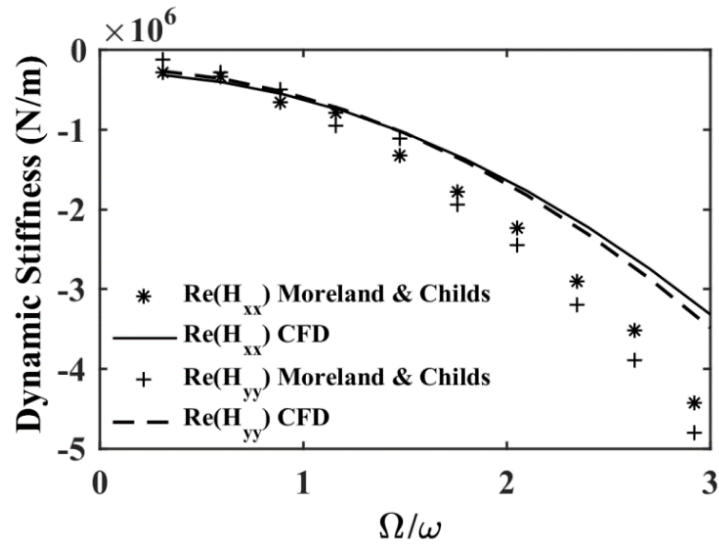


Figure 32. Dynamic stiffness $Re(H_{ii})$ variation versus excitation frequency (experimental data adapted from [49])

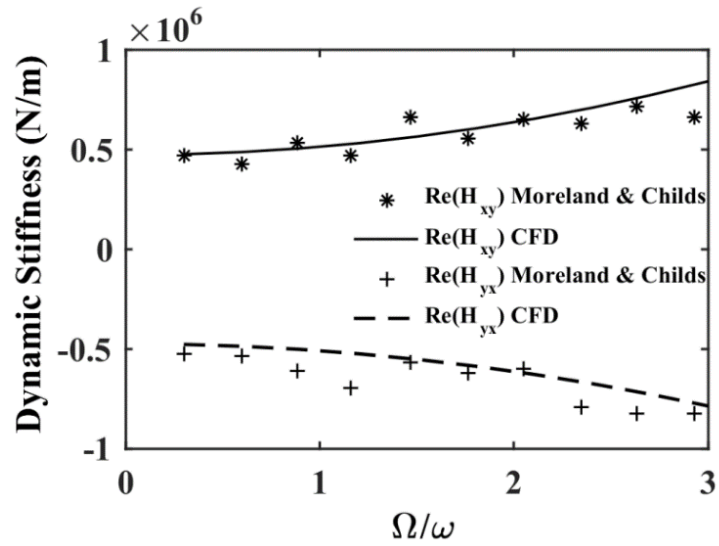


Figure 33. Dynamic stiffness $Re(H_{ij})$ variation versus excitation frequency (experimental data adapted from [49])

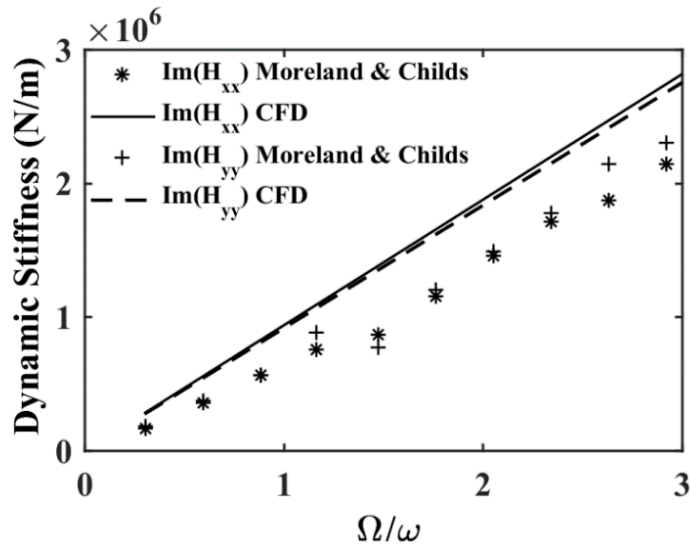


Figure 34. Dynamic stiffness $\text{Im}(H_{ii})$ variation versus excitation frequency (experimental data adapted from [49])

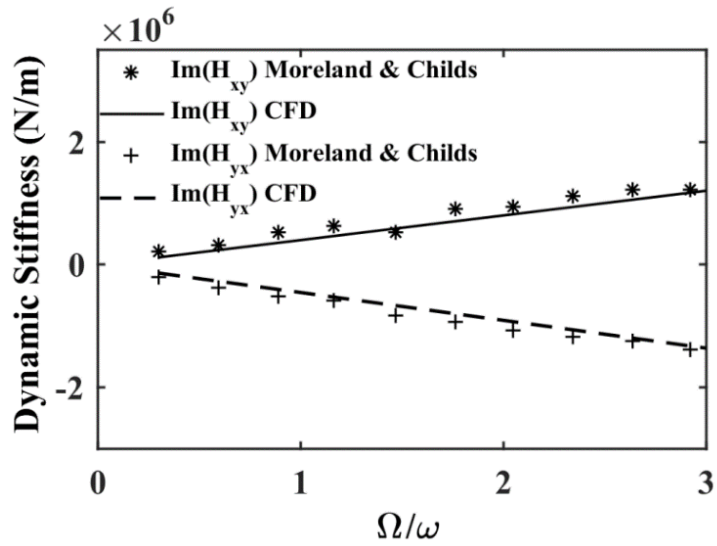


Figure 35. Dynamic stiffness $\text{Im}(H_{ij})$ variation versus excitation frequency (experimental data adapted from [49])

Dynamic stiffness coefficients closely resemble the experimental results of Moreland and Childs [49], as will be shown later in this section. The real parts show almost

quadratic behavior and imaginary parts follow a linear trend; thereby justifying the curve fitting approach and conventional mass, damping, stiffness (MCK) model. The correct approximation of added mass coefficients (especially cross-coupled inertia) requires simulations at high frequency ratios where effect of M_{ij} is more dominant. This part of simulations demands the most computational effort, since convergence is much slower than small frequencies. Other coefficients can be found effectively at a region of low frequency. More efficiently, one can simulate both forward and backward whirl with the smallest number of computational points and extract the most accurate data for K_{ij} and C_{ij} . With the hindsight of delivered data, neglecting cross-coupled inertia term from calculations readily obviates the need to move to large frequencies (Direct inertia is large enough to be captured accurately in low-frequency region).

Table 4 lists the rotordynamic coefficients both from CFD calculations and experimental curve fittings. Best agreement is found in damping and inertia terms. All other coefficients are predicted reasonably well. Please note that the stiffness value deviation stems from two facts. First, as was mentioned by Moreland and Childs [49] the negative direct stiffness requires integration of “stiffeners” to the test rig. Therefore, measured normal force F_n at low frequencies is uncertain due to the contribution of stiffeners to this small force. Consequently, the experimental stiffness coefficients suffer from level of uncertainty. Second, the least-square-fitting approach at wide range of frequency has a negative effect on both experimentally and numerically predicted stiffness values. Referring to Figure 32 and Figure 33, the intercept at $\Omega = 0$ is much closer than what is found from wide frequency curve fitting.

Table 4. Rotordynamic coefficients comparison (experimental data adapted from [49])

	CFD	Experiment
K_{xx} [N/m]	-281425	-450000
K_{yy} [N/m]	-230427	-460000
K_{xy} [N/m]	473330†	590000
K_{yx} [N/m]	-473589†	-640000
C_{xx} [Ns/m]	4490	3450
C_{yy} [Ns/m]	4389	3880
C_{xy} [Ns/m]	1919	1870
C_{yx} [Ns/m]	-2165	-2050
M_{xx} [kg]	7.69	10.11
M_{yy} [kg]	8.24	10.91
M_{xy} [kg]	-0.94	0.06
M_{yx} [kg]	0.79	0.27

† Actual value from static ($\Omega = 0$ hz) simulation was calculated $\pm 320,000$, however wide spectrum curve fitting causes deviation.

All data consistently show negative value for direct stiffness and the magnitude is considerably lower than cross-coupled stiffness. The negative stiffness along with the large direct added mass term imply that the seal behaves negatively in terms of centering forces.

For a circular whirl orbit, neglecting cross-coupled inertia term, one can write the tangential force as [1]:

$$F_t = eC\omega(WFR - FR) \quad (13)$$

where $FR = \Omega/\omega$ is the Frequency Ratio and WFR indicates the Whirl Frequency Ratio. Subsequently, it can be deduced that it is only the forward whirl which has a destabilizing effect provided that $FR < WFR$. Accordingly, Figure 36 supports this idea, and only a small forward low frequency area shows the same sign for F_t and FR . Moreover, the plot shows very smooth curves for F_n and F_t which approves the applicability of the MCK model. The whirl frequency ratio can be found from the intercept of F_t and FR axis which is about $WFR = 0.6$. This value agrees well with the definition:

$$WFR = \frac{k}{C\omega} \quad (14)$$

which is calculated as $WFR = 0.51$ from Table 4. Moreland and Childs [49] read a value of $WFR = 0.8$. It should be noted that the whirl frequency ratio will significantly change with working condition and the current values should not be generalized for all SSGR cases. For synchronous whirl

$$F_t = -eC_{eff}\omega \quad (15)$$

therefore C_{eff} is directly proportional to F_t magnitude at $FR = 1$. Further examination of the graph shows that F_t magnitude at $\Omega = \omega$ is quite small implying that there is not much of effective damping. From the definition:

$$C_{eff} = C(1 - WFR) \quad (16)$$

the CFD value will be only $C_{eff} = 1760 \text{ Ns/m}$, and from experiments [49] $C_{eff} = 730 \text{ Ns/m}$ which confirms the weak effective damping.

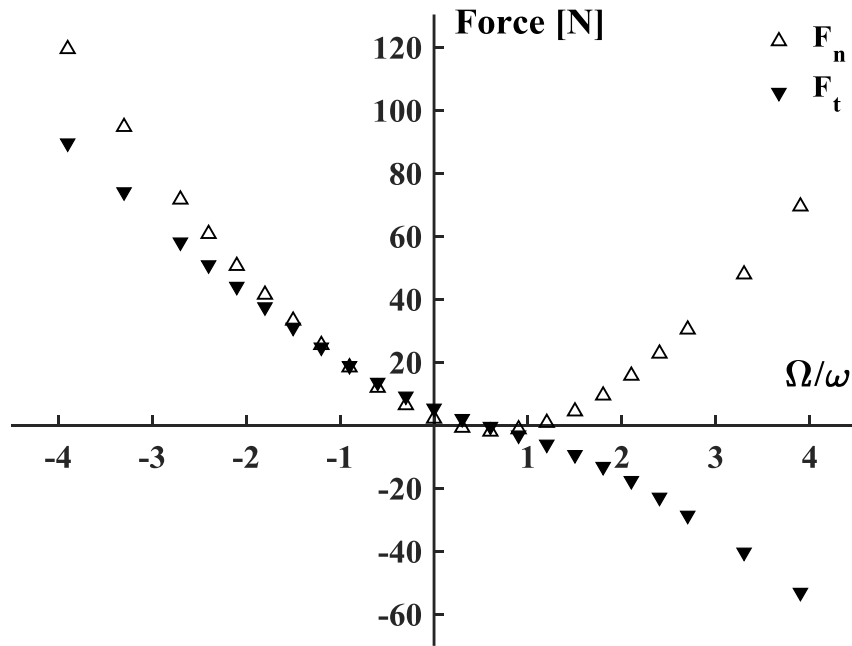


Figure 36. Normal and tangential forces acting on the rotor

The shaft rotational speed (spin speed) retards the leakage rate to a great degree, as is demonstrated by Figure 37. By increasing the shaft rotational speed four times, the leakage rate drops to half the original amount. The sharp drop in leakage is mostly attributed to the enhanced wall shear stress and larger Re_θ .

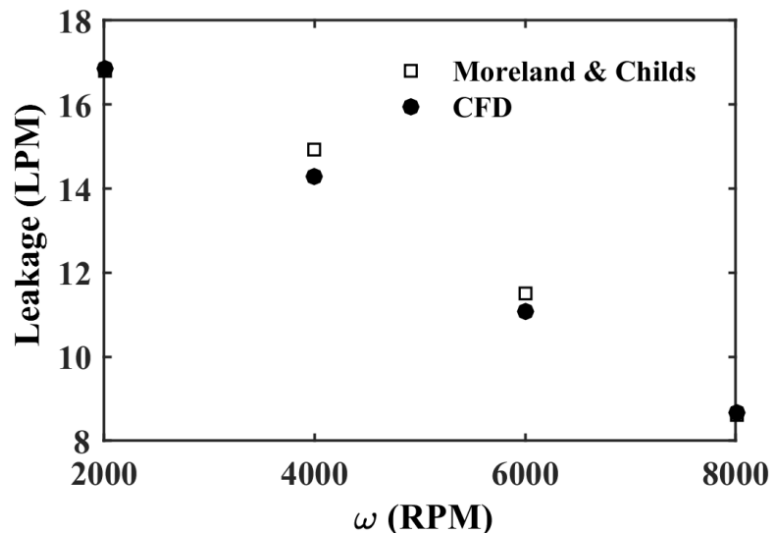


Figure 37. Effect of rotor speed on leakage (experimental data adapted from [49])

Leaking performance has been plotted in Figure 38 for a range of pressure drops to compare the SSGR seal to a plain annular seal and show the superiority of SSGR in reducing leakage rate. The SSGR seal leaks less than the plain annular seal by up to 40%. The growing deviation in the CFD and experimental leakage results has been plotted intentionally to emphasize that at higher pressures the clearance grows slightly. Although this growth is less than 2%, still it has substantial effect concerning leakage

rate prediction. This effect is even more pronounced for the plain seal where Re number is more sensitive to clearance size being as the dominant length scale.

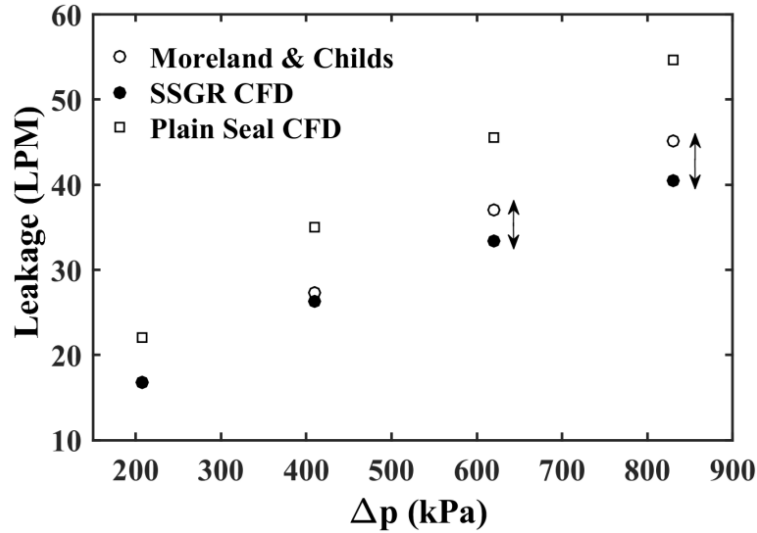


Figure 38. Effect of Δp on leakage (experimental data adapted from [49])

There is no discussion of roughness in [49]. Current study has further investigated the effects of surface roughness. Impact of surface roughness on seal performance should not be neglected. Best predictions will be possible when information regarding roughness is available. Figure 39 shows the effect of surface roughness on leakage, Pre-Swirl Ratio and Outlet Swirl Ratio. The roughness has been imposed on all surfaces (except for the extension) which include both rotor and stator in the seal region. ANSYS CFX [154] Uses sand-grain roughness model to include roughness effects on near-wall turbulent profile. For a few microns of roughness a minor drop in the leakage rate is observable. While OSR remains indifferent to the

roughness, PSR increases with the roughness size ϵ . Referring back to Figure 28 it is observed that the seal flow moves all the way along the rotor at the inlet chamber before entering the seal. Since the roughness is imposed on all surfaces, the roughened rotor at the inlet chamber carries down highly swirling flow and by the time fluid enters the seal, PSR has increased.

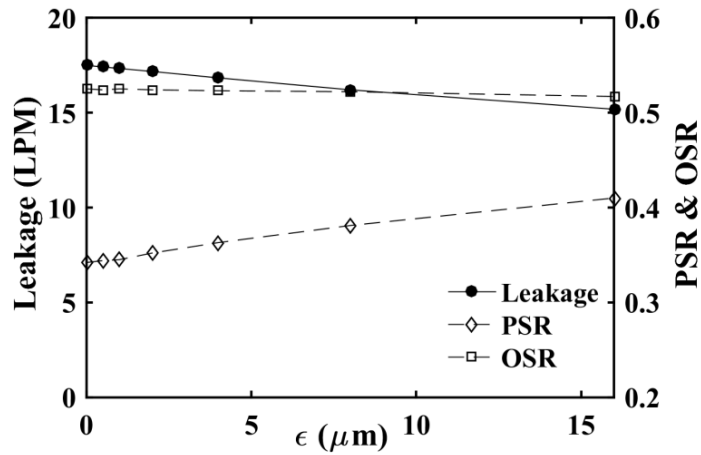


Figure 39. Effect of roughness on leakage, PSR & OSR

Figure 40 demonstrates normal (radial) and tangential impedance variation against the roughness size at zero excitation frequency $\Omega = 0 \text{ Hz}$. Zero frequency normal impedance is representative of the direct stiffness K , and tangential impedance represents the cross-coupled stiffness with negative sign $-k$.

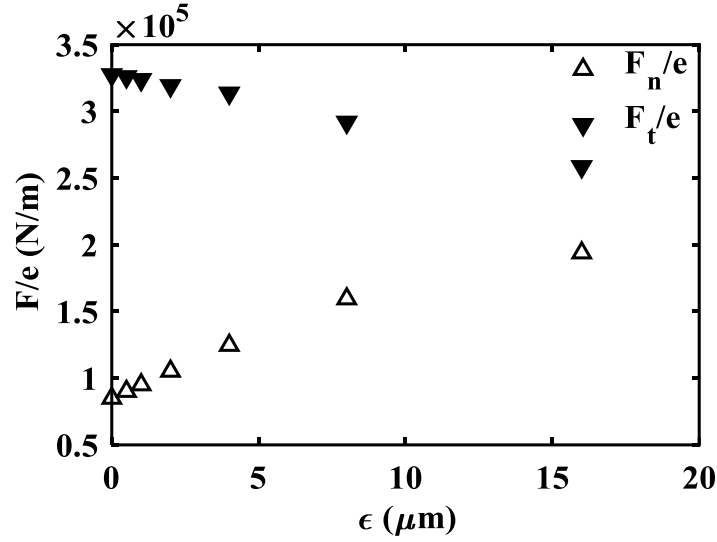


Figure 40. Effect of roughness on normal and tangential impedances at $\Omega=0$

The plot suggests that an increase in roughness has led to a drop in both stiffness values. Such behavior was previously observed in hole-pattern seals by Childs and Fayolle [25] , and it is justified through Bulk-Flow theory if $\partial\lambda/\partial h < 0$ where λ denotes friction factor and h is the film thickness. By film thickness it is meant radial clearance C_r and symbol h is adopted to be consistent with literature. The friction factor and the film thickness are related through the pressure drop:

$$\frac{4 \Delta p}{\rho \Delta z} = \frac{\lambda(\epsilon)W_0(\epsilon)^2}{h(\epsilon)} = Cte \quad (17)$$

where h is a function of roughness due to the blockage effect of the roughness model [154]. Differentiating with respect to ϵ gives the following relation:

$$\frac{W_0^2}{h} \frac{\partial \lambda}{\partial \epsilon} + \frac{2W_0 \lambda}{h} \frac{\partial W_0}{\partial \epsilon} - \frac{\lambda W_0^2}{h^2} \frac{\partial h}{\partial \epsilon} = 0 \quad (18)$$

The second term is negative according to Figure 39, and third term is positive due to the blockage effect ($\partial h/\partial \varepsilon = -1$). Thus, the sign of the first term depends on the absolute values of the second and the third terms:

$$\left| \frac{-\lambda W_0^2 \frac{\partial h}{\partial \varepsilon}}{h^2} \right| = \left| \frac{W_0}{2h} \cdot \frac{\partial h}{\partial \varepsilon} \cdot \frac{\partial W_0}{\partial \varepsilon} \right| = \left| \frac{W_0}{2h} \cdot \frac{\partial W_0}{\partial \varepsilon} \right| \quad (19)$$

and it can be easily calculated that

$$\left| \frac{W_0}{2h} \right| \& \left| \frac{\partial W_0}{\partial \varepsilon} \right| \gg 1 \quad (20)$$

therefore $\partial \lambda/\partial \varepsilon < 0$ to satisfy Eq. 14 condition. Since the seal is operating in fully-turbulent region, the friction factor does not depend on Re number and only depends on the surface roughness [25]:

$$\frac{\partial \lambda}{\partial h} = \frac{\partial \lambda}{\partial \varepsilon} \frac{\partial \varepsilon}{\partial h} = -\frac{\partial \lambda}{\partial \varepsilon} > 0 \quad (21)$$

hence, both the direct and cross-coupled stiffness values will fall. In case of the direct stiffness, it will become even more negative. Figure 40 implies that this drop in the direct stiffness is not negligible by any means. A more physical argument states that the Lomakin centering effect is getting less effective as friction factor reduces, and the direct stiffness grows even more negative. As for the cross-coupled stiffness, $\partial \lambda/\partial \varepsilon < 0$ means that the swirl would not develop by the rough wall as effectively as the smooth wall case.

2.5. Conclusion

A groove-on-rotor annular liquid seal CFD model has been developed and compared to the experimental results of Moreland and Childs [49]. The steady-state Navier-Stokes equations along with a shear stress transport turbulence model are solved in the rotor-fixed domain. Injectors and inlet chamber have been modeled to accurately model the upstream swirl ratio and suppress back flow at the inlet. The model also includes outlet chamber, single labyrinth tooth and an extension domain to accurately reproduce downstream conditions and suppress back flow at the outlet.

The results support the validity of the steady-state RANS CFD simulations applied to circular whirl for precise prediction of rotordynamic coefficients similar with a 2D experimental shake method. Close agreement with experiment occurs with forces and leakage rates, provided that sufficient auxiliary domains are integrated to the model. Damping and inertia coefficients are predicted quite accurately. Stiffness predictions compare reasonably well, although the experimental uncertainty in the low frequency region prevents a rigorous comparison of stiffness values. A wide spectrum least-square-curve-fit also has a negative effect on stiffness value predictions, whether in experiments or CFD simulations. Overall, dynamic coefficient agreement with test affirms that the physics have been reproduced quite accurately.

Negative direct stiffness, large cross-coupled stiffness, small direct damping and substantial direct virtual mass terms fortify the position that long SSGR seals have poor stability characteristics compared to plain annular seals. However, in terms of leakage, SSGR seals show superior performance.

Leakage and OSR do not show an appreciable dependency on excitation frequency. On the other hand, forward and backward whirling motion show noticeably different PSR values. Also, increasing the shaft rotational speed induces sharp drop in leakage rates.

CFD simulations reveal several points that one should be aware of when predicting seal performance. The swirl ratios undergo sharp changes at entrance and exit of the seal (PSR and OSR); thus measuring these values requires non-intrusive equipment at multiple locations. Similar condition rules over CFD simulations, one cannot neglect the upstream conditions, otherwise wrong PSR values affect the results adversely. Furthermore, roughness and surface finish is a crucial parameter in estimation of leakage and stiffness. Best results will be achieved by including this parameter, especially the stiffness coefficients which show more sensitivity to the roughness size. Finally, clearance size typically shows a dependence on magnitude of the seal pressure differential which should not be overlooked, for it is a key factor in prediction of leakage.

3. ROTORDYNAMIC FORCES OF VOLUTES AND DIFFUSERS: A TRANSIENT CFD APPROACH*

3.1. Introduction

Anticipating possible sources of vibration and rotordynamic instability is a vital step in the design process of turbomachinery components. The geometry as well as the complex nature of the flow inside impellers and their associated components such as volutes, leakage passages, and diffuser vanes will not easily lend themselves to rotordynamic analysis. However, similar to the other turbomachinery components, at certain operating conditions, the developed dynamic forces may excite the whirling motion and lead to an undesired instability. Noting that impellers, especially pumps, regularly operate at off-design conditions, and imbalance may easily form after a duration of operation, they are prone to whirling vibration [1]. For this reason, API level II stability criterion requires further analysis to account for “*all sources that contribute to the overall stability*”[15]. Among these sources, impellers have been a special concern of turbomachinery specialists [32, 87, 112]. Due to significance of the topic in power, oil and aviation industries as well as biomedical applications [155, 156], pioneering experimental studies were done to measure such forces despite significant challenges [39, 68, 72]. Dynamic forces of a shrouded impeller mainly arise from the asymmetric distribution of pressure over the impeller front shroud, which is caused by

* Reprinted in part with permission from “Rotordynamic Force Coefficients of Volute and Diffusers for Prediction of Turbomachinery Vibration,” by Mortazavi, F., and Palazzolo, A., 2018. *ASME J. Vib. Acoust.*, 140(3), pp. 031002-031002-031009., Copyright 2018 by ASME.

the eccentric whirling motion of impeller [31]. Theoretical models were developed to gain a deeper knowledge of the problem while reducing the time and cost needed for such analysis [102, 103, 157]. With the advent of Computational Fluid Dynamics (CFD) [158-161] and its wide application in the turbomachinery industry [162-164], several researchers [34, 165] employed quasi-steady and small perturbation models to obtain the dynamic forces caused by the impeller shrouds without the major simplifications of the prior theoretical models. The quasi-steady model has been shown to effectively predict the major portion of the dynamic forces coming from the impeller [35, 126].

A quasi-steady model turns a transient problem into a steady one by solving the problem in the whirling frame [166]. A limitation of the quasi-steady and bulk-flow models compared with the transient model is that while they can be applied to non-axisymmetric problems, these applications are approximate in the sense that some non-zero terms in the rotating frame form of the Navier Stokes equations must be assumed to be negligible. The degree to which accuracy of the rotordynamic impedances is compromised with use of the quasi-steady model is investigated in this section. Therefore, they cannot account for the impact of the volute, diffuser vanes or impellers without a shroud (open impellers). The diffuser helps the conversion of kinetic energy to potential energy by guiding the impeller outflow through a streamlined diffusing passage. Similarly, the volute collects the discharge flow and further converts the energy downstream. This is especially becoming more relevant as the new minimum performance requirements demand addition of diffuser vanes for an efficiency boost.

Several experimental and theoretical impeller rotordynamic studies have accounted for the presence of a volute or diffuser before [69, 72, 73, 102, 103]. Chamieh et al. [72] measured zero whirl frequency forces on an eccentric impeller inside a volute, and Jery continued the work by imposing a dynamic eccentricity [73]. Adkins and Brennen [102] used a theoretical approach to show the effect of the flow rate on the impeller rotordynamic coefficients inside a volute. Tsujimoto et al. [103] used a potential flow model to show the validity of the skew-symmetry assumption for an impeller whirling inside a volute. The current study proposes a transient CFD approach based on mesh deformation techniques to enable the analyst to include the non-axisymmetric features in the CFD model and enhance the accuracy of impeller dynamic force predictions. There is no consensus on the contribution of the volute and the diffuser vanes to the overall rotordynamic forces. Most researchers believe it is a small portion [1, 126]. Although the shroud axial projection acts as a transferring medium for dynamic forces, the pressure and swirl ratio boundary conditions are largely dependent on upstream condition. Volute also contribute to the positive cross coupled stiffness, and usually this contribution is larger than the direct stiffness. The cross coupled stiffness may have a significant influence on rotordynamic stability.

Since a complete pump model shows complex flow physics, a reliable CFD model can provide important quantitative results and qualitative insights to the analyst. A brief comparison of the CFD-based methodologies used to simulate impeller dynamic forces is given in Figure 41. Among all the methods, the subdomain mesh motion approach has been selected, as it best preserves the original grid quality, resembles the

real physics of the problem, and its performance is more computationally efficient compared to the other transient methods (i.e. full rotor or stator mesh motion [140], immersed solid methods [167], and remeshing approaches [168, 169]).

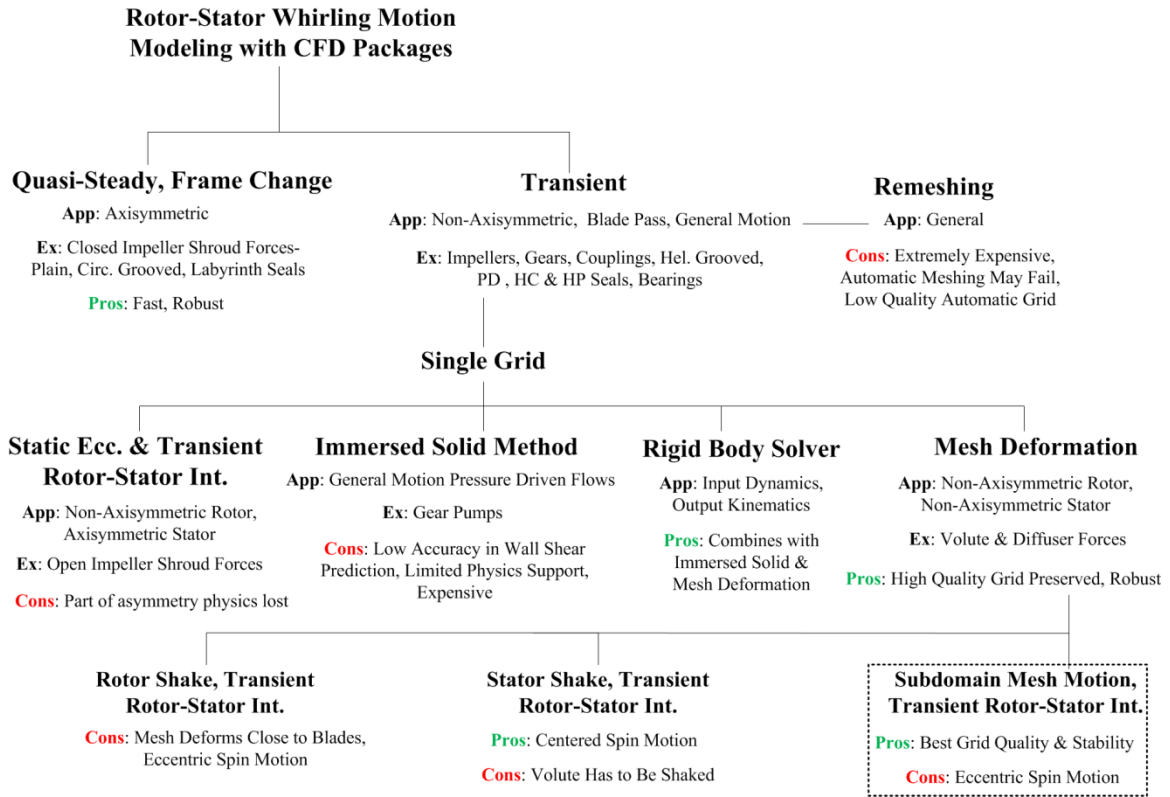


Figure 41. Several commercial CFD methods to model impeller rotordynamic forces

This is the first study to utilize a CFD method to obtain the rotordynamic coefficients of a volute or diffuser, and the approach presented uses a transient model which is not limited by the geometry. The current method's solution has been numerically tested with eccentricities as small as 10% of the original experimental

eccentricity, and the results remain the same as the case with the nominal eccentricity. The same conclusion can be made theoretically for small eccentricity ratios [123]. In other words, this method is not limited by the large eccentricities that are needed in experiments to overcome measurement uncertainties, and which may exceed those in actual operation of the machine. Furthermore, the contributions of the shroud, volute and diffuser vanes are extracted to shed light on the question of “which components dominate, and which components can be neglected, in the analysis?” A parametric study is performed to augment prior results for further investigation of the topic.

The study is organized as follows. First, the dimensions and operating conditions from the experiments of Jery [73], and the CFturbo [170] designed components are presented. Next, the numerical model will be discussed in detail, including boundary conditions, force extraction and grid independency study. The methodology will be validated against experiments of Jery [73] in the results section. That is followed by a comparison of several volute designs in terms of rotordynamic forces and the impact of having diffuser vanes. Finally, results regarding some secondary aspects such as the effect of “Gap A” (The radial gap between the impeller discharge and the diffuser, See Figure 42), clearance profile and spin speed will be presented. The results are then summarized.

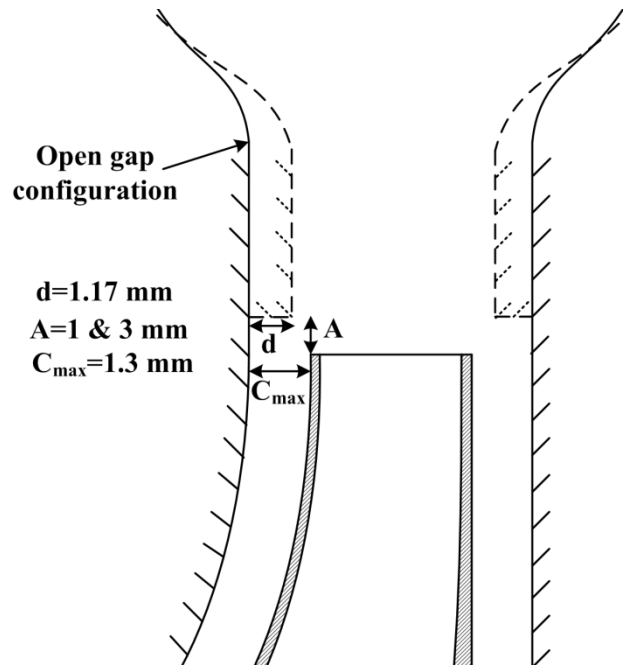


Figure 42. Schematic of Gap A configurations

3.2. Design Parameters and Dimensions

The experimental results from Jery [73] and Jery et al. [171] from CalTech have been employed to validate the numerical approach. Jery's pump case has been selected because more geometrical details have been discussed. Since some of the design parameters are unavailable, the commercial package CFTurbo [170] has been employed to inverse design the unknown parameters. The dimensions and the operating conditions of the pump are given in Table 5. The main dimensions are illustrated in Figure 43a. Details of design procedure using CFTurbo are discussed in Appendix B.

Table 5. Dimensions and operating conditions provided (adapted from [73].) The shroud thickness t_{sh} and the diffuser inlet width b_3 are found from inverse design using CFTurbo

parameter	Value	parameter	Value
β_2	23°	e	0.315 mm
b_2	1.58 cm	L	3.22 cm
b_3	24.75 mm	ϕ	0.092
A_{throat}	20.75 cm ²	ψ	0.49
C_r	0.13 mm	ω	1000 rpm
C_{max}	1.3 mm	Ω/ω	-1.0 to 1.0
D_0	8.0 cm	ω_s	0.57
D_2	16.2 cm	t_{sh}	3.175 mm
D_3/D_2	1.13	Z	5

Jery's original clearance dimensions have been obtained from [102] which has a fairly large clearance. This large cavity may not be representative of today's high performance pumps which have very tight clearances. For this reason, a second clearance has been simulated in addition to the original clearance. The second case has a tight uniform clearance profile. Both clearances are illustrated in Figure 43b.

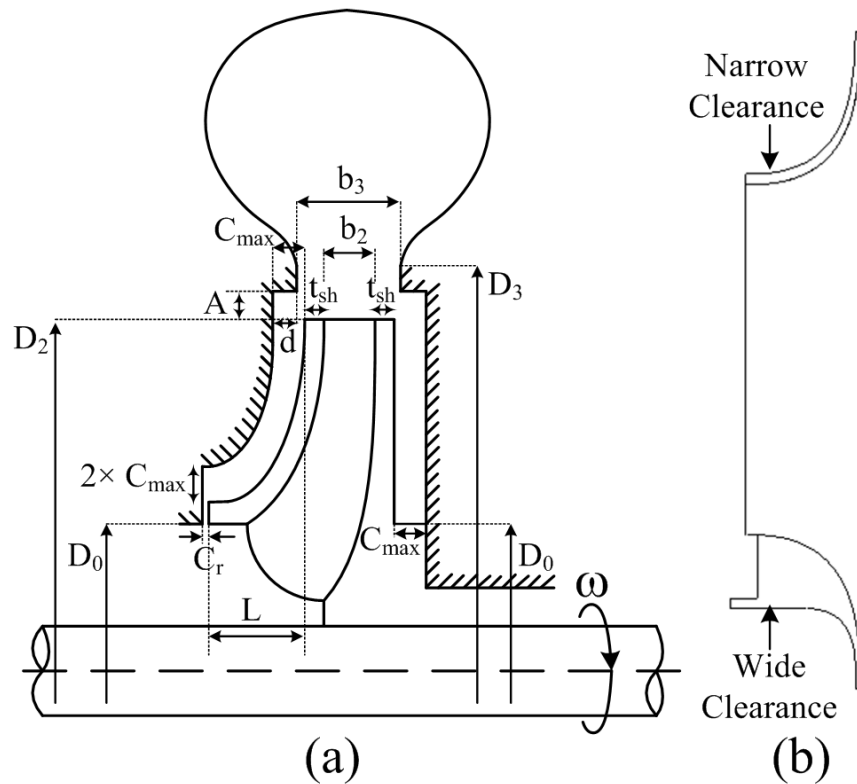


Figure 43. Pump dimensions. (a) main dimensions (b) narrow versus wide clearance

In experimental measurements, sometimes the entrances of a pump side-wall gaps are temporarily sealed using flow restrictor rings in order to reduce the leakage flow. These flow restrictors artificially increase the rotordynamic forces on the impeller front shroud [102]. In the present study, such flow restrictors have been excluded to avoid unrealistically large rotordynamic forces. Also, a face seal has been included in the model to minimize the contributions of transverse fluid induced forces contributed by the seal. Other parameter of interest is the gap (Gap A in Figure 42 and Figure 43) between the impeller discharge and the entrance of the leakage passages. A narrower

gap leads to better efficiency, smoother axial thrust curves, and better stability characteristics for the head-flow curve [22]. On the other hand, it has been reported that by making this opening tighter, severe vibration problems will result [172]. Bolleter et al. [78] investigated the influence of Gap A on impeller rotordynamics. Accordingly, three settings of Gap A have been examined, one of which completely removes the gap (See Figure 42).

For the second part of the study, several matched flow volutes have been designed using CFturbo, as well as a 13-vane diffuser. The number of vanes has been selected such that there is a minimum chance of resonance [173]. The volute cross sections covered in this study include trapezoidal (Trp), rectangular (Rec), circular (Cir), radius based (Rad) and round asymmetric (Rnd) designs. The vaned diffuser (Dif) has a logarithmic spiral-straight 2D design. Figure 44 shows the investigated volute profiles.

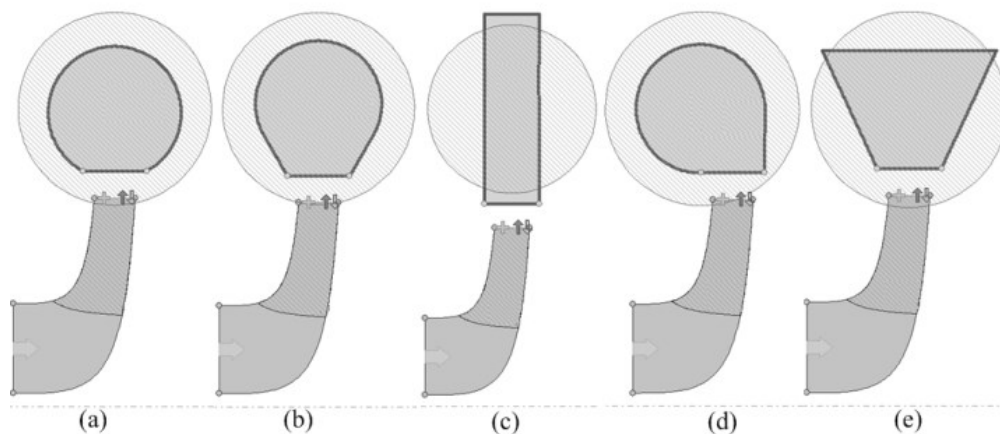


Figure 44. Volute designs from CFturbo. (a) circular (b) radius based (c) rectangular (d) round asymmetric (e) trapezoidal

3.3. Numerical Methodology

3.3.1. Computational Domains

The current model consists of the suction pipe, impeller, rear and front leakage paths, front face seal, diffuser vanes, volute, cutwater, discharge diffuser and the extension pipe at the outlet. For the details of the grid size and the corresponding domain sizes refer to Table 6.

Table 6. Grid size break-down

Domain	Number of nodes
Suction nozzle	57,000
Impeller	522,000
Front leakage path	211,000
Rear leakage path	157,000
Front face seal	86,000
Diffuser	697,000
Volute	79,000
Cutwater	12,000
Cone	38,000
Extension pipe	8,000
Total	1,867,000

Since the rotordynamic forces arise from the close interaction of the side wall gap flow with the primary flow and the diffuser/volute upstream condition, an extended model is required to include all these regions. Figure 45 shows these computational domains. The CFD model consists of several domains. All cases use a high quality fully structured grid with a maximum y^+ (the dimensionless distance from the wall defined as $y^+ = y\sqrt{\tau_w/\rho\nu}$) value of 36 for better accuracy, however y^+ values smaller than 200 would be sufficient. The mesh is generated using ANSYS ICEM CFD [174, 175].

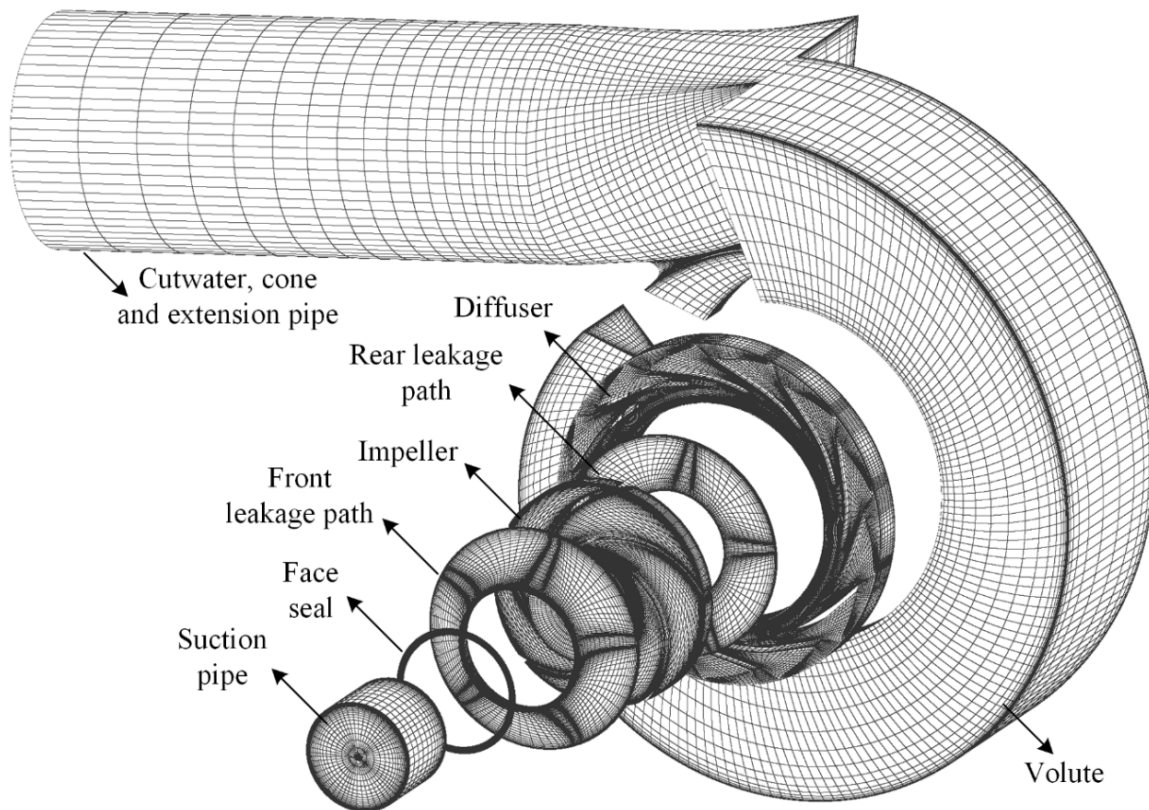


Figure 45. Exploded view of the computational domains

3.3.2. CFD Set-up

The commercial CFD package ANSYS CFX 17.2 has been utilized to solve the transient Reynolds-Averaged Navier-Stokes (RANS) equations with the turbulence model $k-\omega$ SST (Shear Stress Transport), the validity of which has been tested in numerous turbomachinery studies [129, 148, 176, 177]. The inlet mass flow rate and outlet static pressure boundary conditions have been imposed. All the walls use a no-slip boundary condition with a smooth wall condition. A transient rotor-stator interface has been utilized between the rotating and stationary domains. The convergence criteria for the residuals have been set to 10^{-5} . For more information about CFX solver theory, please refer to Appendix A.

3.3.3. Mesh Deformation

The current study uses the mesh deformation technique to model the whirling motion of the impeller inside the casing. The displacements are imposed on boundaries as well as subdomains to reduce total computational cost and improve mesh quality. A diffusion equation for the mesh has to be solved at each time step [154] in order to diffuse the imposed motions on the boundary nodes to the interior nodes. The diffusion equation is solved to reach a residual value of 10^{-5} :

$$\nabla \cdot (\Gamma_{\delta} \nabla \delta) = 0 \quad (22)$$

where the displacement relative to the previous location of the node has been shown with the symbol δ , and Γ_{δ} denotes the mesh stiffness. By expressing the mesh stiffness in terms of cell volume, one can shift the deformation area to the regions with coarser

mesh (far from the walls) and in this way preserve the orthogonality of the grid adjacent to the wall.

$$\Gamma_{\delta} = \left(\frac{\mathcal{V}_{\text{ref}}}{\mathcal{V}} \right)^{C_{\delta}} \quad (23)$$

The reference volume \mathcal{V}_{ref} is set to the mean cell volume size in the grid, and the stiffness exponent C_{δ} has been set to 2.0 in this work. By imposing boundary conditions in the Laplace equation, one can preserve the boundary original shape as well as its normal derivative which improves the mesh orthogonality near the walls [26]. For further details please refer to Appendix A. The mesh deformation boundary conditions are shown in Figure 46 considering both the blade to blade and meridional views. For this problem, a sub-domain has been defined which contains the impeller. Since all the nodes inside the sub-domain have the same whirling displacement, the cells will not be deformed with respect to each other; hence, the mesh quality inside the impeller is preserved. The deformation happens in a region far from the impeller called the absorption domain. Both the sub-domain and the absorption domain are parts of an assembly domain which has the rotational speed of the spinning motion.

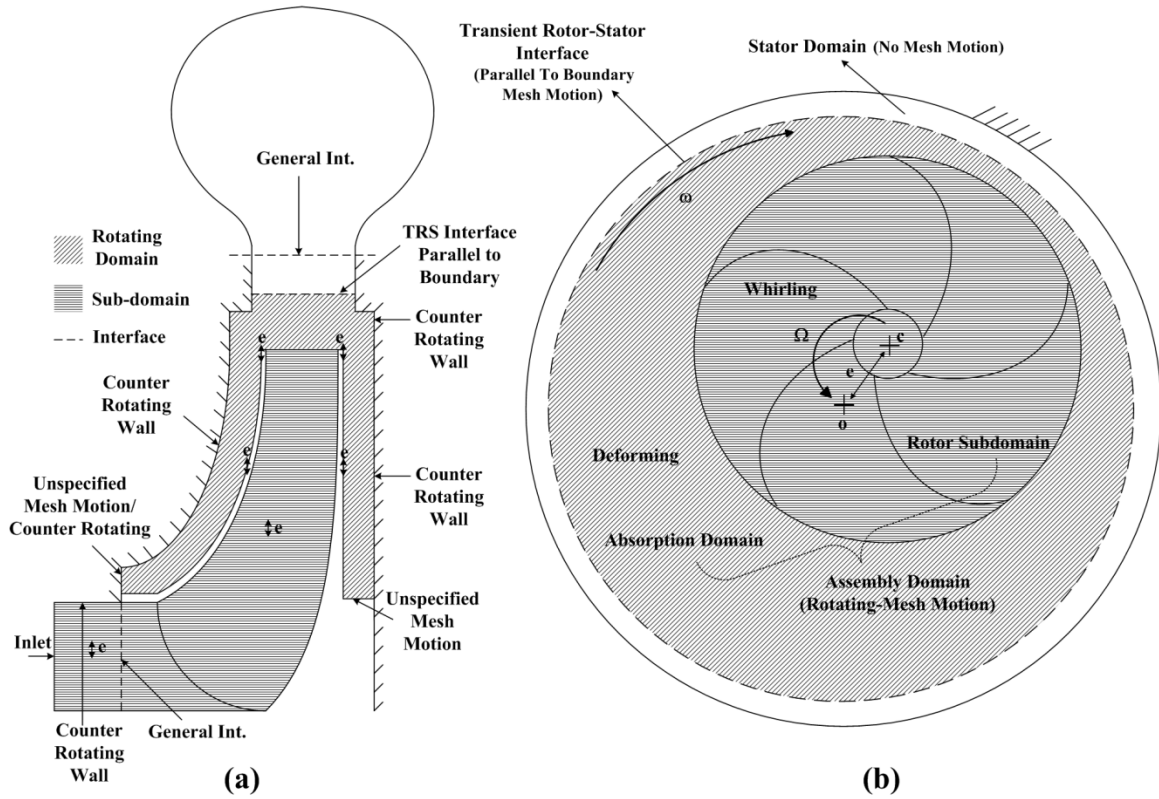


Figure 46. Mesh deformation boundary conditions. (a) blade to blade view (b) meridional view

The circular whirling motion is lagged in one direction by introducing a ramp function in order to avoid rapid mesh distortion:

$$e_x = e \cos(\omega t) \mathbb{H} \left(|\omega|t - \frac{\pi}{2} \right) \quad (24)$$

$$e_y = e \sin(\omega t)$$

where \mathbb{H} is the Heaviside step function. Figure 47 depicts the gradual change in mesh displacement. Note that the x component activates after $\pi/2$ revolution in order to start from $e_x = 0$.

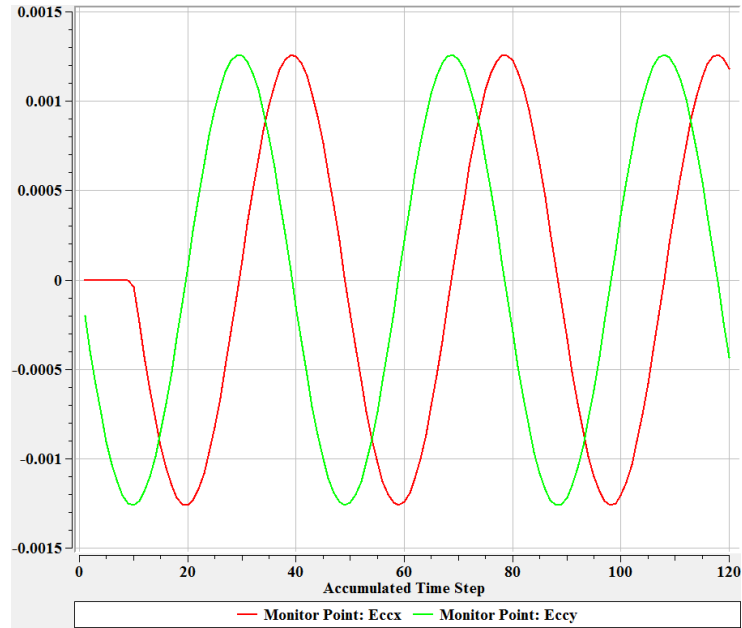


Figure 47. Gradual mesh deformation and the lag in e_x (red curve)

Beside the gradual mesh displacement, the other provision employed here is to improve the convergence criteria of the Mesh Deformation Solver. CFX advanced solver settings allows the user to change the default settings of the governing equation solution schemes. The mesh deformation equations run in pseudo-time. By increasing the number of outer loops for this pseudo-time marching, the mesh diffusion scheme has more time to converge and adapt to the new BCs. In accordance with this change, the target RMS residual of Mesh Deformation equation is reduced from 10^{-4} to 10^{-5} .

Finally, the physical time step of the current problem defines how fast these changes are going to happen. A rule of thumb for turbomachinery time-step Δt is:

$$\Delta t \sim \frac{1}{\omega} - \frac{0.1}{\omega} \quad (25)$$

where ω is the spin speed or the whirl speed whichever that is larger, and it should be expressed in *rad/s* units. Meaning that the rotation per time-step must be smaller than 1/6 cycle, and should be larger than 1/60 cycle. Smaller time-steps are excessive for RANS simulations. Current simulations show that $\Delta t = 0.2/\omega$ provides enough accuracy and makes sure that the mesh does not fold.

3.3.4. Force Extraction Method

The transient stationary frame force results are collected after allowing the solution to reach its periodic state. At least 10 spinning cycles are simulated for each case. There are a number of forces present in this simulation, each of them having its own frequency such as the blade pass peak, spin peak, whirl peak, higher harmonic, etc. Figure 48 shows an example of the frequency peaks present in this study.

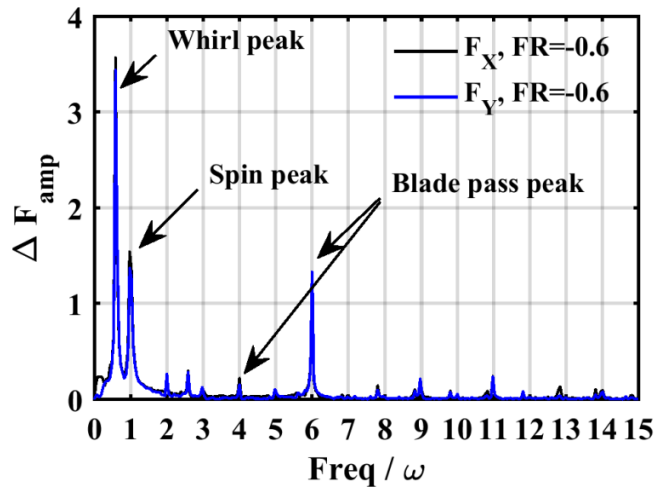


Figure 48. Sample FFT of the dimensionless forces in the stationary frame at $\Omega/\omega=-0.6$

For instance the blade pass peak appears at the frequency ratios $Z_b \pm 1$ as it modulates with the single vane volute (the tongue). However, there is only interest in the whirl frequency peak f_x^Ω, f_y^Ω in accordance to the rotordynamic vibrations motivations of this study. To this end, a Fourier transform will be applied to the stationary frame forces f_x, f_y to extract the whirl component.

$$f_x^\Omega = \sum_{k=1}^N f_x e^{-i\Omega t_k}, \quad f_y^\Omega = \sum_{k=1}^N f_y e^{-i\Omega t_k} \quad (26)$$

$$\begin{cases} f_x^\Omega(t) = \Delta f_x^\Omega \cos(\Omega t + \varphi_x) \\ f_y^\Omega(t) = \Delta f_y^\Omega \cos(\Omega t + \varphi_y) \end{cases} \quad (27)$$

$$\Delta F_X^\Omega = \frac{2\sqrt{\text{Re}(F_X)^2 + \text{Im}(F_X)^2}}{N}, \quad (28)$$

$$\Delta F_Y^\Omega = \frac{2\sqrt{\text{Re}(F_Y)^2 + \text{Im}(F_Y)^2}}{N}$$

$$\varphi_X^\Omega = \text{Atan}\left(\frac{\text{Im}(F_X)}{\text{Re}(F_X)}\right), \quad \varphi_Y^\Omega = \text{Atan}\left(\frac{\text{Im}(F_Y)}{\text{Re}(F_Y)}\right) \quad (29)$$

where N is the number of samples. Here f and F pertain to dimensional and non-dimensional values, respectively. Δ symbolizes the amplitude and φ the phase. With a change of frame one can obtain the normal and tangential dimensionless forces at the whirling frequency F_N^Ω, F_T^Ω :

$$\begin{cases} F_N^\Omega = F_x^\Omega @_{\Omega t=0} \\ F_T^\Omega = F_y^\Omega @_{\Omega t=0} \end{cases} \quad (30)$$

The amplitude and phase angles of the whirling component have been used to reconstruct the normal and tangential forces in the whirling frame. Thus, the impedance curves have been obtained.

Subsequently, a Root Mean Square (RMS) second order curve fitting has been performed to obtain the dynamic coefficients. Owing to the skew symmetry of the rotordynamic force coefficient matrices [73], one set of direct and cross-coupled dynamic coefficients for stiffness, damping and inertia terms will be sufficient. The applicability of the skew-symmetry assumption has been previously validated by the prior theoretical and experimental works in the area of impeller rotordynamic forces [73, 102, 103] which have accounted for transient effects.

All the results in this study have been delivered in dimensionless format to promote comparability and their range of applicability. The dimensionless forces are defined as:

$$F_N = \frac{f_n}{\rho\pi r_2^2 \omega^2 b_2 e}, \quad F_T = \frac{f_t}{\rho\pi r_2^2 \omega^2 b_2 e} \quad (31)$$

Similarly, the dimensionless rotordynamic coefficients are defined as follows. The capital letters K, C, M symbolize the direct values of stiffness, damping and added mass while the small letters k, c, m denote the cross-coupled values. Symbols shown with script letters like $\mathcal{k}, \mathcal{C}, \mathcal{M}$ represent the dimensionless values:

$$\mathcal{K} = \frac{K}{\rho\pi r_2^2 \omega^2 b_2}, \quad \mathcal{k} = \frac{k}{\rho\pi r_2^2 \omega^2 b_2} \quad (32)$$

$$\mathcal{C} = \frac{C}{\rho\pi r_2^2 \omega b_2}, \quad c = \frac{c}{\rho\pi r_2^2 \omega b_2}$$

$$\mathcal{M} = \frac{M}{\rho\pi r_2^2 b_2}, \quad m = \frac{m}{\rho\pi r_2^2 b_2}$$

which are determined from the numerically calculated impedances, fitted to the standard quadratic form model:

$$\begin{bmatrix} F_N \\ F_T \end{bmatrix} = \begin{bmatrix} -\mathcal{K} - c \frac{\Omega}{\omega} + \mathcal{M} \frac{\Omega^2}{\omega^2} \\ k - \mathcal{C} \frac{\Omega}{\omega} - m \frac{\Omega^2}{\omega^2} \end{bmatrix} \quad (33)$$

The dimensionless rotordynamic coefficients are found by using a least square curve fitting method. Impellers are known to show deviations from a second order curve fitting approach, requiring instead a more general transfer function model. Previously, attempts have been made by several scholars to use other methods than the least square curve fitting to improve the rotordynamic coefficients of an impeller [31, 102, 133]. However, in terms of practicality for industrial applications, the least square curve fitting model seems to be a more attractive option.

The zero frequency ratio results ($\Omega/\omega = 0$) require a special treatment in the transient analysis. The circumferential averaging approach previously used by Suzuki et al. [156] has been adopted in this study to find the non-whirling results $\bar{F}^{\Omega=0}$. The steady radial thrust F_0 is subtracted from the results. Figure 49 illustrates the impeller position phase model employed in this approach.

forces. For this reason, the results at these points have been omitted, and instead the closest points at $FR = \pm 0.9$ have been simulated and included.

3.3.5. Shroud, Diffuser and Volute Force Extraction

To specify the contribution of each component to the overall dynamic forces, separate models have been devised and then subtracted from the full model that includes the entire assembly. For the pure contribution of the shroud part of the impeller, an axisymmetric nozzle has been placed after the impeller. The nozzle suppresses potential back flows after the impeller discharge. Then the case was solved using the quasi-steady method (because the shroud is an axisymmetric component). A shift in the rotating component grid is applied to model the quasi-steady eccentric motion as it is pictured in Figure 50.

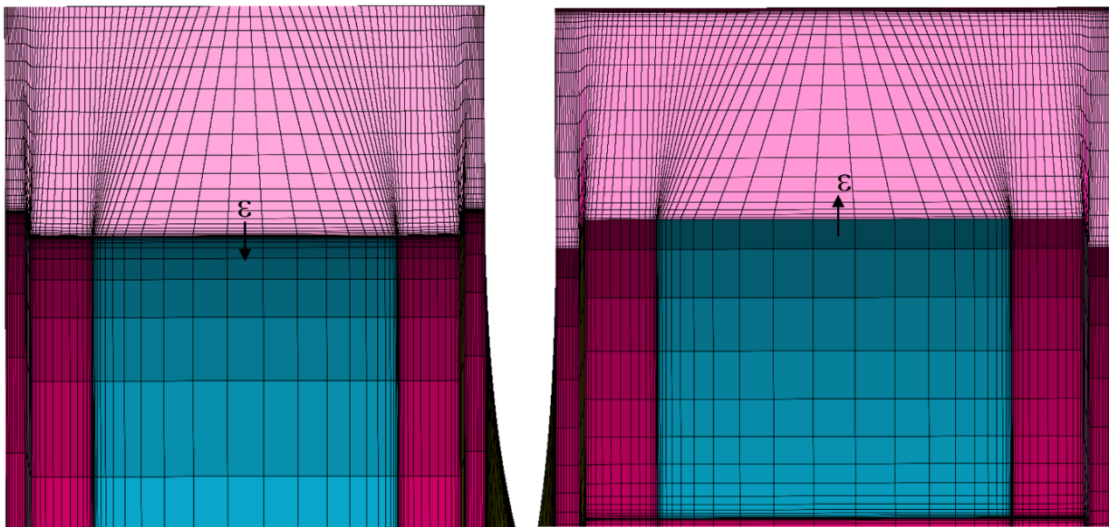


Figure 50. Shifted grid for the quasi-steady model

In the case of including diffuser vanes, the axisymmetric nozzle has been placed after the diffuser (volute removed), and the case has been solved using the transient method. Refer to Figure 51 for an illustration of the axisymmetric nozzle. Then the dynamic forces have been subtracted from the shroud forces to obtain the contribution of the diffuser. Finally, for the volute, the full model transient results have been subtracted from the reduced models.

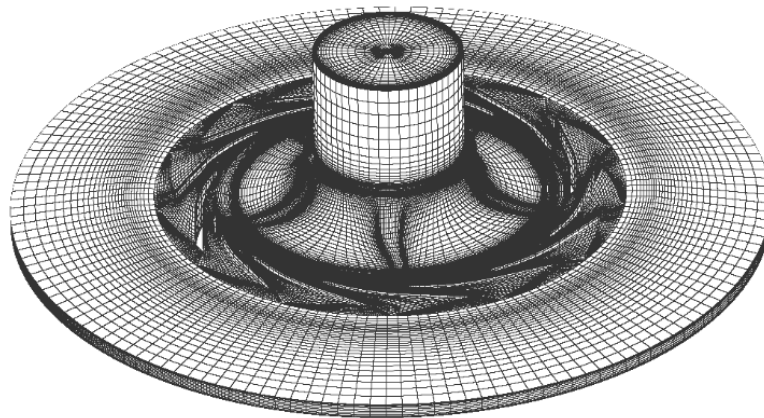


Figure 51. Axisymmetric nozzle added after the diffuser and the volute removed

Special care has been taken to remove the effects of rotating or stationary stall from simulations, especially in the case of the diffuser vanes. Pressure monitor points have been placed at diffuser inlets and pressure fluctuation results have been plotted. Pressure is collected at 39 points (3 points at the throat of each diffuser channel) [178]. Figure 52 shows the monitor points with yellow cross signs.

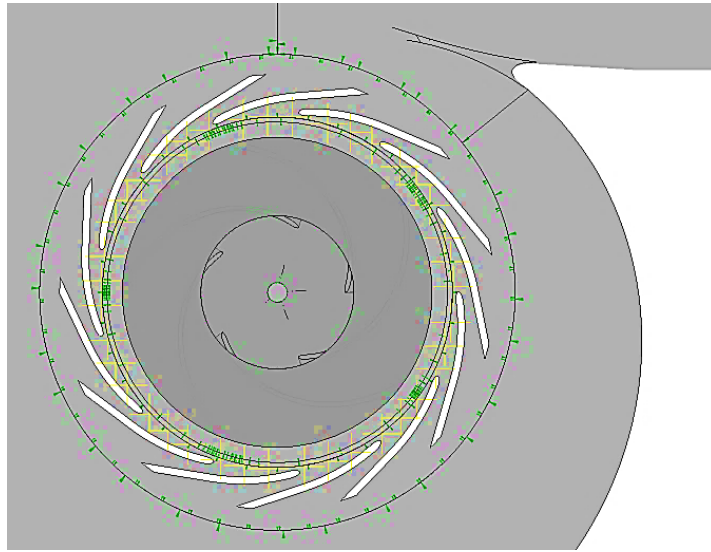


Figure 52. Pressure monitor at diffuser throat marked with yellow crosses

Figure 53 shows no sign of stall. If a stationary or rotating stall was present, a continuous pattern of large pressure drop would appear and advance with time.

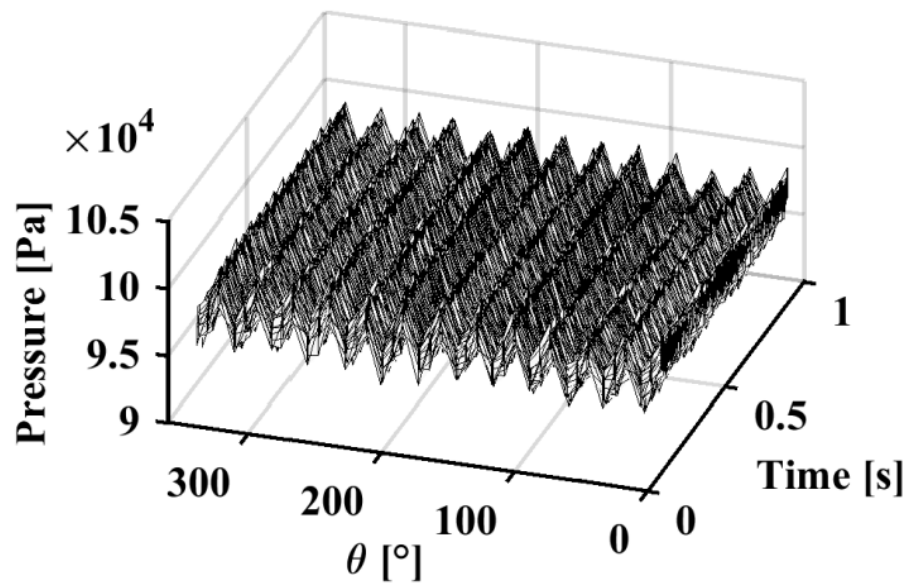


Figure 53. Pressure pulsations at diffuser vanes indicate no sign of stall

If a non-matched diffuser is used in the simulations, the diffuser dynamic force results will be contaminated by the extra impact of flow coefficient. Impellers are typically designed to operate at their maximum efficiency which occurs at a certain flow rate known as the Best Efficiency Point. Here the goal is to obtain the dynamic coefficients at the Best Efficiency Point to omit cases with an off-design operation.

3.3.6. Model Error

The subdomain center of spin is fixed on the initial spot (the center of spin is not whirling with the impeller). This results from the current limitations in defining the rotating frame axis of rotation as a function of time in ANSYS CFX. It will be shown that the error associated with this model will be small provided that the eccentricity ratio to the outer diameter e/D_2 is not too large which is the case in the current model.

Consider an impeller which is spinning about an off-centered axis as shown in Figure 54. In this configuration, the velocity magnitude and therefore static pressure distribution on the opposite sides of the impeller will not be the same. Therefore, a resultant radial force will be formed which is not physical but instead an artifact of the fixed center of spin limitation.

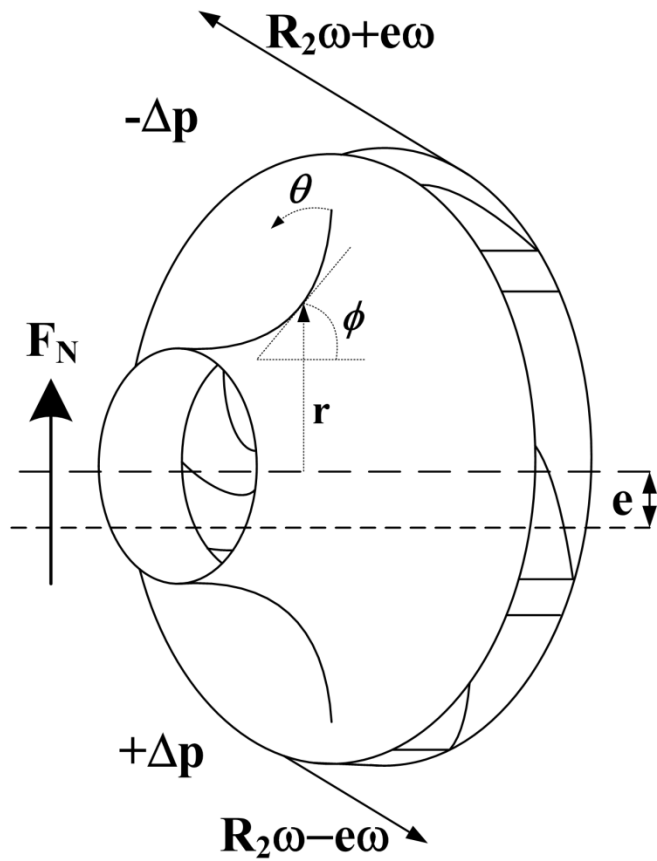


Figure 54. Fictitious force due to the fixed axis of spin

An integration over the impeller front shroud estimates the order of magnitude of this force.

$$\Delta F_{N, fsh} = \frac{2 \int_{\theta=-\pi/2}^{\pi/2} \int_{r=r_0}^{r_2} \int_{\phi=0}^{\pi/2} \frac{1}{2} \rho (e\omega)^2 \cos \theta / \sin \phi \, r dr d\theta d\phi}{\pi r_2^2 \omega^2 b_2 e} \quad (35)$$

The hub and shroud contributions almost cancel each other. It is difficult to estimate the contribution of blades due to their 3D complex profile, but their contribution should be smaller or in the order of the front shroud (the blades also contribute to tangential forces). The majority of rotordynamic forces in a closed 3D centrifugal pump impeller

comes from the front shroud as it has been shown in several prior studies [35, 46, 69, 71, 74]. This fictitious force is not a function of the whirl speed Ω , but its dimensionless magnitude depends on e ; hence, for the smaller whirl orbits this error will be linearly reduced. Simplification of Eq. 8 and division by the total dimensionless normal force yield:

$$\frac{\Delta F_{N, fsh}}{F_N} = \frac{B}{f_n}, \quad B = 2\pi D_0 L \rho (e\omega)^2 \quad (36)$$

where D_0 and L represent the impeller suction diameter and front shroud axial length, respectively. This result shows that the ratio will be negligible as long as the eccentricity and spin speed are small (which is the case in this problem). An impeller without a diffuser and volute is selected and simulated using the quasi-steady method, in order to further quantify this error term. Two eccentric cases are simulated, the first with centered and the second with off-centered spinning. The difference between the two cases quantifies the error. Jery's original eccentricity of $e = 1.26 \text{ mm}$ has been imposed in both cases to present a very conservative extreme case with regards to the error estimation. The remaining simulations are more representative of actual impeller whirl magnitudes, with 25% of the original eccentricity, and therefore the dimensionless error forces will be much smaller relative to the total forces for these cases. Figure 55 compares the two cases and shows this error term is negligible even when using the largest eccentricity.

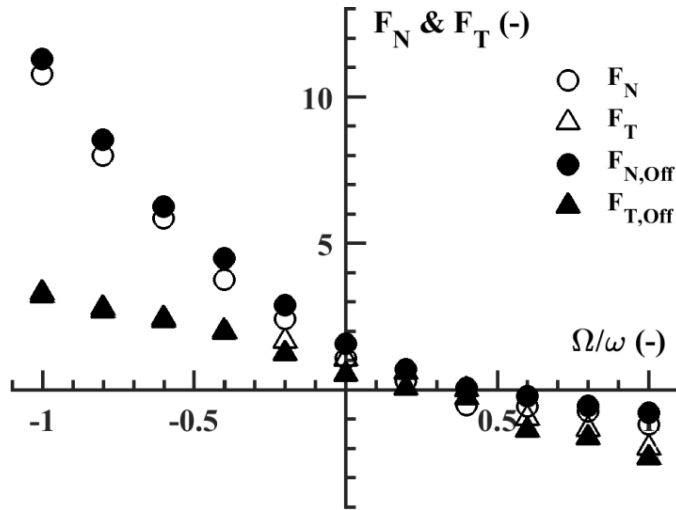


Figure 55. Quasi-steady dimensionless normal and tangential forces with centered and off-centered spinning motion (eccentricity $e=1.26 \text{ mm}$)

3.3.7. Grid Independency

A grid study was performed to demonstrate the independency of the results from the mesh resolution. For the grid independency study, a grid refinement factor of 1.3 is selected [179] and four sets of grids are constructed. Details of the grid sizes are available from Table 7. Figure 56 shows the corresponding grids.

Table 7. Grid sizes selected for the grid independency study

N_{coarse}	N_{medium}	N_{fine}	N_{finer}
379,000	861,000	1,867,000	4,114,000

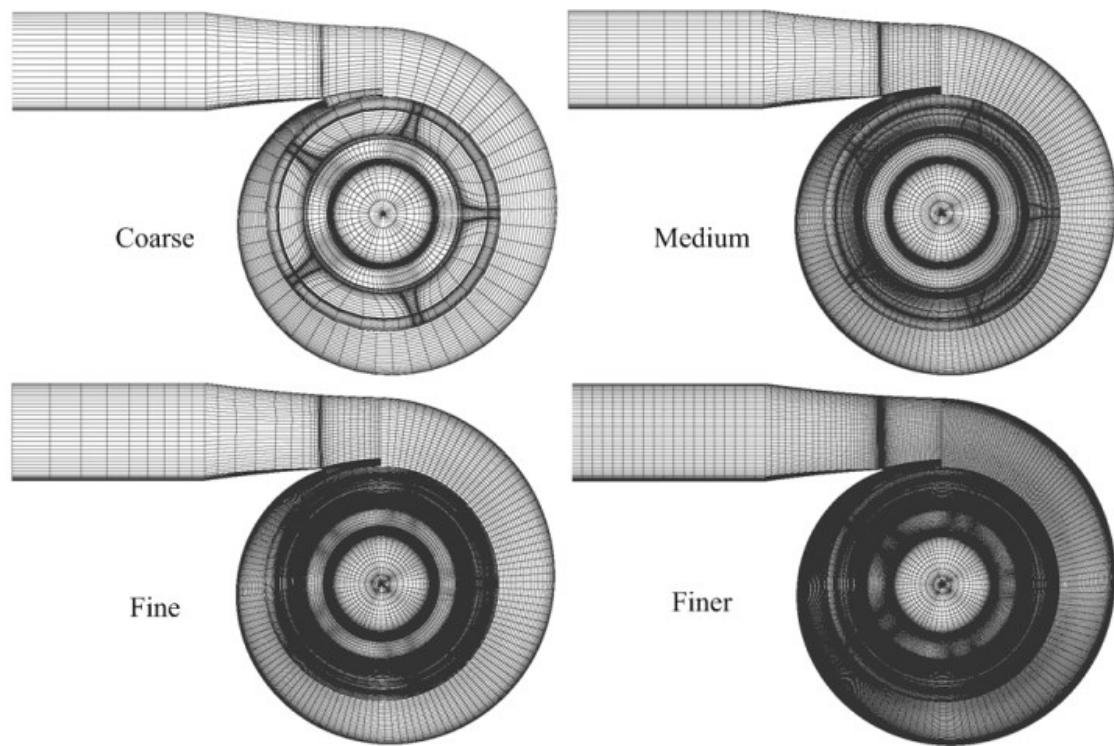


Figure 56. Grids used in the mesh independency study

Three different sets of quantities are monitored to qualitatively show the grid convergence error is minimal [180]. The 3 quantities include 1) Pump head coefficient ψ 2) Pump efficiency η 3) The RMS of absolute dynamic force difference over a range of frequency ratios. The first quantity is indicative of the convergence of the pressure field and continuity equation. The second quantity is indicative of the resolution of boundary layers and prediction of shear stress on walls which typically requires more refined grids. The third parameter is the rotordynamic parameter of interest specific to the problem which is the dynamic force in an average sense. This quantity cannot be defined using a single frequency ratio like the other two, so the RMS value of the difference with respect to the finest grid will be assessed.

$$RMS_{\bar{F}_N} = \sqrt{\frac{\sum_{i=1}^{N_{FR}} (\bar{F}_N^{finer} - \bar{F}_N^{grid})^2}{N_{FR}}} \quad (37)$$

$$RMS_{\bar{F}_T} = \sqrt{\frac{\sum_{i=1}^{N_{FR}} (\bar{F}_T^{finer} - \bar{F}_T^{grid})^2}{N_{FR}}}$$

where N_{FR} defines the number of frequency ratios considered. Figure 57 shows the grid convergence results. According to this plot, the fine mesh (1.867 million nodes) has been selected as the appropriate grid since the grid convergence parameters are almost saturated at this point, and the changes are below 5%. Figure 58 illustrates how the dynamic forces from all the grids almost fall on the same curve. Therefore, one can rely on the coarse grid results if only the dynamic coefficients are sought. This observation reduces the computational cost of the transient solution considerably. The major difference between the impeller and seal case associates to the range of Re number. Inside the liquid annular seals the Re number is in order of 10^4 and sometimes as low as 10^3 while in the front leakage path of the impeller, the Re number is in order of 10^5 , making the utilization of wall-functions and coarse meshes more viable.

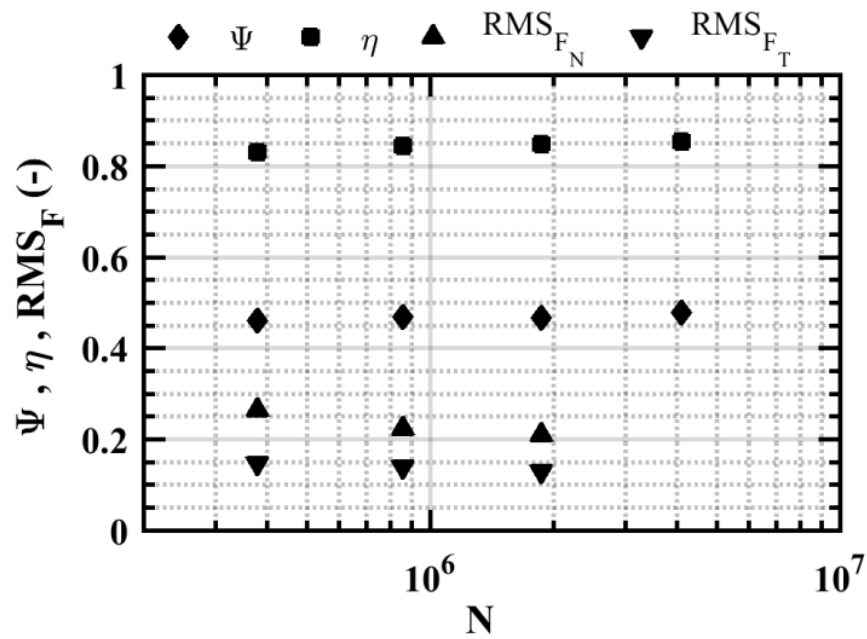


Figure 57. Grid independency results. ψ is the head coefficient, η the efficiency and RMS_F shows the RMS of force value departure from the finest mesh values

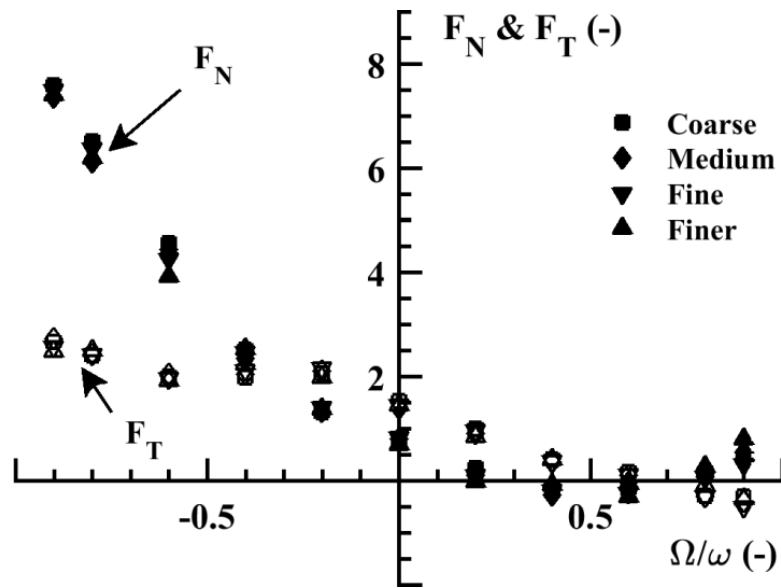


Figure 58. Dimensionless dynamic forces from various grid densities

3.4. Results and Discussion

3.4.1. Validation

The concentric case model was compared with the characteristic measurements by Jery [73]. The numerical characteristics show the same trend as the experimental data. Figure 59 compares the numerical results against experimental values for the head coefficient and the efficiency.

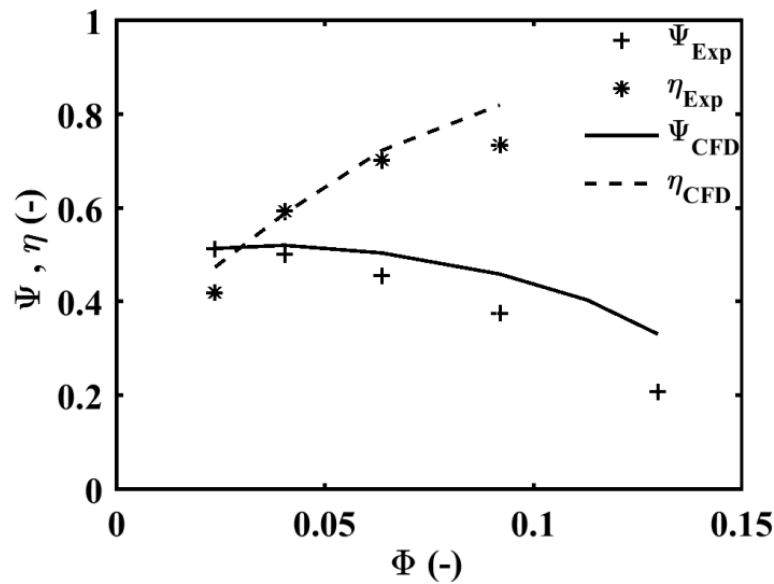


Figure 59. Experimental and numerical pump characteristics (experimental data adapted from [73])

For the whirling case, the measurements from Jery have been compared to the numerical results from both the quasi-steady model and the transient model (See Figure 60). These results refer to the original trapezoidal volute without diffuser vanes which is called Volute A in Jery's work. Also, the clearance profile has been set to the original

wide configuration in order to comply with the test geometry. The superiority of the transient method to the quasi-steady approach clearly manifests itself in these plots. Although one expects that the transient solution will provide more accurate results than the quasi-steady model, the matter of degree of improvement is of strong importance to justify the increased computational time that accompanies the transient approach. Earlier non-CFD theoretical models have emphasized on transient effects which are absent in the quasi-steady models [36, 103]. The deviation in the numerical results is primarily attributed to the uncertainties in the front shroud curve. Furthermore, effects of RANS turbulence modeling, spatial and temporal numerical errors, unknown surface roughness, and the duration of numerical sampling contribute to the model deviation. The quasi-steady model particularly shows more deviation because of transient effects and non-axisymmetric features. The quasi-steady predictions are much closer to the transient predictions if a narrow clearance profile is used where there is a reduction in the contribution of the volute. The results of clearance profile are presented later in coming paragraphs.

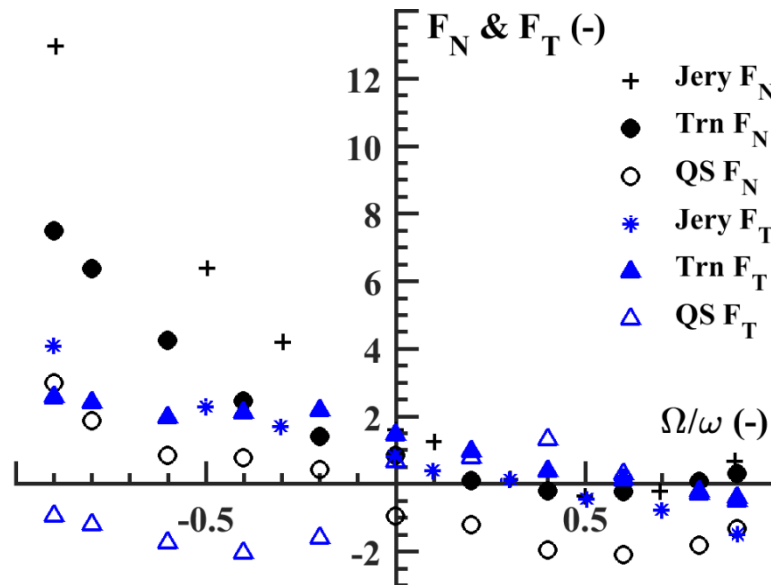


Figure 60. Dimensionless normal and tangential forces, predictions versus experiments. QS and Trn correspond to quasi-steady and transient, respectively (experimental data adapted from [73])

Table 8 compares the rotordynamic coefficients from the transient simulation to the experimental values. Overall, there is a reasonable agreement between all coefficients. The quasi-steady model coefficients are clearly unreliable in this case, as indicated by the results in Figure 60.

Table 8. Force coefficient predictions (experimental data adapted from [73])

Case	\mathcal{K}	h	\mathcal{C}	c	\mathcal{M}	m
Jery	-1.64	0.82	2.94	6.88	6.39	-0.64
CFD	-0.85	1.44	1.74	3.86	4.05	0.59
Rel. Error (%)	48.2	75.6	40.8	43.9	36.6	192

To quantify the contribution of the volute in this case, the total forces have been subtracted from the impeller forces (without volute) and the outcome represents the volute contribution. Figure 61 compares the forces associated with the volute against the impeller forces. The normal contribution is relatively small while the tangential contribution accounts for a bigger share of the total tangential force.

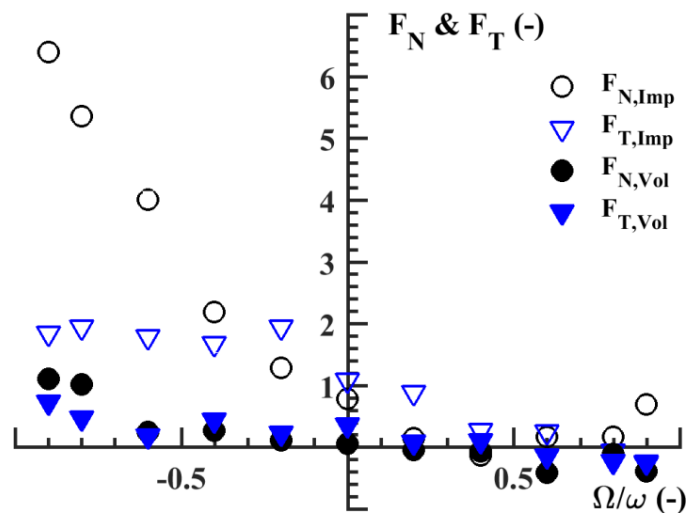


Figure 61. The trapezoidal volute rotordynamic forces versus the impeller for the wide clearance configuration

3.4.2. Volute and Diffuser Rotordynamic Forces

The prior section's validation of the model allows the methodology to be used to explore the rotordynamic behavior of the volute and the diffuser. The five different volute designs and the vaned diffuser have been simulated with the narrow leakage path clearance configuration at the design flow rate, since it is sought to show that the volute and diffuser have a significant influence on the impedances and dynamic coefficients

even for the case that the clearance is similar to the values used in those cases in the literature that exclude the diffuser and volute from their models. This will let the analyst know that if the volute and/or diffuser should be kept in the analysis or not. Also, the narrow clearance may be more practical in the actual applications. Figure 62 presents the total normal and tangential forces exerted on the same impeller operating with various volutes. Except for the rectangular volute, all the volutes follow the same curve, implying that the shape of the volute does not alter the rotordynamic coefficients at the Best Efficiency Point (BEP). Please note that a non-matched volute introduces the effects of the flow rate coefficient which contaminates the results and therefore has been avoided. Also, the rectangular volute shows an uncommon sudden drop of the tangential force at $FR=-0.9$ which has a destabilizing effect.

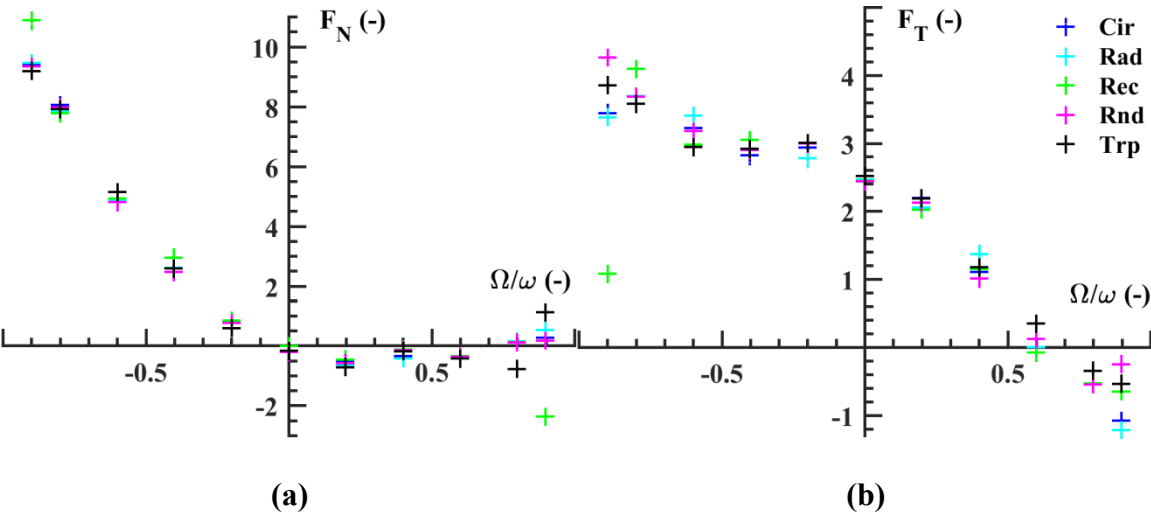


Figure 62. Total dimensionless normal and tangential forces of the same impeller working with various volutes

To better visualize the contribution of the volutes, the dynamic forces has been subtracted from the transient solution of the impeller forces alone (no volute) which serve as the base line forces. As was shown before, the quasi-steady model cannot serve as the base line due to its axisymmetric assumption. Although not shown here, the quasi-steady base line erroneously over-predicts the contribution of the diffuser and the volute. Figure 63 shows that at certain frequency ratios, the volutes contribute comparable forces as the impeller. The introduction of the volutes has shifted the WFR from 0.5 (See Figure 63-b) to 0.65 (See Figure 62-b).

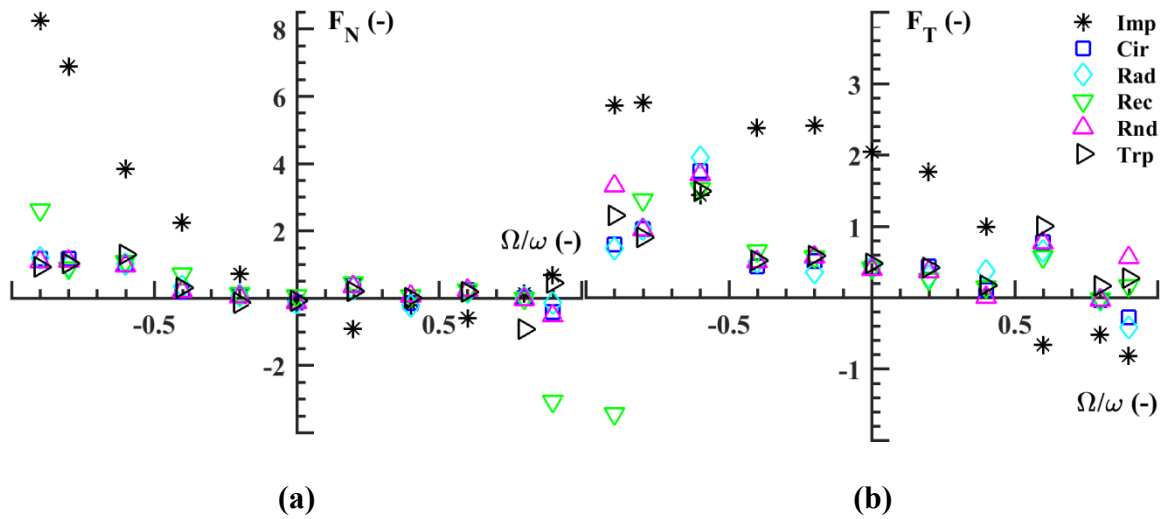


Figure 63. Contributions of the impeller and various volutes to the total normal and tangential forces

Table 9 does a basic comparison between the dimensionless dynamic coefficients of the impeller and the volutes. According to Table 9, all the volutes have a comparable direct stiffness with respect to the impeller. The volutes show about 25% of

the impeller cross coupled stiffness. Furthermore, the volutes provide a direct damping close to 30% of the impeller direct damping (with the exception of the rectangular volute). However, the volute impedances are non-quadratic and their impact is better represented by the rotordynamic forces rather than the rotordynamic coefficients. The effect of non-quadratic curves on the rotordynamic stability can be further investigated using the approach introduced by Kim and Palazzolo [133].

Table 9. Impeller and volute rotordynamic coefficients

Case	\mathcal{K}	\mathcal{h}	\mathcal{C}	c	\mathcal{M}	m
Imp	0.17	1.83	1.92	4.03	5.69	1.39
Cir	0.11	0.58	0.61	0.71	0.95	0.12
Rad	0.11	0.6	0.65	0.66	0.99	0.19
Rec	0.11	0.7	0.08	1.62	0.53	0.89
Rnd	0.11	0.44	0.62	0.69	0.87	-0.64
Trp	0.15	0.54	0.44	0.67	0.63	0.99

The diffuser vanes may be integrated with a volute or be used alone with cross overs. Thus, there is an interest in both cases. Figure 64 exhibits the contributing normal and tangential forces of the diffuser vanes. In this figure, the diffuser and volute forces have been subtracted from the impeller base line forces to quantify the contribution of each component.

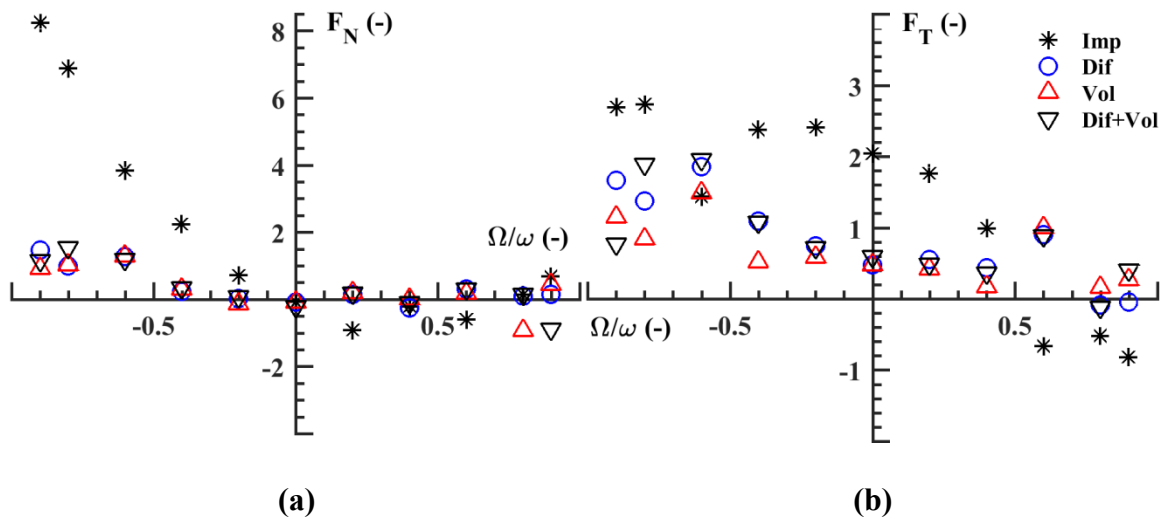


Figure 64. Contributions of the diffuser and the volute to the total normal and tangential forces

Table 10 indicates the rotordynamic coefficients from each component. The tangential forces show more dependency on the presence of the volute or the diffuser compared to the normal forces.

Table 10. Comparison of impeller, diffuser and volute rotordynamic coefficients

Case	\mathcal{K}	k	\mathcal{C}	c	\mathcal{M}	m
Imp	0.17	1.83	1.92	4.03	5.69	1.39
Dif	0.06	0.50	0.89	0.66	1.18	-0.59
Vol	0.15	0.54	0.44	0.67	0.63	0.99
Dif + Vol	0.21	0.60	0.72	0.90	1.13	-0.41

The diffuser has a more pronounced influence over the direct damping and the direct added mass, while the volute has a greater share in the total direct stiffness. Both components drive the forward whirl especially at larger frequency ratios, yet they have a stabilizing effect in the backward whirl region.

3.4.3. Impact of Clearance, Gap A and Spin Speed

As was pointed out in the validation section, the clearance profile plays a role in deciding whether a quasi-steady model is applicable. Observe in Figure 65 that quasi-steady predictions for the narrow clearance have a better agreement to the transient results compared to what was shown in Figure 60 for a wide clearance. However, it should be pointed out that there still is a significant difference between the stiffness predictions and the resultant WFR.

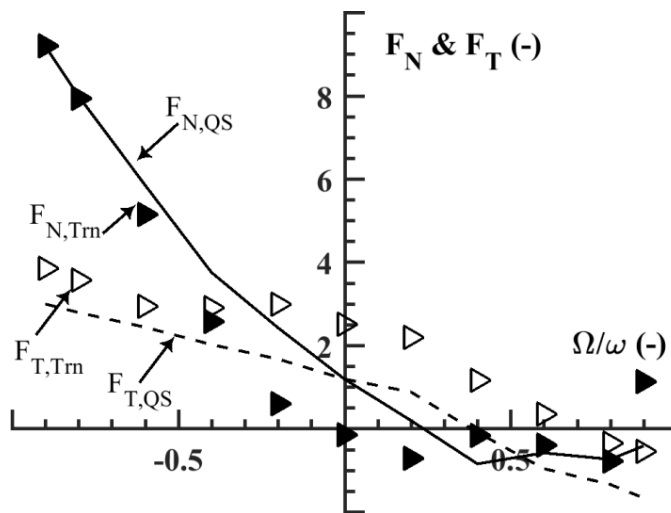


Figure 65. The quasi steady model predictions follow the transient results closely for the narrow clearance configuration. Trapezoidal volute is included in both cases

Figure 66 displays further detail about the influence of the clearance profile. Both configurations use a trapezoidal volute and results have been acquired by the transient model. The immediate observation is that both cases have comparable forces at the sub-synchronous range of the frequency ratio. Table 11 compares the rotordynamic coefficients. The narrow clearance case has a larger cross-coupled and direct (positive) stiffness as well as direct damping, with an overall larger WFR.

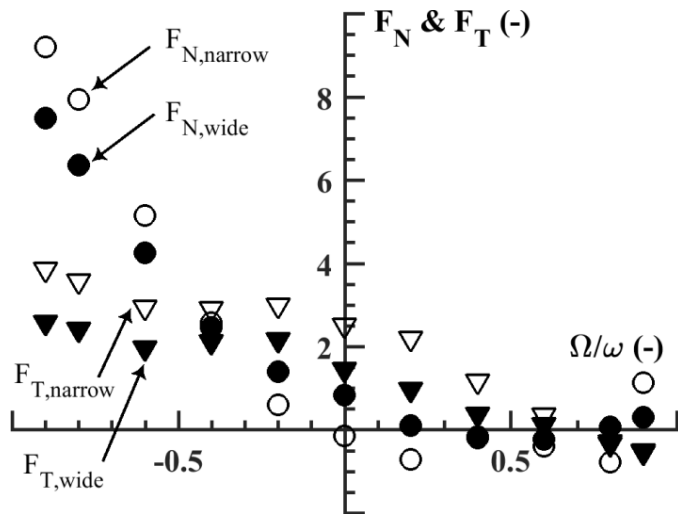


Figure 66. Transient force predictions of the narrow versus wide clearance. Trapezoidal volute is included in both cases

Table 11. Impact of the clearance profile on the rotordynamic coefficients

Clearance	\mathcal{K}	k	\mathcal{C}	c	\mathcal{M}	m	WFR
Narrow	0.32	2.29	2.35	4.65	6.68	0.98	0.65
Wide	-0.85	1.44	1.74	3.86	4.05	-0.59	0.6

The influence of Gap A shown in Figure 42 is revealed by considering the vertical intercept of the tangential forces in Figure 67. The cross-coupled stiffness increases significantly by reducing Gap A. Reduction of Gap A in effect makes it behave similar to a plain annular seal, which is reflected in the trend of the rotordynamic coefficient in Table 12. Overall, the increased WFR of the tight Gap A configuration ($\text{Gap}_A/D_2 = 0.006$) suggest a less favorable stability condition.

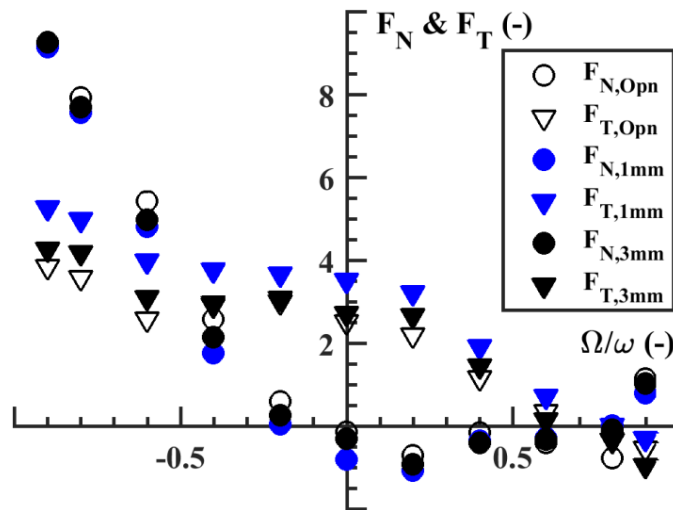


Figure 67. Gap A influence on the dynamic forces

Table 12. Impact of the Gap A on the rotordynamic coefficients

Gap A	\mathcal{K}	k	c	c	\mathcal{M}	m	WFR
Open	0.04	2.36	2.31	4.74	6.27	1.13	0.65
3 mm	0.34	2.60	2.68	4.50	6.77	1.29	0.6
1 mm	0.57	3.23	2.93	4.40	6.98	1.17	0.8

Jery [73] reported that the dimensionless dynamic forces do not show a significant dependence on spin speed. This conclusion could have a major impact on the reduction of influential variables of the problem, therefore it was investigated by numerical means in the present work. Results from four (4) distinct spin speeds were obtained and re-normalized by the reference speed forces at $\omega = 1000$ rpm ($F_N/F_{N,ref}$ and $F_T/F_{T,ref}$). Then all the points should approach unity if the spin speed does not affect the dynamic forces. The numerical and experimental results illustrated in Figure 68 confirm this observation. Points close to the region where F_N and F_T approach zero (For example in Figure 67 close to $\Omega/\omega = 0.4 - 0.8$) have higher relative error and uncertainty, and therefore not plotted in Figure 68. These results show that the dimensionless rotordynamic coefficients are nearly independent of spin speed, unlike the dimensional ones.

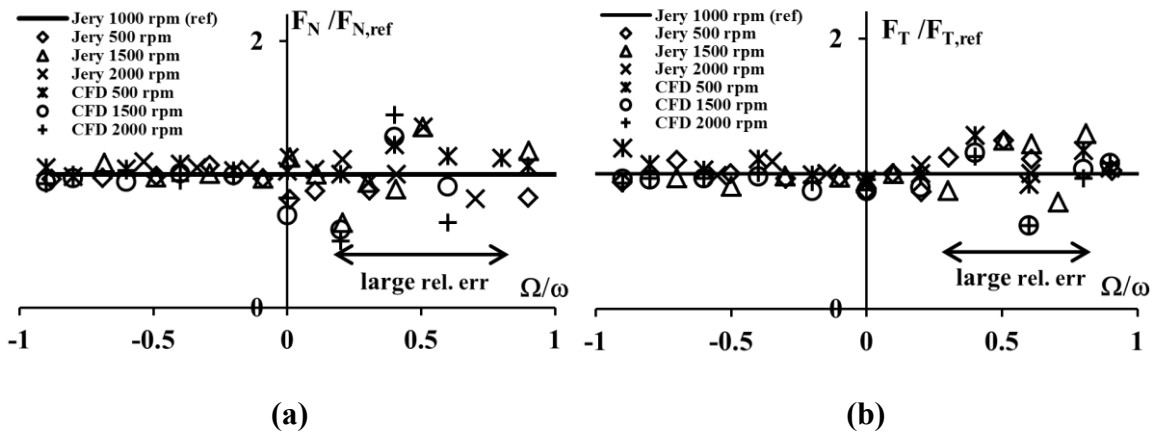


Figure 68. Independency of the dimensionless normal and tangential forces from the spin speed (experimental data adapted from [73])

3.5. Conclusion

A CFD-based, transient methodology was presented to improve rotordynamic force coefficient predictions of impellers under more general conditions where non-axisymmetric components such as volutes or diffusers are present. The proposed approach was shown to considerably improve the predictions compared to the quasi-steady model when the clearance profile grows wider. The grid independency study suggests that even coarse grids can be effectively used to extract the rotordynamic coefficients, provided that vibration and rotordynamic stability are the main goals of the simulation.

The relative contribution of the volute and/or diffuser to the overall dynamic forces depends on the frequency ratio and the front leakage path profile, *where flow rate effects were not considered in this study*. The cross-coupled stiffness from the volutes or the diffuser investigated in this study was calculated to be about 20-30% of the impeller cross coupling. The current impedance curves suggest that the presence of the diffuser or the volute increases the WFR by 0.1-0.15, which shows the destabilizing effect of these components. Furthermore, based on several volute design trials, it was concluded that at the design point, the difference in the volute cross-sectional profile shape is immaterial while its presence has to be considered. The rectangular volute, however, showed an erratic behavior at $FR = \pm 0.9$.

A parameter study showed that by tightening Gap A, which is a common practice for increasing efficiency, the cross-coupled stiffness increased significantly. Results imply that Gap A effectively acts similar to a plain annular seal relative to the

dynamic force coefficients. Moreover, the forces from the narrow and wide clearance profile have comparable sizes in the sub-synchronous region. Spin speed shows little influence on the dimensionless rotordynamic forces, but may influence the dimensional ones.

The focus of the current study was developing the novel methodology, and demonstrating its application only at the design flow rate. Interesting results may be achieved by extending the method to investigate off-design operation, and/or more complex geometries such as an open impeller where conventional methods fail to predict the dynamic forces. The methodology can be further developed to attain alternative formula to the well-known Wachel [14] relation. A limitation of the current study was the unknown front shroud profile of the impeller which had to be inverse-designed. To further validate the current model, it is recommended to run calculations on an impeller with a known front shroud profile and compare the results to experiments. It is also encouraged to utilize higher fidelity turbulence models as the computational horizons expand in near future.

4. OPEN IMPELLER ROTORDYNAMIC FORCES: A TRANSIENT MULTI-FREQUENCY CFD APPROACH*

4.1. Introduction

Energy efficient turbomachinery technology strives to develop more power-dense operating machines. High rotational speeds cause these units to undergo larger forces and more intense vibration levels. Supercritical operation increases the risk to encounter rotordynamic instability as well as non-synchronous fatigue failure problems [47]. To comply with stable operation guidelines set by API [15], a level II stability analysis is required for more complex turbomachinery components such as impellers. Particularly, the open impellers, or the so called unshrouded variety, are popular in high-speed applications given their reduced mass and lower level of centrifugal stresses [181]. There are also other attractive features associated with open impellers, such as multi-phase tolerant operation, higher payload and reduced disk losses [22].

Although closed impeller rotordynamic forces and moments have received much attention in past years [30, 35, 126], open impellers rotordynamic forces (especially centrifugal compressors) have been rarely treated using an analytical or numerical model. The complexity occurs by the 3D nature of the flow inside open impellers, non-axisymmetric geometry, and the tip leakage flow, all negating use of simpler 2D

* Part of the data reported in this section is reprinted with permission from “Rotordynamic Forces on an Open-Type Centrifugal Compressor Impeller in Whirling Motion,” by Yoshida, Y., Tsujimoto, Y., Ishii, N., Ohashi, H., and Kano, F., 1999. *ASME J. Fluids Eng.*, 121(2), pp. 259-265, Copyright 1999 by ASME.

models. Although CFD-based quasi-steady models [34], bulk-flow [32], actuator disk [42, 111], and potential flow solvers [103, 107] all capture some portion of the physics involved in this problem, none can fully cover a broad range of designs and operating conditions. Among these studies, the semi-analytical 2D potential flow model of Hiwata and Tsujimoto [107] predicted reasonably close results to measured forces of Yoshida et al. [66]. The underlying restricting assumptions obviously call for a more general model.

With recent advancements in large scale computing, Computational Fluid Dynamics (CFD) [182-184] has been extensively used and validated for prediction of turbomachinery flows [162, 163] and fluid induced forces in such applications [165]. More recently, a transient CFD-based methodology was utilized by the authors to extract the contribution of volutes and diffusers to the rotordynamic forces of a closed impeller [185]. Since the approach is transient and applicable to non-axisymmetric geometries, it has been modified for open impellers and applied to the current problem. This is the first time that a transient CFD-based model is being used to extract rotordynamic forces of a whirling open impeller. Current results are obtained using a multi-frequency approach [140] which combines forward and backward modes with a binary phase modulation [186] for an even higher computational efficiency and a reduced chance of mesh warping. With the visualization power of CFD, it is once more confirmed [66, 106] that at least some of the major bumps and dips [35, 157] appearing in open impeller impedances occur with a rotating pressure pattern origin (similar to rotating stall). After validation of the proposed CFD methodology against the

experiments of Yoshida et al. [66], the approach is further applied to explore the effect of generic specific speed classes of open impellers. Such general dimensionless rotordynamic impedances at various flow coefficients can be input into non-quadratic, general transfer function models such as the one introduced by Kim and Palazzolo [133] for stability analysis of rotors mounted with similar specific speed impellers. Finally, in order to learn more about the origins of bumps and dips in the leakage path model, rotordynamic forces of a given unshrouded impeller are compared to those of the same shrouded impeller and an isolated leakage path model.

4.2. Geometry and Dimensions

The study by Yoshida et al. [66] was selected for validation purposes,. The same geometry has been used for the numerical simulations. This is a compressor impeller with the specific speed of $\omega_s = 1.3$ which has been tested as a hydraulic pump (See Figure 69). The dimensions and the operating conditions are given in Table 13. In the experiments, an eccentricity of $e = 0.6$ mm has been imposed which corresponds to a maximum eccentricity ratio of $\epsilon = 0.6$. The experimental force data are collected using a spinning frame 4-axis force sensor and then converted to the whirling frame normal and tangential forces. The impeller is made eccentric using two sets of bearings with the outer bearing sleeve rotating at the whirl speed, and the eccentric inner bearing supporting the spinning shaft [66].

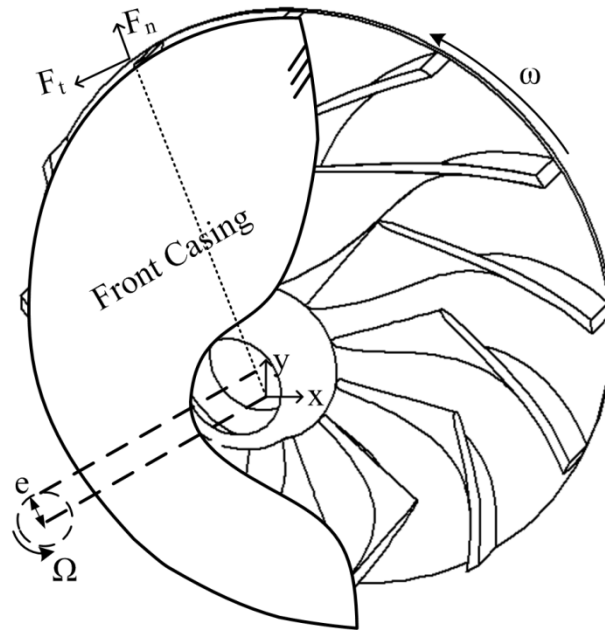


Figure 69. The whirling open impeller and its rotordynamic forces

Table 13. The design parameters and the operating conditions of the validation impeller (adapted from [66])

ω_s	1.3	C_r	1 mm
ω	400 rpm	b_2	23 mm
Ω/ω	-1.45 to +1.40	β_1	32°
D_0	203 mm	β_2	45°
D_2	298 mm	Z	12
D_3	320 mm	t_b	5 mm

For the specific speed study, several open impellers have been designed using CFturbo [170]. All impellers have the same outer diameter D_2 to roughly represent impellers of

the same size. All impellers have the same tip clearance size (uniform), same rotational speed and number of blades. Table 14 provides further detail about these impellers. The operating conditions of each impeller set the impeller's specific speed which in turn determines the hub and shroud profiles. The specific speed evolution of these impellers is depicted in Figure 70.

Table 14. Design properties of the specific speed study impellers

ω_s	H (m)	n (rpm)	Q ($\frac{m^3}{hr}$)	D_0 (mm)	D_2 (mm)	b_2 (mm)	C_r (mm)	Z	L_h (mm)
0.30	10.0	1450	14	72	180	10.2	0.9	6	31.3
0.60	9.0	1450	47	99	180	17.0	0.9	6	49.9
0.90	8.0	1450	88	116	180	23.0	0.9	6	65.5
1.20	7.0	1450	128	129	180	28.0	0.9	6	76.2
1.80	5.5	1450	200	147	180	37.0	0.9	6	92.0

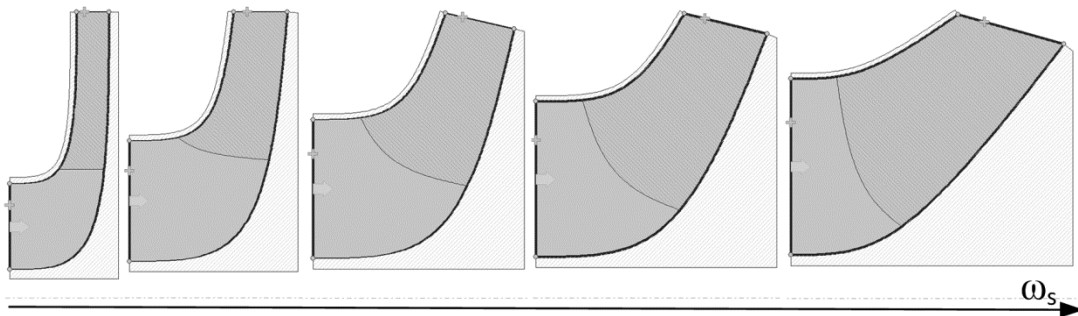


Figure 70. Meridional view of the open impellers for various specific speeds

4.3. Numerical Methodology

4.3.1. CFD Set-up

The velocity and pressure field inside the open impeller are obtained by solving Navier-Stokes equations utilizing Computational Fluid Dynamics (CFD) which has been extensively applied and validated for turbomachinery flows before [166, 187]. For turbulence modeling the Shear Stress Transport (SST) model [148, 188, 189], along with the $\gamma-Re_{\theta}$ transition model has been used [190]. The transition model improves the off-flow (far from design flow) predictions and tip leakage flow modeling. The transition model is further discussed in Appendix A.

The regular outlet mass flow and inlet total pressure boundary conditions are imposed. The flow coefficient of the impeller is set by this flow rate and considering the impeller's discharge dimensions. The Transient Rotor-Stator interface has been used for the rotor-stator interfaces, and the casing wall facing the open impeller is modeled using a counter-rotating wall (solved in the spinning frame). All walls have smooth no-slip boundary conditions. 36 time-steps per rotation cycle has been adopted with 10-15 inner steps to meet the target residual of 10^{-5} .

4.3.2. Computational Domains

To improve the CFD predictions, upstream and downstream components, namely the suction pipe, the rear leakage path, the radial diffuser and the volute, are included in the model. A double discharge volute has been used in the validation case to better replicate the experimental condition and to remove some of the asymmetric effects. The specific speed study does not include a volute, since it reduces the

generality of the obtained results for the open impellers. Structured grids with y^+ values of order unity, have been generated for all the cases. Figure 71 shows the mesh for the tested impeller and the auxiliary domains.

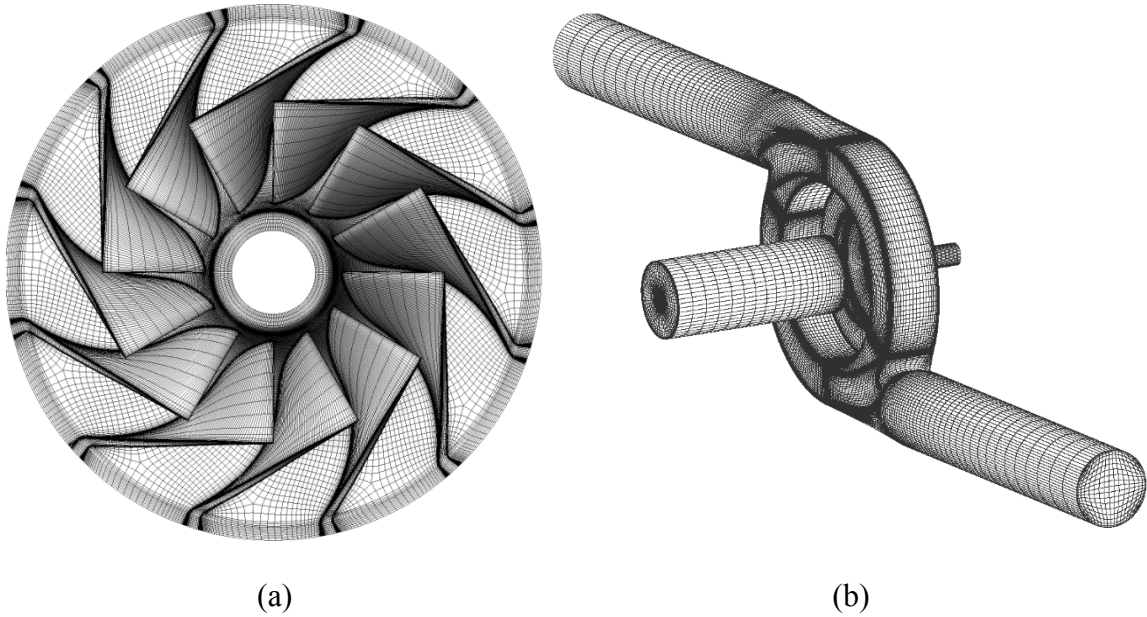


Figure 71. Computational domains (a) impeller (b) Upstream and downstream components

4.3.3. Transient Analysis

For the transient simulations of the whirling open impeller, the mesh deformation approach has been used similar to the earlier work on the volute and diffusers rotordynamic coefficients [185]. A diffusion equation for the mesh has to be solved at each time step [154].

$$\nabla \cdot (\Gamma_{\delta} \nabla \delta) = 0 \quad (38)$$

where the mesh displacement δ is governed with the mesh stiffness parameter Γ_δ . For single frequency simulations, an alternative complex periodic mesh deformation approach has been employed [154]. This scheme is more advantageous in terms of computational cost and reliability. The periodic motion of mesh displacement at the boundaries of the mesh has the general periodic form:

$$\delta = A \sin(\omega t + \varphi) \quad (39)$$

where A is the amplitude, ω the single frequency and φ is the phase. In the periodic mesh deformation, the equation will be solved for the phases using a complex form.

$$\nabla \cdot (\Gamma \nabla \tilde{\delta}) = 0, \quad \tilde{\delta} = \tilde{\delta}_R + i \tilde{\delta}_I \quad (40)$$

and the periodic boundaries:

$$\tilde{\delta} = A[\sin(\omega t + \tilde{\varphi}) - i \cos(\omega t + \tilde{\varphi})] \quad (41)$$

Using separation of variables a solution is found:

$$\begin{cases} \nabla \cdot (\Gamma \nabla \tilde{\delta}_R) = 0, & \tilde{\delta}_R = A \cos \tilde{\varphi} \\ \nabla \cdot (\Gamma \nabla \tilde{\delta}_I) = 0, & \tilde{\delta}_I = A \sin \tilde{\varphi} \end{cases} \quad (42)$$

When $\tilde{\delta}_R$ and $\tilde{\delta}_I$ are known, the mesh displacement in time domain at any instant can be found by transforming the displacements:

$$\delta = \tilde{\delta}_R \cos\left(\omega t - \frac{\pi}{2}\right) + \tilde{\delta}_I \sin\left(\omega t - \frac{\pi}{2}\right) \quad (43)$$

therefore the mesh deformation equation is only solved once in the beginning of the solution. For a circular whirl motion:

$$x = A_x \cos \omega t, \quad y = A_y \sin \omega t, \quad A_x = A_y \quad (44)$$

The complex values has to be slightly modified in order to result in the same motion:

$$\varphi \rightarrow \varphi + \frac{\pi}{2}, \quad A_x \rightarrow A_x + i0, \quad A_y \rightarrow 0 - iA_y \quad (45)$$

One of the advantages of the complex periodic mesh motion method is its tolerance of large amplitude motions. The eccentricity ratio is increased to $\epsilon = 0.5$ in a 2D test-case simulation shown in Figure 72. The regular mesh deformation fails after 4 whirl cycles due to negative volume, while the complex form can continue whirling infinitely. Notice the distorted interface area in the general deformation case.

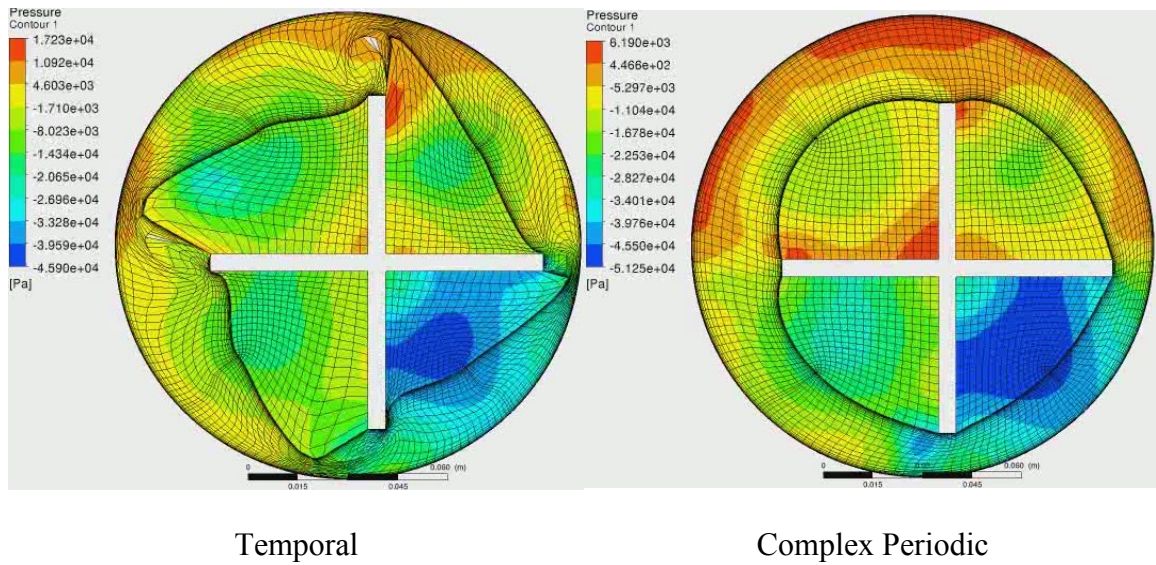


Figure 72. Mesh quality after 4 whirling cycles for $\epsilon=0.5$. Note the folded (detached) cells at the upper side of the propeller in the temporal case.

Figure 73 shows the minimum orthogonality angle of the periodic mesh after 7 whirl cycles at $\epsilon = 0.25$. A remarkable minimum angle of 60° shows how the mesh orthogonality angle has been well-preserved with this approach. The major drawback with the complex periodic mesh motion scheme is its limitation to single frequency motions.

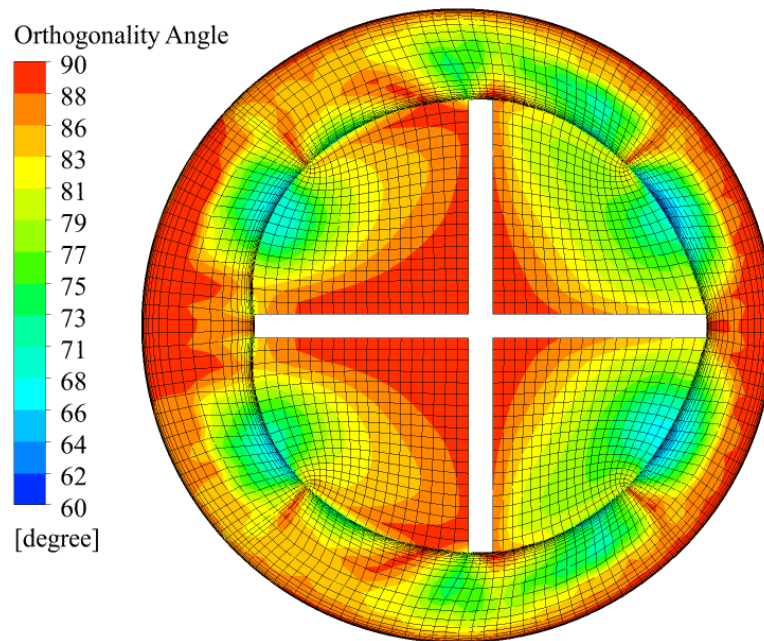


Figure 73. Mesh orthogonality angle well preserved with the complex periodic approach

Prior transient studies with gas seals [140, 142] have further accelerated the simulations using a multi-frequency approach, where several frequencies are modeled simultaneously. In the post process stage, response to each frequency can be extracted using Fast Fourier Transform (FFT). In the current study, a more efficient multi-

frequency approach has been utilized where both forward and backward modes are staggered with frequency ratio steps of $\Delta\Omega/\omega = 0.05$. About 28 frequencies are solved at in a single simulation. In order to increase the reliability of the solution (avoiding sudden mesh distortion) and to further increase the maximum number of modelled frequencies, the peak factor of the overall signal should be minimized. To this end, each mode has been introduced with an initial phase angle:

$$e_x = e \sum_{i=1}^N \cos(\Omega_i t + \varphi_i), \quad e_y = e \sum_{i=1}^N \sin(\Omega_i t + \varphi_i),$$

$$\varphi_i = \pi \left\lfloor \sum_{k=1}^{i-1} (i-k)e \right\rfloor \quad (46)$$

where e denotes the individual mode eccentricity, e_x, e_y show the total eccentricities in x and y directions, Ω_i represents each mode angular speed, the brackets perform the flooring operation. The phase angle φ_i is found using the formula suggested by Schroeder [186] which is given in Eq. (46). In general form, this relation has the form:

$$\varphi_i = \varphi_1 - 2\pi \sum_{k=1}^{i-1} (i-k)\bar{a}_k \quad (47)$$

where \bar{a}_k is the relative amplitude of the k^{th} mode such that $\sum_{i=1}^N \bar{a}_i = 1$. Schroeder's formula theoretically regulates the phases of a periodic signal to reduce the peak-to-peak amplitude. A binary variation (only zero and pi angles) of phase modulation has been selected, since the peak factor improvement is very close to the general phase results, while the post-processing of the results with the binary mode is more

convenient. Figure 74 shows the corresponding phases and orbit shape using the phase modulated combined forward-backward multi-frequency method.

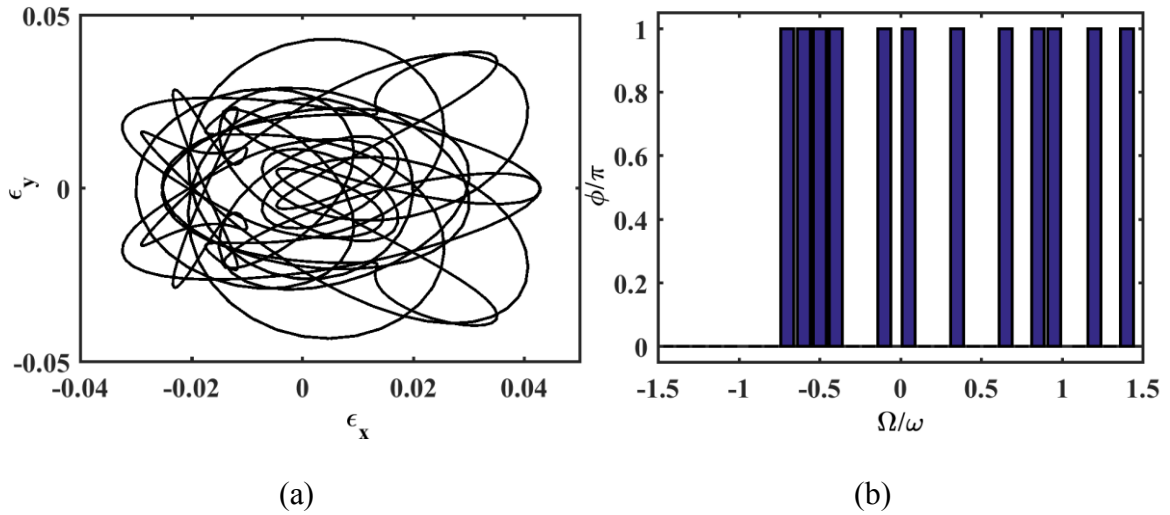


Figure 74. Transient phase modulated multi-frequency modeling. (a) The orbit (b) The imposed phases at each frequency

The individual eccentricity ratio of $\epsilon = 0.005$ for the phase modulated multi-frequency method (corresponding to overall eccentricity ratio of $\epsilon_{tot} \sim 0.05$) produced satisfactory results. Similarly, the individual eccentricity ratio of $\epsilon = 0.005$ for the single frequency method returned acceptable results. Several reasons encourage the usage of smaller eccentricity ratios: **I**) preserving the mesh orthogonality and avoiding mesh warping, **II**) mitigating the nonlinear intermodulation of the imposed modes, **III**) reducing the numerical error associated with the off-axis rotation of the impeller (for further discussion refer to [185]).

The stationary frame forces F_x, F_y are monitored and collected over at least 60 spin cycles, the first 10 cycles discarded for transient effects. Then the whirling frame forces F_n, F_t are reconstructed from the stationary frame forces and averaged over time for each frequency. The single frequency whirling frame forces variation with time is negligible so long as there is no concurrent mechanism present with the same frequency and the force model has skew-symmetry. By doing a time averaging in the whirling frame, one is effectively doing an FFT for the average component, instead of an FFT for the whirl component in the stationary frame. This approach is more convenient and more accurate than performing a FFT in the stationary frame. All forces in this study have the dimensionless form:

$$F = \frac{f}{\rho\pi r_2^2 \omega^2 b_2 e} \quad (48)$$

Here f is the force, ρ is the density, r_2 and b_2 present the impeller discharge radius and width, and ω is the rotational speed. In similar manner, the rotordynamic force coefficients in this work are normalized [78]. The coefficients are found from a least square quadratic curve fit according to Eq. (49).

$$\begin{bmatrix} F_N \\ F_T \end{bmatrix} = \begin{bmatrix} -\mathcal{K} - c \frac{\Omega}{\omega} + \mathcal{M} \frac{\Omega^2}{\omega^2} \\ k - \mathcal{C} \frac{\Omega}{\omega} - m \frac{\Omega^2}{\omega^2} \end{bmatrix} \quad (49)$$

with the dimensionless definitions:

$$\mathcal{K} = \frac{K}{\rho\pi r_2^2 \omega^2 b_2}, \quad c = \frac{c}{\rho\pi r_2^2 \omega b_2}, \quad \mathcal{M} = \frac{M}{\rho\pi r_2^2 b_2} \quad (50)$$

$$\mathcal{k} = \frac{k}{\rho\pi r_2^2 \omega^2 b_2}, \quad \mathcal{C} = \frac{C}{\rho\pi r_2^2 \omega b_2}, \quad m = \frac{m}{\rho\pi r_2^2 b_2}$$

Here $\mathcal{k}, \mathcal{K}, c, \mathcal{C}, m, \mathcal{M}$ represent the dimensionless stiffness, damping and added mass coefficients, with small letters used for cross-coupled coefficients and capital letters for direct coefficients. It has been confirmed in the current study, and other studies concur [73, 103, 185], that the assumption of skew-symmetry applies to this problem. Finally, a sample whirling open impeller set-up case in CFX has been included in Appendix C.

4.3.4. Grid Independency

A grid study was performed in order to find a converged solution with respect to mesh density. Four sets of grids have been selected, each has been refined in accordance to the guidelines of ASME [179] for grid independency study Table 15 gives further detail about the grid sizes.

Table 15. Grid sizes selected for grid independency study

	Impeller	Auxiliary domains	Total
N^1	660,000	313,000	973,000
N^2	1,380,000	686,000	2,066,000
N^3	2,968,000	1,470,000	4,438,000
N^4	6,870,000	3,291,000	10,161,000

The head coefficient ψ , efficiency η and the radial thrust F_0 (decomposed into F_{0x}, F_{0y}) are selected as the parameters of interest. The subscript 0 denotes a non-

whirling (concentric) solution. As expected, the radial thrust almost vanishes at the Best Efficiency Point (BEP). According to Figure 75 the third grid with the size of 4,438,000 elements has been selected for the simulations.

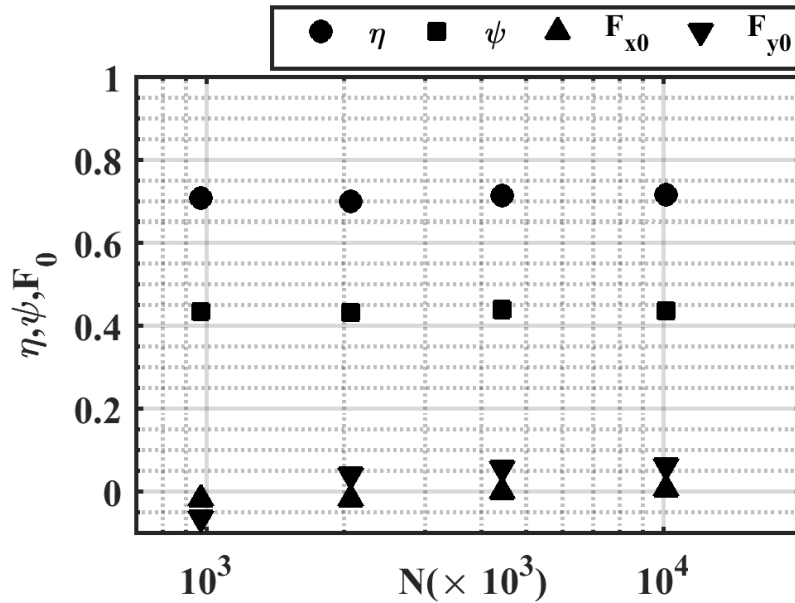


Figure 75. Grid independency results for the open impeller

4.4. Results and Discussion

4.4.1. Validation

The zeroth order solution (non-whirling) has been validated using the head-flow characteristics available from the experiments of Yoshida et al. [66] (See Figure 76). The design flow rate for the compressor is $\phi_d = 0.424$ but actual efficiency measurements for the pump mode are not available. The CFD efficiency results suggest that the pump mode BEP occurs close to $\phi = 0.33$.

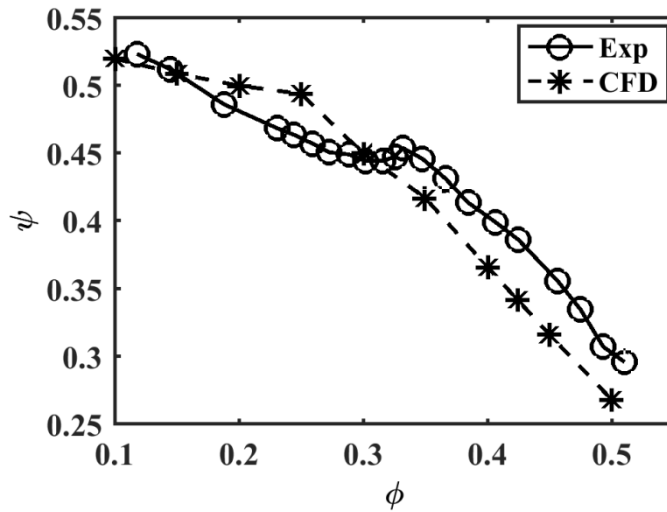


Figure 76. The open impeller head-flow characteristic in the pump mode (experimental data adapted from [66])

The dimensionless normal and tangential forces (rotordynamic forces) from CFD solution are compared against the measurements of Yoshida et al. [66] at several flow coefficients. The experimental dimensionless force measurements have an uncertainty of ± 1.5 . Considering the complexity of the problem, Figure 77 shows good agreement between CFD and experiments at BEP and off-flow conditions. Almost all of the figures imply that this open impeller rotordynamic forces are not well-represented with a quadratic force model, which is partly due to the fact that this impeller is a compressor being tested or simulated as a pump. Perhaps results at $\phi = 0.424$ are the only set of data that can use a quadratic model because the bumps and dips are weaker and they more closely follow the second order curve fit. Almost all flow coefficient results show a low frequency bulged area in the forward mode which may be attributed to the co-rotating tip leakage flow [33, 191]. For such bumpy impedances, a more

general transfer function approach is recommended such as the one suggested by Kim and Palazzolo [133].

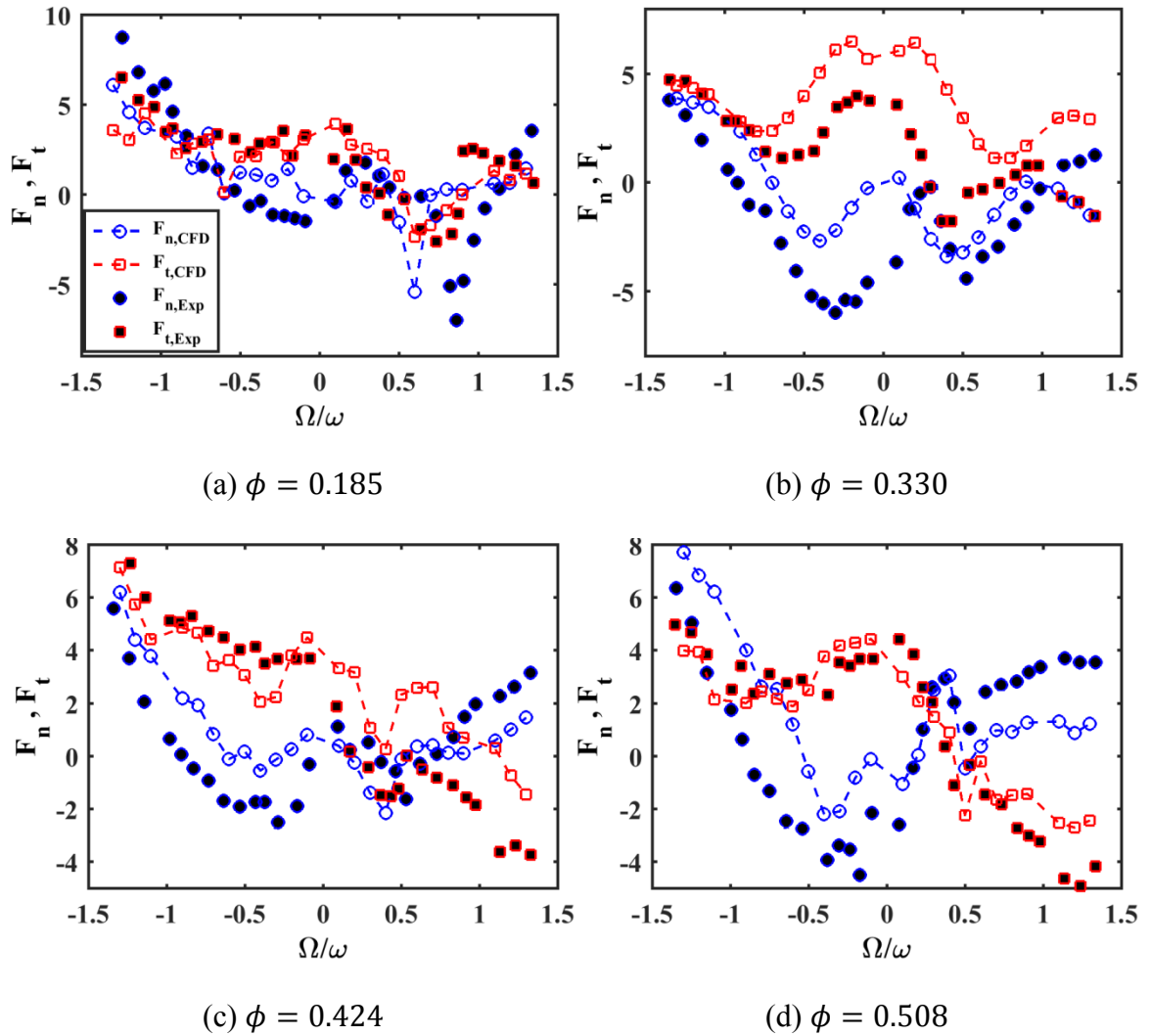


Figure 77. Predictions of CFD-based rotordynamic forces vs experiments (experimental data adapted from [66]) at multiple flow rates: (a) $\phi=0.185$ (b) $\phi=0.330$ (c) $\phi=0.424$ (d) $\phi=0.508$

The tangential force data at multiple flow coefficients appears to be destabilizing in the subcritical forward whirl region. In this region, the condition for self-excited instability $F_t \cdot \Omega > 0$ is satisfied. The tangential force keeps feeding energy to the whirling motion, the whirling motion causes a centrifugal force and an even larger orbit. Consequently rotordynamic forces get larger and the loop continues [47]. The CFD results slightly over-predict the destabilizing margin of forward whirl where $F_t \cdot \Omega > 0$.

In order to further evaluate the multi-frequency approach, a comparison with the single frequency method has been made (at $\phi = 0.330$). Both simulations use the same single mode eccentricity ratio of $\epsilon = 0.005$. The results from Figure 78 exhibit the same trend in the single frequency and the multi frequency results.

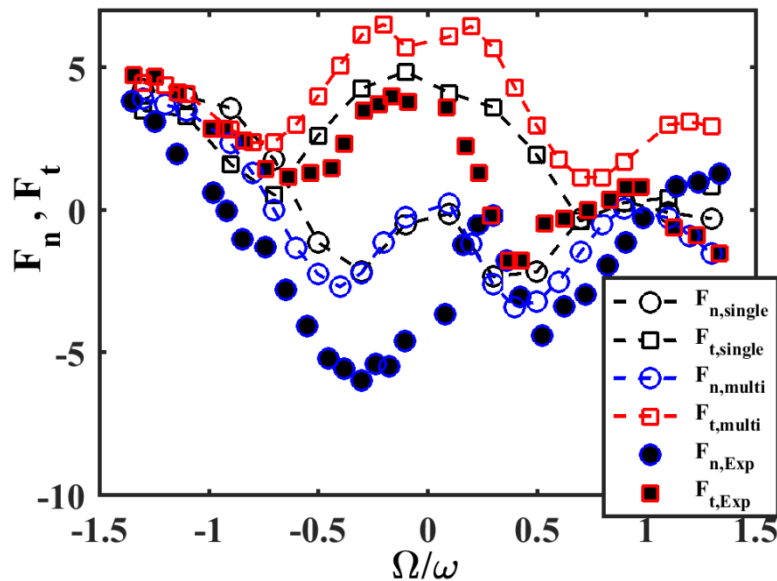


Figure 78. Comparison of single frequency vs multi frequency results at $\phi=0.330$ (experimental data adapted from [66])

The normal forces are predicted to be almost identical while the tangential forces show certain departure. This is in part due to the nonlinearities present in the multi-frequency approach and the superior mesh quality preservation of the single frequency approach. On the other hand, the multi-frequency method performs about 20 times faster which offers considerable savings in terms of the computational cost.

4.4.2. Rotating Stall

In the original publication by Yoshida et al. [66], the authors point toward a sudden jump appearing in the impedances, occurring at $\phi = 0.285$ and the frequency ratio $\Omega/\omega = 0.8$ which is re-illustrated in Figure 79.

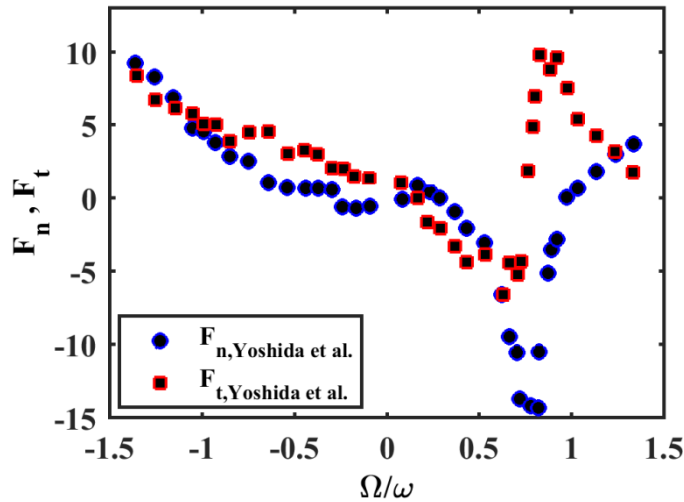


Figure 79. Sudden jump appearing at $\phi=0.285$, $\Omega/\omega=0.79$ in the original experimental study (adapted from [66])

Such jumps are also present in CFD results and cause the impedances to be distorted close to those frequencies. Yoshida et al. [66] mention that this jump is caused by an

impeller rotating stall. If this is true, the concentric case at the same flow rate should exhibit forces appearing at the same frequency due to the rotating stall. Considering that, the FFT results of the concentric CFD case at $\phi = 0.285$ showed a large peak appearing close to $\Omega/\omega = 0.8$. Furthermore, the whirling case showed a large spike appearing at the same frequency range (See Figure 80). However, since the jump is about two orders of magnitude larger than the neighboring points, it was concluded that this force is not scaling with the eccentricity, rendering the cause of the force something other than the whirling motion.

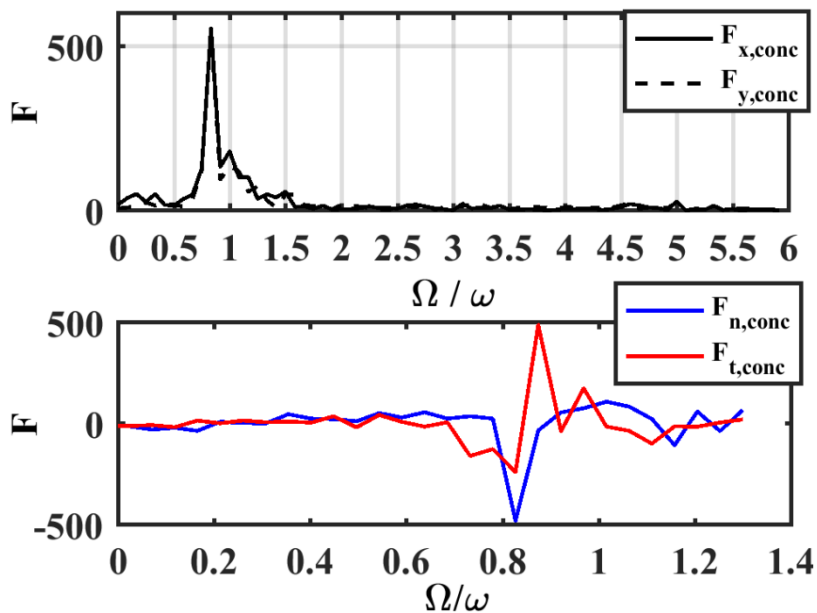


Figure 80. Non-dimensional forces in the stationary and the whirling frames at $\phi=0.285$

Further visual inspection with transient CFD simulations revealed a 3 lobe rotating stall appearing at the impeller eye and extending inside the impeller at this flow rate (See

Figure 81). It was confirmed that the impeller rotating stall pattern has a frequency ratio of $\Omega/\omega = 0.83$. This is in agreement with the observations of Yoshida et al. [66]. Notice that the stall pattern appears at the tip clearance region and it is attributed to the tip leakage flow.

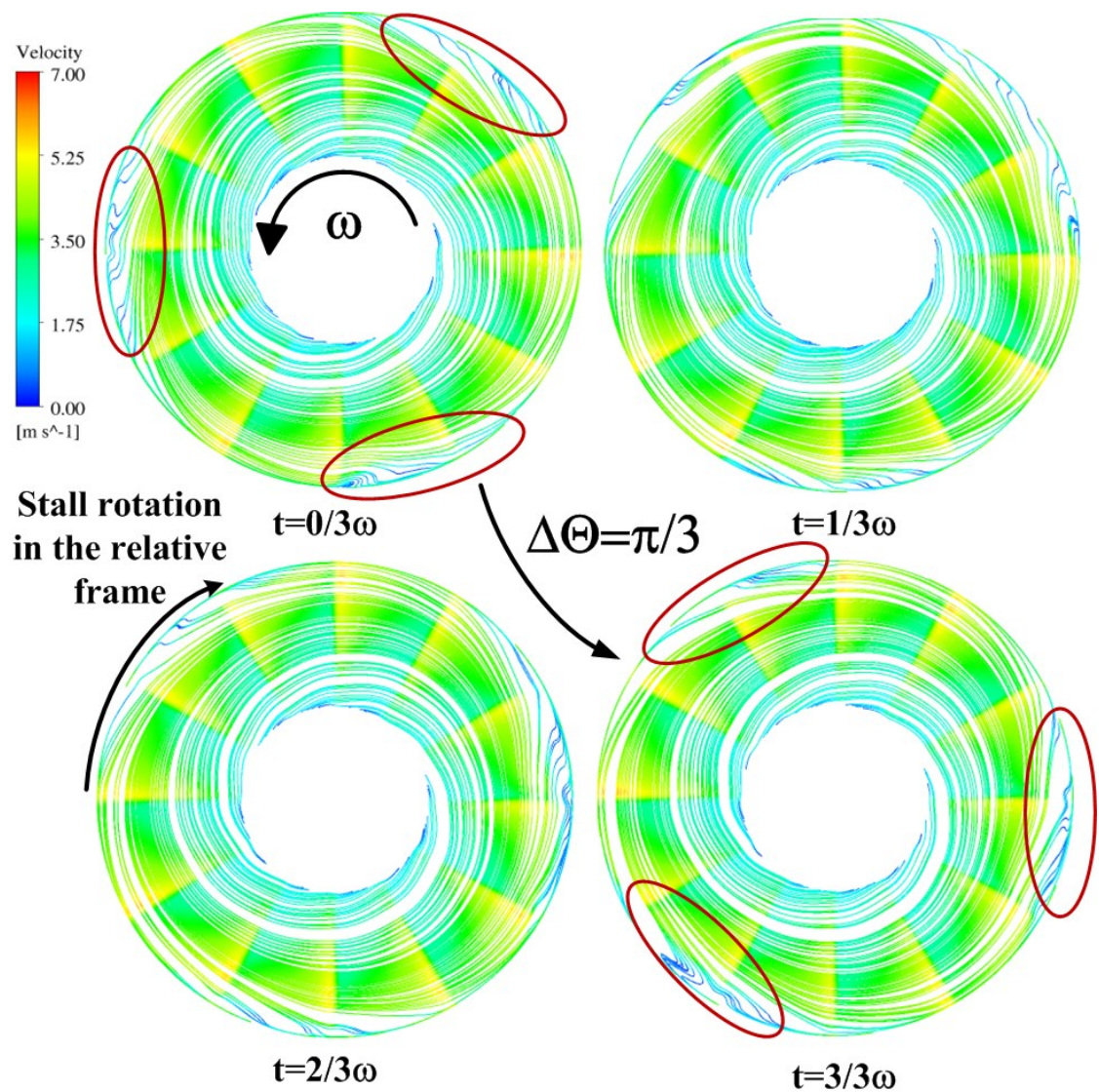


Figure 81. Rotating stall appearing in CFD results. Co-rotating stall at the impeller eye at $\phi=0.285$, $\Omega/\omega=0.83$

A second visualization attempt with pressure coefficient iso-surface revealed the 3 lobe structure in 3D at the impeller eye close to the tip area (See Figure 82). When the pressure coefficient increases or decreases, the asymmetric pattern disappears.

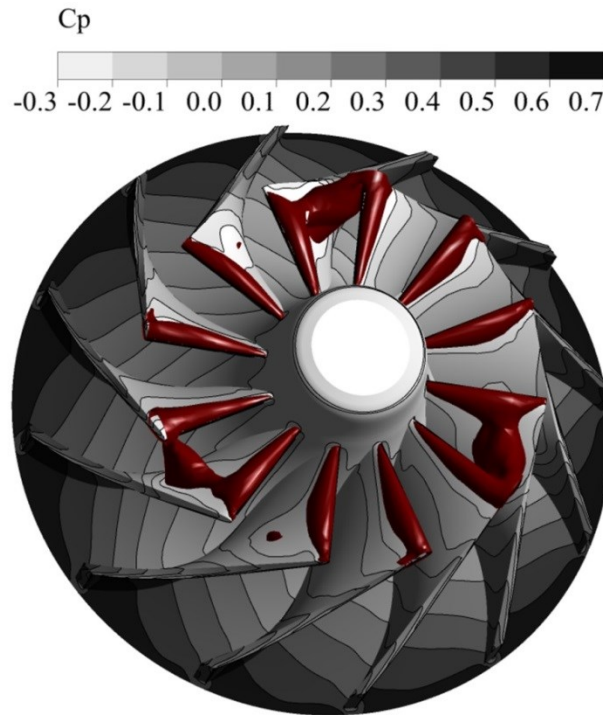


Figure 82. $C_p=-0.15$ iso-surface showing the three lob tip vortex structure

Such interaction between rotating stall and whirling motion, and the whirl induced stall have been further documented in other experiments done by Yoshida et al. [80].

4.4.3. Specific Speed Effect

This part of the study aims to provide more general rotordynamic data for open impellers. The objective is to find dimensionless rotordynamic force data which are applicable to impellers of the same class. Basically, such attempt better fits open

impellers rather than closed impellers. In an open impeller, the tip clearance profile is ruled by the specific speed and clearance size, both of which are universal designs, at least to a great extent. On the other hand, a closed impeller has a front leakage path clearance instead of tip clearance. This front leakage path clearance is ruled by the casing profile and there is no consensus on the design of casing profiles. Therefore such dimensionless data is exclusively sensible for open impellers.

To this end, a series of impeller designs characterized with a general dimensionless number called the specific speed are studied. There are other well-known dimensionless groups present as well:

$$\psi = \frac{gH}{U_2^2}, \quad \phi = \frac{Q}{2\pi r_2 b_2 U_2}, \quad \eta = \frac{\rho g H Q}{T \omega}, \quad \omega_s = \frac{\omega Q^{1/2}}{(gH)^{3/4}} \quad (51)$$

where ψ is the head coefficient, ϕ is the flow coefficient, η is the efficiency and ω_s represents the specific speed of the impeller, H is the pump head, U_2 is the discharge circumferential velocity, Q shows the flow rate, and T is the torque acting on the impeller. The power coefficient Π can be reconstructed with the aforementioned groups. These characteristics are plotted in Figure 83 for the simulated specific speeds at the design flow. This checks whether the simulated impellers actually represent the designed specifications.

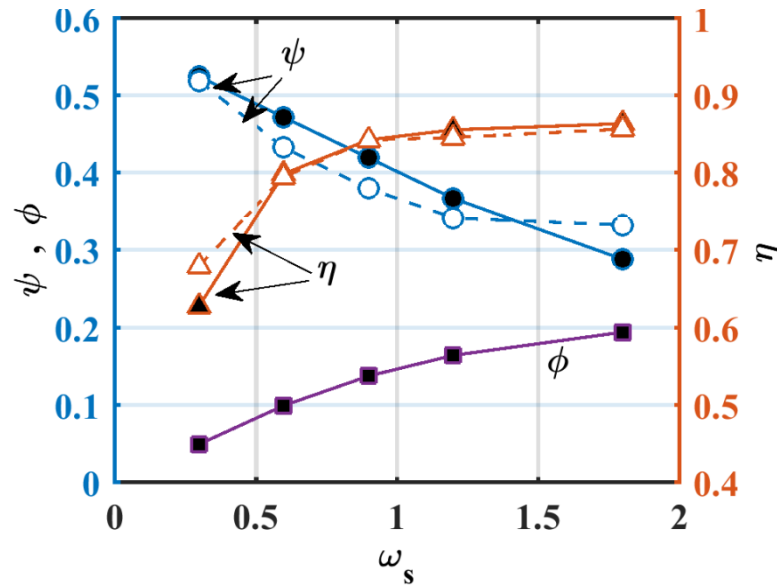


Figure 83. Design and simulation characteristics of the investigated open impellers. Filled markers denote the design values and blank markets show the simulated values.

It is well known that when the same pump impeller is scaled and run under the same flow coefficient, the other dimensionless groups retain their original value within a few percent (with the exception of Re number [21, 192]) so transition effects should not be dominant. If the dimensionless forces of a given impeller with a certain specific speed remain unchanged after scaling, then the same dimensionless rotordynamic forces are applicable to all the impellers of the same class. A numerical simulation has been done to check this postulation for a sample impeller with the specific speed of $\omega_s = 0.3$. Figure 84 shows that this hypothesis is highly accurate, provided that the specific speed ω_s , the flow coefficient ϕ and the eccentricity ratio ϵ match (See Table 16). The twice-scaled impeller has basically the same dimensionless rotordynamic forces with a

bumpier curve. These fluctuations occur due to the larger Re number as well as the larger absolute eccentricity.

Table 16. Scaled impellers' dimensionless groups

Impeller	ω_s	ϕ	ϵ_{Ω_i}	ψ	η
1x	0.3	0.049	0.005	0.519	0.682
2x	0.3	0.049	0.005	0.531	0.709

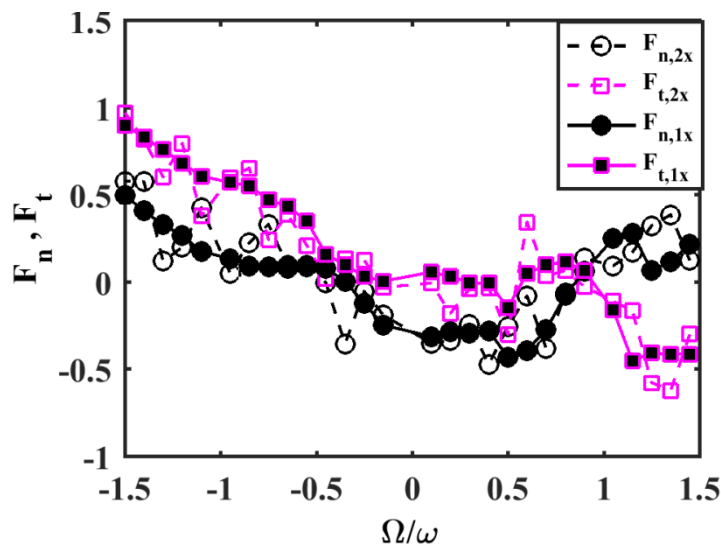


Figure 84. Rotordynamic forces of the original and the scaled impeller for the same eccentricity ratio and flow coefficient

Next, the individual impellers are simulated for their impedances at their design flow rate. Figure 85 gives a clear trend in the rotordynamic behavior based on the specific speed. Notice that these impedances (all pump impellers) have relatively smoother and more quadratic curves compared to the compressor impeller case. The

lower specific speeds have comparably smaller rotordynamic forces, especially since the normalized form of the dimensionless forces, with the impeller discharge width b_2 , implies larger dimensional forces as ω_s increases. One expects such a trend due to elongation of the hub surface in the axial direction when moving from 2D centrifugal to 3D mixed flow impellers. In addition, the increased blade lean angles at higher specific speeds provide more effective surface area for the pressure field to work on. However, there is a trade-off between the increased effective surface area of the impeller and its capacity to generate head. This leads to a saturation in the size of the dimensionless forces as the specific speed increases.

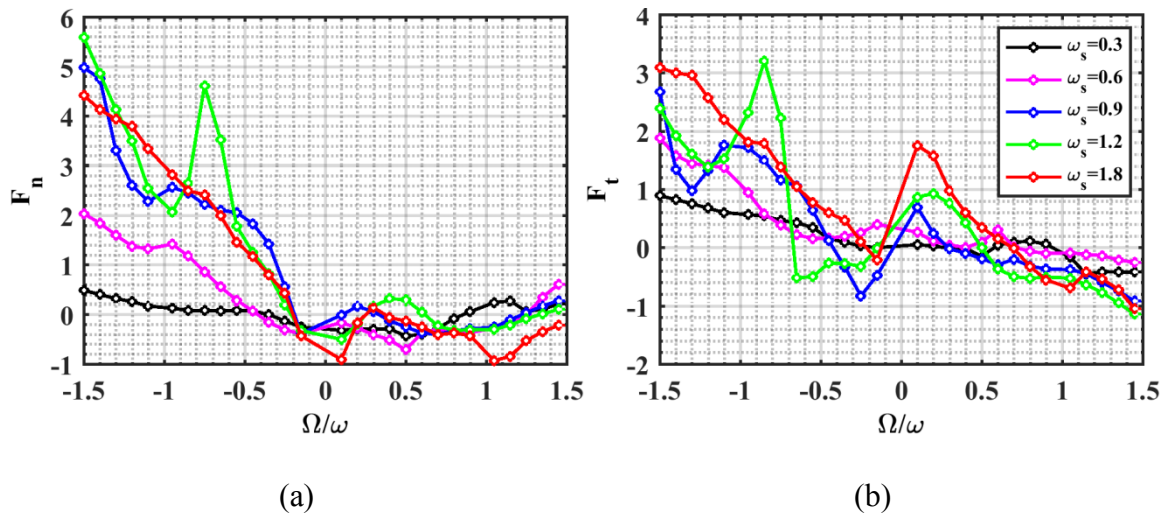


Figure 85. Effect of the specific speed on the rotordynamic forces of the open impellers. (a) normal forces (b) tangential forces

A quadratic curve fit to the design flow data yields the rotordynamic force coefficients. Although a second order presentation has definite shortcomings, such data

have useful industrial applications such as rotordynamic stability analysis and machinery vibration balancing Table 17 reveals an upward trend in the cross-coupled stiffness value. Considering the stiffness values, and the examination of the destabilizing region in Figure 85, the impellers with higher specific speeds are more destabilizing. Some of them even feed the backward whirl due to the condition $F_t \cdot \Omega > 0$. The destabilizing mechanism is the same as the forward whirl case which was explained in the Validation section.

Table 17. Comparison of the open impeller rotordynamic force coefficients versus specific speed, for the same eccentricity ratio ($\epsilon=0.005$) at the design flow ($\phi/\phi_d=1$)

ω_s	\mathcal{K}	k	\mathcal{C}	c	\mathcal{M}	m
0.3	0.21	0.11	0.39	0.09	0.28	-0.07
0.6	0.26	0.10	0.53	0.65	0.68	-0.36
0.9	-0.34	0.07	0.86	1.50	0.93	-0.29
1.2	-0.42	0.25	1.00	1.70	1.00	-0.19
1.8	-0.20	0.60	1.20	1.70	0.92	-0.23

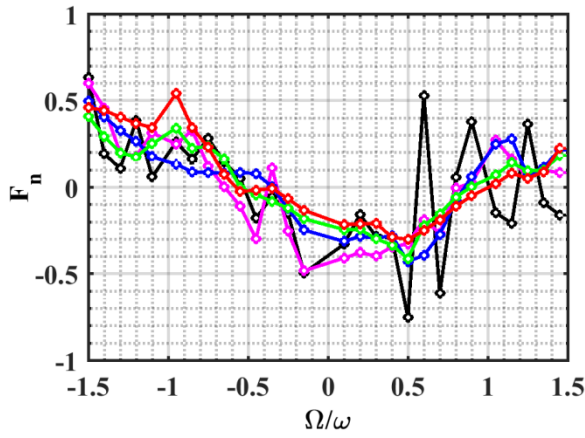
Example: An example is provided to clarify how this dimensionless data can be applied to other impellers of the same class.

Consider a pump open impeller with specifications of 2000 rpm rotational speed, 670 m³/hr flow rate and a head of 19 m. The impeller falls under the class of $\omega_s = 1.8$ impeller types, however the operating condition is suggesting that the

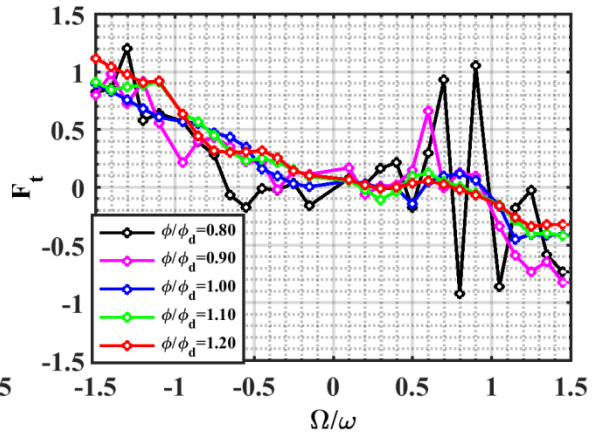
dimensions are slightly larger than the impeller simulated in this study. The example impeller has an outer diameter about $D_2 = 222$ mm and an outlet width of approximately $b_2 = 80$ mm. Referring back to Table 17, the dimensionless cross-coupled stiffness $k = 0.6$ can be used to estimate the dimensional value of $k = 81,350$ N/m by substituting the new dimensions.

Such calculations are valid provided that the impeller of the same class is operating under the same flow coefficient and eccentricity ratio. The dependence on flow coefficient and eccentricity ratio is further discussed in the following paragraphs.

Pumps are frequently run at part-load or over-flow conditions. It is expected to see a rise in the steady radial thrust under these conditions, but the rotordynamic forces of open impellers in off-flow mode need further investigation. Hence, the off-flow rotordynamic forces are simulated for each specific speed. A flow rate range of $0.8 < \phi/\phi_d < 1.2$ has been selected based on the practicality of the results. Also, excessive off-flow conditions may cause the formation of strong rotating stall forces which will mask the rotordynamic forces, and therefore such conditions are avoided. Figure 86 to Figure 90 show the results for each specific speed. Irregular peaks consistently appear at off-flow conditions, with greater conspicuousness at part-load condition.

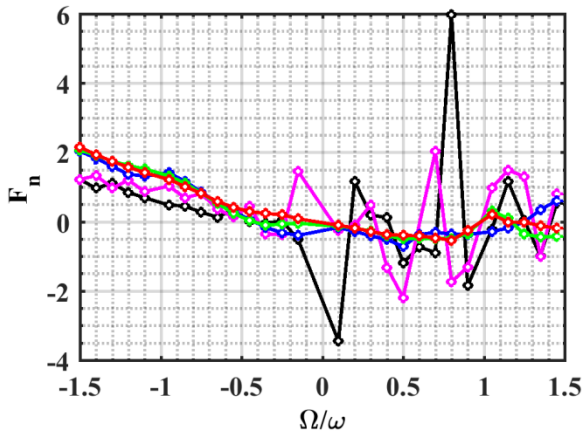


(a)

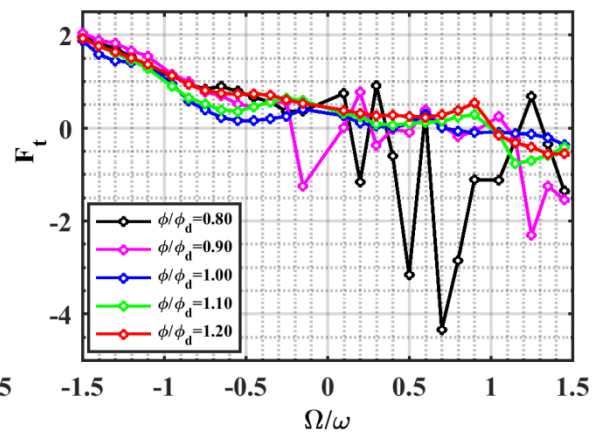


(b)

Figure 86. Off-flow rotordynamic forces for $\omega_s=0.3$. (a) normal forces (b) tangential forces



(a)



(b)

Figure 87. Off-flow rotordynamic forces for $\omega_s=0.6$. (a) normal forces (b) tangential forces

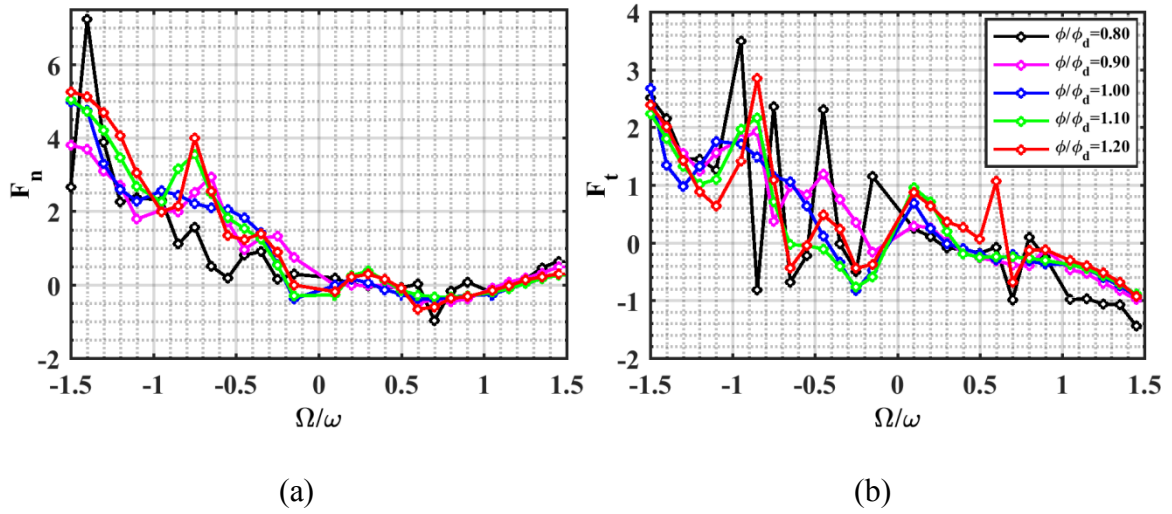


Figure 88. Off-flow rotordynamic forces for $\omega_s=0.9$. (a) normal forces (b) tangential forces

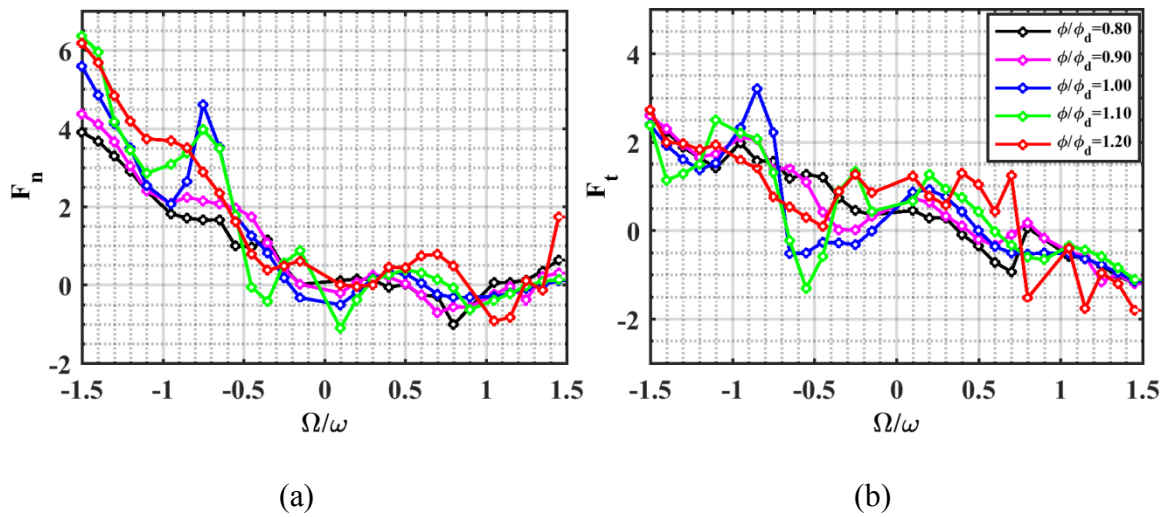


Figure 89. Off-flow rotordynamic forces for $\omega_s=1.2$. (a) normal forces (b) tangential forces

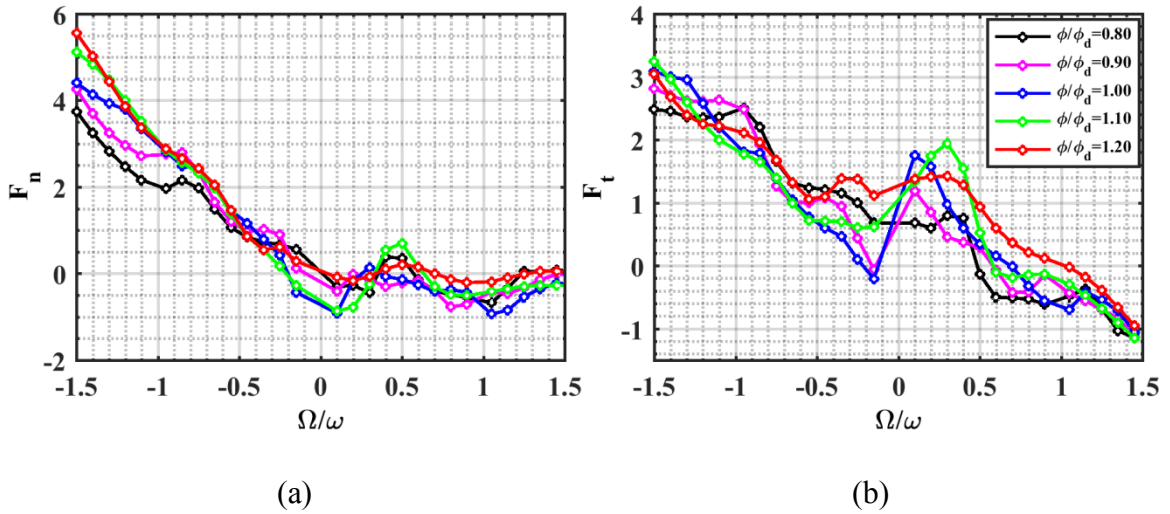


Figure 90. Off-flow rotordynamic forces for $\omega_s=1.8$. (a) normal forces (b) tangential forces

Prior observations identified interactions between stall and whirling components. In scenarios where the rotordynamic forces are sizable compared to the stall forces, it is possible to estimate the contribution of rotating stall to the total normal and tangential forces using a phase-averaging technique, as was employed in the experimental work of Yoshida et al. [80]. This approach was not utilized here due to the excessive computational time required at each frequency. The paper by Hussain and Reynolds [193] was among the first publications to use this method in fluid dynamics. The following steps can be followed to estimate the contribution of the rotordynamic forces and the rotating stall forces to the total normal and tangential forces (The schematic is shown in Figure 91):

1. Impose a single whirling motion on an impeller which has a rotating stall at the same frequency. The whirling motion starts at $t^* = 0$.

2. Repeat the same single frequency whirl, this time at $t^* = 1/8\omega$. At least 8 different phase lags are required for an acceptable stall signal reconstruction.
3. Collect the force data and average F_x, F_y at $t = nt^*$, $n = 1, 2, 3 \dots$ for each case.
4. Assuming skew-symmetry, the total normal and tangential forces are found at different phase lags.
5. This total force should be sinusoidal signal over one period. The average for F_x shows $F_{n,\Omega}$ due to whirling motion and the average of F_y shows $F_{t,\Omega}$ due to the whirling motion. The amplitude and phase lags of these two signals can be used to reconstruct the rotating stall contribution to the normal and tangential forces.
6. This process should be repeated for other frequencies, as well.

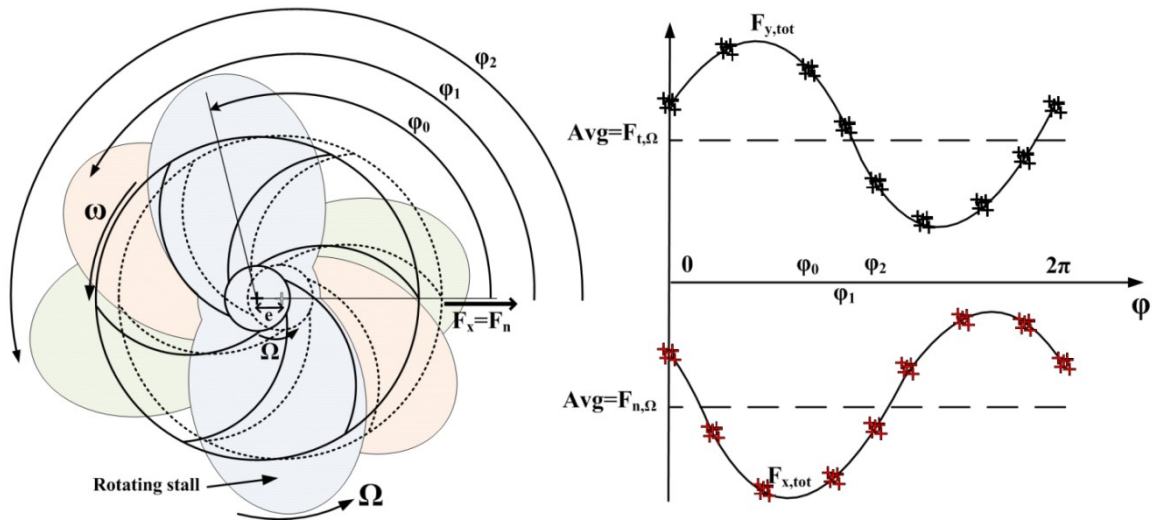


Figure 91. Phase averaging schematic

Figure 90 also demonstrates that open impeller rotordynamic forces are flow rate dependent. The dependency is more pronounced when the stiffness coefficients are interpolated from the zero-frequency crossings. Such sample plot is found for $\omega_s = 0.3$ in the relative flow rate ratio of $0.5 < \phi/\phi_d < 1.5$ to better reveal the trends (See Figure 92). The plot exhibits a drop in the cross-coupled stiffness as the flow rate decreases to the point that the cross-coupled stiffness k changes sign, and will then drive backward whirl. Similar declining trend in cross-coupled stiffness was noted for other specific speeds. This outcome is consistent with the previous results obtained for axial flow compressors [42, 43].

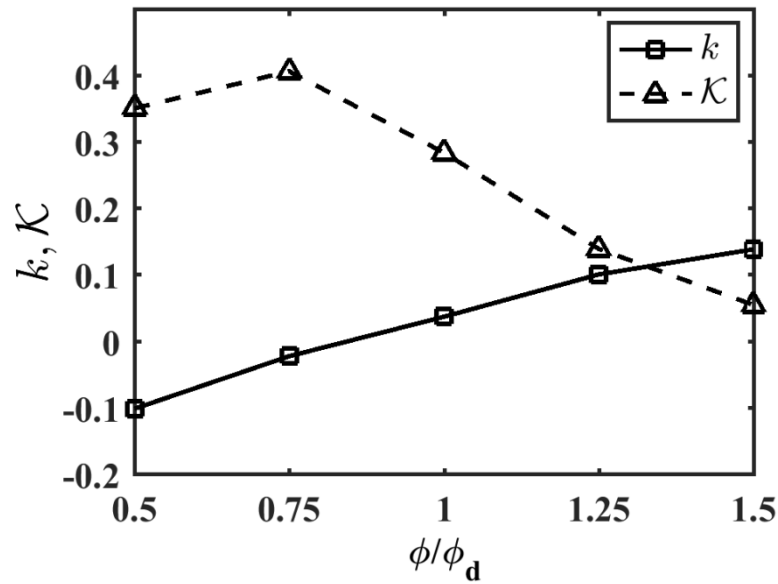


Figure 92. Stiffness values for $\omega_s=0.3$ versus the relative flow rate. K is the dimensionless direct stiffness and k is the dimensionless cross-coupled stiffness.

As it was stated earlier, the dimensionless rotordynamic forces should have the same eccentricity ratio to be extendable to larger or smaller impellers of the same class. In other words, the forces should be normalized with eccentricity ratio rather than eccentricity. This releases a new dimension in the denominator. Since the projected effective area of impellers with higher specific speed grows as the hub gets longer, the hub axial length seems to be the appropriate scaling dimension for open impellers. Bhattacharyya et al. [77] have used a similar length scale in their earlier investigations on cavitating inducers. The newly suggested dimensionless force has the form:

$$F = \frac{f}{\rho\pi r_2^2 \omega^2 b_2 (e/C_r) L_h} \quad (52)$$

where C_r is the tip clearance and L_h symbolizes the hub axial length. Figure 93 has been plotted for the rotordynamic forces using this new dimensionless format. The concentration of normal force data increases as well, but not as much as tangential forces. Comparing the results with those of Figure 85, the dimensionless forces are much closer now with this new format. In fact, the tangential forces of all the impellers now have about the same slope which suggests the strong dependency of the direct damping on the hub axial length. The direct damping coefficient for open impellers is therefore estimated as:

$$C = 0.0115\rho\pi r_2^2 \omega b_2 \frac{L_h}{C_r} \quad (53)$$

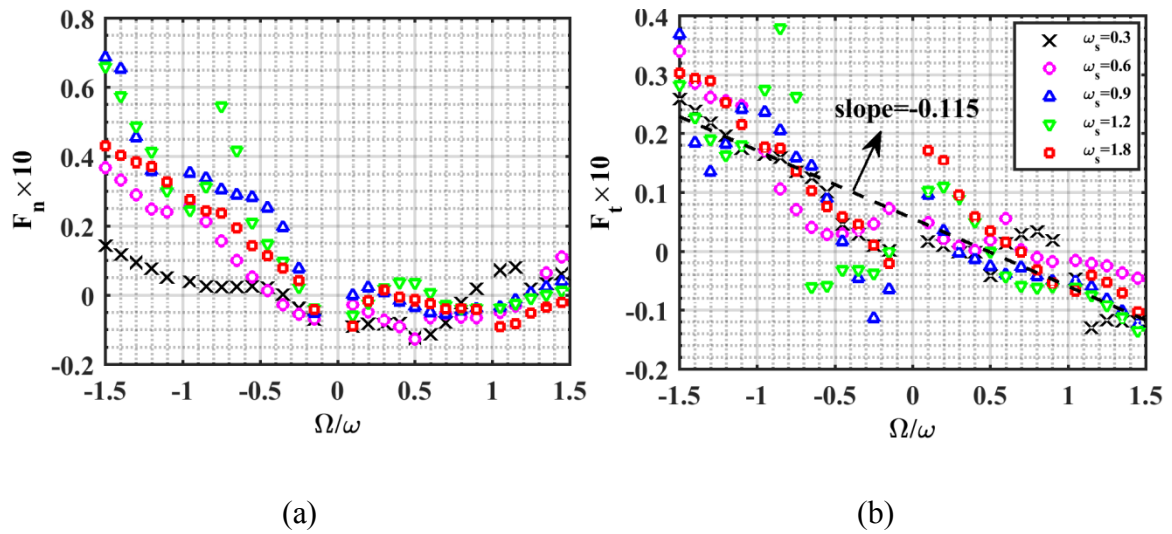


Figure 93. New dimensionless format for rotordynamic forces for various specific

4.4.4. Bumps and Dips in Closed Impellers

Earlier results of Childs [157] and Kim and Palazzolo [35] suggests appearance of bumps and dips in isolated secondary path models where there are no blades or vanes present. In order to investigate this phenomena, a shroud, front shroud and front casing have been appended to one of the centrifugal impellers ($\omega_s = 0.6$) to form an equivalent closed impeller with secondary flow path. Furthermore, a second case has been set up with an isolated leakage path model (ILPM) according to Figure 94.

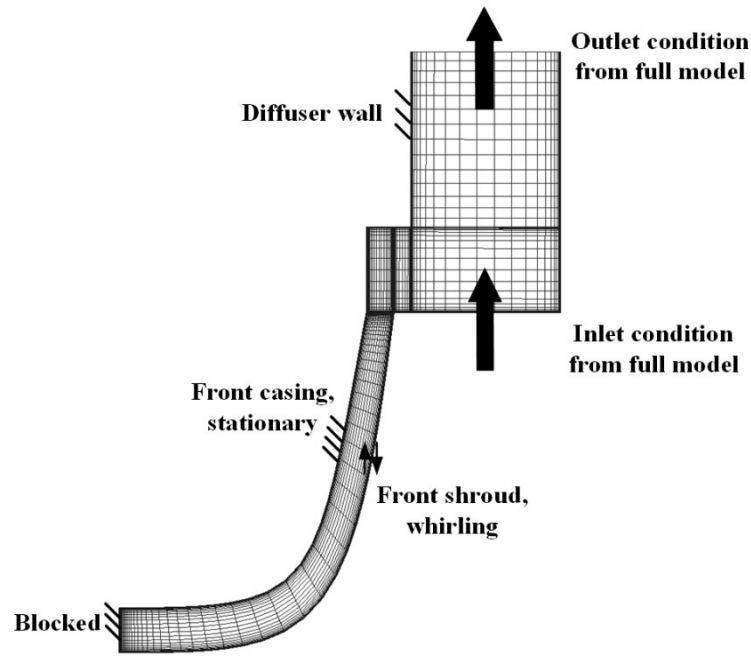


Figure 94. Isolated leakage path model ILPM for the impeller related flows

The boundary conditions are imposed at the impeller discharge (inlet) and the diffuser discharge (outlet). These conditions are extracted from the full model and then averaged over area to impose a uniform inlet condition similar to a Bulk-flow or leakage path model problem. Although these boundary conditions are too simplified, they prove useful in terms of understanding the origins of bumps and dips. All cases are simulated using the phase modulated multi-frequency approach with the single mode eccentricity ratio of $\epsilon = 0.005$.

Next, the results at design flow for the full open impeller model, full closed impeller model and the ILPM are compared in Figure 95. The results of the closed impeller are further broken down into primary passage and secondary passage contributions.

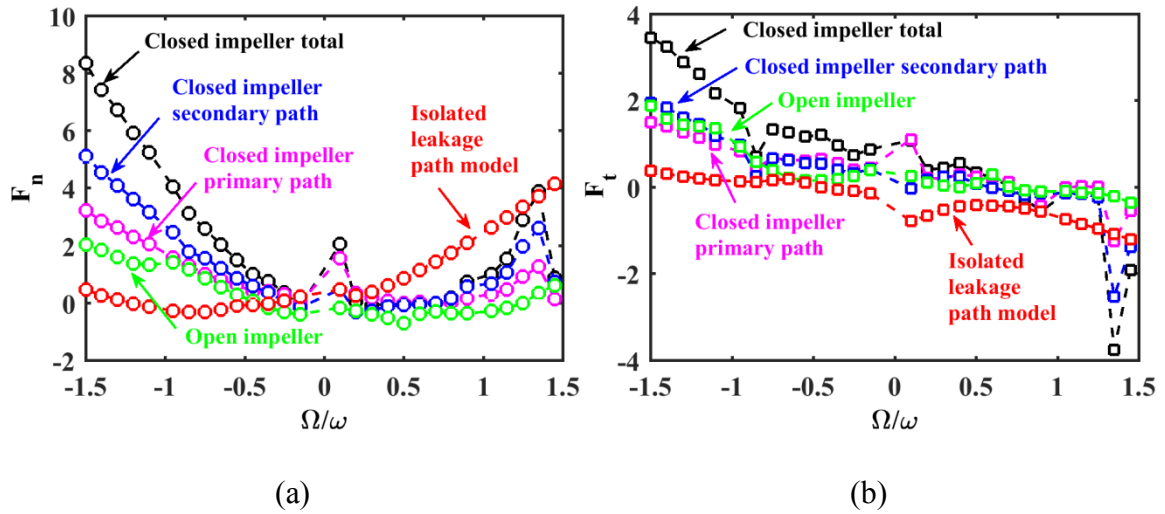


Figure 95. Comparison of rotordynamic forces for closed impeller, open impeller and ILPM. (a) normal forces (b) tangential forces

Despite the earlier conviction that the majority of a closed impeller rotordynamic forces come from the leakage path, it is observed that both primary and secondary paths have about the same contribution. Therefore a notably lower cross-coupled stiffness will be resulted if one only considers the front shroud forces. The results argue for larger rotordynamic forces occurring in the shrouded variation. Furthermore, an ILPM with an averaged boundary condition will result in appreciably different results from the full model, both quantitatively and qualitatively; therefore, it is recommended to let the extended CFD model establish the boundary conditions of the leakage path. It is noteworthy that all impedances to some degree show bumps and dips at $FR = +0.2$, even the ILPM.

Revisiting the earlier results [35, 157], the bumps and dips in an ILPM appear at the same frequency ratio range and they get stronger with an increased inlet swirl. In

comparison, an increased swirl ratio in a full model occurs when the flow rate reduces, and similar with the ILPM, bumps and dips also appear. This situation is applied in the current problem by increasing the swirling component of inlet velocity V_θ . Consequently, the bumps and dips grow significantly both in amplitude and frequency due to an increased swirl inflow velocity (See Figure 96). The non-whirling ILPM simulation results show null forces except for a minuscule peak (order of thousand times smaller) at $FR = 0.2$ as illustrated in Figure 97. Therefore, the bumps and dips in ILPM are either caused by a self-induced hydrodynamic instability or they form as a result of a weak mode excitation. Such early excitation of stall mode due to the whirling motion has been previously measured by Yoshida et al [80] for a closed impeller, as well.

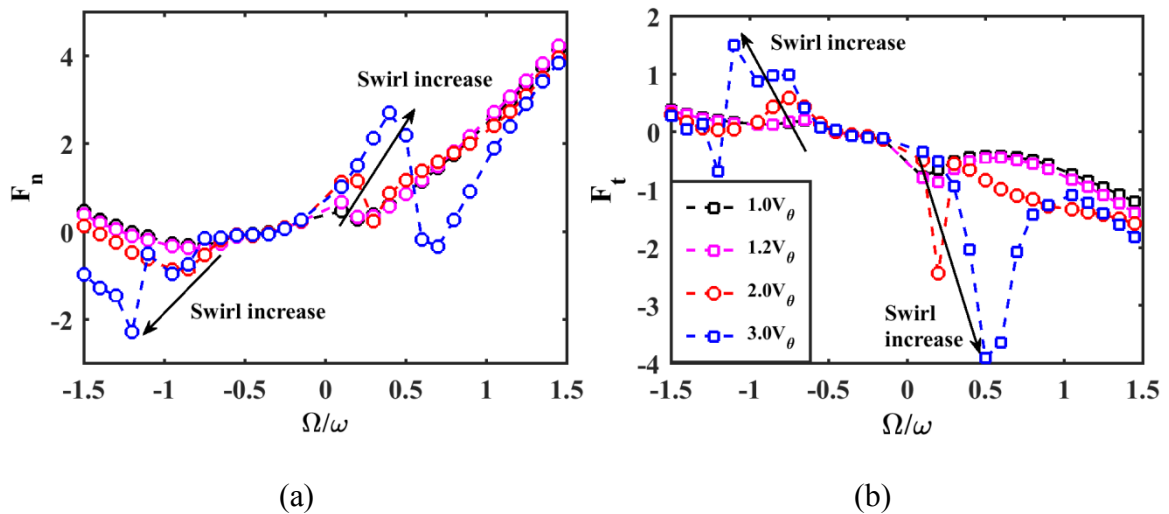


Figure 96. Bumps and dips in ILPM getting stronger as the inlet swirl velocity increases by a factor of 3. (a) normal forces (b) tangential forces

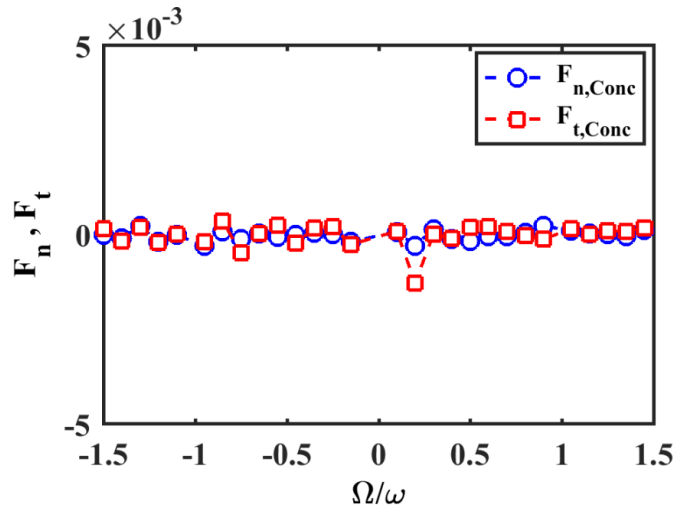


Figure 97. Concentric ILPM results showing a minuscule peak at $\Omega/\omega=0.2$ for the inflow swirl condition of $2V_\theta$

4.5. Conclusion

A new CFD-based transient, phase modulated, multi-frequency approach was presented to determine rotordynamic forces of open impellers. The CFD model used a SST turbulence model as well as the $\gamma - Re_\theta$ transition model and mesh deformation. The approach was validated against the experimental data of Yoshida et al. [66] at BEP and off-flow conditions. The multi-frequency approach shows good agreement with the single frequency approach and with experiments, provided that a small individual eccentricity ratio of order $\epsilon = 0.005$ is utilized. Under such conditions, the phase modulated multi-frequency approach could accommodate about 30 frequencies simultaneously with a computational speed-up of order 20 times. Furthermore, it was demonstrated that sudden jumps appearing in the impedances at lower flow rates

(bumps and dips) stem from the interaction of the rotating stall with the whirling motion.

The approach was extended to a spectrum of impellers with various specific speeds. First, it was shown that a scaled impeller has the same dimensionless forces provided that both cases have the same eccentricity ratio and the flow coefficient. Results showed considerable dependency of the rotordynamic forces on the hub length, generally getting more destabilizing when the specific speed increases. Simulations indicated that some of the impellers can drive both the forward and backward modes.

An isolated leakage path model ILPM for a shrouded impeller was constructed to investigate impedance bumps and dips without the perturbations coming from the primary flow path. The bumps and dips are a strong function of the swirl inflow velocity to the leakage path, and are only excited in the whirling mode. In addition, it was learned that contributions from the primary and secondary flow path to the total rotordynamic forces are comparable in size. This implies that the accuracy of the API level II stability analysis may greatly benefit by including the primary flow path, along with the secondary flow path in the impeller force model.

Future work should include further investigation and development of computationally-efficient phase-averaging schemes [80] utilized for isolating contributions to impeller forces due to whirl-induced stall forces. It is also proposed that an inviscid linear stability analysis such as the one done by Tsujimoto et al. [106] for vaneless diffusers be applied to open impellers. Alternatively, such an analysis should be applied to closed impeller bulk-flow models which also have previously shown

similar resonances [157]. This may better illuminate the nature of the interaction between the rotating pressure patterns and the whirling motion, and identify the excited modes.

In conclusion, the results have served to elucidate the bump-dip characteristics observed in test and simulation studies. Specifically, the results further support that these fluctuations are caused by various types of hydrodynamic instabilities which lead to rotating vortices or pressure patterns. Further studies are needed to develop a unified theory for fully explaining the bump-dip response behavior in impeller impedance plots. This goal should include axial impellers and centrifugal compressors, along with centrifugal pumps.

5. STANDALONE CFD CODE FOR LIQUID ANNULAR SEALS

5.1. Introduction

Modern powerful computers and latest advancement in the field of computational science have enabled engineers to do complex modeling with less restrictive simplifications [194]. As a result, more accurate predictions lead to more effective analysis and design. On the other hand, some of manual steps can be further automated to save human effort and accelerate engineering analysis procedure. Accordingly, CFD can be tailored to the needs of turbomachinery industry for faster and more accurate results.

One has to take several steps to obtain the dynamic forces and rotordynamic coefficients of turbomachinery components such as seals and impellers by means of CFD. These steps include generation of the Computer Aided Design (CAD) model, generation of the computational space or the mesh, setting up the correct simulation problem by defining Boundary Conditions (BCs) and appropriate models, initializing the solution process, post processing for useful hydraulic/aerodynamic variables and forces, and finally another post processing step for the dynamic coefficients. Not only this procedure needs proper training and requires considerable time, but it also increases the risk of errors and failures to be occurred during multiple steps. Furthermore, this automated procedure will serve as a corner stone for future Multi-Disciplinary Analysis and Optimization (MDAO) developments. Obviously such effort requires years of provision and implementation of several code pieces for multiple generations. Current

CFD code has been developed de novo in FORTRAN and means to serve as a basis for the future generations of the solver.

Accordingly, this section discusses the development of the code. The appropriate form of laminar and turbulent equations will be introduced. A powerful scheme to solve these coupled equations will be illustrated in detail. Several aspects of the code, including various turbulence models, wall-functions, non-uniform grid and wall treatment will be discussed. Performance boost schemes such as Multigrid (MG) will be discussed. Finally, the code will be compared and validated against several laminar and turbulent cases including plain annular seals at low and high Re numbers.

5.2. Governing Equations

5.2.1. Momentum and Continuity Equations

The governing equations include conservative form of Navier-Stokes, energy and continuity equations. The momentum equations should be modified before introducing turbulence equations. The continuity equation remains unchanged. According to Wilcox [195] the conservative form of NS with Boussinesq [196] assumption will be:

$$\frac{\partial(\rho u_i)}{\partial t} + \frac{\partial(\rho u_j u_i)}{\partial x_j} = -\frac{\partial p}{\partial x_i} + \frac{\partial}{\partial x_j} (t_{ij} + \rho \tau_{ij}^*) \quad (54)$$

where

$$\begin{aligned}
t_{ij} &= 2\mu\bar{S}_{ij}, & \rho\tau_{ij}^* &= 2\mu_t\bar{S}_{ij} - \frac{2}{3}\rho k\delta_{ij}, & \bar{S}_{ij} &= S_{ij} - \frac{1}{3}\frac{\partial u_k}{\partial x_k}\delta_{ij}, \\
S_{ij} &= \frac{1}{2}\left(\frac{\partial u_i}{\partial x_j} + \frac{\partial u_j}{\partial x_i}\right)
\end{aligned} \tag{55}$$

Where t_{ij} shows the stress tensor due to the molecular viscosity while $\rho\tau_{ij}^*$ is attributed to the eddy viscosity μ_t . The last term in Reynolds stress definition $-2/3\rho k\delta_{ij}$ causes incompressible flow ($\bar{S}_{ii} = 0$) to reduce to Prandtl's original formulae for kinetic energy $\tau_{ii}^* = -2\rho k$ where k is the turbulent kinetic energy. Therefore governing equations in the conservative form in cylindrical rotating frame will be [197]:

$$\frac{\partial w_r}{\partial r} + \frac{w_r}{r} + \frac{1}{r}\frac{\partial w_\theta}{\partial \theta} + \frac{\partial w_z}{\partial z} = 0 \tag{56}$$

$$\begin{aligned}
&\frac{\partial w_r}{\partial t} + \frac{\partial(w_r w_r)}{\partial r} + \frac{1}{r}\frac{\partial(w_\theta w_r)}{\partial \theta} + \frac{\partial(w_z w_r)}{\partial z} + \frac{w_r^2 - w_\theta^2}{r} \\
&= -\frac{1}{\rho}\frac{\partial p}{\partial r} + \frac{\partial \tau_{rr}}{\partial r} + \frac{1}{r}\frac{\partial \tau_{\theta r}}{\partial \theta} + \frac{\partial \tau_{zr}}{\partial z} + \frac{\tau_{rr} - \tau_{\theta\theta}}{r} \\
&+ \text{ROT}(+2\omega w_\theta + r\omega^2)
\end{aligned} \tag{57}$$

$$\begin{aligned}
&\frac{\partial w_\theta}{\partial t} + \frac{\partial(w_r w_\theta)}{\partial r} + \frac{1}{r}\frac{\partial(w_\theta w_\theta)}{\partial \theta} + \frac{\partial(w_z w_\theta)}{\partial z} + 2\frac{w_r w_\theta}{r} \\
&= -\frac{1}{r\rho}\frac{\partial p}{\partial \theta} + \frac{\partial \tau_{r\theta}}{\partial r} + \frac{1}{r}\frac{\partial \tau_{\theta\theta}}{\partial \theta} + \frac{\partial \tau_{z\theta}}{\partial z} + 2\frac{\tau_{r\theta}}{r} \\
&+ \text{ROT}(-2\omega w_r)
\end{aligned} \tag{58}$$

$$\begin{aligned}
& \frac{\partial w_z}{\partial t} + \frac{\partial(w_r w_z)}{\partial r} + \frac{1}{r} \frac{\partial(w_\theta w_z)}{\partial \theta} + \frac{\partial(w_z w_z)}{\partial z} + \frac{w_z w_r}{r} \\
& = -\frac{\partial p}{\partial z} + \frac{1}{r} \frac{\partial(r \tau_{rz})}{\partial r} + \frac{1}{r} \frac{\partial \tau_{\theta z}}{\partial \theta} + \frac{\partial \tau_{zz}}{\partial z}
\end{aligned} \tag{59}$$

here ROT is a switch function between the rotating and the stationary frame. The stress terms are defined as [198]:

$$\begin{aligned}
\tau_{zz} &= 2(\nu + \nu_t) \left(\frac{\partial w_z}{\partial z} \right) - \frac{2}{3} k \\
\tau_{rr} &= 2(\nu + \nu_t) \left(\frac{\partial w_r}{\partial r} \right) - \frac{2}{3} k \\
\tau_{\theta\theta} &= 2(\nu + \nu_t) \left(\frac{1}{r} \frac{\partial w_\theta}{\partial \theta} + \frac{w_r}{r} \right) - \frac{2}{3} k \\
\tau_{zr} = \tau_{rz} &= (\nu + \nu_t) \left(\frac{\partial w_r}{\partial z} + \frac{\partial w_z}{\partial r} \right) \\
\tau_{z\theta} = \tau_{\theta z} &= (\nu + \nu_t) \left(\frac{\partial w_\theta}{\partial z} + \frac{1}{r} \frac{\partial w_z}{\partial \theta} \right) \\
\tau_{r\theta} = \tau_{\theta r} &= (\nu + \nu_t) \left(\frac{\partial w_\theta}{\partial r} - \frac{w_\theta}{r} + \frac{1}{r} \frac{\partial w_r}{\partial \theta} \right)
\end{aligned} \tag{60}$$

5.2.2. Rotating Frame

The governing equations have used the kinematic condition $\mathbf{V} = \mathbf{W} + \mathbf{U}$ notation, $\mathbf{W} = (w_r, w_\theta, w_z)$ referring to the relative velocity vector inside a rotating frame and $\mathbf{U} = (0, r\omega, 0)$ is the added circumferential velocity. To include rotating frame effects, the kinematic condition in rotating frame is adopted to come up with [199]:

$$\frac{d\mathbf{V}}{dt} = \frac{\partial \mathbf{W}}{\partial t} + \frac{\partial \omega}{\partial t} \times \mathbf{r} + \mathbf{W} \cdot \nabla \mathbf{W} + \omega \times (\omega \times \mathbf{r}) + 2\mathbf{W} \times \omega \quad (61)$$

The second term can be dropped since the current code will not account for transient effects of rotational speed variation. All these terms replace the Left Hand Side (LHS) of momentum equation since it is only the convective terms of momentum balance are affected in rotational frame. The pressure gradient and diffusion terms are invariant to change of frame and therefore remain intact. The fictitious Coriolis and Centrifugal forces have been moved to Right Hand Side (RHS) and the equations are re-written. Please note that for an incompressible fluid, the continuity equation does not change by rotational effects. The centrifugal force only works in r direction, and Coriolis term works both in r and θ direction but will not have a component in z direction since rotational speed ω is parallel to the shaft.

$$2\mathbf{W} \times \omega = 2 \begin{bmatrix} \hat{e}_r & \hat{e}_\theta & \hat{e}_z \\ w_r & w_\theta & w_z \\ 0 & 0 & \omega \end{bmatrix} = (2\omega w_\theta)\hat{e}_r - (2\omega w_r)\hat{e}_\theta \quad (62)$$

5.2.3. Turbulence Modeling

Ideally, a universal set of equations are sought to model turbulence while they should be computationally inexpensive to solve industrial flows. Algebraic models are too simple to cover general applications. To further increase the number of physical equations, Prandtl [200] took the moment of the momentum equation and performed a Reynolds averaging. He reduced the number of unknowns, by taking the trace of Reynolds stress tensor and after simplifying the terms he come up with the turbulence kinetic energy equation. It can be readily shown that this one equation model needs the

length scale and two closure coefficients known a priori. Two equation models introduce a second differential equation to model the length scale l or any equivalent. This is the simplest “complete” set of equations will be achieved that do not need a knowledge of characteristics of turbulence nature of the problem. With this notion Kolmogorov [201] introduced a new parameter ω called specific dissipation rate which is frequency in fact. Then on dimensional grounds the interacting turbulence parameters are related as:

$$\mu_T \sim \frac{\rho k}{\omega}, \quad l \sim \frac{k^{1/2}}{\omega}, \quad \epsilon \sim \omega k \quad (63)$$

Various two-equation models either use these parameters or an equivalent set that can be easily found by manipulating these parameters. Overall, since the present application is mostly ruled by wall-bounded flows the k - ω family has been chosen for turbulence modeling over k - ϵ . Also this family of models can be easily upgraded to more complex versions such as Menter’s BSL and SST which are famous in turbomachinery applications due to their success in modeling swirling internal flows [149, 202, 203]. Furthermore, the k - ω equations can be integrated straight to the wall with physical BCs which allows for modeling near wall viscous effects.

5.2.3.1. Wilcox k - ω

Wilcox k - ω model [204] in Cartesian coordinates in compact form is given below:

$$\frac{\partial k}{\partial t} + \frac{\partial u_j k}{\partial x_j} = \tau_{ij}^* \frac{\partial u_i}{\partial x_j} - \beta^* k \omega + \frac{\partial}{\partial x_j} \left[(v + \sigma_k \nu_t) \frac{\partial k}{\partial x_j} \right] \quad (64)$$

$$\frac{\partial \omega}{\partial t} + \frac{\partial u_j \omega}{\partial x_j} = \hat{\gamma}_1 \frac{\omega}{k} \tau_{ij}^* \frac{\partial u_i}{\partial x_j} - \beta_1 \omega^2 + \frac{\partial}{\partial x_j} \left[(v + \sigma_\omega v_t) \frac{\partial \omega}{\partial x_j} \right] \quad (65)$$

Closure coefficients

$$\beta_1 = \frac{3}{40}, \quad \beta^* = \frac{9}{100}, \quad \sigma_{k1} = \frac{1}{2}, \quad \sigma_{\omega 1} = \frac{1}{2} \quad (66)$$

$$\hat{\gamma}_1 = \frac{\beta_1}{\beta^*} - \sigma_{\omega 1} \frac{\kappa^2}{\sqrt{\beta^*}}, \quad \kappa = 0.41$$

Auxiliary relations

$$\epsilon = \beta^* k \omega, \quad l = \frac{k^{1/2}}{\omega}, \quad v_t = \frac{k}{\omega} \quad (67)$$

In order to find the cylindrical form, first one should re-write the equations in the vector format:

$$\begin{aligned} \frac{\partial k}{\partial t} + \nabla \cdot (\mathbf{W}k) &= \left[v_t (\nabla \mathbf{W} + \nabla \mathbf{W}^T) - \frac{2}{3} k \mathbf{I} \right] \\ &: \nabla \mathbf{W} - \beta^* k \omega + \nabla \cdot [(v + \sigma_k v_t) \nabla k] \end{aligned} \quad (68)$$

$$\begin{aligned} \frac{\partial \omega}{\partial t} + \nabla \cdot (\mathbf{W}\omega) &= \gamma_1 \frac{\omega}{k} \left[v_t (\nabla \mathbf{W} + \nabla \mathbf{W}^T) - \frac{2}{3} k \mathbf{I} \right] \\ &: \nabla \mathbf{W} - \beta_1 \omega^2 + \nabla \cdot [(v + \sigma_\omega v_t) \nabla \omega] \end{aligned} \quad (69)$$

One needs to further break down the convection terms, turbulent shear stress terms τ_{ij}^* , velocity gradients, ∇k and $\nabla \omega$ in cylindrical form. The gradient of velocity field [205]:

$$\nabla \mathbf{W} = \begin{bmatrix} \frac{\partial w_r}{\partial r} & \frac{1}{r} \left(\frac{\partial w_r}{\partial \theta} - w_\theta \right) & \frac{\partial w_r}{\partial z} \\ \frac{\partial w_\theta}{\partial r} & \frac{1}{r} \left(\frac{\partial w_\theta}{\partial \theta} + w_r \right) & \frac{\partial w_\theta}{\partial z} \\ \frac{\partial w_z}{\partial r} & \frac{1}{r} \frac{\partial w_z}{\partial \theta} & \frac{\partial w_z}{\partial z} \end{bmatrix} \quad (70)$$

with the strain rate tensor and stress tensor [198, 205]:

$$\begin{aligned} \tau_{ij}^* &= 2\nu_t \bar{S}_{ij} - \frac{2}{3} k \delta_{ij} = \nu_t (\nabla \mathbf{W} + \nabla \mathbf{W}^T) - \frac{2}{3} k \mathbf{I} \\ &= \nu_t \begin{bmatrix} 2 \frac{\partial w_r}{\partial r} - \frac{2}{3} \omega & \frac{1}{r} \left(\frac{\partial w_r}{\partial \theta} - w_\theta \right) + \frac{\partial w_\theta}{\partial r} & \frac{\partial w_r}{\partial z} + \frac{\partial w_z}{\partial r} \\ \frac{1}{r} \left(\frac{\partial w_r}{\partial \theta} - w_\theta \right) + \frac{\partial w_\theta}{\partial r} & \frac{2}{r} \left(\frac{\partial w_\theta}{\partial \theta} + w_r \right) - \frac{2}{3} \omega & \frac{\partial w_\theta}{\partial z} + \frac{1}{r} \frac{\partial w_z}{\partial \theta} \\ \frac{\partial w_r}{\partial z} + \frac{\partial w_z}{\partial r} & \frac{\partial w_\theta}{\partial z} + \frac{1}{r} \frac{\partial w_z}{\partial \theta} & 2 \frac{\partial w_z}{\partial z} - \frac{2}{3} \omega \end{bmatrix} \end{aligned} \quad (71)$$

Convection terms [205] operating on a vector field \overline{Wk} and $\overline{W\omega}$:

$$\nabla \cdot (Wk) = \frac{\partial (w_r k)}{\partial r} + \frac{w_r k}{r} + \frac{1}{r} \frac{\partial (w_\theta k)}{\partial \theta} + \frac{\partial (w_z k)}{\partial z} \quad (72)$$

$$\nabla \cdot (W\omega) = \frac{\partial (w_r \omega)}{\partial r} + \frac{w_r \omega}{r} + \frac{1}{r} \frac{\partial (w_\theta \omega)}{\partial \theta} + \frac{\partial (w_z \omega)}{\partial z} \quad (73)$$

and finally the gradients of k and ω [205]:

$$\nabla k = \frac{\partial k}{\partial r} \hat{e}_r + \frac{1}{r} \frac{\partial k}{\partial \theta} \hat{e}_\theta + \frac{\partial k}{\partial z} \hat{e}_z \quad (74)$$

$$\nabla \omega = \frac{\partial \omega}{\partial r} \hat{e}_r + \frac{1}{r} \frac{\partial \omega}{\partial \theta} \hat{e}_\theta + \frac{\partial \omega}{\partial z} \hat{e}_z \quad (75)$$

Knowing these terms, the turbulence kinetic energy and specific dissipation rate in conservative form and 3D cylindrical coordinate will assume the following form:

Turbulence Specific Kinetic Energy Equation,

$$\begin{aligned} \frac{\partial k}{\partial t} + \frac{\partial(w_r k)}{\partial r} + \frac{w_r k}{r} + \frac{1}{r} \frac{\partial(w_\theta k)}{\partial \theta} + \frac{\partial(w_z k)}{\partial z} \\ = P_k - \beta^* k \omega + \frac{\partial \tau_{kr}}{\partial r} + \frac{\tau_{kr}}{r} + \frac{1}{r} \frac{\partial \tau_{k\theta}}{\partial \theta} + \frac{\partial \tau_{kz}}{\partial z} \end{aligned} \quad (76)$$

Turbulence Specific Dissipation Rate Equation,

$$\begin{aligned} \frac{\partial \omega}{\partial t} + \frac{\partial(w_r \omega)}{\partial r} + \frac{w_r \omega}{r} + \frac{1}{r} \frac{\partial(w_\theta \omega)}{\partial \theta} + \frac{\partial(w_z \omega)}{\partial z} \\ = \gamma_1 P_\omega - \beta \omega^2 + \frac{\partial \tau_{\omega r}}{\partial r} + \frac{\tau_{\omega r}}{r} + \frac{1}{r} \frac{\partial \tau_{\omega \theta}}{\partial \theta} + \frac{\partial \tau_{\omega z}}{\partial z} \end{aligned} \quad (77)$$

where P_k and P_ω denote the turbulence production terms [120]:

$$P_\omega = \frac{\omega}{k} P_k \quad (78)$$

$$\begin{aligned} P_k = \nu_t \left\{ 2 \left[\left(\frac{\partial w_r}{\partial r} \right)^2 + \left(\frac{1}{r} \frac{\partial w_\theta}{\partial \theta} + \frac{w_r}{r} \right)^2 + \left(\frac{\partial w_z}{\partial z} \right)^2 \right] \right. \\ \left. + \left(\frac{\partial w_\theta}{\partial r} - \frac{w_\theta}{r} + \frac{1}{r} \frac{\partial w_r}{\partial \theta} \right)^2 + \left(\frac{\partial w_r}{\partial z} + \frac{\partial w_z}{\partial r} \right)^2 \right. \\ \left. + \left(\frac{\partial w_\theta}{\partial z} + \frac{1}{r} \frac{\partial w_z}{\partial \theta} \right)^2 \right\} \end{aligned} \quad (79)$$

and turbulence diffusion terms are defined as:

$$\begin{aligned}
\tau_{kr} &= (\nu + \sigma_k \nu_t) \frac{\partial k}{\partial r}, & \tau_{k\theta} &= \frac{1}{r} (\nu + \sigma_k \nu_t) \frac{\partial k}{\partial \theta} \\
\tau_{kz} &= (\nu + \sigma_k \nu_t) \frac{\partial k}{\partial z}, & \tau_{\omega r} &= (\nu + \sigma_\omega \nu_t) \frac{\partial \omega}{\partial r} \\
\tau_{\omega\theta} &= \frac{1}{r} (\nu + \sigma_\omega \nu_t) \frac{\partial \omega}{\partial \theta}, & \tau_{\omega z} &= (\nu + \sigma_\omega \nu_t) \frac{\partial \omega}{\partial z}
\end{aligned} \tag{80}$$

The rotating frame does not appear as a derived term in turbulence model equations, the way that is conventional in momentum equations. This is due to empirical nature of turbulence models. There are several publications (mostly for k - ϵ model) that consider rotation effect as a multiplier in production term [206, 207]. Yet, the results are not affected much by including this factor. Hence, the model equations will be used without any modification.

5.2.3.2. Menter's BSL

The case of interest in this work (seals) possesses swirling streamlines, and turbulent boundary layers at several locations of geometry are not fully-developed (inlet plenum, outlet chamber, or early stages of flow development inside the seal). For these cases, Wilcox k - ω model should be improved by adding some extra terms. Also the classical Wilcox model is sensitive to free-stream values of ω which will cause difficulties in convergence of developing flows with unknown inlet BCs. The Baseline (BSL) model developed by Menter [208] uses a blending function to gradually evolve k - ω to k - ϵ in regions far from the wall. Later this model can be upgraded to Menter's

Shear Stress Transport (SST) [188] by adding the shear stress transport term. The BSL model is described with following equations:

Turbulence kinetic energy

$$\begin{aligned} \frac{\partial k}{\partial t} + \frac{\partial U_j k}{\partial x_j} = & \nu_t \frac{\partial U_i}{\partial x_j} \left(\frac{\partial U_i}{\partial x_j} + \frac{\partial U_j}{\partial x_i} \right) - \frac{2}{3} k \delta_{ij} \frac{\partial U_i}{\partial x_j} - \beta^* k \omega \\ & + \frac{\partial}{\partial x_j} \left[(\nu + \sigma_{k3} \nu_t) \frac{\partial k}{\partial x_j} \right] \end{aligned} \quad (81)$$

Turbulence specific dissipation rate

$$\begin{aligned} \frac{\partial \omega}{\partial t} + \frac{\partial U_j \omega}{\partial x_j} = & \hat{\nu}_3 \left[\frac{\partial U_i}{\partial x_j} \left(\frac{\partial U_i}{\partial x_j} + \frac{\partial U_j}{\partial x_i} \right) - \frac{2}{3} \omega \delta_{ij} \frac{\partial U_i}{\partial x_j} \right] - \beta_3 \omega^2 \\ & + \frac{\partial}{\partial x_j} \left[(\nu + \sigma_{\omega 3} \nu_t) \frac{\partial \omega}{\partial x_j} \right] + \frac{2(1 - F_1) \sigma_{\omega 2}}{\omega} \frac{\partial k}{\partial x_j} \frac{\partial \omega}{\partial x_j} \end{aligned} \quad (82)$$

The terms with the Kronecker delta δ_{ij} will disappear for incompressible flow, and the last term in the ω equation is the extra diffusion term that will be activated while moving away from the wall and the $k-\epsilon$ form of equation will dominate. The constants with subscript 3 have to be modified to allow for the blending. The constants will be calculated by applying the blending function F_1 to mix $k-\epsilon$ and $k-\omega$ constants. For an arbitrary quantity ϕ , the blend reads:

$$\phi_3 = F_1 \phi_1 + (1 - F_1) \phi_2 \quad (83)$$

where following constants will be used:

Wilcox [204] constants,

$$\beta_1 = \frac{3}{40}, \quad \beta^* = \frac{9}{100}, \quad \sigma_{k1} = \frac{1}{2}, \quad \sigma_{\omega 1} = \frac{1}{2} \quad (84)$$

$$\hat{\gamma}_1 = \frac{\beta_1}{\beta^*} - \sigma_{\omega 1} \frac{\kappa^2}{\sqrt{\beta^*}}, \quad \kappa = 0.41$$

Jones-Launder [209] constants,

$$\beta_2 = 0.0828, \quad \beta^* = \frac{9}{100}, \quad \sigma_{k2} = 1.0, \quad \sigma_{\omega 2} = 0.856 \quad (85)$$

$$\hat{\gamma}_2 = \frac{\beta_2}{\beta^*} - \sigma_{\omega 2} \frac{\kappa^2}{\sqrt{\beta^*}}, \quad \kappa = 0.41$$

and eddy-viscosity definition remains the same,

$$\nu_t = \frac{k}{\omega} \quad (86)$$

The blending function F_1 should be defined such that it approaches unity far from the wall, and vanishes in the majority of boundary layer which Wilcox model is superior:

$$F_1 = \tanh(\text{arg}g_1^4), \quad \text{arg}g_1 = \max\left(\min\left(\frac{\sqrt{k}}{0.09\omega y}, \frac{0.45\omega}{\zeta}\right); \frac{400\nu}{y^2\omega}\right) \quad (87)$$

where ζ denotes the absolute value of the vorticity (reduces to $\partial U/\partial y$ near the wall), and y is the distance to the nearest wall. The blending function terms are all based on basic physical arguments such as mixing length ratio, etc.

The blending term is adapted to cylindrical formulation:

$$\frac{\partial k}{\partial x_j} \frac{\partial \omega}{\partial x_j} = \frac{\partial k}{\partial x_j} \delta_{ij} \frac{\partial \omega}{\partial x_i} = \nabla k \cdot \nabla \omega \quad (88)$$

and since

$$\nabla k = \left(\frac{\partial k}{\partial r}\right) \hat{e}_r + \left(\frac{1}{r} \frac{\partial k}{\partial \theta}\right) \hat{e}_\theta + \left(\frac{\partial k}{\partial z}\right) \hat{e}_z \quad (89)$$

then

$$\frac{2(1 - F_1)\sigma_{\omega 2}}{\omega} \frac{\partial k}{\partial x_j} \frac{\partial \omega}{\partial x_j} = \frac{2(1 - F_1)\sigma_{\omega 2}}{\omega} \left(\frac{\partial k}{\partial r} \frac{\partial \omega}{\partial r} + \frac{1}{r^2} \frac{\partial k}{\partial \theta} \frac{\partial \omega}{\partial \theta} + \frac{\partial k}{\partial z} \frac{\partial \omega}{\partial z} \right) \quad (90)$$

and the vorticity vector in cylindrical coordinate is calculated from [205]:

$$\begin{aligned} \nabla \times W = & \left(\frac{1}{r} \frac{\partial w_z}{\partial \theta} - \frac{\partial w_\theta}{\partial z} \right) \hat{e}_r + \left(\frac{\partial w_r}{\partial z} - \frac{\partial w_z}{\partial r} \right) \hat{e}_\theta \\ & + \left(\frac{\partial w_\theta}{\partial r} + \frac{w_\theta}{r} - \frac{1}{r} \frac{\partial w_r}{\partial \theta} \right) \hat{e}_z \end{aligned} \quad (91)$$

therefore:

$$\zeta = \sqrt{\left(\frac{1}{r} \frac{\partial w_z}{\partial \theta} - \frac{\partial w_\theta}{\partial z} \right)^2 + \left(\frac{\partial w_r}{\partial z} - \frac{\partial w_z}{\partial r} \right)^2 + \left(\frac{\partial w_\theta}{\partial r} + \frac{w_\theta}{r} - \frac{1}{r} \frac{\partial w_r}{\partial \theta} \right)^2} \quad (92)$$

σ_{k3} and $\sigma_{\omega 3}$ values should be calculated at boundaries for BCs. The code is upgraded to BSL model with a switch function to change from standard k - ω to BSL k - ω . Figure 98 demonstrates how blending function of Baseline model varies from wall to core flow, both for pipe flow and flow inside an annulus at $Re=6000$. Both simulations use wall-functions. The pipe flow curve starts at larger radius since the inner wall is absent in pipe flow. The blending function quickly drops to about zero at both flows while approaching the core flow. This plot clearly shows a large portion of flow switches to

$k-\epsilon$ formulation for better free-stream accuracy. Figure 99 shows the vorticity magnitude predicted for the same flows by BSL model.

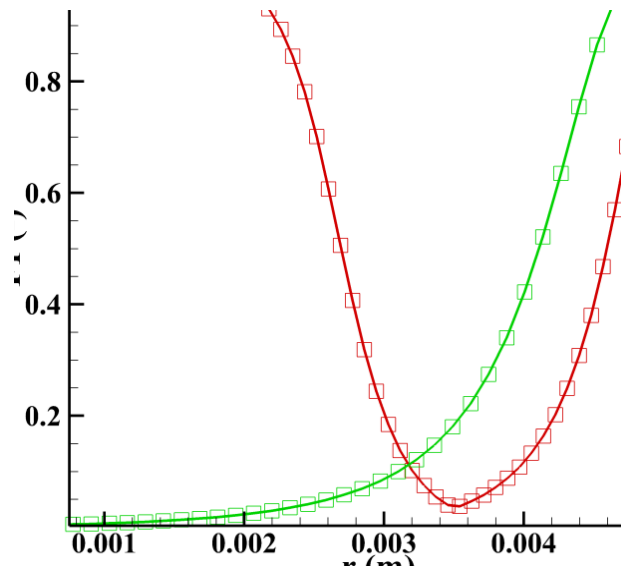


Figure 98. BSL blending function

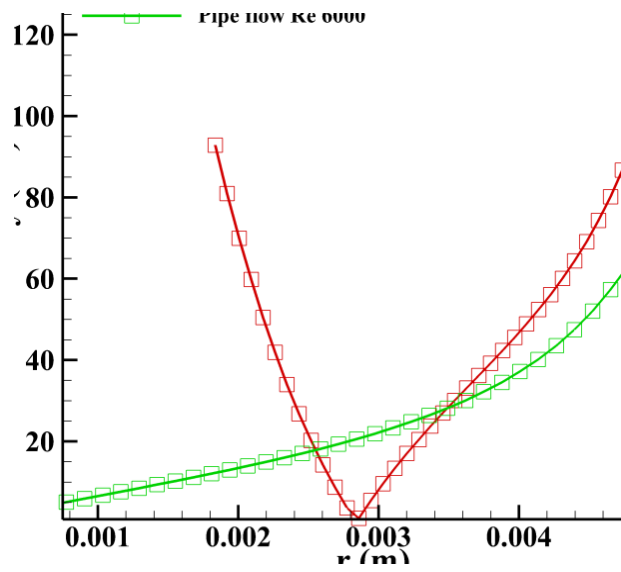


Figure 99. Vorticity magnitude in BSL model

The plot suggests that in annular flow for the same Re number, the vorticity magnitude is greater close to the wall compared with the pipe flow. In this problem, vorticity magnitude presents the velocity gradient and shear rate and thereby explains why friction factors are larger in the annular flow.

5.2.3.3. Menter's SST

Shear Stress Transport (SST) model is basically an upgraded version of BSL model where the eddy viscosity is transported via the shear stress through the domain. This extra physic is modeled with a blending function F_2 . The impact of such migration will be more pronounced in flows with strong pressure gradients, swirling flows and separating flows. Also the $k-\epsilon$ part of the model reduces the model sensitivity to inlet turbulence properties. All the BSL calculations are required for the SST model, except for the inner constants which should be slightly modified.

The impact of this term will be evident in strong positive pressure gradient flows where there is strong vorticity ζ inside the boundary layer. Menter [208] describes how ν_t must be related to vorticity ζ inside the regions of high vorticity and defines the new eddy-viscosity relation:

$$\nu_t = \frac{a_1 k}{\max(a_1 \omega; \zeta F_2)} \quad (93)$$

where $a_1 = 0.3$ is a constant coming from Bradshaw et al. [210] observation that inside boundary layer:

$$\frac{\tau_{xy}}{\rho k} \cong 0.3 \quad (94)$$

and F_2 is a blending function that ensures ν_t will not go to infinity at low vorticity regions $\zeta \rightarrow 0$, instead it reduces to its classic definition:

$$F_2 = \tanh(\text{arg}_2^2), \quad \text{arg}_2 = \max\left(\frac{2\sqrt{k}}{0.09\omega y}; \frac{400\nu}{y^2\omega}\right) \quad (95)$$

The inner constants of SST must be modified a bit because of this subtle change to the eddy-viscosity (inner constant of Wilcox are no more applicable):

$$\beta_1 = \frac{3}{40}, \quad \beta^* = \frac{9}{100}, \quad \sigma_{k1} = 0.85, \quad \sigma_{\omega1} = 0.65 \quad (96)$$

$$\hat{\gamma}_1 = \frac{\beta_1}{\beta^*} - \sigma_{\omega1} \frac{\kappa^2}{\sqrt{\beta^*}}, \quad \kappa = 0.41$$

A Switch parameter SST has been incorporated into the code to change the inner constants for BSL model and activate the modified definition of eddy viscosity at the bulk of fluid and boundaries.

5.2.3.4. Production Limiter

Similar to k - ϵ model, SST produces fictitious turbulence near stagnation and sudden acceleration regions, although much smaller compared to k - ϵ model. For this reason, the production term in two turbulence equations will be limited using following production limiter.

$$\rho P_k = \min\left(\tau_{ij} \frac{\partial w_i}{\partial x_j}, 10\beta^* k\omega\right) \quad (97)$$

5.2.3.5. Wilcox Low-Re version of k - ω

Sometimes the flow Re number is locally low so that transitional effects appear. For instance, the k prediction near the wall shows over prediction in low Re flows. The standard $k-\omega$ is developed for high Re number flows. To account for low Reynolds effects following closure coefficients must be modified [211]:

$$\begin{aligned}\alpha_{LR} &= \alpha_{HR} [Damping\ function], \\ \beta_{LR}^* &= \beta_{HR}^* [Damping\ function]\end{aligned}\tag{98}$$

These damping functions approach unity when Re number is sufficiently large or in the free-stream flow. The modified version of coefficients will be:

$$\begin{aligned}\alpha_{LR} &= \frac{5}{9} \frac{\alpha_0 + \frac{Re_T}{R_\omega}}{1 + \frac{Re_T}{R_\omega}} (\alpha^*)^{-1}, & \beta_{LR}^* &= \frac{9}{100} \frac{\frac{5}{18} + \left(\frac{Re_T}{R_\beta}\right)^4}{1 + \left(\frac{Re_T}{R_\beta}\right)^4} \\ \alpha^* &= \frac{\alpha_0^* + Re_T/R_k}{1 + Re_T/R_k}\end{aligned}\tag{99}$$

$$\beta = 3/40, \quad \sigma^* = 1/2, \quad \sigma = 1/2, \quad \alpha_0^* = \beta/3$$

$$\alpha_0 = 1/10, \quad R_\beta = 8, \quad R_k = 6, \quad R_\omega = 27/10$$

where Re_T is turbulence Reynolds number and shows the ratio of the eddy viscosity to the molecular viscosity which is calculated for each node:

$$Re_T = \frac{k}{\omega \nu}\tag{100}$$

A switch function ‘‘HR2LR’’ has been put in the code to automatically change the coefficients from, the high Re version to low Re version and vice versa. This

modification only affects the dissipation term in k equation, and the production term in ω equation. Hence, the new coefficients only appear in source terms. Thus, the additional implementation and allocation cost is negligible, however, the damping terms lead to a more stiff problem and stricter mesh refinement close to the wall. The low Re version is solved by directly integrating the equations to the wall without a wall-function, therefore it is much more computationally expensive.

5.3. Pseudo-Compressibility Method

In incompressible flows, there is no coupled equation to momentum equations for pressure. In order to create this coupling one can employ Chorin's [212] Artificial Compressibility Method or Pseudo Compressibility Method (PCM) to substitute the gradient of density in the continuity equation with the gradient of pressure. Such that

$$\frac{\partial \rho}{\partial \tau} + \rho \left(\frac{w_r}{r} + \frac{\partial w_r}{\partial r} + \frac{1}{r} \frac{\partial w_\theta}{\partial \theta} + \frac{\partial w_z}{\partial z} \right) = 0 \quad (101)$$

is replaced with

$$\hat{\beta} \frac{\partial p}{\partial \tau} + \rho \left(\frac{w_r}{r} + \frac{\partial w_r}{\partial r} + \frac{1}{r} \frac{\partial w_\theta}{\partial \theta} + \frac{\partial w_z}{\partial z} \right) = 0 \quad (102)$$

here the first term shows the pseudo-time marching term. The pseudo compressibility factor $\hat{\beta}$ is usually selected between 0.1 to 10 [213], but small values correspond to the incompressible flow and larger ones to the compressible flow at limit $\hat{\beta} = \infty$. The pseudo sound speed is found from the relation (for 1D flow):

$$\lambda = u \pm \sqrt{u^2 + 1/\hat{\beta}} \quad (103)$$

Therefore small $\hat{\beta}$ refers to large sound speed and incompressible flow. But very small $\hat{\beta}$ does not allow for pseudo-compressibility method to converge fast. A default value of 0.1 is selected which usually works good in terms of stability and convergence rate. However, the value of $\hat{\beta}$ is problem dependent and some cases a larger value is required for the solver stability.

5.4. MacCormack Scheme

Current CFD code uses the Finite Difference Method (FDM) to solve the governing equations. Several discretization schemes have been tested before selecting the final scheme. These include Forward-Time Central-Space (FTCS) method, upwind method and MacCormack (McCk) method[214, 215]. Among these McCk scheme which is an explicit method proved to be the best option for a variety of reasons.

- McCk has second order accuracy in both time and space ($T.E = O(\Delta x^2, \Delta t^2)$) [1].
- It is well developed scheme and there is enough documentation to trouble shoot the code.
- McCk allows for several speed boost strategies such as flux splitting or McCk semi-implicit rapid solver. Also it can be upgraded to implicit version after some modifications [216].
- It is has a good capability of handling shocks and sudden changes in derivatives (nonlinearities) due to its predictor corrector nature.
- The explicit formulation makes the debugging easier.
- The computational molecules are small which results in faster performance.

- The h-ellipticity factor is large which suits multigrid engines. This will be discussed later in more detail.
- The explicit formulation suits parallel computation.
- The predictor corrector nature of the code removes the need for a staggered grid. The collocated grid will be used with McCk without the checker board effect and without the need for artificial viscosity to damp the pressure fluctuations. For example for the FTCS method one needs to use artificial viscosity [217] and a staggered grid to remove the checker board effect. The staggered grid has the special arrangement of boomerang cells shown in Figure 100, the size of active arrays is different for u, v and p . In fact, using staggered grid there is no pressure BC on walls [2].

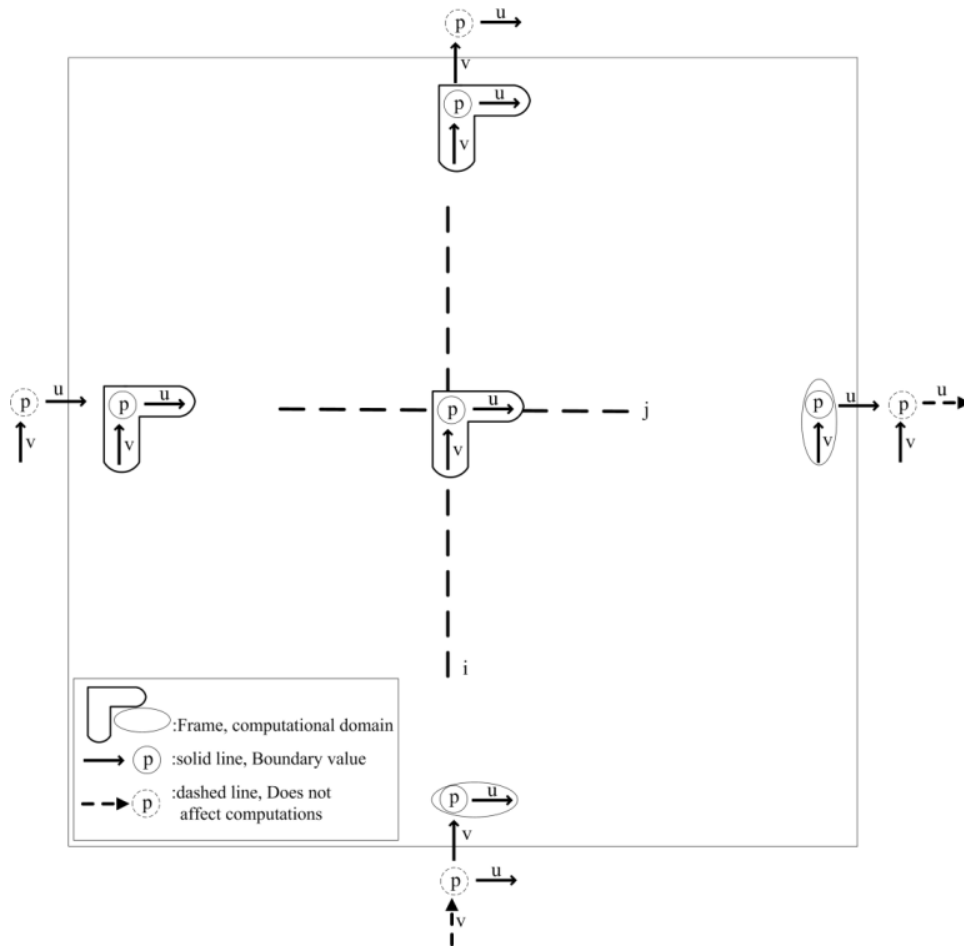


Figure 100. Staggered grid

Especial care should be taken while sweeping for u , v and p in staggered grids. Pressure contour for cavity flow at $Re=1000$ is compared to the case with a collocated grid (Figure 101). Not only the values are different, but also the profile is smoother with the staggered grid and there are no wiggles.

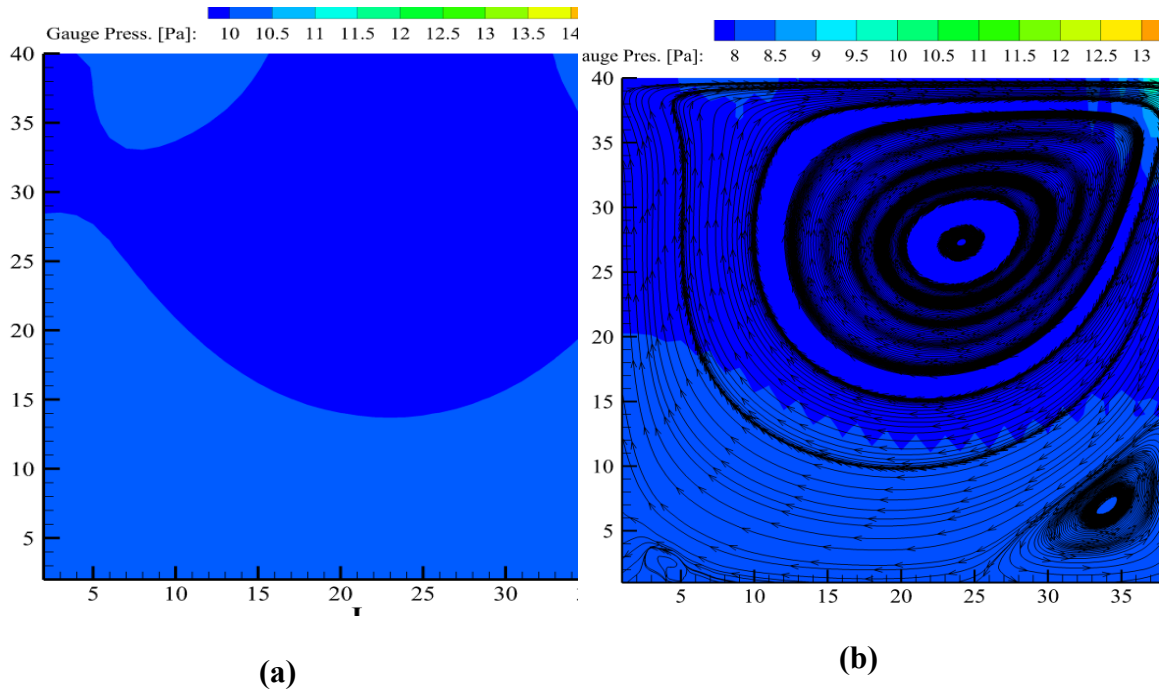


Figure 101. FTCS method (a) Pressure field with staggered grid. (b) Pressure field with collocated grid. I and J shows the node number in x and y directions

5.4.1. 2D Cartesian Version

The details of the scheme for an incompressible isothermal 2D Cartesian case is explained here and later it is applied to the full 3D cylindrical problem. Considering the following conservative form of equations:

$$\frac{\partial \mathbf{U}}{\partial t} + \frac{\partial \mathbf{E}}{\partial x} + \frac{\partial \mathbf{F}}{\partial y} = 0 \quad (104)$$

where the unknown and flux vectors are given by

$$\mathbf{U} = \begin{bmatrix} p \\ u \\ v \end{bmatrix}, \quad \mathbf{E} = \begin{bmatrix} \frac{\rho u}{\hat{\beta}} \\ u^2 + \frac{p}{\rho} - \frac{\tau_{xx}}{\rho} \\ uv - \frac{\tau_{xy}}{\rho} \end{bmatrix}, \quad \mathbf{F} = \begin{bmatrix} \frac{\rho v}{\hat{\beta}} \\ uv - \frac{\tau_{xy}}{\rho} \\ v^2 + \frac{p}{\rho} - \frac{\tau_{yy}}{\rho} \end{bmatrix} \quad (105)$$

and the stress terms are expanded as:

$$\tau_{xx} = 2\mu \frac{\partial u}{\partial x}, \quad \tau_{xy} = \mu \left(\frac{\partial u}{\partial y} + \frac{\partial v}{\partial x} \right), \quad \tau_{yy} = 2\mu \frac{\partial v}{\partial y} \quad (106)$$

The McCk method uses a predictor-corrector scheme shown in Eqs. (107) and (108),

Predictor:

$$\mathbf{U}_{i,j}^* = \mathbf{U}_{i,j}^n - \frac{\Delta t}{\Delta x} (\mathbf{E}_{i+1,j}^n - \mathbf{E}_{i,j}^n) - \frac{\Delta t}{\Delta y} (\mathbf{F}_{i,j+1}^n - \mathbf{F}_{i,j}^n) \quad (107)$$

Corrector:

$$\mathbf{U}_{i,j}^{n+1} = \frac{1}{2} \left[(\mathbf{U}_{i,j}^n + \mathbf{U}_{i,j}^*) - \frac{\Delta t}{\Delta x} (\mathbf{E}_{i,j}^* - \mathbf{E}_{i-1,j}^*) - \frac{\Delta t}{\Delta y} (\mathbf{F}_{i,j}^* - \mathbf{F}_{i,j-1}^*) \right] \quad (108)$$

The predictor step finds an intermediate value shown with superscript * and the corrector step uses the previous time-step and the intermediate step results to correct the estimation for the current time-step values. The predictor step is a backward difference, and the corrector step is an average of last step and prediction step minus a backward difference which removes the error due to usage of forward differencing in provisional step. An alternative approach exists that rotates the backward/forwarding differencing between derivatives of $x - y$ momentum at each step to remove any bias from one sided differencing, which is not implemented in the current code.

One thing should be noted before moving forward. The viscous terms in the flux vectors \mathbf{E} and \mathbf{F} in fact contain derivatives in themselves. Such viscous derivatives would be discretized in a special manner. For example the viscous term in $\partial\mathbf{E}/\partial x$ in x direction should be discretized in the opposite direction that was used for \mathbf{E} . While the cross-derivative viscous term in y direction must be discretized centrally in the same term. The same is true about the viscous terms in \mathbf{F} . For example,

$$\mathbf{E}_3 = uv - \frac{\tau_{xy}}{\rho} = uv - v \frac{\partial u}{\partial y} - v \frac{\partial v}{\partial x} \quad (109)$$

In the predictor step, the term $\mathbf{E}_{3_{i,j}}^n$ should be differenced as

$$\mathbf{E}_{3_{i,j}}^n = u_{i,j}^n v_{i,j}^n - v \frac{u_{i,j+1}^n - u_{i,j-1}^n}{2\Delta y} - v \frac{v_{i,j}^n - v_{i-1,j}^n}{\Delta x} \quad (110)$$

Notice that the cross-derivative is discretized as 2nd order central while the stream derivative is discretized as 1st order backward in opposite direction of \mathbf{E}^* which is forward. While in corrector step,

$$\mathbf{E}_{3_{i,j}}^* = u_{i,j}^* v_{i,j}^* - v \frac{u_{i,j+1}^* - u_{i,j-1}^*}{2\Delta y} - v \frac{v_{i+1,j}^* - v_{i,j}^*}{\Delta x} \quad (111)$$

The cross-derivative remains the same and the stream derivative changes to 1st order forward difference. The detailed terms will be:

$$\begin{bmatrix} U_{1\ i,k}^n \\ U_{2\ i,k}^n \\ U_{3\ i,k}^n \end{bmatrix} = \begin{bmatrix} p_{i,k}^n \\ u_{i,k}^n \\ v_{i,k}^n \end{bmatrix} \quad (112)$$

$$\begin{bmatrix} E_{1\ i,k}^n \\ E_{2\ i,k}^n \\ E_{3\ i,k}^n \end{bmatrix} = \begin{bmatrix} \frac{\rho u_{i,k}^n}{\hat{\beta}} \\ u_{i,k}^n u_{i,k}^n + \frac{p_{i,k}^n}{\rho} - 2\nu \frac{u_{i,k}^n - u_{i-1,k}^n}{\Delta x} \\ u_{i,k}^n v_{i,k}^n - \nu \left(\frac{u_{i,k+1}^n - u_{i,k-1}^n}{2\Delta y} + \frac{v_{i,k}^n - v_{i-1,k}^n}{\Delta x} \right) \end{bmatrix} \quad (113)$$

$$\begin{bmatrix} F_{1\ i,k}^n \\ F_{2\ i,k}^n \\ F_{3\ i,k}^n \end{bmatrix} = \begin{bmatrix} \frac{\rho v_{i,k}^n}{\hat{\beta}} \\ u_{i,k}^n v_{i,k}^n - \nu \left(\frac{u_{i,k}^n - u_{i,k-1}^n}{\Delta y} + \frac{v_{i+1,k}^n - v_{i-1,k}^n}{2\Delta x} \right) \\ v_{i,k}^n v_{i,k}^n + \frac{p_{i,k}^n}{\rho} - 2\nu \frac{v_{i,k}^n - v_{i,k-1}^n}{\Delta y} \end{bmatrix} \quad (114)$$

$$\begin{bmatrix} E_{1\ i,k}^* \\ E_{2\ i,k}^* \\ E_{3\ i,k}^* \end{bmatrix} = \begin{bmatrix} \frac{\rho u_{i,k}^*}{\hat{\beta}} \\ u_{i,k}^* u_{i,k}^* + \frac{p_{i,k}^*}{\rho} - 2\nu \frac{u_{i+1,k}^* - u_{i,k}^*}{\Delta x} \\ u_{i,k}^* v_{i,k}^* - \nu \left(\frac{u_{i,k+1}^* - u_{i,k-1}^*}{2\Delta y} + \frac{v_{i+1,k}^* - v_{i,k}^*}{\Delta x} \right) \end{bmatrix} \quad (115)$$

$$\begin{bmatrix} F_{1\ i,k}^* \\ F_{2\ i,k}^* \\ F_{3\ i,k}^* \end{bmatrix} = \begin{bmatrix} \frac{\rho v_{i,k}^*}{\hat{\beta}} \\ u_{i,k}^* v_{i,k}^* - \nu \left(\frac{u_{i,k+1}^* - u_{i,k}^*}{\Delta y} + \frac{v_{i+1,k}^* - v_{i-1,k}^*}{2\Delta x} \right) \\ v_{i,k}^* v_{i,k}^* + \frac{p_{i,k}^*}{\rho} - 2\nu \frac{v_{i,k+1}^* - v_{i,k}^*}{\Delta y} \end{bmatrix} \quad (116)$$

5.4.2. 3D Cylindrical Version

The same approach is adapted to 3D cylindrical coordinate and by including the turbulence models and Reynolds stress terms. The general format of the governing equations is described as:

$$\frac{\partial \mathbf{U}}{\partial t} + \left(\frac{\partial \mathbf{E}}{\partial r} + \frac{\mathbf{E}}{r} \right) + \frac{1}{r} \frac{\partial \mathbf{F}}{\partial \theta} + \frac{\partial \mathbf{G}}{\partial z} + \mathbf{H} = 0 \quad (117)$$

Please note that one should not worry about the expanded production terms that will not assume the classical form of McCk scheme. In fact, these terms act as source term and should be numerically treated similar to the pressure gradient term in laminar flow under vector \mathbf{H} . A spot for energy equation has been saved in all the vectors. Next generations of the code can add energy equation for thermal and compressibility effects by upgrading these vectors.

The flux vectors:

$$\mathbf{U} = \begin{bmatrix} p \\ w_r \\ w_\theta \\ w_z \\ \dots \text{energy} \dots \\ k \\ \omega \end{bmatrix} \quad (118)$$

$$\mathbf{E} = \begin{bmatrix} \frac{\rho w_r}{\hat{\beta}} \\ w_r w_r - \tau_{rr} \\ w_r w_\theta - \tau_{r\theta} \\ w_r w_z - \tau_{rz} \\ \dots \text{energy} \dots \\ w_r k - \tau_{kr} \\ w_r \omega - \tau_{\omega r} \end{bmatrix} \quad (119)$$

$$\mathbf{F} = \begin{bmatrix} \frac{\rho w_\theta}{\hat{\beta}} \\ w_\theta w_r - \tau_{\theta r} \\ w_\theta w_\theta - \tau_{\theta\theta} \\ w_\theta w_z - \tau_{\theta z} \\ \dots \text{energy} \dots \\ w_\theta k - \tau_{k\theta} \\ w_\theta \omega - \tau_{\omega\theta} \end{bmatrix} \quad (120)$$

$$\mathbf{G} = \begin{bmatrix} \frac{\rho w_z}{\hat{\beta}} \\ w_z w_r - \tau_{zr} \\ w_z w_\theta - \tau_{z\theta} \\ w_z w_z - \tau_{zz} \\ \dots \text{energy} \dots \\ w_z k - \tau_{kz} \\ w_z \omega - \tau_{\omega z} \end{bmatrix} \quad (121)$$

$$\mathbf{H} = \begin{bmatrix} 0 \\ \frac{1}{\rho} \frac{\partial p}{\partial r} + \frac{\tau_{\theta\theta}}{r} - \frac{w_\theta^2}{r} + \text{ROT}(-2\omega w_\theta - r\omega^2) \\ \frac{1}{\rho r} \frac{\partial p}{\partial \theta} + \frac{w_r w_\theta}{r} - \frac{\tau_{r\theta}}{r} + \text{ROT}(2\omega w_r) \\ \frac{1}{\rho} \frac{\partial p}{\partial z} \\ \dots \text{energy} \dots \\ -P_k + \beta^* k \omega \\ -\hat{\gamma} \frac{\omega}{k} P_k + \beta \omega^2 \end{bmatrix} \quad (122)$$

or in expanded form:

$$\mathbf{U} = \begin{bmatrix} p \\ w_r \\ w_\theta \\ w_z \\ \text{energy} \\ k \\ \omega \end{bmatrix} \quad (123)$$

$$\mathbf{E} = \left[\begin{array}{c} \frac{\rho w_r}{\hat{\beta}} \\ w_r w_r - 2(\nu + \nu_t) \left(\frac{\partial w_r}{\partial r} \right) + \frac{2}{3} k \\ w_r w_\theta - (\nu + \nu_t) \left(\frac{\partial w_\theta}{\partial r} - \frac{w_\theta}{r} + \frac{1}{r} \frac{\partial w_r}{\partial \theta} \right) \\ w_r w_z - (\nu + \nu_t) \left(\frac{\partial w_r}{\partial z} + \frac{\partial w_z}{\partial r} \right) \\ \dots \text{energy} \dots \\ w_r k - (\nu + \sigma_k \nu_t) \frac{\partial k}{\partial r} \\ w_r \omega - (\nu + \sigma_\omega \nu_t) \frac{\partial \omega}{\partial r} \end{array} \right] \quad (124)$$

$$\mathbf{F} = \left[\begin{array}{c} \frac{\rho w_\theta}{\hat{\beta}} \\ w_\theta w_r - (\nu + \nu_t) \left(\frac{\partial w_\theta}{\partial r} - \frac{w_\theta}{r} + \frac{1}{r} \frac{\partial w_r}{\partial \theta} \right) \\ w_\theta w_\theta - 2(\nu + \nu_t) \left(\frac{1}{r} \frac{\partial w_\theta}{\partial \theta} + \frac{w_r}{r} \right) + \frac{2}{3} k \\ w_\theta w_z - (\nu + \nu_t) \left(\frac{\partial w_\theta}{\partial z} + \frac{1}{r} \frac{\partial w_z}{\partial \theta} \right) \\ \dots \text{energy} \dots \\ w_\theta k - \frac{1}{r} (\nu + \sigma_k \nu_t) \frac{\partial k}{\partial \theta} \\ w_\theta \omega - \frac{1}{r} (\nu + \sigma_\omega \nu_t) \frac{\partial \omega}{\partial \theta} \end{array} \right] \quad (125)$$

$$\mathbf{G} = \begin{bmatrix} \frac{\rho w_z}{\hat{\beta}} \\ w_z w_r - (\nu + \nu_t) \left(\frac{\partial w_r}{\partial z} + \frac{\partial w_z}{\partial r} \right) \\ w_z w_\theta - (\nu + \nu_t) \left(\frac{\partial w_\theta}{\partial z} + \frac{1}{r} \frac{\partial w_z}{\partial \theta} \right) \\ w_z w_z - 2(\nu + \nu_t) \left(\frac{\partial w_z}{\partial z} \right) + \frac{2}{3} k \\ \dots \text{energy} \dots \\ w_z k - (\nu + \sigma_k \nu_t) \frac{\partial k}{\partial z} \\ w_z \omega - (\nu + \sigma_\omega \nu_t) \frac{\partial \omega}{\partial z} \end{bmatrix} \quad (126)$$

H

$$= \begin{bmatrix} 0 \\ \frac{1}{\rho} \frac{\partial p}{\partial r} + 2(\nu + \nu_t) \left(\frac{1}{r^2} \frac{\partial w_\theta}{\partial \theta} + \frac{w_r}{r^2} \right) - \frac{2}{3} \frac{k}{r} - \frac{w_\theta^2}{r} + \text{ROT}(-2\omega w_\theta - r\omega^2) \\ \frac{1}{\rho r} \frac{\partial p}{\partial \theta} + \frac{w_r w_\theta}{r} - (\nu + \nu_t) \left(\frac{1}{r} \frac{\partial w_\theta}{\partial r} - \frac{w_\theta}{r^2} + \frac{1}{r^2} \frac{\partial w_r}{\partial \theta} \right) + \text{ROT}(2\omega w_r) \\ \frac{1}{\rho} \frac{\partial p}{\partial z} \\ \dots \text{energy} \dots \\ -P_k + \beta^* k \omega \\ -\hat{\gamma}_1 \frac{\omega}{k} P_k + \beta \omega^2 \end{bmatrix} \quad (127)$$

Production term P_k is defined as:

$$\begin{aligned} P_k = \nu_t \left\{ 2 \left[\left(\frac{\partial w_r}{\partial r} \right)^2 + \left(\frac{1}{r} \frac{\partial w_\theta}{\partial \theta} + \frac{w_r}{r} \right)^2 + \left(\frac{\partial w_z}{\partial z} \right)^2 \right] \right. \\ \left. + \left(\frac{\partial w_\theta}{\partial r} - \frac{w_\theta}{r} + \frac{1}{r} \frac{\partial w_r}{\partial \theta} \right)^2 + \left(\frac{\partial w_r}{\partial z} + \frac{\partial w_z}{\partial r} \right)^2 \right. \\ \left. + \left(\frac{\partial w_\theta}{\partial z} + \frac{1}{r} \frac{\partial w_z}{\partial \theta} \right)^2 \right\} \quad (128) \end{aligned}$$

Introduction of rotating frame terms to the code brings new source terms to the play. As an attempt to stabilize the code against these new source terms, an under-relaxation scheme has been implemented in accordance with Patankar's recommendation [218].

$$\mathbb{S} = \alpha \mathbb{S}^m + (1 - \alpha) \mathbb{S}^{m-1} \quad (129)$$

where \mathbb{S} is the source term which in current application refers to centrifugal and Coriolis terms in \mathbf{H} vector, and α is the under-relaxation parameter. This approach reduces large gradients in source terms and helps to linearization approximations which ensure stability. Applying the explicit non-uniform corrector-predictor McCk scheme, one gets the following provisional and final steps:

Predictor:

$$\begin{aligned} \mathbf{U}_{i,j,k}^* = \mathbf{U}_{i,j,k}^n &- \frac{\Delta t}{\Delta r_{i+1}} (\mathbf{E}_{i+1,j,k}^n - \mathbf{E}_{i,j,k}^n) - \frac{\Delta t}{r_i} (\mathbf{E}_{i,j,k}^n) \\ &- \frac{\Delta t}{r_i \Delta \theta_{j+1}} (\mathbf{F}_{i,j+1,k}^n - \mathbf{F}_{i,j,k}^n) - \frac{\Delta t}{\Delta z_{k+1}} (\mathbf{G}_{i,j,k+1}^n - \mathbf{G}_{i,j,k}^n) \\ &- \Delta t (\mathbf{H}_{i,j,k}^n) \end{aligned} \quad (130)$$

Corrector:

$$\begin{aligned} \mathbf{U}_{i,j,k}^{n+1} = \frac{1}{2} \left[(\mathbf{U}_{i,j,k}^n + \mathbf{U}_{i,j,k}^*) &- \frac{\Delta t}{\Delta r_i} (\mathbf{E}_{i,j,k}^* - \mathbf{E}_{i-1,j,k}^*) - \frac{\Delta t}{r_i} (\mathbf{E}_{i,j,k}^*) \right. \\ &- \frac{\Delta t}{r_i \Delta \theta_j} (\mathbf{F}_{i,j,k}^* - \mathbf{F}_{i,j-1,k}^*) - \frac{\Delta t}{\Delta z_k} (\mathbf{G}_{i,j,k}^* - \mathbf{G}_{i,j,k-1}^*) \\ &\left. - \Delta t (\mathbf{H}_{i,j,k}^*) \right] \end{aligned} \quad (131)$$

The detailed non-uniform discretized terms in turbulent mode are given in Appendix D.

5.5. SIMPLE Method

The laminar version of the code is also able to operate with a pressure-based solver coupling which matches well with a linear Multigrid scheme instead of the complicated nonlinear Multigrid. The family of Semi-Implicit Pressure Linked Equations (SIMPLE) techniques started in Imperial College by Caretto, Patankar and Spalding [218-220] has been selected as the pressure based solver. Furthermore, because of the McCk scheme, there is no need to use a staggered grid or artificial viscosity in the SIMPLE algorithm which suggests the two algorithms go well together.

This approach breaks the velocity and pressure field into guess \mathbf{U}_0 and correction values \mathbf{U}' :

$$\begin{aligned}\mathbf{U} &= \mathbf{U}_0 + \mathbf{U}' \\ p &= p_0 + p'\end{aligned}\tag{132}$$

where the subscript 0 shows the guess values, the primed values denote the corrections and \mathbf{U} is the divergent free corrected velocity (the same unknown vector as before). The momentum equations should be solved as the first step:

$$\mathbf{U}_{0t} + \mathbf{U}^m \cdot \nabla \mathbf{U}^m = -\frac{1}{\rho} \nabla p^m + \nu \Delta \mathbf{U}^m\tag{133}$$

Here superscript m shows the iteration value. The step was originally solved implicit but McCk is an explicit scheme and here an explicit solution is sought. The equation has the basic format of full NS, therefore, one can use the previously developed McCk to

obtain \mathbf{U}_0 without any change of algorithm. The BCs remain the same. Next, Pressure Poisson Equation (PPE) should be solved:

$$\Delta p' = \frac{\rho}{\Delta t} \nabla \cdot \mathbf{U}_0 \quad (134)$$

The RHS is already available from last step, including the boundary points. Note that $\frac{\nabla \cdot \mathbf{U}_0}{\Delta t} = \frac{1}{\rho A} \frac{\partial \dot{m}}{\partial x_i}$ is nothing other than the specific mass flow source at the computational node. In Patankar [218] notation the mass flow is calculated at the cell faces because he uses FVM and the whole mass flow notation makes sense for the entire CV, while current notation uses velocity divergence because current code is based on FDM. The LHS will be discretized using central difference. Since the equation is fully elliptic it is solved using Gauss-Seidel (GS) method. For example in 2D:

$$p'_{i,k} = \frac{\Delta y^2}{2(\Delta x^2 + \Delta y^2)} (p'_{i+1,k} + p'_{i-1,k}) + \frac{\Delta x^2}{2(\Delta x^2 + \Delta y^2)} (p'_{i,k+1} + p'_{i,k-1}) - \frac{\rho \Delta x^2 \Delta y^2}{2\Delta t (\Delta x^2 + \Delta y^2)} \left(\frac{u_{0\ i+1,k} - u_{0\ i-1,k}}{2\Delta x} + \frac{v_{0\ i,k+1} - v_{0\ i,k-1}}{2\Delta y} \right) \quad (135)$$

Since the last term on RHS will not change during GS iterations, it is called $Div_{i,k}$,

$$p'_{i,k} = \frac{\Delta y^2}{2(\Delta x^2 + \Delta y^2)} (p'_{i+1,k} + p'_{i-1,k}) + \frac{\Delta x^2}{2(\Delta x^2 + \Delta y^2)} (p'_{i,k+1} + p'_{i,k-1}) + Div_{i,k} \quad (136)$$

Solving this step can be accelerated by Multigrid. BCs are needed for p' . Rhie and Chow [221] remark that the BC for p' will be $p'_n = 0$ at all boundaries. This BC works well with the update step:

$$\mathbf{U}^{m+1} = \mathbf{U}_0 - \frac{\Delta t}{\rho} \nabla p' \quad (137)$$

If $\nabla p'_{BC} = 0$ then

$$\mathbf{U}_{BC}^{m+1} = \mathbf{U}_{0 BC} \quad (138)$$

which is reasonable, since the provisional velocity field upon convergence is the same as corrected velocity and they should have the same BC. What is more, from the corrected momentum equation:

$$(\mathbf{U}_0 + \mathbf{U}')_t + \mathbf{U}^m \cdot \nabla \mathbf{U}^m = -\frac{1}{\rho} \nabla(p_0 + p') + \nu \Delta \mathbf{U}^m \quad (139)$$

at the walls:

$$\nabla(p_{0 BC} + p'_{BC}) = \mu \Delta \mathbf{U}_{BC}^m \quad (140)$$

in addition to the condition that $p_0 = p^m$, and therefore,

$$\nabla p_{0 BC} = \mu \Delta \mathbf{U}_{BC}^m \quad (141)$$

and,

$$\nabla p'_{BC} = 0 \quad (142)$$

After the pressure correction is found, the velocity and pressure must be updated:

$$\mathbf{U}^{m+1} = \mathbf{U}_0 - \frac{\Delta t}{\rho} \nabla p' \quad (143)$$

$$p^{m+1} = p^m + p'$$

In discretized form:

$$\begin{aligned}
u_{i,k}^{m+1} &= u_{0\ i,k} - \frac{\Delta t}{\rho} \frac{p'_{i+1,k} - p'_{i-1,k}}{2\Delta x} \\
v_{i,k}^{m+1} &= v_{0\ i,k} - \frac{\Delta t}{\rho} \frac{p'_{i,k+1} - p'_{i,k-1}}{2\Delta y} \\
p_{i,k}^{m+1} &= p_{i,k}^m + p'_{i,k}
\end{aligned} \tag{144}$$

The BCs for \mathbf{U}_0 and p' are already provided. There is no need to calculate the $m + 1$ values at boundaries, because at the next step these boundary values will be calculated from the interior points again which will override the old BCs.

5.6. Stability

Since an explicit scheme is being used, the maximum allowable time step is ruled by the stability criteria. Three linear constraints need to be met: the diffusion stability condition, the advection stability condition and the mesh Re number stability condition which appears for schemes with central differencing. The two turbulence model equations have similar forms to the energy equation with dissipation, source and sink terms. A safety factor of 0.1 is selected. This safety factor must be multiplied because first of all the stability criteria used here correspond to linear forms but some of the terms in the equations are actually nonlinear. Second, there are source terms in the equations that may require under-relaxation.

The linear advection stability criterion:

$$\Delta t_1 = CFL_1 * \min\left(\frac{\Delta r}{w_r}, \frac{r\Delta\theta}{w_\theta}, \frac{\Delta z}{w_z}\right), \quad CFL_1 \leq 1 \tag{145}$$

The first stability criteria should not change. Basically, the mesh size is divided by the convection speed. The convective mechanism is still the velocity vectors, so the classic wave equation stability says:

$$\frac{\partial u}{\partial t} + C \frac{\partial u}{\partial x} = 0 \rightarrow \Delta t \leq CFL_1 \frac{\Delta x}{C} \quad (146)$$

Since there are three velocity vectors, each equation of motion needs three of the aforementioned conditions.

The linear diffusion stability:

$$\Delta t_2 = CFL_2 * \min \left(\frac{\Delta r^2}{\nu + \nu_t}, \frac{r^2 \Delta \theta^2}{\nu + \nu_t}, \frac{\Delta z^2}{\nu + \nu_t}, \frac{\Delta r^2}{\nu + \sigma_k \nu_t}, \frac{\Delta r^2}{\nu + \sigma_\omega \nu_t}, \frac{r \Delta \theta^2}{\nu + \sigma_k \nu_t}, \frac{r \Delta \theta^2}{\nu + \sigma_\omega \nu_t}, \frac{\Delta z^2}{\nu + \sigma_k \nu_t}, \frac{\Delta z^2}{\nu + \sigma_\omega \nu_t} \right), \quad (147)$$

$$CFL_2 \leq 0.5$$

6 terms have been added for the new diffusion terms in turbulence models. One can reduce these nine terms to three terms since:

$$\nu + \nu_t > (\nu + \sigma_\omega \nu_t = \nu + \sigma_k \nu_t) ; \sigma_k = \sigma_{k1} = \frac{1}{2} ; \sigma_\omega = \sigma_{\omega 1} = \frac{1}{2} \quad (148)$$

Assuming that $\nu + \nu_t > 0$ everywhere. Therefore, it is sufficient to only keep the momentum diffusion terms:

$$\Delta t_2 = CFL_2 * \min \left(\frac{\Delta r^2}{\nu + \nu_t}, \frac{r^2 \Delta \theta^2}{\nu + \nu_t}, \frac{\Delta z^2}{\nu + \nu_t} \right), \quad CFL_2 \leq 0.5 \quad (149)$$

The mesh Reynolds number or the convection to diffusion stability criterion:

$$\Delta t_3 = \min \left(\frac{2(\nu + \nu_t)}{w_r^2}, \frac{2(\nu + \nu_t)}{w_\theta^2}, \frac{2(\nu + \nu_t)}{w_z^2}, \frac{2(\nu + \sigma_k \nu_t)}{w_r^2}, \frac{2(\nu + \sigma_\omega \nu_t)}{w_r^2}, \frac{2(\nu + \sigma_k \nu_t)}{w_\theta^2}, \frac{2(\nu + \sigma_\omega \nu_t)}{w_\theta^2}, \frac{2(\nu + \sigma_k \nu_t)}{w_z^2}, \frac{2(\nu + \sigma_\omega \nu_t)}{w_z^2} \right) \quad (150)$$

This time the viscosity appears in the numerator:

$$(\nu + \sigma_\omega \nu_t = \nu + \sigma_k \nu_t) < \nu + \nu_t ; \quad \sigma_k = \sigma_{k1} = \frac{1}{2} ; \quad \sigma_\omega = \sigma_{\omega 1} = \frac{1}{2} \quad (151)$$

And the nine terms reduce to three terms:

$$\Delta t_3 = \min \left(\frac{2(\nu + \sigma_k \nu_t)}{w_r^2}, \frac{2(\nu + \sigma_k \nu_t)}{w_\theta^2}, \frac{2(\nu + \sigma_k \nu_t)}{w_z^2} \right) \quad (152)$$

And the final time step is selected as:

$$\Delta t = \mathbf{0.1} \min(\Delta t_1, \Delta t_2, \Delta t_3) \quad (153)$$

5.7. Non-uniform Discretization

A uniform grid typically leads to inefficient and lengthy solution. This slow convergence affects debugging procedure adversely. Therefore, the grid should be set up in non-uniform distribution to reduce convergence time. Most notably, a non-uniform grid in 3D version of the code can reduce the computational cost by 100 times.

5.7.1. Bulk of Fluid

In McCk scheme one needs forward, central, and backward difference approximations to first derivatives. All the second derivatives disappear when using McCk scheme and there is no worry about them unless in case of boundary conditions which will be discussed later. Forward difference first derivative of variable ϕ with the special spacing Δx reads:

$$\left(\frac{\partial\phi}{\partial x}\right)_i = \frac{\phi_{i+1} - \phi_i}{\Delta x_{i+1}} \quad (154)$$

Backward difference first derivative:

$$\left(\frac{\partial\phi}{\partial x}\right)_i = \frac{\phi_i - \phi_{i-1}}{\Delta x_i} \quad (155)$$

Central difference first derivative (second order):

$$\left(\frac{\partial\phi}{\partial x}\right)_i = \frac{\phi_{i+1} - \phi_{i-1}}{\Delta x_{i+1} + \Delta x_i} \quad (156)$$

Define the local spacing as:

$$\begin{cases} \Delta x_i = x_i - x_{i-1} \\ \Delta x_{i+1} = x_{i+1} - x_i \end{cases} \quad (157)$$

The Truncation Error (TE) for the first derivative central difference is calculated as [213]:

$$TE = -\frac{\Delta x_{i+1}^2 - \Delta x_i^2}{2(\Delta x_{i+1} + \Delta x_i)} \left(\frac{\partial^2\phi}{\partial x^2}\right) + O(\Delta x_{i+1}^3, \Delta x_i^3) \quad (158)$$

If uniform grid is adopted, the first term on RHS vanishes and the derivative is truly second order. If non-uniform grid is adopted, the second order term will remain as:

$$TE = -\frac{(1-AR)\Delta x_i}{2} \left(\frac{\partial^2 \phi}{\partial x^2} \right) + O(\Delta x_{i+1}^3, \Delta x_i^3) \quad (159)$$

where $AR = \Delta x_{i+1}/\Delta x_i$ denotes the aspect ratio of adjacent mesh cells. If $AR \leq 1.2$ the multiplier will reduce to 0.1 and the scheme will formally maintain as second order scheme. Therefore, in the non-uniform formula for mesh generation a constraint has been enforced to ensure AR does not exceed 1.2 or be lower than 0.8.

5.7.2. Boundary Conditions

Boundary conditions require second order approximations and since they are located at the sides of the boundary, they need one sided (forward/backward) discretization. Pressure boundary condition requires a second order second derivative of normal component of velocity. Fully developed and constant gradient conditions are stated as second order first derivatives.

Lagrange polynomials l_i are used to find an N order polynomial [222]:

$$\phi = \phi_0 l_0 + \dots + \phi_i l_i + \dots + \phi_N l_N = \sum_{i=0}^N \phi_i l_i \quad (160)$$

$$l_i = \prod_{\substack{m=0 \\ m \neq i}}^N \frac{x - x_m}{x_i - x_m} = \frac{x - x_0}{x_i - x_0} \dots \frac{x - x_{i-1}}{x_i - x_{i-1}} \frac{x - x_{i+1}}{x_i - x_{i+1}} \dots \frac{x - x_N}{x_i - x_N} \quad (161)$$

An N order polynomial can be used for a first derivative with Nth order of accuracy. Therefore, the interest is in 2nd order polynomial (with N+1=3 points) to obtain its first derivative and 3rd order polynomial to obtain its second derivative (with N+1=4 points). For second order polynomial:

$$\phi_i = l_i(x_i)\phi_i + l_{i+1}(x_i)\phi_{i+1} + l_{i+2}(x_i)\phi_{i+2} \quad (162)$$

$$\left(\frac{\partial\phi}{\partial x}\right)_i = l'_i(x_i)\phi_i + l'_{i+1}(x_i)\phi_{i+1} + l'_{i+2}(x_i)\phi_{i+2} \quad (163)$$

here x_i remains fixed because the multipliers l_i are defined about this fixed point. ϕ_i are the known function values which are not function of x . To calculate functions l_i :

$$\begin{cases} l_i = \frac{x - x_{i+1}}{x_i - x_{i+1}} \cdot \frac{x - x_{i+2}}{x_i - x_{i+2}} \\ l_{i+1} = \frac{x - x_i}{x_{i+1} - x_i} \cdot \frac{x - x_{i+2}}{x_{i+1} - x_{i+2}} \\ l_{i+2} = \frac{x - x_i}{x_{i+2} - x_i} \cdot \frac{x - x_{i+1}}{x_{i+2} - x_{i+1}} \end{cases} \quad (164)$$

and the derivatives:

$$\begin{cases} l'_i = \frac{2x - (x_{i+2} + x_{i+1})}{(x_i - x_{i+1})(x_i - x_{i+2})} \\ l'_{i+1} = \frac{2x - (x_{i+2} + x_i)}{(x_{i+1} - x_i)(x_{i+1} - x_{i+2})} \\ l'_{i+2} = \frac{2x - (x_{i+1} + x_i)}{(x_{i+2} - x_i)(x_{i+2} - x_{i+1})} \end{cases} \quad (165)$$

and finally if the original equation is substituted back, from a parabolic polynomial fit one gets a second order forward approximation for the first derivative [223]:

$$\begin{aligned} \left(\frac{\partial\phi}{\partial x}\right)_i &= \frac{-\phi_i[(\Delta x_{i+1} + \Delta x_{i+2})^2 - (\Delta x_{i+1})^2]}{\Delta x_{i+1}\Delta x_{i+2}(\Delta x_{i+1} + \Delta x_{i+2})} \\ &\quad + \frac{\phi_{i+1}(\Delta x_{i+1} + \Delta x_{i+2})^2}{\Delta x_{i+1}\Delta x_{i+2}(\Delta x_{i+1} + \Delta x_{i+2})} \\ &\quad - \frac{\phi_{i+2}(\Delta x_{i+1})^2}{\Delta x_{i+1}\Delta x_{i+2}(\Delta x_{i+1} + \Delta x_{i+2})} \end{aligned} \quad (166)$$

In similar manner the backward derivative is derived as:

$$\begin{aligned} \frac{\partial \phi}{\partial x} \Big|_i &= \frac{\phi_i [(\Delta x_i + \Delta x_{i-1})^2 - (\Delta x_i)^2]}{\Delta x_i \Delta x_{i-1} (\Delta x_i + \Delta x_{i-1})} - \frac{\phi_{i-1} (\Delta x_i + \Delta x_{i-1})^2}{\Delta x_i \Delta x_{i-1} (\Delta x_i + \Delta x_{i-1})} \\ &\quad + \frac{\phi_{i-2} (\Delta x_i)^2}{\Delta x_i \Delta x_{i-1} (\Delta x_i + \Delta x_{i-1})} \end{aligned} \quad (167)$$

Following the same procedure for the second derivatives using cubic polynomials and 4 points, the second order forward second derivative is found as:

$$\begin{aligned} \frac{\partial^2 \phi}{\partial x^2} \Big|_i &= \phi_i \left[\frac{6\Delta x_{i+1} + 4\Delta x_{i+2} + 2\Delta x_{i+3}}{\Delta x_{i+1} (\Delta x_{i+1} + \Delta x_{i+2}) (\Delta x_{i+1} + \Delta x_{i+2} + \Delta x_{i+3})} \right] \\ &\quad - \phi_{i+1} \left[\frac{4(\Delta x_{i+1} + \Delta x_{i+2}) + 2\Delta x_{i+3}}{\Delta x_{i+1} \Delta x_{i+2} (\Delta x_{i+2} + \Delta x_{i+3})} \right] \\ &\quad + \phi_{i+2} \left[\frac{4\Delta x_{i+1} + 2(\Delta x_{i+2} + \Delta x_{i+3})}{\Delta x_{i+2} \Delta x_{i+3} (\Delta x_{i+1} + \Delta x_{i+2})} \right] \\ &\quad - \phi_{i+3} \left[\frac{4\Delta x_{i+1} + 2\Delta x_{i+2}}{\Delta x_{i+1} (\Delta x_{i+2} + \Delta x_{i+3}) (\Delta x_{i+1} + \Delta x_{i+2} + \Delta x_{i+3})} \right] \end{aligned} \quad (168)$$

and the backward derivative:

$$\begin{aligned}
\left. \frac{\partial^2 \phi}{\partial x^2} \right)_i &= \phi_i \left[\frac{6\Delta x_i + 4\Delta x_{i-1} + 2\Delta x_{i-2}}{\Delta x_i(\Delta x_i + \Delta x_{i-1})(\Delta x_i + \Delta x_{i-1} + \Delta x_{i-2})} \right] \\
&\quad - \phi_{i-1} \left[\frac{4(\Delta x_i + \Delta x_{i-1}) + 2\Delta x_{i-2}}{\Delta x_i \Delta x_{i-1}(\Delta x_{i-1} + \Delta x_{i-2})} \right] \\
&\quad + \phi_{i-2} \left[\frac{4\Delta x_i + 2(\Delta x_{i-1} + \Delta x_{i-2})}{\Delta x_{i-1} \Delta x_{i-2}(\Delta x_i + \Delta x_{i-1})} \right] \\
&\quad - \phi_{i-3} \left[\frac{4\Delta x_i + 2\Delta x_{i-1}}{\Delta x_{i-2}(\Delta x_{i-1} + \Delta x_{i-2})(\Delta x_i + \Delta x_{i-1} + \Delta x_{i-2})} \right]
\end{aligned} \tag{169}$$

Since these boundary conditions are computed only a few times at each iteration, the additional cost is negligible and polynomial fitting approach is justified. Notice that all the derivatives reduce to the conventional uniform finite difference form when setting $\Delta x_i = \Delta x$.

5.7.3. Algebraic Grid Spacing Formulation

Since a simple annular seal geometry perfectly fits the coordinate system, a linear scalar description of 1D computational domain (r coordinate) will give satisfactory results to construct the domain [224]:

$$r(s) = s(r_{N+2} - r_1) + r_1 \tag{170}$$

where s is called the stretching function. In fact, $r = r(\xi)$ where parameter $\xi \in [0, I]$ with I is a maximum value, and s is a parametric variable defined over a unit space $s \in [0,1]$ to simplify the mapping from computational to real domain. In other words:

$$r = r(s(\xi)) \tag{171}$$

A proper representation of stretching function s has to be determined. For uniform distribution, the following simple parametric relation is available:

$$s = \frac{\xi}{I}, \quad \xi = i - 1, \quad I = N + 1, \quad i = 1, 2, \dots, N + 2 \quad (172)$$

If it is desired to cluster the grid points at only one side of the connector, Vinkur's [225] tangent hyperbolic formulae can be used:

$$s(\xi) = 1 + \frac{\tanh[\varrho(\xi/I - 1)]}{\tanh \varrho} \quad (173)$$

If one is interested in double sided stretching $ss(\xi)$ (useful in pipe flow, and many internal flows):

$$ss(\xi) = \frac{1}{2} \left[1 + \frac{\tanh[\varrho(\xi/I - 1/2)]}{\tanh \varrho/2} \right] \quad (174)$$

where ϱ is the stretching factor. If one increases ϱ the nodes tend to cluster near edges, and reducing ϱ spreads the nodes along the connector. This formulation is simple and only requires one parameter ϱ . It assures that the derivative of stretching function at the wall reduces to the required spacing Δs found from y^+ calculation:

$$\left. \frac{dss}{d\xi} \right|_1 = \Delta s \quad (175)$$

If the spacing on two sides are not equal, $\Delta s_2 \neq \Delta s_1$, then two parameters are defined:

$$s(\xi) = \frac{ss(\xi)}{A + (1 - A)ss(\xi)} \quad (176)$$

$$A = \sqrt{\frac{\Delta s_2}{\Delta s_1}} \quad (177)$$

$$\hat{B} = \frac{1}{I\sqrt{\Delta s_1 \Delta s_2}} \quad (178)$$

Parameter \hat{B} is used to find the stretching factor by solving a transcendental equation:

$$\frac{\sinh \varrho}{\varrho} = \hat{B} \quad (179)$$

This method gives the proper spacing near the wall but does not ensure small aspect ratio to reduce truncation error which should be manageable by increasing number of points.

5.7.3.1. An alternative algebraic method

To control both the spacing of the first node and the aspect ratio AR of the spacing, one can devise following method instead:

$$\Delta r_{i+1} = AR\Delta r_i, \quad AR = 1.1 - 1.2, \quad \Delta r_2 = f(y^+) \quad (180)$$

The total number of nodes in r direction are equal to $N_r + 2$ and N_r is an even number.

Therefore:

$$2 \sum_{i=2}^{(N_r+2)/2} \Delta r_i = R_{out} - R_{in} - \epsilon_\Delta \quad (181)$$

ϵ_Δ is used to control the total length by adjusting the length of the farthest cells from the wall. Hence:

$$\Delta r_2 = \frac{R_{out} - R_{in} - \epsilon_\Delta}{2(1 + AR + \dots + AR^{(N+2)/2-3})} \quad (182)$$

By guessing a suitable value for N_r and using a shooting method it is possible to match Δr_2 to the desired value. After Δr_2 is found, the total length is adjusted by:

$$\Delta r_{\frac{N_r+2}{2}} = \Delta r_{\frac{N_r+2}{2}+1} = AR^{(N+2)/2-3} \Delta r_2 - \frac{\epsilon_\Delta}{2} \quad (183)$$

This way both the spacing and the aspect ratio are controlled. For the opposite wall the mesh must be built up in reverse order:

$$\Delta r_{i+1} = AR \Delta r_{i+2} \rightarrow r_i = r_{i+1} - AR(r_{i+2} - r_{i+1}) \quad (184)$$

5.7.3.2. A hybrid approach

One can mix the latter method with the tangent hyperbolic to take advantage of both methods benefits. It is possible to reduce AR inside the inner layer by using the fixed AR progression and then use the tangent hyperbolic in the middle to connect the two boundary layer meshes to each other. This way, the number of unnecessary points between boundary layers can be reduced.

5.7.3.3. Comparison of algorithms

The uniform distribution is compared to the tangent hyperbolic stretch function and constant Aspect Ratio (AR) distribution. All the grids meet this condition, even the nonuniform grids have a slightly smaller Δs_{wall} to allow for more number of nodes inside the viscous sublayer ($Re = 5000$ Figure 102 compares all three algorithms).

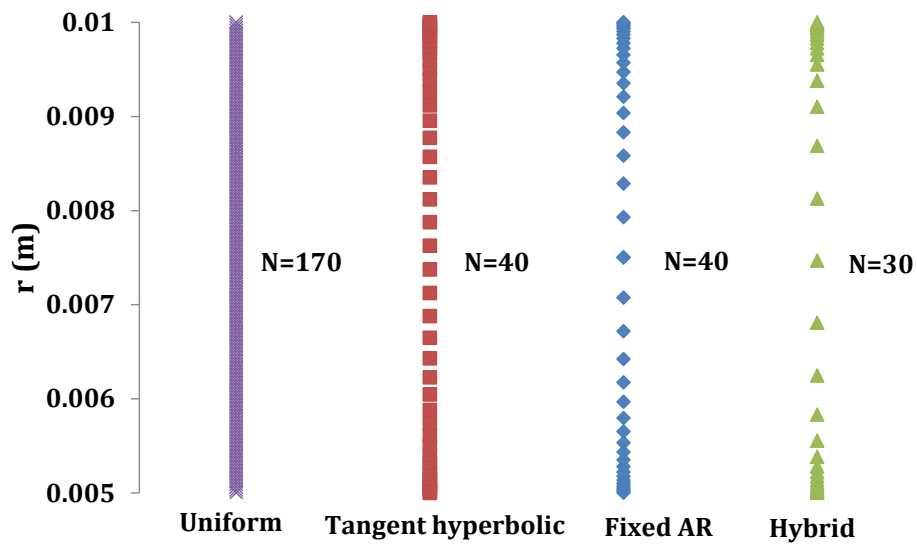


Figure 102. Comparison of on-uniform distribution schemes

The second condition examines the maximum and minimum aspect ratio through the entire length for the sake of discretization order of accuracy. It is shown that AR condition ($0.8 < AR < 1.2$) is met through all grids except the Hybrid method (See Figure 103).

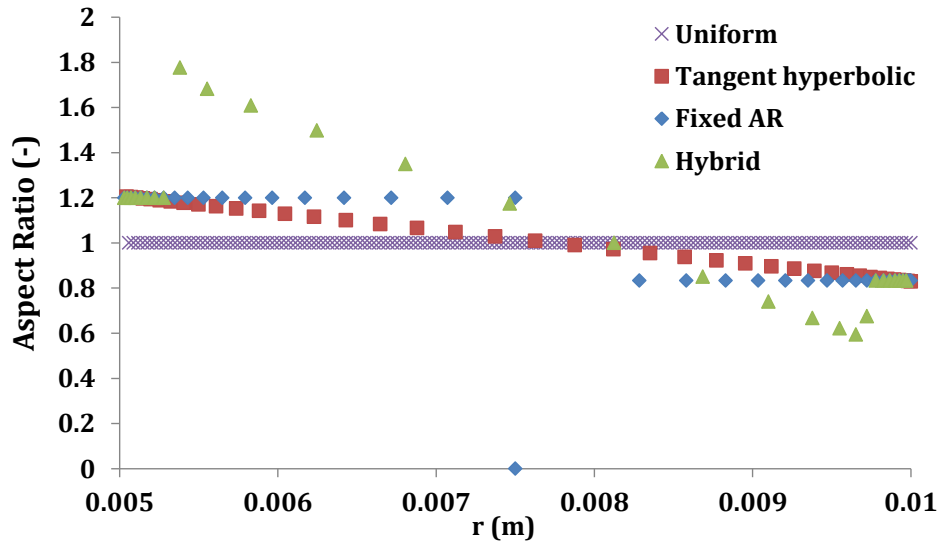


Figure 103. Aspect ratio distribution

A quick inspection of the near wall spacing, grid density and AR suggest that hybrid configuration meets all the conditions with least cost. The uniform grid computational cost is almost 6 times the hybrid version. For pipe flow (instead of annulus flow) this ratio grows even bigger. And this comparison is only done for low Re 1D flow. In 3D wall-bounded flows with large Re numbers, current modification leads to faster computations as much as 200 times compared to the uniform grid. The AR of hybrid method remains in the bound of $0.6 < AR < 1.8$ which only occurs outside the log layer since 10 layers of $AR = 1.2$ mesh inside the viscous sublayer and the log layer have been enforced (where wall shear and friction factor are calculated). Outside the inner layer, the velocity gradients reduce sharply and slightly larger AR will not affect the solution. The tangent hyperbolic grid gives the smoothest and most controllable grid. The advantage is that one can tweak the first node spacing from both

sides and increase the number of nodes to reduce the AR (if it is not already satisfactory). Table 18 compares these algorithms for the test grid:

Table 18. Assessment of various grid distributions

Mesh metric	Uniform	Tangent hyperbolic	Fixed AR	Hybrid
Grid points N	170	40	40	30
First node Δs_1	2.92e-5	1.97e-5	1.34e-5	1.34e-5
Max AR	1.00	1.20	1.2	1.78
Min AR	1.00	0.83	0.8	0.59

5.7.3.4. 2D and 3D non-uniform mesh generation

The flowchart in Figure 104 shows how the process was automated for more than one direction, and by solving the root of the transcendental equation. A bisection algorithm [226] is used for root-finding due to its robustness.

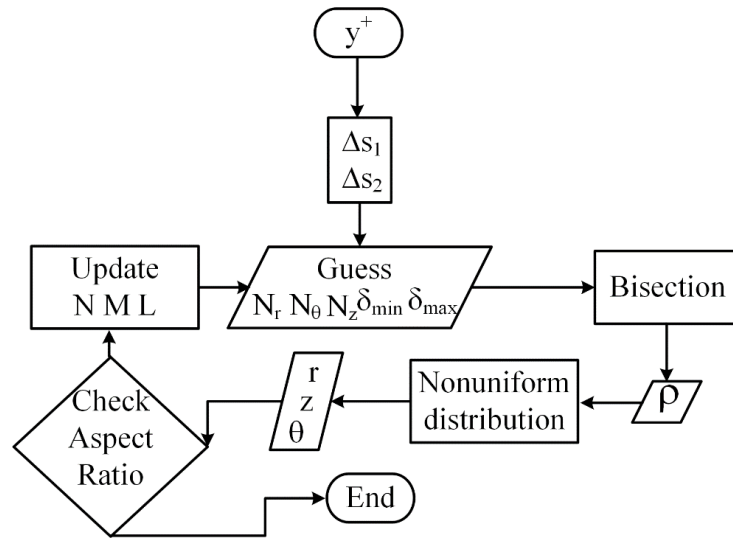


Figure 104. Grid generation flow chart

The generated mesh for uniform and non-uniform formulation in 2D is shown in Figure 105 and Figure 106.

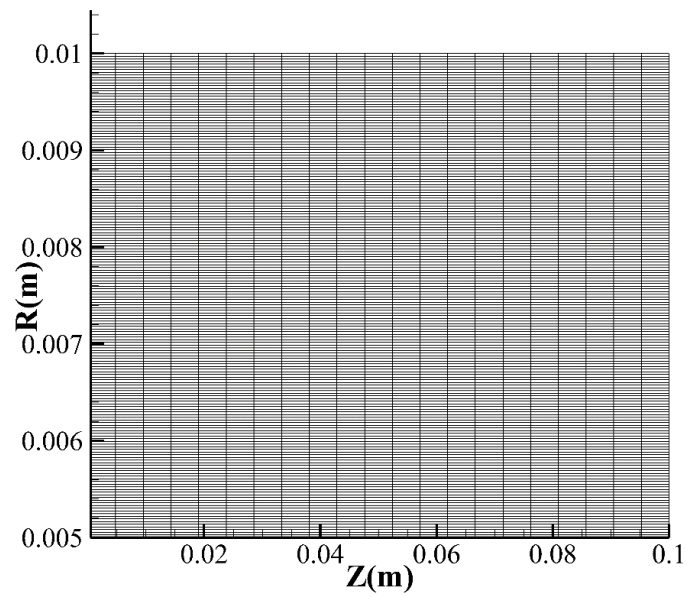


Figure 105. Uniform grid

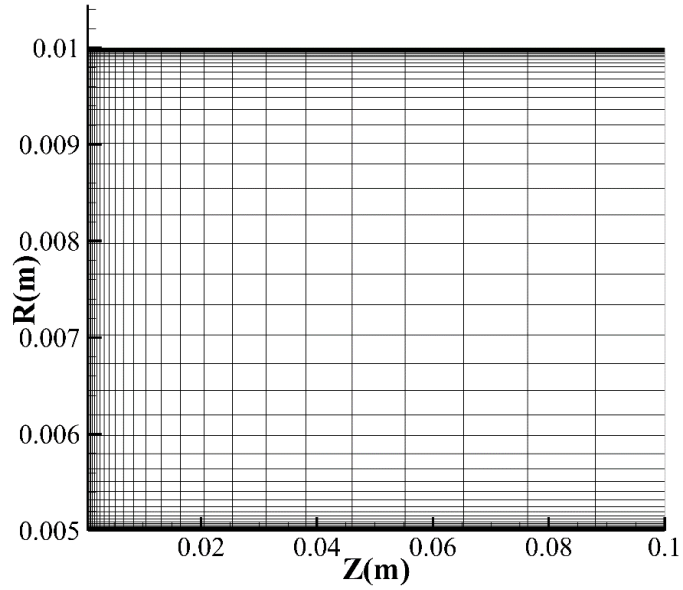


Figure 106. Non-uniform grid

The mesh is suitable for annulus turbulent flow at $Re=5000$ and satisfies both spacing and aspect ratio constraints.

5.8. Boundary Conditions

5.8.1. Wall

Wall velocity boundary condition is set as no-slip. For seal flow:

$$w_z = w_{wall}, \quad w_r = 0, \quad w_\theta = r\omega_{wall} - ROTr\omega \quad (185)$$

where ω denotes the rotating frame rotational speed. The pressure BC is found from the simplified momentum equation (in this context) at the wall:

$$\frac{\partial p}{\partial r} = \nu \frac{\partial^2 w_r}{\partial r^2} + \frac{w_\theta^2}{r} \quad (186)$$

which is implemented using second order one sided derivatives. The turbulent BCs for the smooth wall will be [204]:

$$k = 0, \quad \omega = \frac{2500\nu}{\varepsilon^2} \quad (187)$$

where ε is an infinitesimal number showing roughness and it should be smaller than $1\mu\text{m}$ for the seal applications with tight clearances. Alternatively, one can use Menter's expression at wall [208]:

$$\omega \approx 10 \frac{6\nu}{\beta_1 \Delta y^2} \quad (188)$$

where Δy is the distance between the wall and the first node.

5.8.2. Roughness Treatment

The roughness formula for ω has been updated to an implicit formula that varies each iteration:

$$\left\{ \begin{array}{l} \omega_w = \frac{u_\tau^2}{\nu} S_R \\ S_R = \begin{cases} \left(\frac{50}{\varepsilon^+}\right)^2 & \varepsilon^+ < 25 \\ \frac{100}{\varepsilon^+} & \varepsilon^+ \geq 25 \end{cases} \\ \varepsilon^+ = \frac{u_\tau \varepsilon}{\nu} \\ u_\tau = \sqrt{\frac{\tau_w}{\rho}} \\ \tau_w = \mu \sqrt{\left(\frac{\partial w_z}{\partial r}\right)^2 + \left(\frac{\partial w_\theta}{\partial r} - \frac{w_\theta}{r}\right)^2} \end{array} \right. \quad (189)$$

This formula depends on the turbulence scales close to the wall and uses a dimensionless roughness parameter ε^+ to find the roughness scale S_R and ω_w . The direct dimensional implementation of roughness ε will be insensitive to turbulence wall scales and could result in wrong regime prediction. Please note that a $\varepsilon = 10\mu m$ in a seal with tight clearance may lead to fully rough flow but in a pipe may be treated as a hydraulically smooth flow. Therefore one should leave the decision to be made by the code if the wall is considered as rough or smooth.

5.8.3. Inlet

The velocity and pressure inlet BC can be either Dirichlet condition:

$$\phi = f(r) \quad (190)$$

or Neumann condition in the form of direct profile definition, extrapolation, or fully developed condition.

$$\frac{\partial \phi}{\partial z} = 0 \quad (191)$$

For turbulence BCs, turbulent intensity is approximately equal to:

$$I = 0.16Re^{-1/8} \quad (192)$$

and the turbulent kinetic energy is found from:

$$k = \frac{3}{2}(U_\infty I)^2 \quad (193)$$

for ω :

$$\omega = \frac{k^{1/2}}{l} \quad (194)$$

and the value of length scale is problem dependent. For pipe flow

$$l = 0.038D_H \rightarrow \omega = \frac{k^{1/2}}{0.038D_H} \quad (195)$$

where D_H is the equivalent hydraulic diameter. The turbulence length scale for the seal flow has been proposed by Hendricks et al. [121] based on Prandtl mixing length theory:

$$\begin{cases} l_m = Hr_2 y, & \frac{y}{C_r} \leq \frac{Hr_1}{Hr_2} \\ l_m = Hr_1 C_r, & \frac{y}{C_r} > \frac{Hr_1}{Hr_2} \end{cases}, \quad Hr_1 = 0.09, \quad Hr_2 = 0.435 \quad (196)$$

where y shows the local normal distance from the nearest wall, Hr_1, Hr_2 are two parameters suggested by Hendricks. Alternatively, the zero-gradient condition could be used for the turbulence inlet conditions as well.

5.8.4. Outlet

At outlet all variables except pressure use the zero-gradient (fully-developed) condition:

$$\frac{\partial \phi}{\partial z} = 0 \quad (197)$$

The pressure can use either Dirichlet BC or constant pressure gradient (fully-developed):

$$\left(\frac{\partial p}{\partial z}\right)_{N_z} = \left(\frac{\partial p}{\partial z}\right)_{N_z-1} \quad (198)$$

where N_z is the number of nodes in z direction.

5.8.5. Symmetry

Symmetry condition may appear at the inner radius $r = 0$. All variables have zero gradient condition:

$$\frac{\partial \phi}{\partial r} = 0 \quad (199)$$

5.8.6. Periodic

Including the third dimension (θ) requires a new set of BCs. On planes of constant θ either periodic, symmetric or wall boundary conditions can be used. The wall and symmetry BCs are similar to what was implemented before but periodic condition requires special care otherwise a discontinuity will appear in solution which remains difficult to distinguish as the grid becomes finer. With turbulent flow it may lead to early divergence. If the total number of nodes in θ direction starts with $j = 1$ and finishes with $j = N_\theta$, then at ghost-plane $j = 0$:

$$\phi_{i,0,k}^m = \phi_{i,N_\theta,k}^m \quad (200)$$

And at ghost-plane $j = N_\theta + 1$:

$$\phi_{i,N_\theta+1,k}^m = \phi_{i,1,k}^m \quad (201)$$

Since neither value of $\phi_{i,N_\theta,k}^m$ nor $\phi_{i,1,k}^m$ is known, these nodes should be solved with regular McCk formulation and with the above mentioned ghost-node values. The

schematic in Figure 107 shows the correct implementation of periodics with McCk scheme:

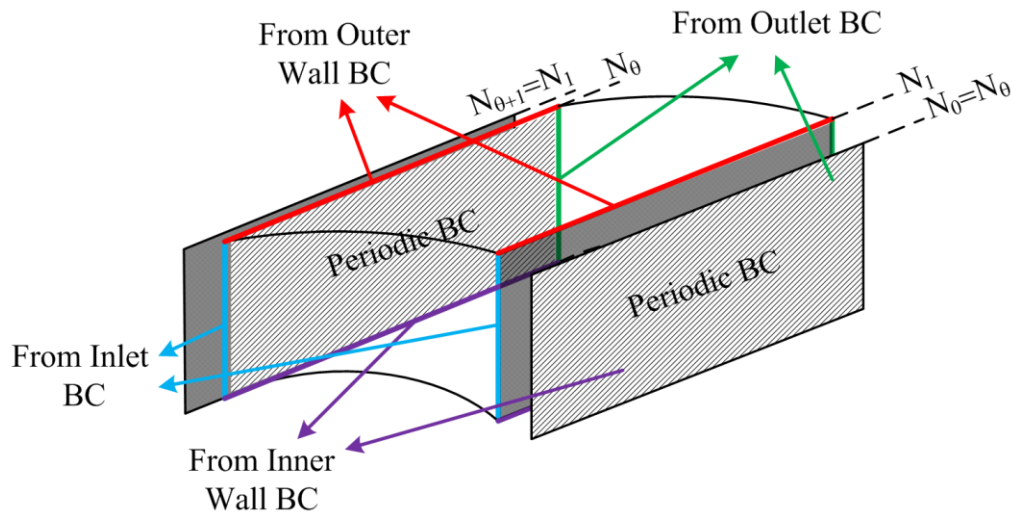


Figure 107. Correct implementation of periodic boundary conditions

Periodic boundary conditions are expensive BCs both in terms of computational cost and implementation effort. They are computationally expensive because they need to solve the whole McCk scheme with associated fluxes and unknown vectors. They are costly in terms of implementation because they need manual adjustment of flux vectors for the neighboring periodics and consider exceptions in the code. Figure 108 flow chart summarizes the adjustments needed to implement periodic BCs:

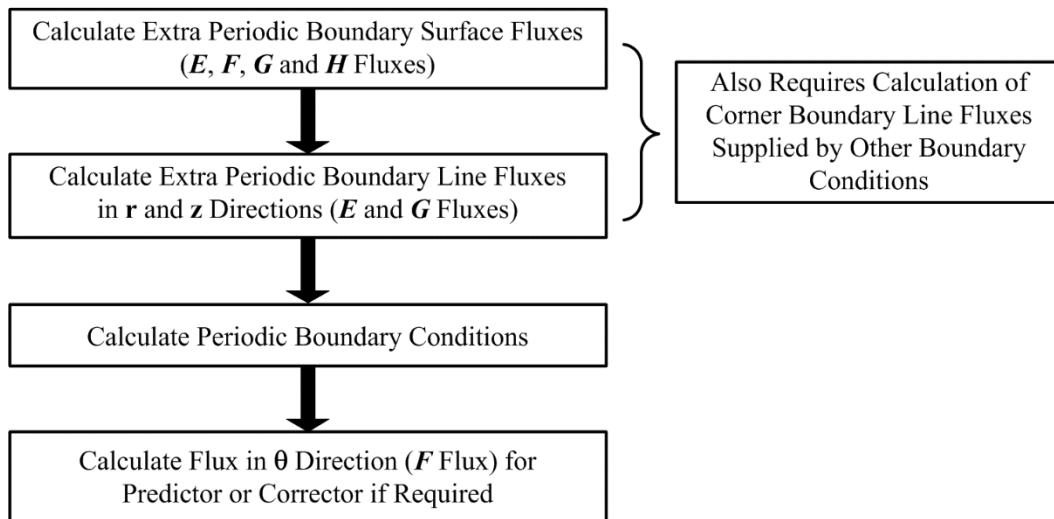


Figure 108. Steps to implement periodic boundary conditions

For example, in the case of wall BC in θ direction, the first 3 steps are not required.

5.8.7. Interface

To reduce the errors associated with interpolation, bilinear interpolation is used.

For a domain given below (x_1, x_2, y_1, y_2 are known and x_p, y_p are desired):

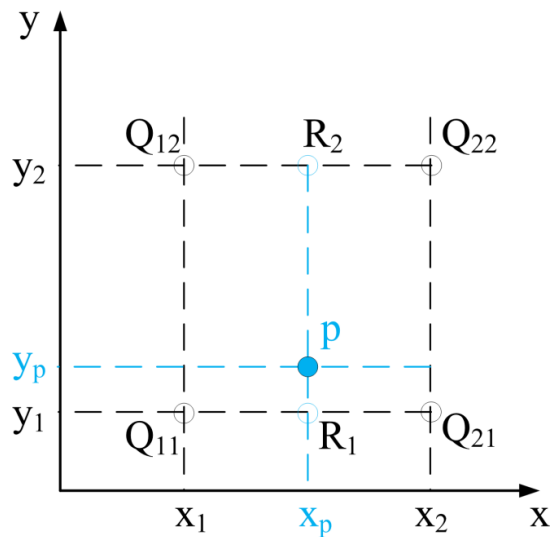


Figure 109. Bilinear interpolation

The bilinear interpolation is found by consecutive linear interpolation in x and y directions:

$$f(R_1) \approx \frac{x_2 - x_p}{x_2 - x_1} f(Q_{11}) + \frac{x_p - x_1}{x_2 - x_1} f(Q_{21})$$

$$f(R_2) \approx \frac{x_2 - x_p}{x_2 - x_1} f(Q_{12}) + \frac{x_p - x_1}{x_2 - x_1} f(Q_{22})$$
(202)

Another linear interpolation in y direction is done:

$$f(p) \approx \frac{y_2 - y_p}{y_2 - y_1} f(R_1) + \frac{y_p - y_1}{y_2 - y_1} f(R_2) \rightarrow$$

$$f(p) \approx \frac{1}{(y_2 - y_1)(x_2 - x_1)} [f(Q_{11})(x_2 - x_p)(y_2 - y_p)$$

$$+ f(Q_{21})(x_p - x_1)(y_2 - y_p)$$

$$+ f(Q_{12})(x_2 - x_p)(y_p - y_1)$$

$$+ f(Q_{22})(x_p - x_1)(y_p - y_1)]$$
(203)

which for the uniform grid problem reduces to:

$$\phi_{ik} \approx \frac{1}{4} [\phi_{i-1 k-1} + \phi_{i+1 k-1} + \phi_{i-1 k+1} + \phi_{i+1 k+1}]$$
(204)

5.9. Wall-Function

Even though k - ω model is capable of modeling viscous sublayer, in industrial practices such approach will be avoided. Near the wall variables change rapidly and ω varies by several orders of magnitude (for perfectly smooth wall ω should go to infinity at the wall). This requires extremely fine mesh near the wall and the stiffness of solution

is inevitable. All the difficulties of central differencing schemes near the wall will follow in its wake, as well.

The alternative approach is to use High Re version of equations along with a proper wall-function. The idea is to avoid modeling the viscous sublayer, and find the correct value of velocity and shear stress inside the log layer[227]. Since the shear stress remains constant all through the log-layer, buffer layer and viscous sublayer, this approach is satisfactory for industrial applications where there is an interest in friction factors, pressure distribution and mass flow. In fact mass flow is slightly under-predicted by wall-functions, since a portion of displacement thickness δ^* is not modelled, unless the missing layer is approximated for mass flow calculations. However, since this thickness is a small percentage of the total width in High Re flows, the results will be usually satisfactory.

Therefore, the wall-function approach tries to find the shear stress, k and ω at the first node after the wall. To find the shear stress at the first node after the wall, law of the wall transcendental equation is solved for u_τ (which indirectly says that y^+ of the first node must be small enough to be located inside the log-layer):

$$U_{1st\ node} = u_\tau \left[\frac{1}{\kappa} \ln \left(\frac{u_\tau y_{1st\ node}}{\nu} \right) + \mathbb{B} \right], \quad \mathbb{B} = 0.50, \quad (205)$$

$$\kappa = 0.41$$

here \mathbb{B} and κ are constant which can be determined analytically. Since

$$u_\tau = \sqrt{\frac{\tau_w}{\rho}} \quad (206)$$

the shear stress at the wall will be found. When solved for u_τ , it is possible to immediately calculate k and ω at the first node by the advantage of the known law-of-wall asymptotic solution inside the log layer:

$$k_{1^{st}node} = \frac{u_\tau^2}{\sqrt{\beta^*}}, \quad \omega_{1^{st}node} = \frac{u_\tau}{\kappa y_{1^{st}node} \sqrt{\beta^*}} \quad (207)$$

In practice though, it is better to use the following equivalent wall-functions, because in separated flows $u_\tau < 0$ and ω will become negative too which is not physical. These new wall-functions are positive definite:

$$k_{1^{st}node} = \frac{u_\tau^2}{\sqrt{\beta^*}}, \quad \omega_{1^{st}node} = \frac{k^{1/2}}{\kappa y \beta^{*1/4}} \quad (208)$$

Later, Wilcox [204] showed it is better to keep pressure-gradient term denoted by χ (although small, to the first order) for transcendental equation for the independency of solution from grid density (for k - ω model):

$$\left\{ \begin{array}{l} U = u_\tau \left[\frac{1}{\kappa} \ln \left(\frac{u_\tau y}{\nu} \right) + \mathbb{B} - 0.48 \frac{u_\tau y}{\nu} \chi \right] \\ k_{1^{st}node} = \frac{u_\tau^2}{\sqrt{\beta^*}} \left[1 + 1.16 \frac{u_\tau y}{\nu} \chi \right] \\ \omega_{1^{st}node} = \frac{u_\tau}{\kappa y \sqrt{\beta^*}} \left[1 - 0.32 \frac{u_\tau y}{\nu} \chi \right] \\ \chi = \frac{\nu}{\rho u_\tau^3} \frac{dp}{dx} \end{array} \right. \quad (209)$$

It should be noted that wall-functions do not provide a flaw-less solution, however for current application the results are satisfactory. For viscous sublayer modeling more than 10 nodes are required inside the inner layer. Even the highest quality meshes rarely

meet this condition for complex geometries, not to mention the numerical difficulties. Therefore, wall-functions can be used as a trade-off between accuracy and computational cost.

5.9.1. Wall-Function Implementation

The idea is that BCs at wall have to be replaced with BCs at the nodes adjacent to the wall. The BCs at the node adjacent to the wall (with distance y_p to the wall) are partially found from law of the wall and Navier-Stokes equations.

$$@y_p : \begin{cases} \vec{W} \cdot \hat{n} = 0 \rightarrow w_n = 0 \text{ (in this context } w_r = 0) \\ p = p_w \rightarrow \text{use the same BC as the wall} \\ u_\tau \text{ and } \tau_w \rightarrow \text{from law of the wall} \\ k \text{ and } \omega \rightarrow \text{from wall-} - \text{ functions} \\ w_z \text{ and } w_\theta \rightarrow \text{from wall shear stress} \end{cases} \quad (210)$$

After the wall shear is obtained by finding the root of the law of the wall, the velocity BC can be updated from (211):

$$\tau_w = -(\mu + \mu_t) \frac{\partial w_z}{\partial r} \quad (211)$$

This process will be repeated each iteration till convergence is achieved. The following flow chart shows the procedure of integrating wall-function into the code and substituting wall BCs with adjacent node values.

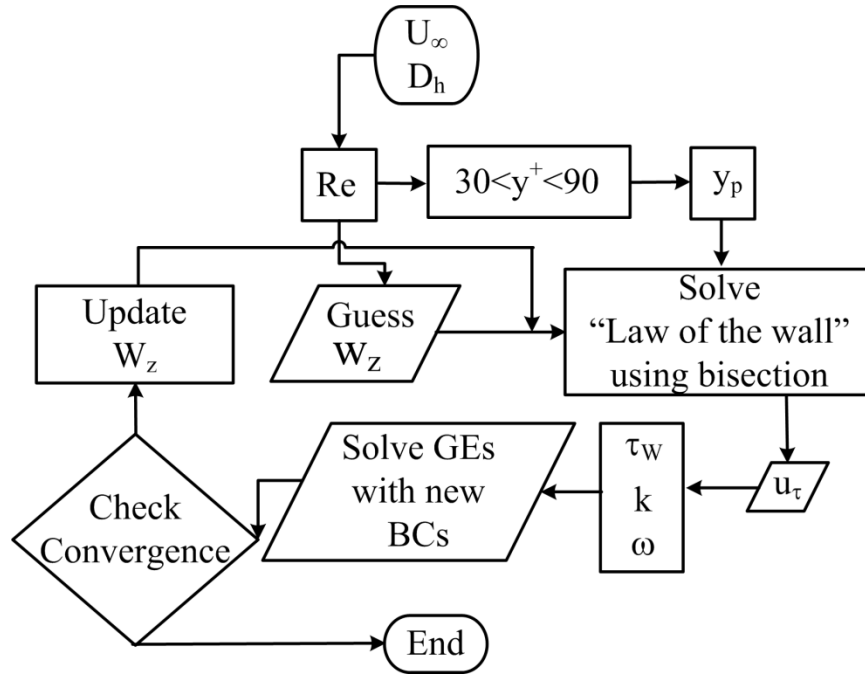


Figure 110. Wall-function implementation flow chart

5.9.2. Wall Roughness Modeling for Wall-Functions

The approach used in CFX [154] and publications before CFX [228] has been followed for roughness modeling. The theory is based on sand-roughness measurements and theoretical arguments of Schlichting [229]. The law of the wall is slightly modified to account for roughness effect. The roughness appears as a shift in the log layer which can totally destroy the viscous sublayer if the relative roughness is large enough.

$$u^+ = \frac{1}{\kappa} \ln y^+ + \mathbb{B} - \Delta \mathbb{B} \quad (212)$$

The ΔB term contains the roughness information:

$$\Delta B = \frac{1}{\kappa} \ln(1 + 0.3\varepsilon^+) , \quad \varepsilon^+ = \frac{u_\tau \varepsilon}{\nu} \quad (213)$$

where ε^+ is the dimensionless roughness value. Same discussions in the roughness treatment of wall BC without wall-functions apply to the version with the wall-functions. Please note that when $\varepsilon^+ = 0$ the original law of the wall is retained which corresponds to a smooth wall.

5.9.3. *Connecting Log-layer to the Wall*

After the solution is obtained using wall-functions, depending on Re number, a portion of the velocity profile is not modeled and therefore not accounted for when a flow rate is calculated. If the Re number is relatively small ($Re < 50,000$) this portion may contribute to a considerable portion of total flow rate. Hence, to accurately model the leakage flow rate in seals which have typically small Re numbers, the lost portion of the inner layer needs to be modelled. A well-accepted general formula that covers the profile from the wall all the way through the log layer is known as Reichardt's law of the wall [230, 231] and is formulated as:

$$u^+ = \frac{\ln(1 + \kappa y^+)}{\kappa} + 7.8 \left(1 - e^{-\frac{y^+}{11}} - \frac{y^+}{11} e^{-0.33y^+} \right) \quad (214)$$

$$u^+ = \frac{u}{u_\tau}, \quad y^+ = \frac{y u_\tau}{\nu} \quad (215)$$

Since u_τ is a known variable at all the nodes adjacent to the wall after the solution, the velocity profile can be estimated inside the viscous sublayer and buffer layer all the way to the wall-adjacent node. Then the completed velocity profile is integrated for the full leakage rate.

5.9.4. *Automatic Wall-Functions*

To make the code insensitive to the first node distance from the wall, a blended formula for ω and k will be used to cover both regions of viscous sublayer and log layer as well as regions in between them (buffer layer). The solution to the log layer and viscous sublayer is known as:

$$\omega_{vis} = \frac{6\nu}{\beta y_p^2}, \quad \omega_{log} = \frac{u_\tau}{\beta^{*1/4} \kappa y_p} \quad (216)$$

Menter [232] blends the two solutions so that each of them prevail based on magnitude of the distance from the wall y_p :

$$\omega_p = \sqrt{\omega_{vis}^2 + \omega_{log}^2} \quad (217)$$

Note that at small y_p the viscous solution prevails as it is a function of y_p^{-2} but at large y_p the log layer solution dominates since it is a function of y_p^{-1} . As regards to k a zero gradient BC can be applied, since this BC applies both to the viscous sublayer and log layer [233]. In fact the near wall asymptotic solution of kinetic energy yields [204]:

$$k \sim y^2 \quad \text{as } y \rightarrow 0 \quad (218)$$

which is differed from the relation $\partial k / \partial y = 0$ when $y \rightarrow 0$. Alternatively, one can use the viscous sublayer k solution and blend it with log layer solution. The behavior of k near the wall is found from the continuity equation as [234]:

$$k^+ = A^+ y^{+2} + O(y^{+3}) \quad (219)$$

where $k^+ = k / u_\tau^2$. The value of the coefficient A^+ is dependent on Re number, growing at higher Re numbers [235]:

$$0.025 < A^+ < 0.05 \quad (220)$$

Other researchers such as Kreplin and Eckelmann [236] have used a fixed value of $A^+ = 0.035$. Since the seals have a low Re number, the lowest value of A^+ is retrieved [228]. Therefore the blending components are given as:

$$k_{vis} = \frac{0.025y^2u_\tau^4}{\nu^2}, \quad k_{log} = \frac{u_\tau^2}{\beta^{*1/2}} \quad (221)$$

$$k_p = \sqrt{k_{vis}^2 + k_{log}^2} \quad (222)$$

For u_τ the blending formula of Menter will be used:

$$\text{@vis.sub. } u^+ = y^+ \rightarrow u_{\tau,vis} = \sqrt{\frac{uv}{y}} \quad (223)$$

$$u_{\tau,log} = \frac{u}{\frac{1}{\kappa} \ln y^+ + \mathbb{B} - \Delta \mathbb{B}} \quad (224)$$

and,

$$u_{\tau,p} = \sqrt[4]{u_{\tau,vis}^4 + u_{\tau,log}^4} \quad (225)$$

5.9.5. Swirling Flow Wall-Functions

The update to the rotating frame requires adjustments to τ_w calculations. The wall shear and y^+ calculation is now based on two velocity components w_z and w_θ . Starting from law of the wall (for simplicity of relations without surface roughness):

$$W_{rel} = u_\tau \left[\frac{1}{\kappa} \ln(y^+) + \mathbb{B} \right] \quad (226)$$

where $W_{rel} = \sqrt{w_z^2 + w_{\theta,rel}^2}$ is the total tangential velocity component relative to the wall, and:

$$\sqrt{\frac{\tau_w}{\rho}} = \frac{\kappa}{\ln(y^+) + \mathbb{B}\kappa} W_{rel} \quad (227)$$

here $\tau_w = \sqrt{\tau_{wz}^2 + \tau_{w\theta}^2}$ is the total shear stress at the wall, using kinetic energy equation solution close to the wall and multiplying the LHS of previous equation by \sqrt{k} :

$$\tau_w = \frac{\kappa \rho k^{\frac{1}{2}} \beta^{*1/4}}{\ln(y^+) + \mathbb{B}\kappa} W_{rel} \quad (228)$$

It is implicitly assumed that the total tangential velocity follows the law of the wall similar to the 2D equilibrium flows. Experiments by Backshall and Landis [237] confirm this assumption. Next, the total shear stress is decomposed into the axial and circumferential components by assuming a linear relation [237, 238]:

$$\left\{ \begin{array}{l} \tau_{wz} = \frac{w_z}{y_p} \\ \tau_{w\theta} = \frac{w_{\theta,rel}}{y_p} \\ \tau_w = \frac{W_{rel}}{y_p} \end{array} \right. \rightarrow \left\{ \begin{array}{l} \frac{\tau_{wz}}{\tau_w} = \frac{w_z}{W_{rel}} = \cos \Theta \\ \frac{\tau_{w\theta}}{\tau_w} = \frac{w_{\theta,rel}}{W_{rel}} = \sin \Theta \end{array} \right. \quad (229)$$

and each shear stress component will be:

$$\begin{cases} \tau_{wz} = \frac{\kappa \rho k^{\frac{1}{2}} \beta^{*1/4}}{\ln(y^+) + \mathbb{B}\kappa} w_z \\ \tau_{w\theta} = \frac{\kappa \rho k^{\frac{1}{2}} \beta^{*1/4}}{\ln(y^+) + \mathbb{B}\kappa} w_{\theta,rel} \end{cases} \quad (230)$$

At this point there are two methods to proceed. The approach of Rhode et al. [122] is to directly substitute this term in momentum equation at the node adjacent to the wall as a source term. To be consistent with current code methodology, the following approach has been adopted instead. For example for the inner wall:

$$(\mu + \mu_t) \frac{\partial w_z}{\partial r} = \frac{\kappa \rho k^{\frac{1}{2}} \beta^{*1/4}}{\ln(y^+) + \mathbb{B}\kappa} w_z \quad (231)$$

and w_z can be calculated from this relation. The procedure for w_θ is slightly different. Demko [114, 239] in his dissertation gives a detailed explanation of how to derive wall-functions for labyrinth seals. These wall-functions in general can be slightly different from what is formulated here because the relative magnitude of w_r, w_θ, w_z may be different in a general 3D cavity with stationary or rotating side walls. Here the forms suitable for a plain annular seal with one rotating and one stationary axial wall are found. The wall shear stress sensed by the rotating wall forms with respect to the relative velocity of the flow field to the wall. Therefore for a rotating wall instead of w_θ one should use $w_{\theta,p} - w_{\theta,s}$ where subscript p denotes the node adjacent to the wall and s refers to a point on the wall (See Figure 111). In the case of rotating inner wall:

$$w_{\theta,rel} = w_{\theta,p} - R_{in}\omega \quad (232)$$

but the total relative velocity profile is written as:

$$W_{rel} = w_{\theta,rel}\hat{e}_\theta + w_{z,rel}\hat{e}_z + w_{r,rel}\hat{e}_r \quad (233)$$

by assuming an impenetrable wall:

$$W_{rel} = (w_{\theta,p} - R_{in}\omega)\hat{e}_\theta + (w_{z,p} - V_{z,wall})\hat{e}_z + w_{r,p}\hat{e}_r \quad (234)$$

here $V_{z,wall}$ shows the axial movement of the wall. If the wall does not have such axial speed and the radial velocity component near the wall is neglected (this term should be kept if the analysis is done for a radial wall which in that case the w_z term should be dropped instead), the relation simplifies to:

$$W_{rel} = (w_{\theta,p} - R_{in}\omega)\hat{e}_\theta + w_{z,p}\hat{e}_z \quad (235)$$

The wall shear stress acts in the negative direction of W_{rel} . The θ component of wall shear will be found as:

$$\tau_{w\theta} = \tau_w \frac{w_{\theta,p} - R_{in}\omega}{|W_{rel}|} \quad (236)$$

The assumption of all wall-function approaches is applied, meaning that the shear stress at point p equals to the wall shear stress at point s :

$$\tau_{w\theta,p} = \tau_{w\theta,s} \quad (237)$$

The LHS of this equation will be expanded in cylindrical coordinates as:

$$\tau_{w\theta} = (\mu + \mu_t) \left(\frac{\partial w_{\theta,rel}}{\partial r} - \frac{w_{\theta,rel}}{r} \right) \quad (238)$$

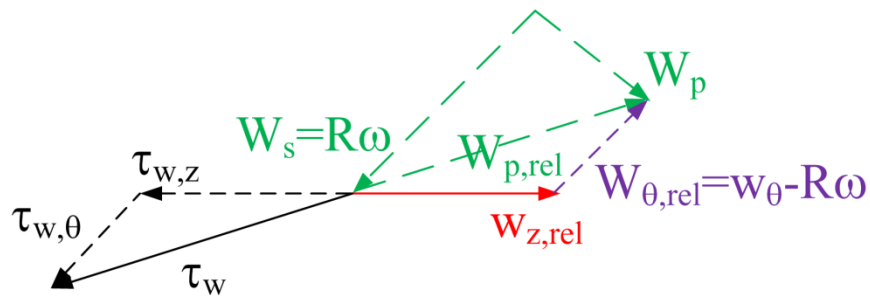
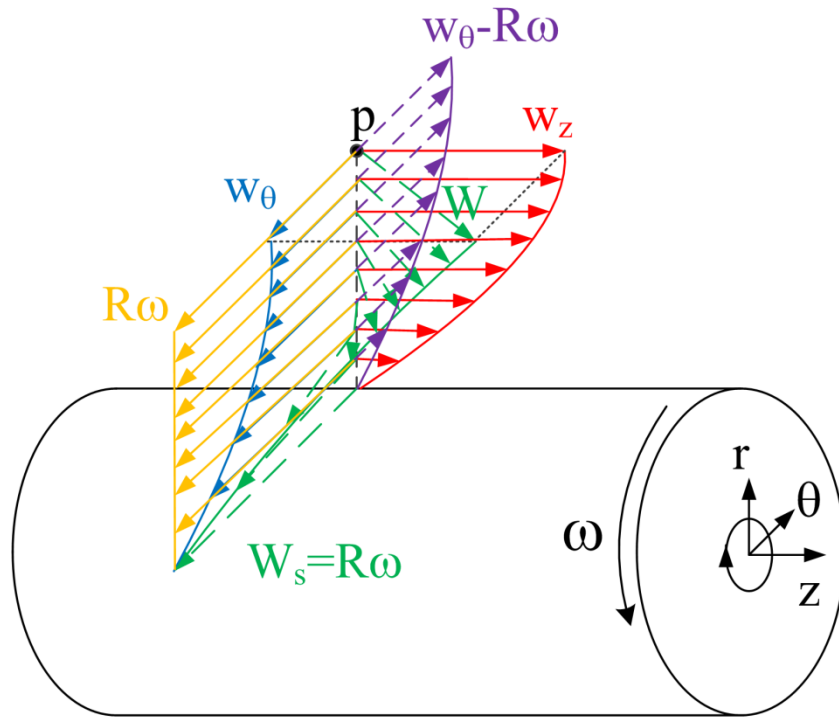


Figure 111. Swirling wall-function

If it is assumed $R_{in}/r \cong 1$ and substituting the above equation in the wall-function, the following relation is found which agrees with Rhode et al.[122] expression:

$$(\mu + \mu_t) \left(\frac{\partial w_{\theta,p}}{\partial r} - \frac{w_{\theta,p}}{r} \right) = \tau_w \frac{w_{\theta,p} - R_{in}\omega}{|W_{rel}|} + (\mu + \mu_t)\omega \quad (239)$$

and $w_{\theta,p}$ can be found from current relation.

5.10. Multigrid

Multigrid scheme has been selected to accelerate the code. Some of the basic expressions and operators used in the derivation of the equations will be presented. Multigrid method is a heavily used speed-up scheme in CFD problems. The method is most effective in linear PDEs but it has been extended for nonlinear PDEs as well [213].

The main idea behind the multigrid method lies in the fact that low frequency errors present in a problem only damp well on a low frequency grid (coarse grid) while the high frequency error damps well on a high frequency grid (fine grid). Since in most of the cases the error is mixture of these frequencies, a mixture of grids best resolves the residual (error) terms.

5.10.1. Ellipticity

The multigrid method is most efficient on pure space type (full elliptic) problems [240]. Current code at this current form deals with steady incompressible NS which in inviscid form is fully elliptic and in viscous form is mixed elliptic-parabolic. The compressible viscous NS is mixed hyperbolic-parabolic [241]. Therefore, there is a good deal of ellipticity present in the incompressible problem which can be handled by multigrid method. The transient version of NS breaks into series of steady state time step solutions. At each step multigrid can be applied.

5.10.2. A Comparison of Elliptic Solvers

Table 19 is adapted from Trottenberg et al. [240] and compares the order of operations need for convergence of a 2D Poisson problem using various schemes. The convergence criterion typically shows itself as $\log Err$ in the number of operations.

Table 19. Comparison of efficient elliptic solvers (adapted from [240])

Method	(O) of operations in 2D
Gaussian Elimination	$O(N^2)$
Jacobi Iteration (JAC)	$O(N^2 \log Err)$
Gauss-Seidel Iteration (GS)	$O(N^2 \log Err)$
Successive Over-relaxation (SOR)	$O(N^{3/2} \log Err)$
Alternative Direction Implicit (ADI)	$O(N \log N \log Err)$
Fast Fourier Transform (FFT)	$O(N \log N)$
Total Reduction	$O(N)$
Multigrid (Iterative)	$O(N \log N)$
Full Multigrid (FMG)	$O(N)$

Some of the schemes presented here are specifically suitable and efficient for Elliptic problems like the “Total Reduction” method, while Multigrid method can be applied to all sorts of equations. Furthermore, this is the order of operations, but within the same order some schemes can be several times faster than the others. For instance, the Gauss-Seidel (GS) method and the Jacobi method has the same order, but GS can easily outperform Jacobi by 10 times.

5.10.3. *Parallelizability vs Smoothing*

Some schemes are good smoothers, some are good parallelizable schemes. For example, Jacobi is not a good smoother, but because it is fully explicit, then it is also fully parallel. On the other hand, GS with over-relaxation presents a good smoother and

poor parallel scheme. Table 20 is adapted from Trottenberg et al. [240]. N is the number of cells and $\bar{\omega}$ is the over-relaxation parameter.

Table 20. Smoothing vs parallelizability (adapted from [240])

Relaxation scheme	Smoothing factor	Smoothing	Parallel degree
JAC, $\bar{\omega} = 1$	1	No	N , Full
JAC, $\bar{\omega} = 0.8$	0.6	Acceptable	N , Full
GS, $\bar{\omega} = 1$	0.5	Good	$\leq \sqrt{N}$, Square Root

Because current code is based on McCk scheme which is fully explicit, the multigrid version of it will support full parallelizability.

5.10.4. H-Ellipticity Measure

The “h-ellipticity” is measure that serves as the necessary and sufficient condition for the existence of smoothing properties associated with a given operator \mathbb{L}_h . Certain operators do not satisfy this measure and therefore cannot sooth out the errors on the coarser grids. A common solution is to add artificial viscosity to cause “artificial ellipticity” and artificially increase this measure for multigrid operation [240]. If one shows h-ellipticity with E_h , the negative or zero values of E_h shows non-ellipticity. For example:

-2nd order first derivative central difference operator is non-elliptic $E_h = 0$.

$$\mathbb{L}_h = \frac{1}{2h} [-1 \quad 0 \quad 1] \tag{240}$$

-2nd order parabolic central difference operator is non-elliptic $E_h = 0$.

$$\mathbb{L}_h = \frac{1}{h^2} \begin{bmatrix} 0 & -1 & 0 \\ 0 & 2 & 0 \\ 0 & -1 & 0 \end{bmatrix} \quad (241)$$

-2nd order and 1st order mixed derivative hyperbolic operators are non-elliptic $E_h = 0$.

which is basically the nature of the operator not the discretization.

$$\mathbb{L}_h = \frac{1}{4h^2} \begin{bmatrix} -1 & 0 & 1 \\ 0 & 0 & 0 \\ 1 & 0 & -1 \end{bmatrix}, \quad \mathbb{L}_h = \frac{1}{h^2} \begin{bmatrix} 0 & 0 & 0 \\ -1 & 1 & 0 \\ 1 & -1 & 0 \end{bmatrix} \quad (242)$$

-2nd order 2nd derivative central difference (frequently used in diffusion discretization) is naturally elliptic with $E_h = 0.25$:

$$\mathbb{L}_h = \frac{1}{h^2} \begin{bmatrix} 0 & -1 & 0 \\ -1 & 4 & -1 \\ 0 & -1 & 0 \end{bmatrix} \quad (243)$$

-1st order forward or backward first derivative is elliptic with $E_h = \sqrt{2}/2$ (strong ellipticity, same reason that this operator removes the checker-board effect).

$$\mathbb{L}_h = \frac{1}{2h} [-1 \quad 1 \quad 0] \quad (244)$$

Since the McCk scheme uses first order one sided derivatives subsequently as predictors and correctors, there is a good deal of ellipticity in the discretization and MG is able to work effectively with this scheme.

5.10.5. Transfer Operators

The transfer operators \mathbb{I} , from coarse to fine \mathbb{I}_H^h , and fine to coarse \mathbb{I}_h^H will be discussed in this section. The process from the fine to coarse (Restriction) is more straight forward. First option is the injection technique:

$$\mathbb{I}_h^H = \begin{bmatrix} 0 & 0 & 0 \\ 0 & 1 & 0 \\ 0 & 0 & 0 \end{bmatrix} \quad (245)$$

at each point. Another method is the Full Weighting (FW) approach, with operator:

$$\mathbb{I}_h^H = \frac{1}{16} \begin{bmatrix} 1 & 2 & 1 \\ 2 & 4 & 2 \\ 1 & 2 & 1 \end{bmatrix} \quad (246)$$

which in 1D will reduce to:

$$\mathbb{I}_h^H = \frac{1}{4} [1 \quad 2 \quad 1] \quad (247)$$

or the Half Weighting (HW) technique:

$$\mathbb{I}_h^H = \frac{1}{8} \begin{bmatrix} 0 & 1 & 0 \\ 1 & 4 & 1 \\ 0 & 1 & 0 \end{bmatrix} \quad (248)$$

Current code is mostly based on FW method. The other transfer operator is the coarse to fine or prolongation operator. In 2D a bilinear interpolation will be used as suggested by Trottenberg et al. [240] with compact notation as an operator:

$$\mathbb{I}_H^h = \frac{1}{4} \begin{bmatrix} 1 & 2 & 1 \\ 2 & 4 & 2 \\ 1 & 2 & 1 \end{bmatrix} \quad (249)$$

The order of interpolation for both FW and the bilinear interpolation is 2. The injection operator order of interpolation is 0. If the order of the linear operator is m , and order of

restriction and prolongation operators are m_i and m^j , the following criteria should be satisfied (by local Fourier analysis) [240]:

$$m_i + m^j > m \tag{250}$$

Hence, FW plus bilinear interpolation works good for the class of problems where order of operators are not larger than 3. But injection plus bilinear interpolation may diverge.

5.10.6. Cycles and Numerical Efficiency

The most famous cycles are the V and W cycles shown below:

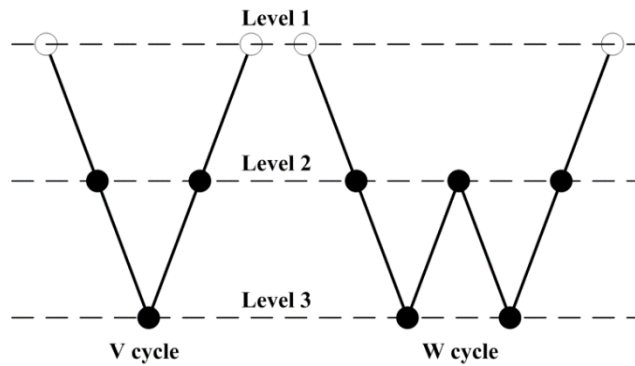


Figure 112. V and W cycles for 3 level multigrid

However there are more advanced adaptive cycles that change the number of grids and shape of cycles according to solution. These are called F-cycle structures. The efficiency (CPU time for convergence) of the cycle is a function of several factors, such as its order of convergence, order of computational work and perhaps scalability in parallel mode. The V cycle has the cheapest computational work (and F is much better than W); however, the W and F cycles have superior convergence factor. Depending on

the problem, one of these economy factors will prevail. V-cycle is usually more efficient for simple problems, whereas F-cycle and W-cycle offer better efficiency for more complicated problems.

5.10.7. Multigrid Solver

The implementation of multigrid scheme involves the following common steps:

1- Solving the governing equations. Here \mathbb{L} shows a linear operator, and superscript f shows the fine mesh:

$$\mathbb{L}(\phi^f) = 0 \quad (251)$$

2-If the exact values were known, the equation above would have taken the form:

$$\mathbb{L}(\phi_{exact}) = 0 \quad (252)$$

Since the numerical results do not meet the exact values, Eq. (251) assumes the following form:

$$\mathbb{L}(\phi_{num}^f + \mathbb{R}^f) = 0 \rightarrow \mathbb{R}^f = -\mathbb{L}(\phi_{num}^f) \quad (253)$$

where \mathbb{R} symbolizes the numerical residual. The residual \mathbb{R}^f , as well as ϕ_{num}^f should be stored for further process.

3-Using a “Restrictor” operator, the residuals from the fine grid are interpolated into the coarse grid (See Figure 113). The operator can be a bilinear interpolator.

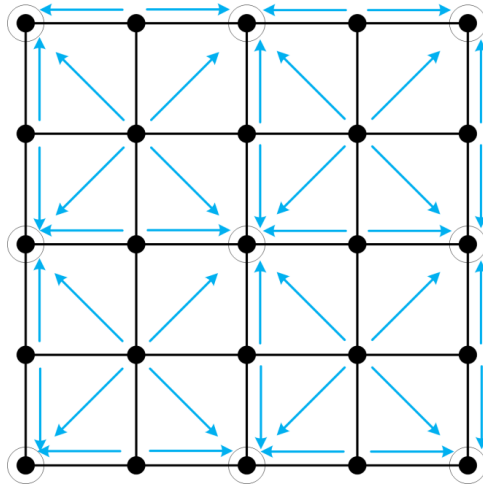


Figure 113. Restriction from fine grid to coarse grid

One or several “Smoothing” passes will be done on the error of fine grid (\mathbb{R}^f) using the coarse grid:

$$\mathbb{L}(\Delta\phi_{num}^c + \mathbb{R}^f) = 0 \quad (254)$$

where $\Delta\phi_{num}^c$ represents the low frequency error values that satisfy the governing equations in presence of \mathbb{R}^f . Please pay attention that during these passes, the fine grid residual must be kept fixed as a source term for the coarse grid smoothness values $\Delta\phi_{num}^c$

4-Using a “Prolongation” operator, extrapolate the fine grid error terms $\Delta\phi_{num}^f$ from the coarse grid error terms $\Delta\phi_{num}^c$ (See Figure 114).

5-Pass on the fine grid after adding the error terms:

$$\mathbb{L}(\phi_{num}^f + \mathbb{R}^f + \Delta\phi_{num}^f) = 0 \quad (255)$$

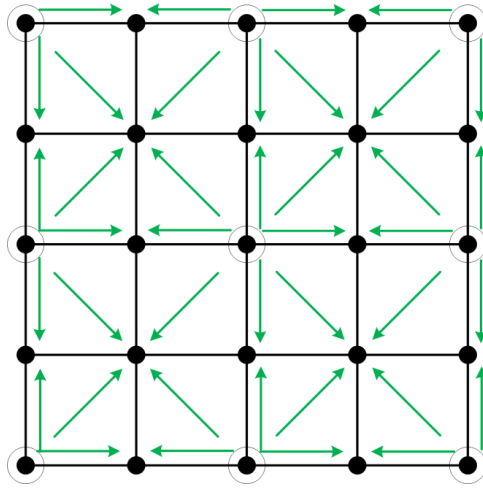


Figure 114. Prolongation from the coarse grid to fine

Since these smoothness values are being added to the fine grid results, the error is substantially reduced

$$\begin{aligned} \mathbb{L}(\phi_{num}^f + \mathbb{R}^f + \Delta\phi_{num}^f) &= 0, & \Delta\phi_{num}^f &= \Delta\phi_{num}^c = -\mathbb{R}^f \Rightarrow \\ & & & (256) \\ L(\phi_{num}^f) &= 0 \end{aligned}$$

which means convergence is achieved. The procedure of passing on smooth and coarse grids and number of coarse grids (levels) can be different. Here a “V” cycle with 2 or 3 levels has been used, but other cycles such as “W” cycles and flexible cycles “F” are among other options that commercial software present.

5.10.7.1. Linear 2D multigrid example

The objective is to extend the multigrid from 1D to 2D [242]. A 2D Laplace heat conduction equation is solved. The main challenge of this stage is to extend the transfer operators to 2D. Bilinear interpolation over the bulk and boundary regions is required

for accurate interpolation. Contours in Figure 115 show how the restricted and prolonged domains agree with the original medium domain. This figure validates the accuracy of 2D prolongation and restriction subroutines.

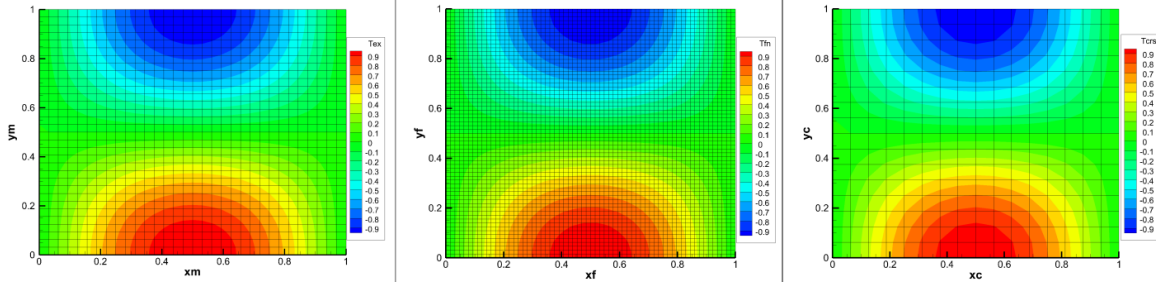


Figure 115. Left) original domain. Middle) Prolonged fine domain. Right) Restricted coarse domain

In simple multigrid procedure, the “Relaxation” procedure is only done on the coarsest grid plus on the way back up to the finest grid. So the correction terms are not smoothed during the move downward toward the coarser grids (only pure transfer of residuals takes place). The procedure adopted here based on Pletcher et al. [241] recommendation, further smooths the correction terms on each level to damp more residual errors. However, the procedure demands slightly more attention. The residuals \mathbb{R}^i from each intermediate level have to be subtracted from the intermediate linear operator $\mathbb{L}(\Delta\phi^i)$ to get the residual of residual \mathbb{R}'^i :

$$\mathbb{R}'^i = \mathbb{R}^i - \mathbb{L}(\Delta\phi^i) \quad (257)$$

and then this new residual is used for the coarser grid to find new corrections $\Delta\phi'$:

$$\mathbb{L}(\Delta\phi') = \mathbb{R}' \quad (258)$$

On the return way to the same level, the corrections are added to the old correction and the sum of these will be solved for the old residual \mathbb{R}^i . In this way:

$$\mathbb{L}(\Delta\phi^i + \Delta\phi') = \mathbb{R}^i \Rightarrow$$

$$\mathbb{L}(\Delta\phi^i) + \mathbb{L}(\Delta\phi') = \mathbb{R}^i \Rightarrow \quad (259)$$

$$\mathbb{L}(\Delta\phi^i) + \mathbb{R}^i - \mathbb{L}(\Delta\phi^i) = \mathbb{R}^i \checkmark$$

Furthermore, the level of multigrid process is extended to 4 to compare the gains. The revised procedure for a 4 level V cycle multigrid is illustrated in Figure 116:

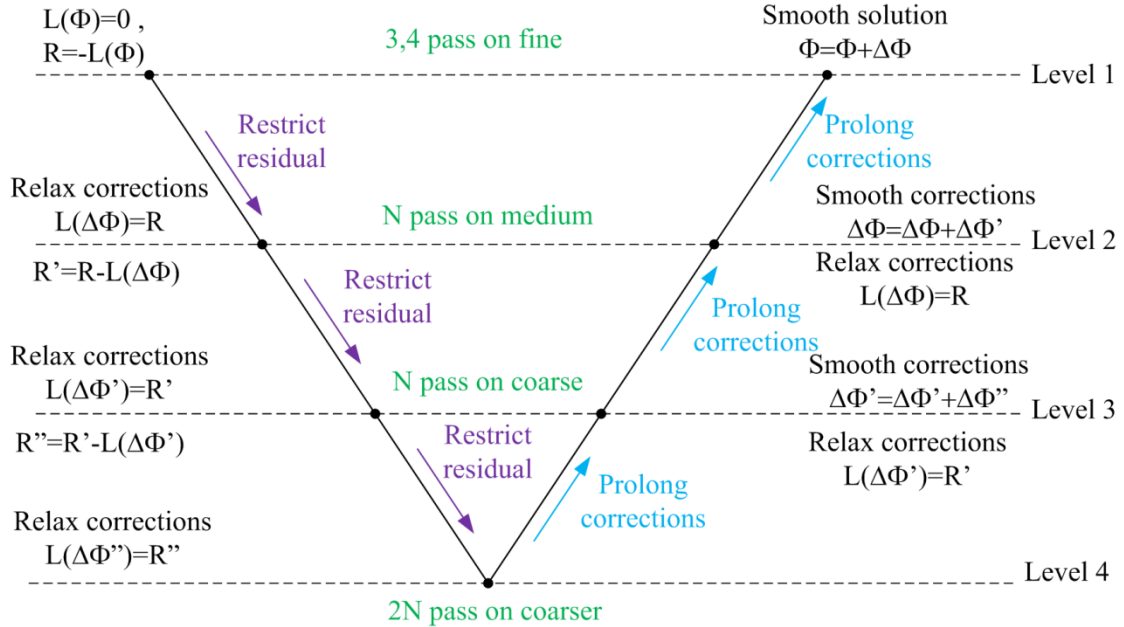


Figure 116. Revised 4 level multigrid V cycle

A 2D Laplace heat conduction equation with simple BCs is solved. The BCs are illustrated in Figure 117:

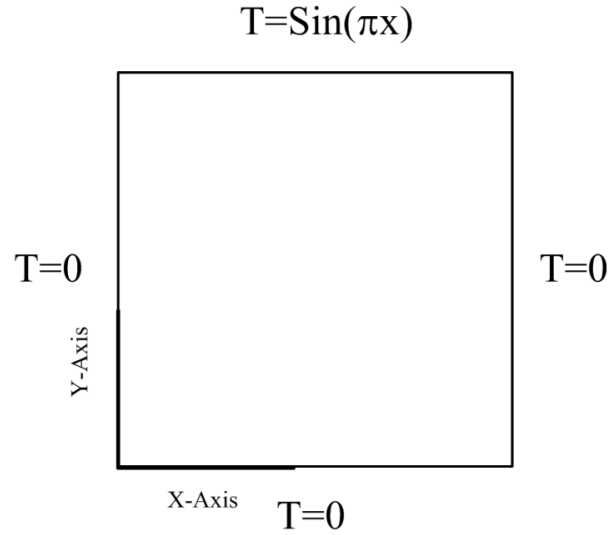


Figure 117. (a) Boundary conditions. (b) Exact solution.

This problem has the exact solution [243]:

$$T = \frac{\sin \pi x \sinh \pi y}{\sinh \pi} \quad (260)$$

The numerical solution (without multigrid) using Jacobi central scheme will be discretized as follows:

$$\frac{\partial^2 T}{\partial x^2} + \frac{\partial^2 T}{\partial y^2} = 0 \Rightarrow \quad (261)$$

$${}^f T_{i,j}^{n+1} = \frac{{}^f \Delta y^2 ({}^f T_{i-1,j}^n + {}^f T_{i+1,j}^n) + {}^f \Delta x^2 ({}^f T_{i,j-1}^n + {}^f T_{i,j+1}^n)}{2({}^f \Delta y^2 + {}^f \Delta x^2)}$$

and the residual:

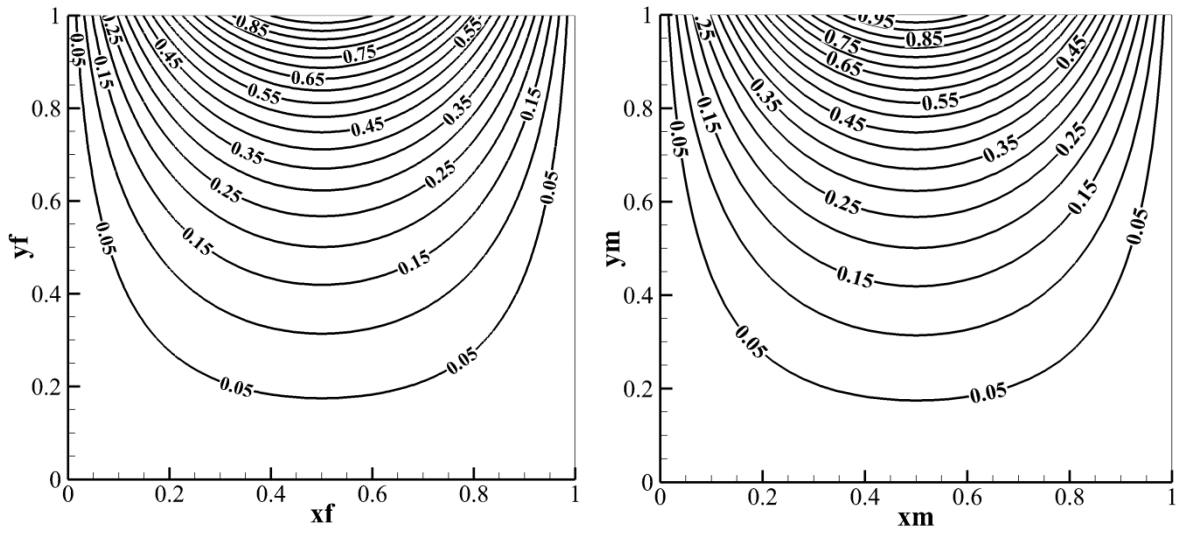
$$f R_{i,j}^{n+1} = \frac{-f T_{i-1,j}^{n+1} + 2f T_{i,j}^{n+1} - f T_{i+1,j}^{n+1}}{f \Delta x^2} + \frac{-f T_{i,j-1}^{n+1} + 2f T_{i,j}^{n+1} - f T_{i,j+1}^{n+1}}{f \Delta y^2} \quad (262)$$

After transferring to the coarse grid, the following smoothing pass will be done or so called “relaxed”:

$$\frac{\Delta T_{i-1,j}^n - 2\Delta T_{i,j}^{n+1} + \Delta T_{i+1,j}^n}{c \Delta x^2} + \frac{\Delta T_{i,j-1}^n - 2\Delta T_{i,j}^{n+1} + \Delta T_{i,j+1}^n}{c \Delta y^2} = c R_{i,j}^{n+1} \quad (263)$$

which is basically the same operator as the solution operator (since it is linear) with the added residual. One should pay attention to set the initial condition for relaxing iterations as zero, since the corrections ΔT approach zero as solution continues and any other value will hinder fast convergence. The boundary values for residuals do not enter the computation on coarse grids, so there is no need to find them. However, the boundary values of the solution variable are required and have to be restricted or imposed directly.

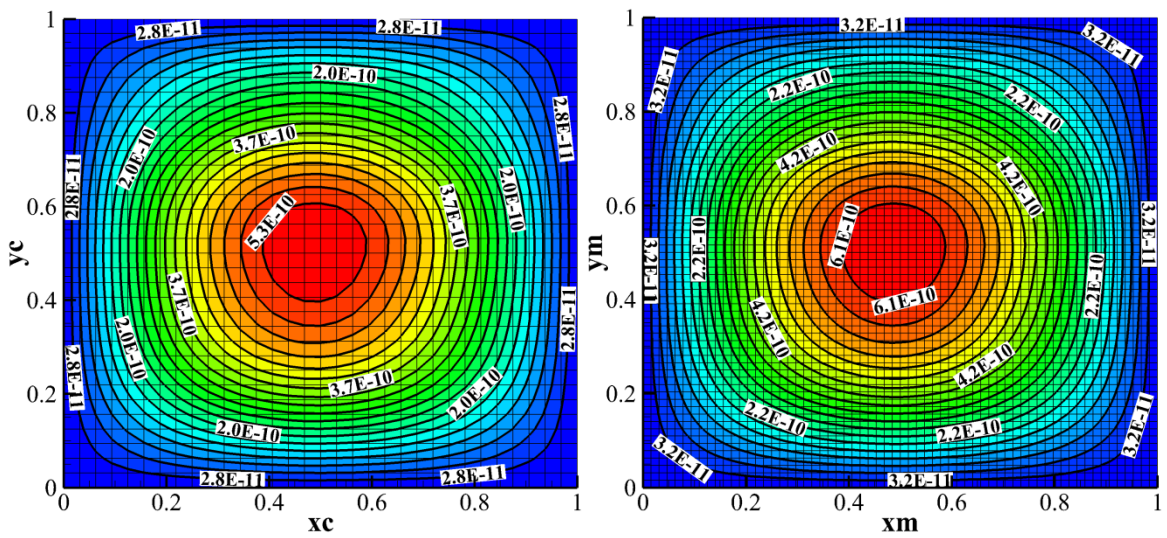
Figure 118 compares the multigrid solution to the exact solution. The errors on both the coarse and medium grids are well damped, as shown in Figure 119:



(a)

(b)

Figure 118. (a) Numerical multigrid solution (b) Exact solution.



(a)

(b)

Figure 119. Multigrid converged residuals on (a) Coarse grid (b) Medium grid

Table 21 compares the performance of single grid, 2 level, 3 level, and 4 level V cycle 2D multigrid in terms of elapsed solution time to reach the second norm of error $L_2 = 1E^{-12}$. Finally Successive Over-Relaxation (SOR) method uses an over-relaxation factor of $\bar{\omega} = 1.45$. All grids have the finest mesh size of 129×129 .

Table 21. Speed-up achieved using 2D Multigrid

Grids	Lvl 1 (no MG)	Lvl 2	Lvl 3	Lvl 4	Lvl 4 SOR
Sol. Time [s]	179.68	17.72	4.33	2.95	2.37
Speed-up	1	10x	41x	61x	75x

According to this table, by combining the multigrid method and SOR only on 2D linear problem, a speed-up of 75x is realized. Therefore, it is reasonable to expect 100x boost in 3D cases which justifies the extra work needed to implement this method for full nonlinear Navier-Stokes equations. The number of iterations is not a good indicative of speed-up since most of iterations in MG version happen on the coarse grid which can be several times less expensive than the fine grid iterations.

Figure 120 shows the convergence rates of all solution schemes, having in mind that iterations run on the 3 level coarser grids are 64 times cheaper. The graph clearly shows the undamped low frequency error component in the level 1 (no MG) convergence history. Soon after the solution starts, the high frequency errors are damped (steep slope) then suddenly the slope reduces (only low frequency errors

remained). However, such discontinuity is not present in the 4 level MG which means all the frequencies are getting damped homogenously.

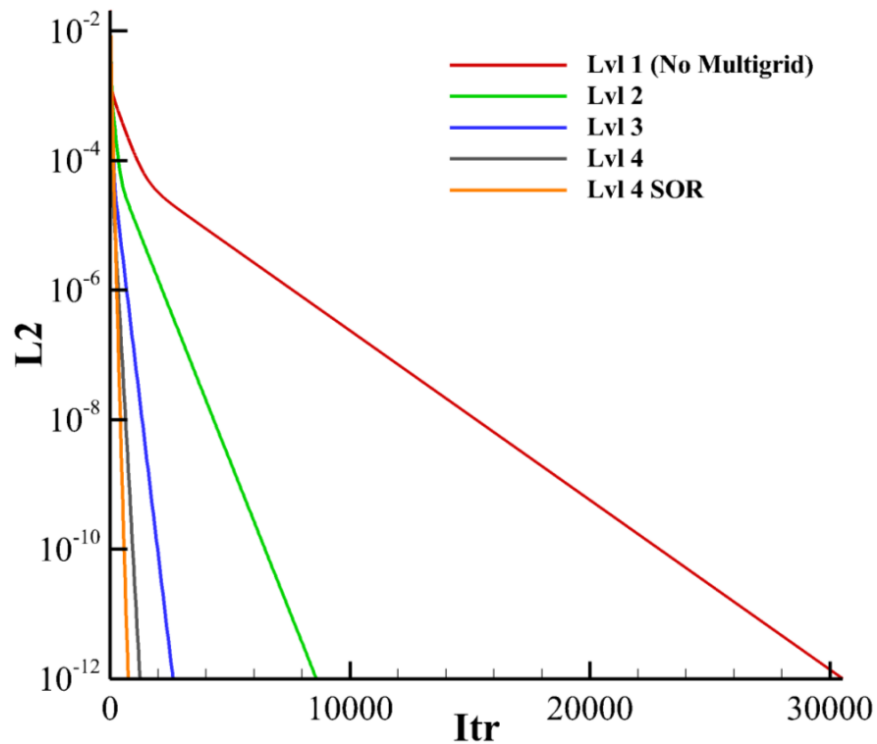


Figure 120. Convergence history of multigrid versus single grid

5.10.8. Nonlinear Multigrid

So far the algorithm for linear multigrid method was covered which is suitable for the SIMPLE solver and applies MG only to Pressure Poisson Equation (PPE). The PCM solver uses density based coupled equations and one should further expand the algorithm to nonlinear form to fully benefit from MG speed-up. To this end, a simple 1D nonlinear case example followed by a 2D NS solution will be introduced.

5.10.8.1. 1D nonlinear multigrid example

The generalized Burgers' equation has the nonlinear format [241]:

$$\frac{\partial u}{\partial t} + (c + bu) \frac{\partial u}{\partial x} = v \frac{\partial^2 u}{\partial x^2} \quad (264)$$

b and c are some constants. Burger's equation is a parabolic equation which can be representative of boundary layer equations if one rewrites the equations in the following form:

$$\frac{\partial u}{\partial x} + u \frac{\partial u}{\partial y} = v \frac{\partial^2 u}{\partial y^2} \quad (265)$$

By choosing $v = 1/2$, $b = -1$ the generalized equation will assume the conservative form:

$$\frac{\partial u}{\partial x} - \frac{\partial u^2}{\partial x} = 2v \frac{\partial^2 u}{\partial x^2} \quad (266)$$

and has the exact solution [244]:

$$u = \frac{1}{2} \left[1 + \tanh \frac{x - x_0}{4v} \right] \quad (267)$$

The nonlinear approach known as Geometric [245] or Full Approximation Storage "FAS" multigrid [241], is introduced here. Many cases in literature have derived the equation in the Δ form. In so many instances, including this code, the equations have been developed in standard form and delta form is not helpful. Hence, a more general approach is sought and the notation of Trottenberg et al. [240] will be followed.

1- Assume the nonlinear form of the approximate solution:

$$\begin{aligned}\mathbb{N}_h \mathbb{w}_h + \mathbb{d}_h &= \mathbb{f}_h \\ \mathbb{N}_H \mathbb{w}_H + \mathbb{d}_H &= \mathbb{f}_H\end{aligned}\tag{268}$$

where h, H show the fine and the coarse grids. \mathbb{N} denotes the nonlinear operator. \mathbb{w}, \mathbb{f} symbolize the approximate solution and an optional source term. \mathbb{d} shows the defect (residual).

2- The exact solution is written as:

$$\begin{aligned}\mathbb{N}_h(\mathbb{w}_h + \mathbb{v}_h) &= \mathbb{f}_h \\ \mathbb{N}_H(\mathbb{w}_H + \mathbb{v}_H) &= \mathbb{f}_H\end{aligned}\tag{269}$$

where \mathbb{v} represents the correction to the approximate solution.

3- If one subtracts the exact solution from the approximate solution:

$$\begin{aligned}\mathbb{N}_h(\mathbb{w}_h + \mathbb{v}_h) - \mathbb{N}_h \mathbb{w}_h &= \mathbb{d}_h \\ \mathbb{N}_H(\mathbb{w}_H + \mathbb{v}_H) - \mathbb{N}_H \mathbb{w}_H &= \mathbb{d}_H\end{aligned}\tag{270}$$

where h, H show the fine and the coarse grids, respectively. \mathbb{N} denotes the nonlinear operator. \mathbb{w}, \mathbb{v} and \mathbb{d} show the exact, approximate and the defect (residual) variables, respectively. The key equation is

$$\mathbb{N}_H(\mathbb{w}_H + \mathbb{v}_H) - \mathbb{N}_H \mathbb{w}_H = \mathbb{d}_H\tag{271}$$

which will be used to find the correction \mathbb{v}_H on the coarse grid, and later prolonged to the fine grid for smoothing the solution. At this point the nonlinear problem will be

solved for \mathbb{w} using any suitable scheme. Then the defect \mathbb{d} will be calculated. The defect will be calculated from the definition (in this case $\mathbb{f} = 0$):

$$\mathbb{d} = \mathbb{f} - \mathbb{N}_h \mathbb{w}_h \quad (272)$$

4- Next, the defect and the solution are restricted and stored onto the coarse grid.

$$\mathbb{w}_H = \mathbb{I}_h^H \mathbb{w}_h, \quad \mathbb{d}_H = \mathbb{I}_h^H \mathbb{d}_h \quad (273)$$

5- The nonlinear operator using the restricted solution is calculated and stored:

$$\mathbb{N}_H \mathbb{w}_H \quad (274)$$

6- At this point two of the terms for the FAS equation are calculated:

$$\mathbb{N}_H(\mathbb{w}_H + \mathbb{v}_H) = \mathbb{d}_H + \mathbb{N}_H \mathbb{w}_H \quad (275)$$

7- The new velocity is defined:

$$\mathbb{w}_H = \mathbb{w}_H + \mathbb{v}_H, \quad \mathbb{f}_H = \mathbb{d}_H + \mathbb{N}_H \mathbb{w}_H \quad (276)$$

So FAS should be solved for \mathbb{w}_H :

$$\mathbb{N}_H(\mathbb{w}_H) = \mathbb{f}_H \quad (277)$$

The terms in **bold** should not change. These terms remain unchanged as the values restricted from the fine grid. The reason lies in Eq. (270) where both the fine and coarse grids should represent the same correction values \mathbb{v} . It is obvious if the source term is updated, the corrections obtained by FAS will not relate to \mathbb{w}_h .

1) Subtract the restricted fine solution \mathbb{w}_H from the new coarse solution \mathbb{w}_H to obtain the coarse correction:

$$\mathbb{V}_H = \mathbb{W}_H - \mathbb{U}_H \quad (278)$$

2) Prolongate the correction to the fine grid using the transfer operator:

$$\mathbb{V}_h = \mathbb{I}_H^h \mathbb{V}_H \quad (279)$$

3) Smooth the solution:

$$\mathbb{U}_h = \mathbb{U}_h + \mathbb{V}_h \quad (280)$$

4) Relax the solution on the fine grid and repeat the cycle till convergence.

$$\mathbb{N}_h(\mathbb{U}_h) = \mathbb{f}_h \quad (281)$$

Moving to the FAS MG, one needs the residual and the solution to be passed to the coarse grid. The residual for McCk will be:

$$\mathbb{R}_i = \frac{1}{2} \left[\frac{1}{\Delta t} (-2\mathbf{U}_i^{n+1} + \mathbf{U}_i^n + \mathbf{U}_i^*) - \frac{1}{\Delta x} (\mathbf{E}_i^* - \mathbf{E}_{i-1}^*) \right] \quad (282)$$

In addition, the nonlinear \mathbb{N} operator needs to be calculated. The multi-level FAS MG is basically similar to the Correction Storage (CS) MG, only minor changes should be applied when passing to more coarse levels as shown below. Note that here one does not relax the corrections, instead the solution is relaxed. Also, both the solution and the residual will be passed at each level. In Figure 121, the symbol N shows the nonlinear operator and S stands for the source term. R symbolizes the residual as was the case in the linear version. Excessive smoothing passes on the medium and coarse grids should be avoided.

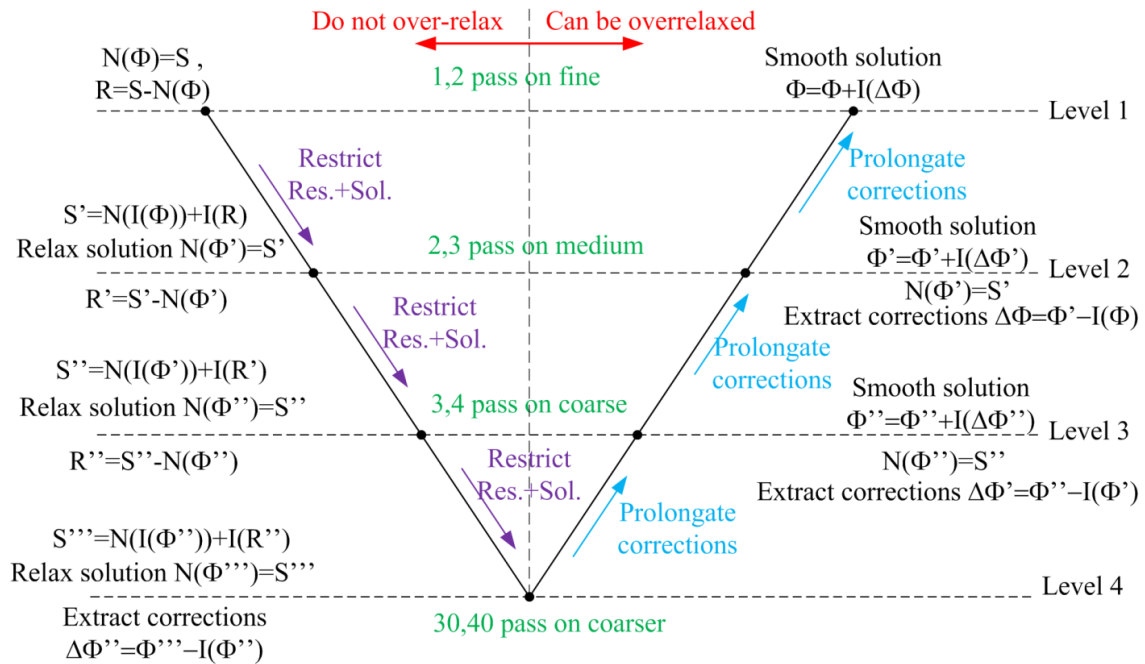


Figure 121. FAS multigrid algorithm for 4 level V cycle

Unlike the CS MG, in FAS MG the solution will converge on the coarser grids, as well. If the solution on the coarsest grid diverges or converges to the wrong solution, then the other ones will not converge in similar manner. Figure 122 illustrates this fact by comparing the solution on 4 grid levels of the same multigrid run.

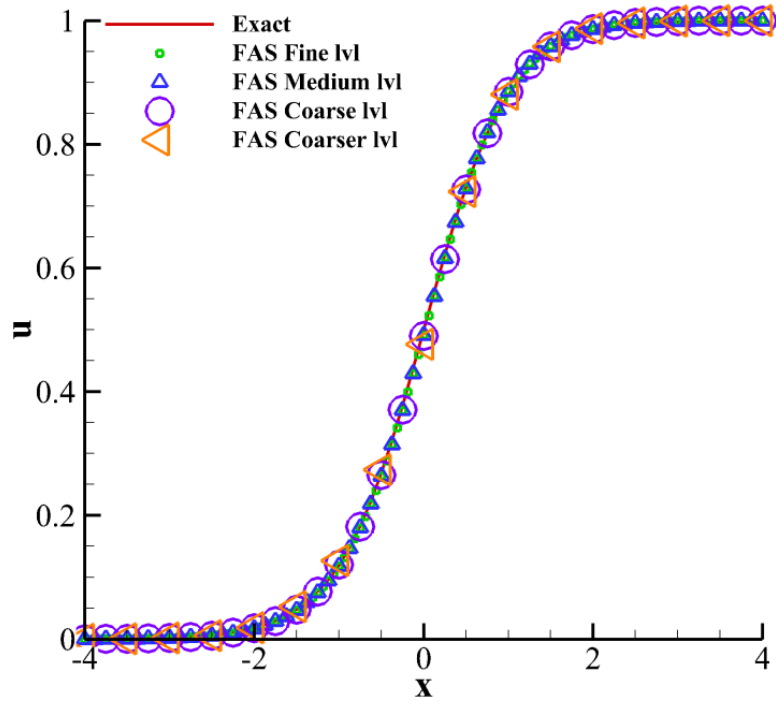


Figure 122. FAS solution converges on all levels (CS solution only converges on the fine grid)

Table 22 compares the speed-up achieved with FAS MG.

Table 22. FAS speed-up on 65 node grid

	McCk	McCk FAS Lvl 2	McCk FAS Lvl 3	McCk FAS Lvl 4	McCk FAS Lvl 4 SOR
Sol. Time [s]	84.46	17.97	4.38	1.7	0.79
Speed-up(x)	1	4.7	19.3	49.7	106.9

The results are quite satisfactory since the governing equation is mixed parabolic-elliptic and the full ellipticity is departed now (which is the best element for MG methods). Still, the 4 level FAS MG McCk was able to achieve about 100X speed-up compared to the standard McCk on 1D domain. This in part is due to the high ellipticity of one sided first derivatives in McCk.

Figure 123 compares the convergence rates of different levels of FAS. The iterations account for the sum of all inner and outer iterations, not only the outer fine iterations.

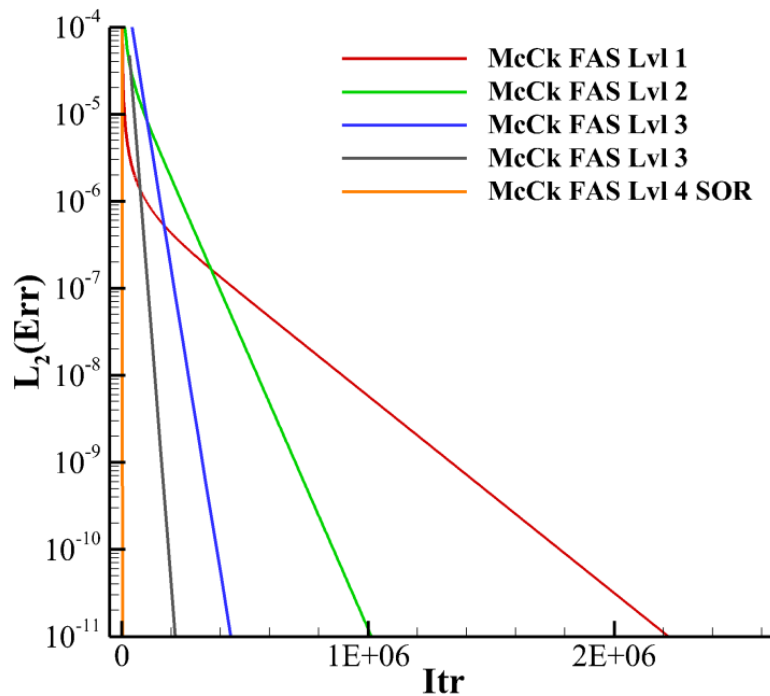


Figure 123. Accelerated convergence rate of McCk with FAS MG scheme

Despite these large savings in computational time, the convergence ratio is about $\hat{q}^m = 0.990$ for the 4 Lvl FAS-MG SOR. Whereas in the case of the linear elliptic Poisson eq. with a 4 Lvl CS-MG the convergence factor of $\hat{q}^m = 0.67$ was achieved which was much more satisfactory. The drop in convergence factor is perhaps associated with the parabolic nature of the problem, the pseudo-compressibility factor β , and its iteration matrix eigenvalues. However to solve the full NS equations such limitations of scheme and stability are imperative.

5.10.8.2. 2D nonlinear multigrid example

The same methodology is applied to NS equations coupled with the continuity equation through PCM. The solver scheme is McCk. Cavity flow is selected to test the algorithm and the performance boost. The problem is solved on a 64×64 grid for $Re = 1000$. Presence of pressure makes the convergence on the coarser grids more difficult than the 1D Burger's equation. Therefore, the Pressure Compatibility Condition is introduced on the different levels of grids to improve pressure convergence. The compatibility condition will be discussed in the next section. Also SOR does not work very well with FAS-MG after the addition of pressure.

The outer loops set the time step for the finest mesh then the time step is doubled for each coarser level of mesh in the inner loops. The results given in Table 23 are obtained after the convergence for pressure has reached $L_2(p) = 10^{-13}$.

Table 23. FAS multigrid speed-up for cavity flow at Re=1000

	McCk	McCk FAS Lvl 2	McCk FAS Lvl 3	McCk FAS Lvl 4
Sol. Time [s]	973.4	78.2	34.1	15.5
Speed-up(x)	1	12.4	28.5	62.8

As the results in the table suggest, FAS could do a satisfactory job with 2D coupled NS equations and about 63 times speed-up was achieved. The performance is slightly lower than the Burger's 1D results which is probably due to the difficulties caused by the pressure and limitations on SOR.

5.11. Pressure Compatibility Condition

Implementation of Pressure Compatibility Condition (PCC) can improve pressure (continuity equation) convergence. This procedure is first shown for the pressure based solver and then it will be adapted to the density based solver. According to Briley [246], the solution to PPE:

$$\nabla^2 p' = \frac{\rho}{\Delta t} \nabla \cdot \mathbf{U}_0 \quad (283)$$

does not generally satisfy the constraint due to the numerical errors:

$$\int_A \nabla^2 p dA = \int_C \frac{\partial p}{\partial n} dC \quad (284)$$

In 2D, A shows the integral area of computational domain, and C shows the domain surrounding circumference (perimeter). This error can be calculated and subtracted from the RHS of PPE. Before solving PPE, calculate:

$$\text{PCC} = \int_A \nabla^2 p dA - \int_C \frac{\partial p}{\partial n} dC \quad (285)$$

over the computational domain. Boundary values should be found using one-sided discretization. Then solve the modified form of PPE:

$$\nabla^2 p' = \frac{\rho}{\Delta t} \nabla \cdot \mathbf{U}_0 - \frac{\text{PCC}}{A} \quad (286)$$

Adding the artificial pressure dissipation is necessary for convergence of SIMPLE at higher Re numbers, otherwise checkerboard effect causes divergence. By adding the PCC condition, the Re=1000 solution converged while all variables (including pressure) could go to machine accuracy (See Figure 124). Previously pressure could not reach such convergence level.

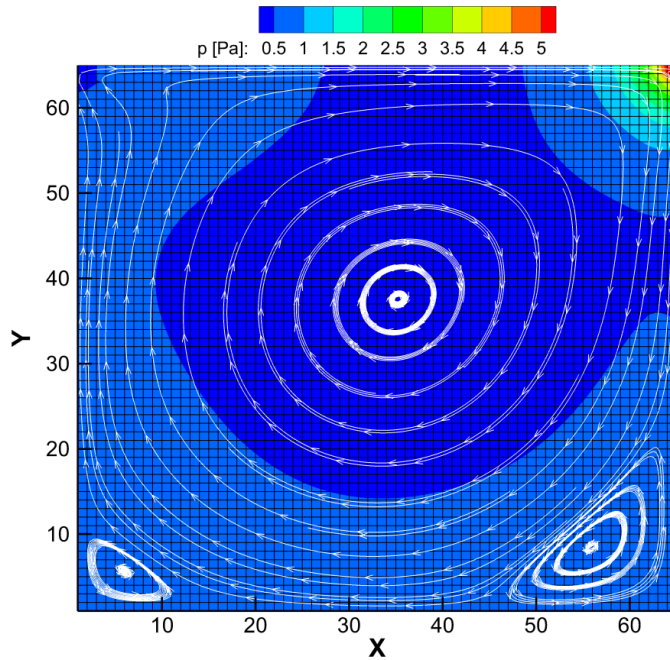


Figure 124. SIMPLE solution to cavity flow at Re=1000 on 65 by 65 grid, using pressure compatibility condition

5.11.1. Adaptation to Pseudo-Compressibility Method

The PCC can be adapted to McCK PCM to reduce $L_2(p)$ and the residual of continuity equation. Basically the pressure compatibility source term should be calculated and added as a source term to the RHS of continuity equation.

$$\frac{\partial p}{\partial t} + \frac{\partial \rho u / \beta}{\partial x} + \frac{\partial \rho v / \beta}{\partial y} = \frac{\text{PCC}}{\Delta t} \quad (287)$$

The PCC term can be either added as a source term to both predictor and corrector steps (\mathbf{H}, \mathbf{H}^* vectors), or can be added directly at the corrector step. Please note that since PCC is a second order second derivative term, the breakdown into predictor-corrector forward/backward discretization will not affect the results.

$$\begin{aligned}
p_{i,j}^{n+1} = \frac{1}{2} \left[(p_{i,j}^n + p_{i,j}^*) - \frac{\Delta t}{\Delta x} (\mathbf{E}_{1i,j}^* - \mathbf{E}_{1i-1,j}^*) - \frac{\Delta t}{\Delta y} (\mathbf{F}_{1i,j}^* - \mathbf{F}_{1i,j-1}^*) \right. \\
\left. + \Delta t \mathbf{S}_{1i,j}^n \right] + \text{PCC}
\end{aligned} \tag{288}$$

To obtain the correct continuity equation residuals, one has to add PCC term to the continuity equation:

$$\begin{aligned}
\mathbb{R}_{1i,j}^{n+1} = \frac{1}{2} \left[-\frac{1}{\Delta x} (\mathbf{E}_{1i+1,j}^n - \mathbf{E}_{1i,j}^n) - \frac{1}{\Delta y} (\mathbf{F}_{1i,j+1}^n - \mathbf{F}_{1i,j}^n) \right. \\
\left. - \frac{1}{\Delta x} (\mathbf{E}_{1i,j}^* - \mathbf{E}_{1i-1,j}^*) - \frac{1}{\Delta y} (\mathbf{F}_{1i,j}^* - \mathbf{F}_{1i,j-1}^*) \right] + \frac{\text{PCC}}{\Delta t}
\end{aligned} \tag{289}$$

where $\mathbb{R}_{1i,j}^{n+1}$ represent the continuity equation residual at each node. Using this PCC adaptation, the McCk PCM scheme is able to achieve machine accuracy for both pressure and continuity residual. Figure 125 compares the results obtained by McCk PCM solver with fully converged pressure residuals (compatibility condition satisfied) against the case without PCC. To show the improvement in convergence of the continuity equation, the residual \mathbb{R}_1 is plotted with and without PCC in Figure 126.

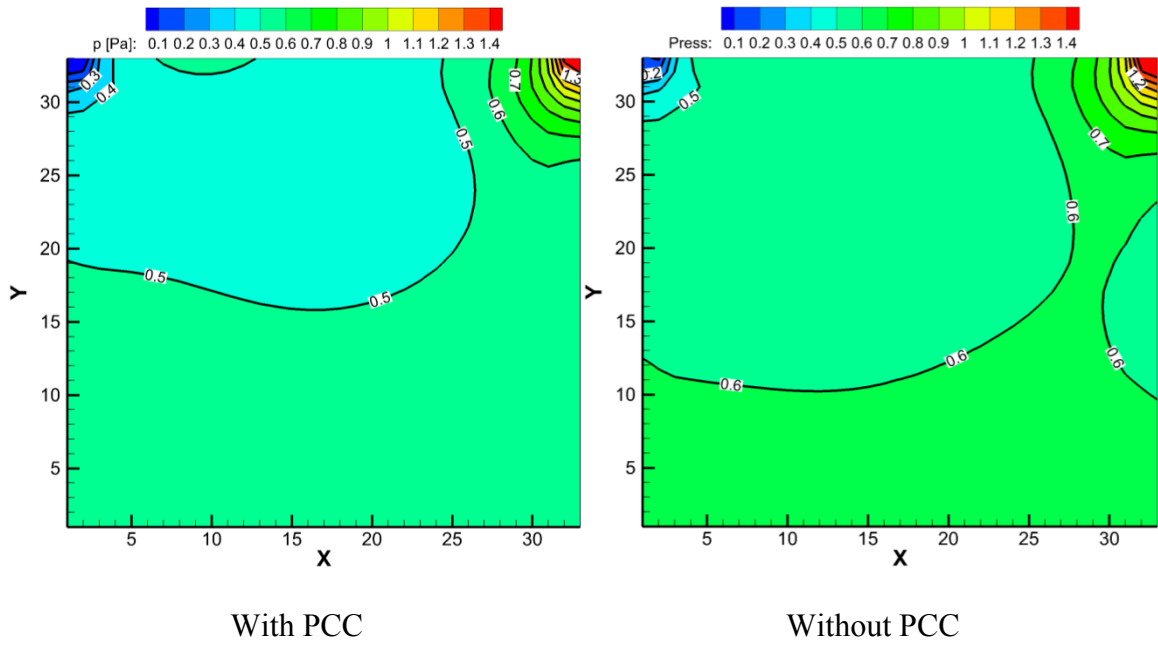


Figure 125. Pressure fields at $Re=100$ for cavity flow with and without PCC

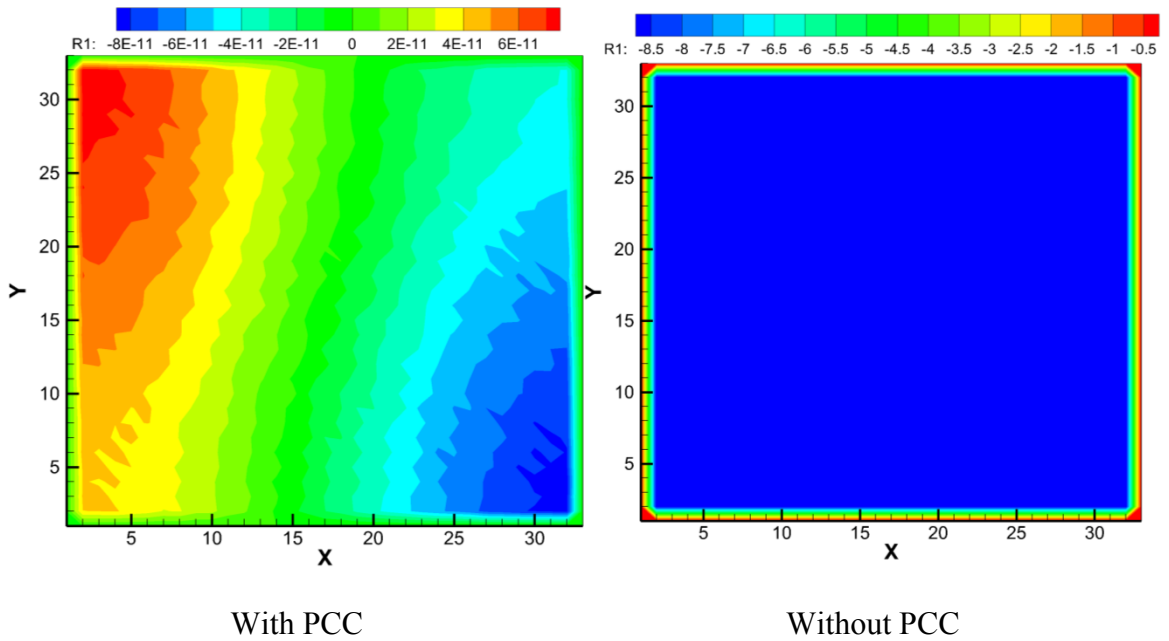


Figure 126. Continuity equation residual with and without PCC

5.12. Parallel Version

An additional way to reduce the solution time is to change the code from single core to parallel version over multiple cores. Details of this adaptation is delivered in the following sections.

5.12.1. MPI

Message Passing Interface (MPI) is a set of libraries used to communicate messages between multiple processes in order to parallelize a code. MPI is also well-developed on FORTRAN and suits the current code. In order to speed-up the code, one can use a distributed memory parallel variation which is enabled by MPI.

In précis, the BCs and the domain are broken into ideally same size sub-domains or pencils. Each process tries to solve its own pencil. New boundaries will form as the original domain is partitioned. These BCs should be passed between processes to update each other of the latest solution. Care has to be taken that all processes move forward with the latest iteration data, with the same time advancement, and not to overwrite newly obtained data before sharing it with other processors.

A typical problem involves developing a serial code, upgrading to single core MPI code, developing 2 core parallel, and then developing multiple core parallel version as it is shown in Figure 127.

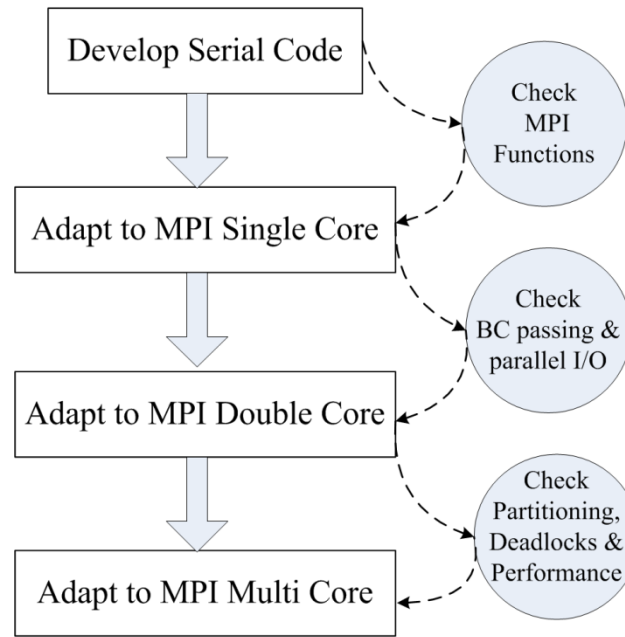


Figure 127. Typical parallelizing steps using MPI

5.12.2. Speed-up Expectation

Certain code takes t_1 seconds to run on serial mode and t_N on parallel mode with N tasks. The actual speed-up ratio is therefore defined as:

$$S = \frac{t_1}{t_N} \quad (290)$$

and the parallel efficiency is defined as:

$$\eta_N = \frac{S}{N} \quad (291)$$

However, in reality, codes are not 100% parallel in nature. There are certain operations which are serial by nature. If the serial fraction of the code is f_s , then no matter how many tasks are running, $f_s t_1$ portion of operation time always computes in serial. It is

the $(1 - f_s)t_1$ portion of the code that can be parallelized. If this parallel portion ideally scales linearly with number of tasks (processors) then the parallel solution time will be:

$$t_N = \left[f_s + \frac{(1 - f_s)}{N} \right] t_1 \quad (292)$$

This relation is known Amdahl's law [247]. It states that if a code is 95% ($f = 0.05$) parallelizable, the max speed-up one can expect from the code ($N \rightarrow \infty$) will be 20x. This is still idealistic. In reality, network latency, memory latency, competition over cache and resources and processor idling causes more deviation from this linear scaling. The practical speed-up relation will be within the limit:

$$S = \frac{t_1}{t_N} < \frac{1}{f_s + \frac{1 - f_s}{N}} < \frac{1}{f_s} \quad (293)$$

As the size of arrays increases, the parallel portion of the code relatively increases. Therefore, the same code parallelizability increases for larger sizes with an acceptable speed-up potential. Fortunately, CFD problems often involve large mesh sizes. Therefore, such investment should be reasonable.

5.12.3. MPI Laminar Helical Flow

The parallel scheme is first applied to laminar helical flow (laminar seal flow) before its adaptation to the turbulent version. The details of BCs and the exact solution are introduced later in the validation section. The geometry is illustrated in Figure 128.

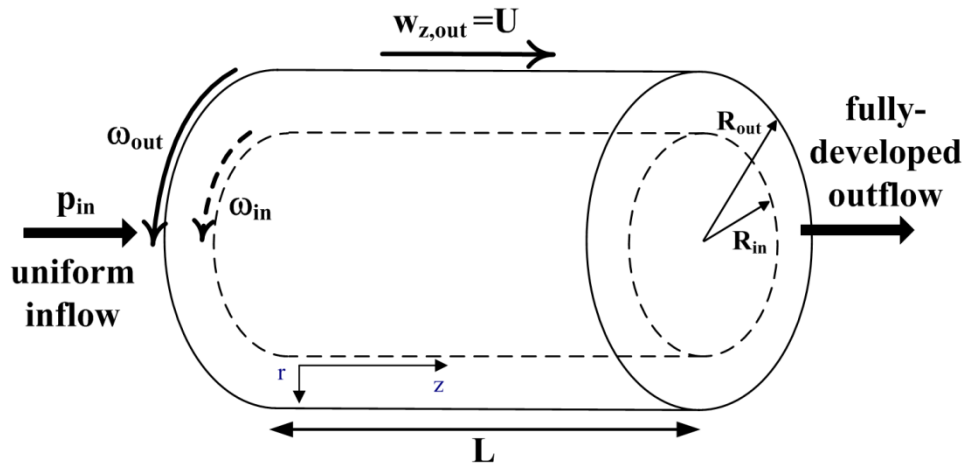


Figure 128. Boundary conditions for the laminar helical flow

The domain is only partitioned in r (radial) direction, since the seal flow has sharp gradients in radial direction and if 1D partition is selected, it is reasonable to be along this direction which usually has more nodes. Figure 129 shows the selection of partitions (pencils).

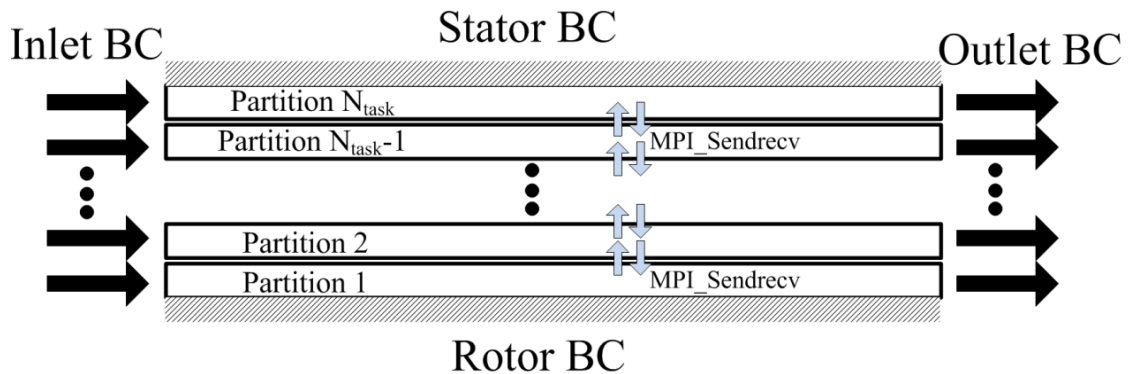


Figure 129. Radial partitioning of the annular domain

5.12.3.1. Overlap

Note that there is an overlap region between each two pencils. The portioning is intentionally made overlapping so that the same code can apply to serial, dual and multi core simulations. In single core simulation, the inner and outer boundary is supplied by wall condition. In parallel, the inner and outer BC for intermediate pencils comes from the adjacent partitions. Hence, the adjacent partition needs to share the boundary of the current partition. The boundary is solved as an interior node for the adjacent partition and then passed to current partition as a boundary node (will not be solved in current node). Since the overlapping nodes are only solved once, the total cost will not increase. Figure 130 depicts these overlapping partitions.

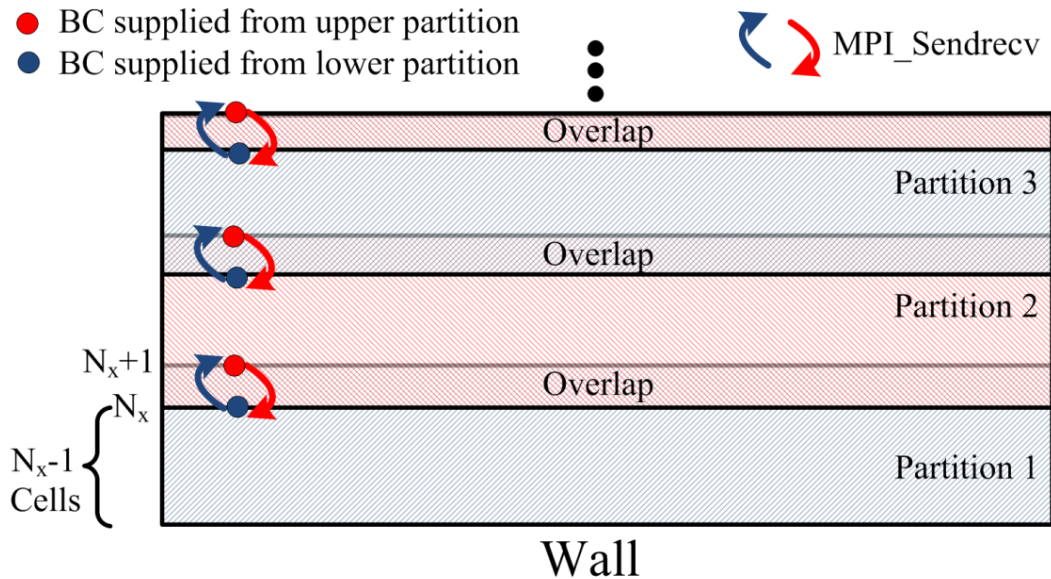


Figure 130. Overlapping cells and passing boundary conditions

5.12.3.2. Explicit BC and synchrony

At the beginning of each time-step, the boundary values from last time step are shared between processors. This is natural to the McCk scheme due to its explicit formulation. Thus, there is no asynchrony (delay) in supplied boundary values which is an actual problem with implicit solvers. The BCs need to be shared two times at each time step, once in the predictor step, and once in the corrector step. *MPI_Sendrecv* function has been used for this purpose. A local residual target causes some processes finish earlier than the others and deadlock occurs. Therefore a global residual target has to be enforced.

5.12.3.3. Partition sizing

Due to the overlapping nodes, care should be taken in setting each partition size and when the final results are assembled into a single file. The single core (total) number of nodes in r direction is $N_r + 2$ (2 for boundary nodes) and the total number of cells is $N_r + 1$. If n_{task} number of tasks (processors, partitions, pencils, cores, ...), are selected, the total number of cell size in a single partition N_x can be found from the following:

$$N_x = \left[\frac{N + 1}{n_{task}} \right] + 1 \quad (294)$$

If it is a single core run, the +1 is dropped. The bracket is used to make sure each partition has an integer number of cells. Because of this, the last partition cell size may be different from the other partitions and it is shown with N_{xl} which can be found from:

$$N_{xl} = N + 1 - (n_{task} - 1)(N_x - 1) \quad (295)$$

5.12.3.4. Results

The accuracy of the solution will be discussed in the validation case. Figure 131 shows the speed-up gained using MPI for this problem. This form of scaling analysis is called strong analysis which the size of the problem is fixed and the number of cores are increased.

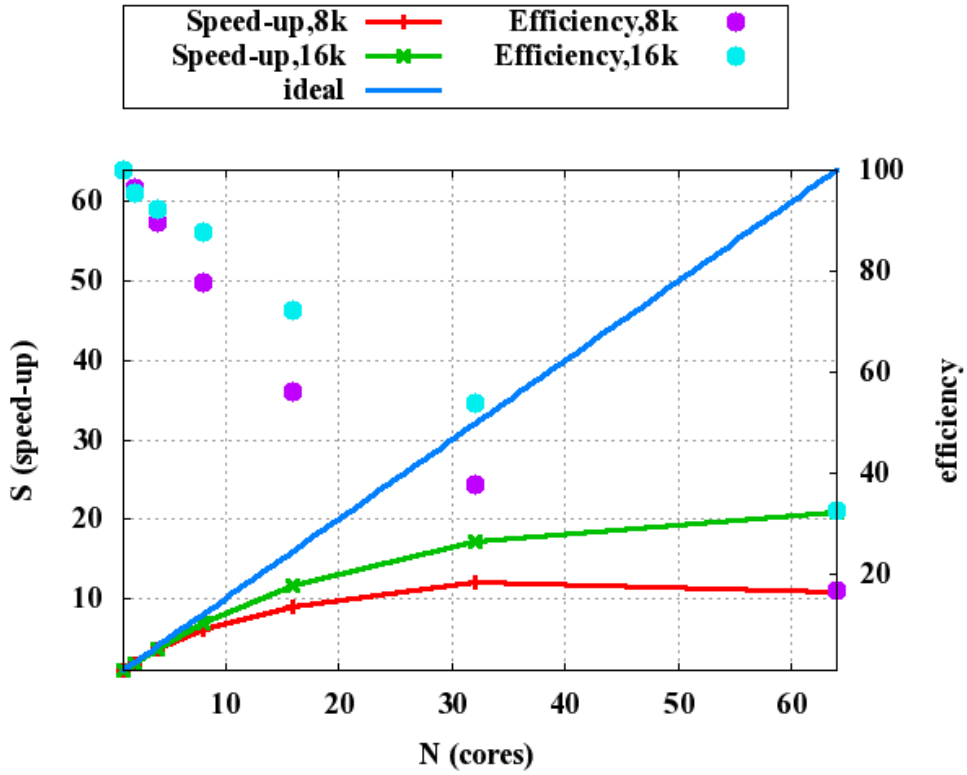


Figure 131. Speed-up achieved for helical flow with MPI parallel

Ideally the speed-up curve should follow a linear growth with the number of core. However, in reality the parallel efficiency drops as the number of cores increase (See Figure 131). With the 256×64 grid, the MPI version could achieve 21X speed-up over 64 cores. The realistic number of cores for a regular PC is 8 cores which gives a almost 90% efficiency. Table 24 shows the speed gain and elapsed time for the solution with the second norm of axial velocity's convergence of $L_2(w_z) = 10^{-6}$:

Table 24. Speed-up and solution time data for the 256×64 grid

Cores	Solution Time (s)	Speed-up (x)	Parallel efficiency (%)
1	230.4	1.0	100
2	120.6	1.9	95.4
4	62.4	3.7	92.2
8	32.8	7.0	87.7
16	19.9	11.6	72.3
32	13.3	17.2	53.8
64	11.0	20.9	32.6

5.12.4. MPI Turbulent Annular Seal

The methodology applied to the laminar helical flow for parallel version has been modified and extended to the turbulent seal version. Effects of computational imbalance are discussed and addressed.

5.12.4.1. Collective operations

Collective operations are required to receive or send data simultaneously to or from multiple processors. The main collective operations are *broadcast*, *gather*, *scatter*, and *reduce* (*MPI_Bcast*, *MPI_Gather*, *MPI_Scatter* and *MPI_Reduce*) [248]. All collective operations are blocking, and there is no need to use *MPI_Barrier* to enforce synchrony. Figure 132 shows the *broadcast* operation as an example.

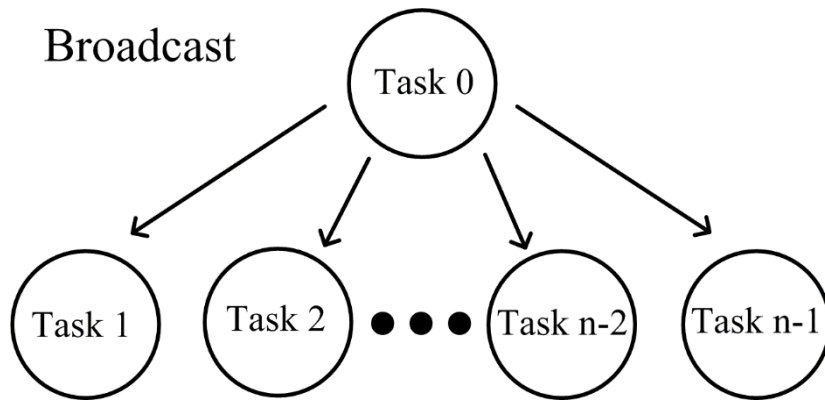


Figure 132. MPI broadcast operation

In this problem, the collective operation *MPI_Allreduce* has been utilized to set the global time-step for stability reasons. Basically, each processor finds its own maximum allowable time-step locally and then shares the local time-step with all other processors to find the global maximum allowable time-step. This is in fact set by the minimum of all shared time-steps. Such communication is necessary to make sure all partitions advance in time with the same speed, otherwise the BCs shared at the end of each time step will be asynchronous. Figure 133 shows this collective operation.

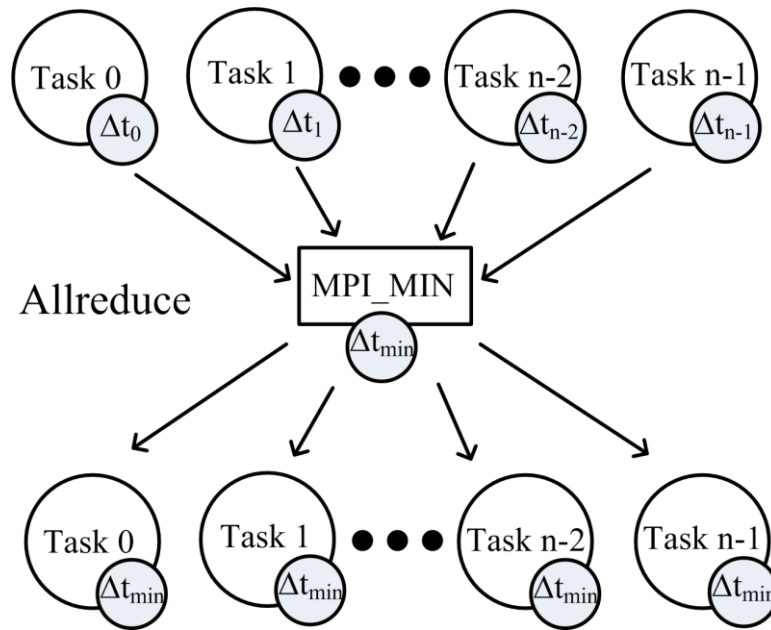


Figure 133. MPI allreduce operation used to set the global time step

MPI_Allreduce is equivalent to an *MPI_Reduce* followed by an *MPI_Bcast*, but this compact version makes the code shorter, improves the efficiency and the reliability of communication.

5.12.4.2. Two by two communications

Previously in the laminar regime, the parallel code used a simultaneous send and receive between all adjacent processes. Meaning there was no priority that a given processes communicates with the one process before or the one after it. This flexible scheduling will cause competition and idling on a very efficient communication scheme, since two of the processes “go on a rendezvous” and the other adjacent two are idle. A more efficient scheme (but more troublesome to implement) is to schedule two by two communications at a time. In the first step, the odd processors only meet with

the processors ahead of them, and even processors only meet with the ones before them. In the second step, this order is reversed. As a result, all tasks always have a matching task exclusively waiting for them and idling is avoided. The two by two communication is shown in Figure 134.

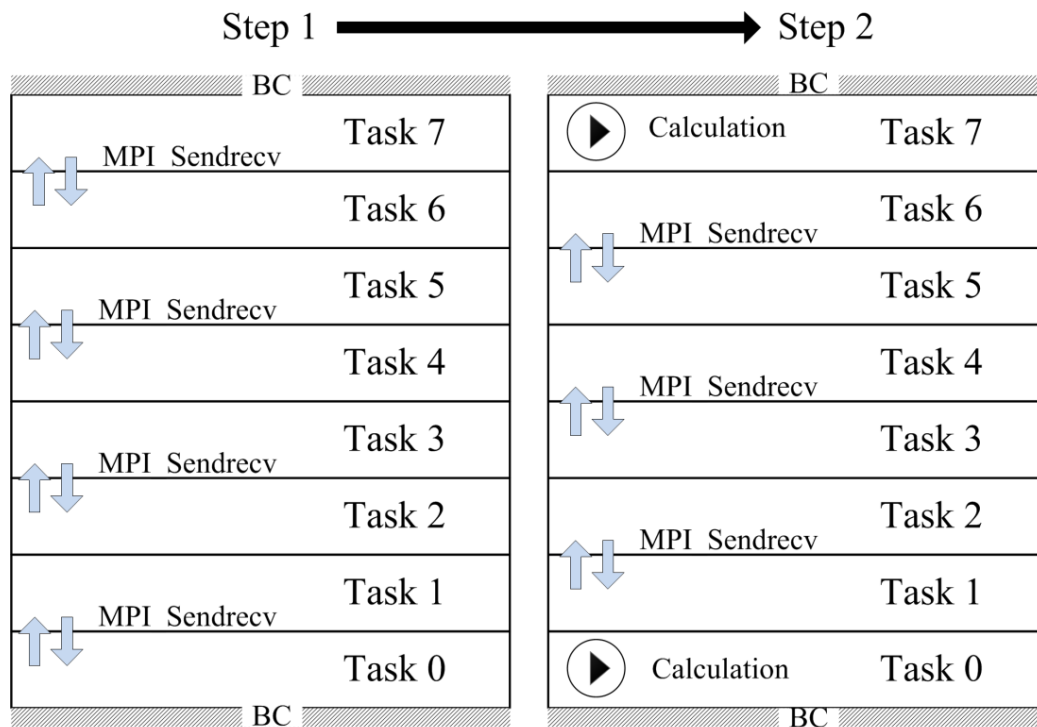


Figure 134. Two by two communication

This approach has a second advantage: the boundary partitions only participate in the first step and they can start doing their own calculations sooner than the other partitions. This is desirable because the boundary processors always have larger loads due to the extra BC calculations which the intermediate partitions are exempt from.

5.12.4.3. Speed-up results

A grid size of $64 \times 64 = 4096$ grid points has been selected to model the developing flow inside the plain annular seal. A wall-function has been used to avoid modeling the inner layer. At first, the parallel version does not show a great scaling in contrast to the laminar version. The best speed-up for this problem is about 3 times as stated in Table 25.

Table 25. Speed-up results for turbulent annular seal on a 64×64 grid with $L_2(w_z)=10^{-4}$

Cores	Solution Time (s)	Speed-up (x)	Parallel efficiency (%)
1	502.5	1.0	100
2	269.0	1.9	93.4
4	193.3	2.6	65.0
8	186.1	2.7	33.7
16	195.3	2.6	16.1

5.12.4.4. Load balancing

Time probes can be inserted in the code to identify the bottleneck in the parallel performance. The communication time consumed by each communication phase is aggregated to a total communication time for each task. The results showed two important trends, both of which reduce parallel performance. First, the maximum total communication time rapidly grows when the number of partitions increase. Second, the

communication time for the intermediate partitions is several time larger than the boundary nodes. This was not the case in the laminar mode, and the reason will be discussed in the coming sections. In any case, these two observations point toward a load imbalance between boundary partitions and intermediate partitions. More specifically the intermediate partitions finish their job early and wait for the boundary partitions.

Imbalance easily limits the maximum speed-up attainable. To reduce its effects, the uniform partitioning, which was adopted in the laminar mode, has been upgraded to a biased partitioning for the boundaries. In other words, the number of assigned nodes in the boundaries will be substantially lower than the intermediate nodes to balance the load. A parameter called *master* has been defined in the *decomposition* subroutine to control the level of bias for the master partitions and slave partitions. The last partition has N_{xl} cells which is ideally very close to the master partition cells N_{xm} . In order to accommodate integer number of cells in each partition, the leftover cells are passed to the last partition (but still $N_{xl} < N_x$). Figure 135 shows the new balanced partitioning.

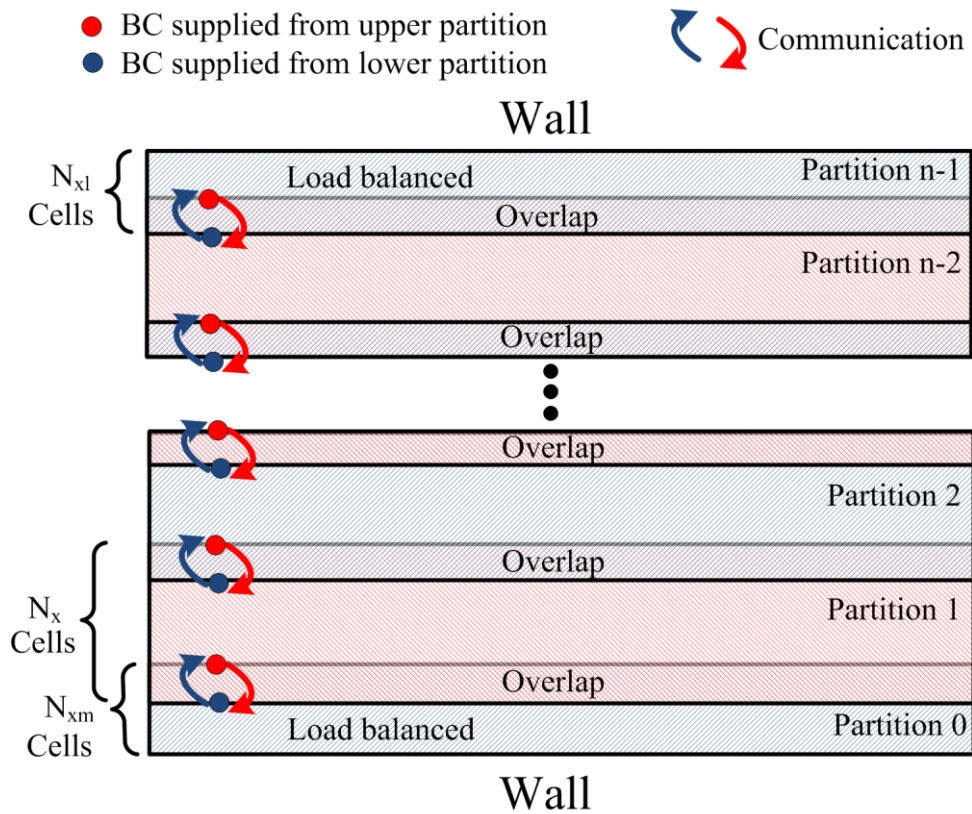


Figure 135. Balancing the loads of the partitions

5.12.4.5. Extra wall load

As was discussed before, the boundary partitions in the current problem have extra load which was not present in the laminar mode. The reason is that the boundary processes contain the wall BC in turbulent mode. In most of turbulent applications, a wall-function is used to reduce the difficulties present due to direct wall modeling. The wall-function solves a transcendental equation at each time step which has to be iterated for a large number using the bisection algorithm. This extra calculation induces a large imbalance in the wall partitions. This is usually more costly for the rotating walls.

The minimum number of nodes that can be assigned to certain partition is 3 nodes due the McCk stencil shape. In other words, if the number of partitions is increased to the point that master partition has 3 nodes and slave partitions have 8 nodes, then the imbalance is unavoidable. So the imbalance multiplier is only helpful if this ratio of master to slave can be maintained at a high ratio.

5.12.4.6. Improving parallel performance

In order to improve speed-up, the wall-function problem was changed to a high Re problem without wall-function. This reduces the imbalance. Also a fully-developed BC was used to minimize the number of nodes in z direction and increase the number of nodes in r direction. This way the imbalance due to BCs will reduces and the total load on each partition is kept constant. The domain size is 256×16 . The large nodes in r direction allows for better load balancing. The new results are given in Table 26:

Table 26. Improved speed-up results

Cores	Solution Time (s)	Speed-up (x)	Parallel Efficiency (%)	Comm. Time (s)	Load Balance Factor
1	78.1	1.0	100	0.5	1.0
2	41.1	1.8	94.9	1.8	1.0
4	28.1	2.8	69.3	1.6	0.9
8	17.1	4.6	57.2	3.2	0.6
16	8.6	9.0	56.4	2.2	0.4

According to the table the speed-up on 16 core increased from 3 times to 9 times due to better load balancing and reducing the communication overhead. This new performance is acceptable and close to the laminar version (12x on 16 cores). The speed-up probably increases more than 9, but current small size of the problem causes minimum node number per partition with 32 core tests on Ada and results are not available. Figure 136 shows the speed-up and efficiency results.

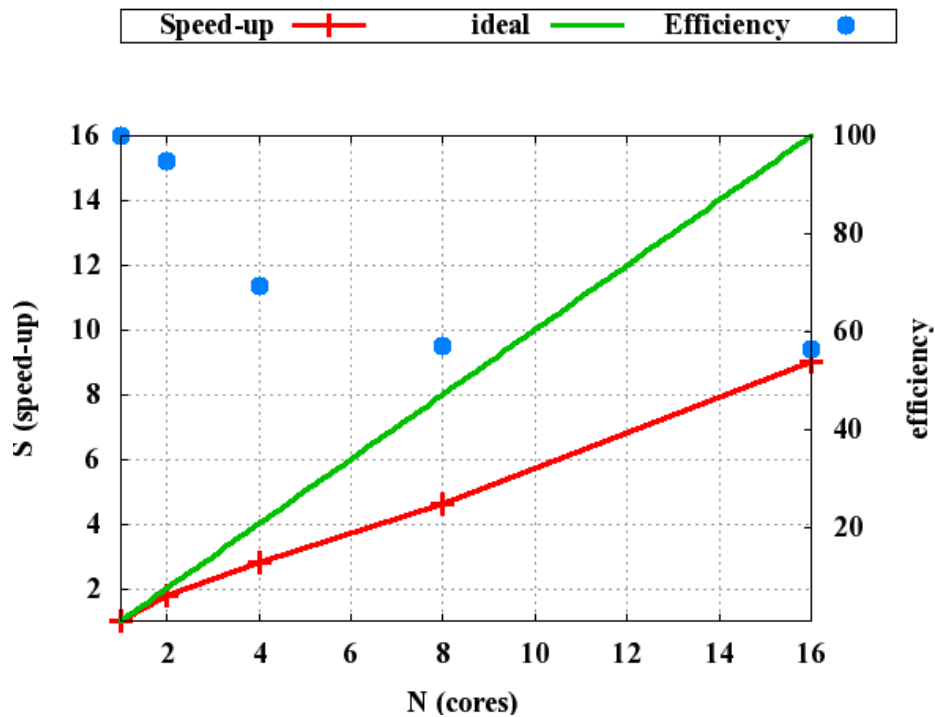


Figure 136. Speed-up improvement for the turbulent annular seal code after adding load balance

Figure 137 shows the communication time for this problem. The communication time is measured for the processor with lowest load (highest communication time).

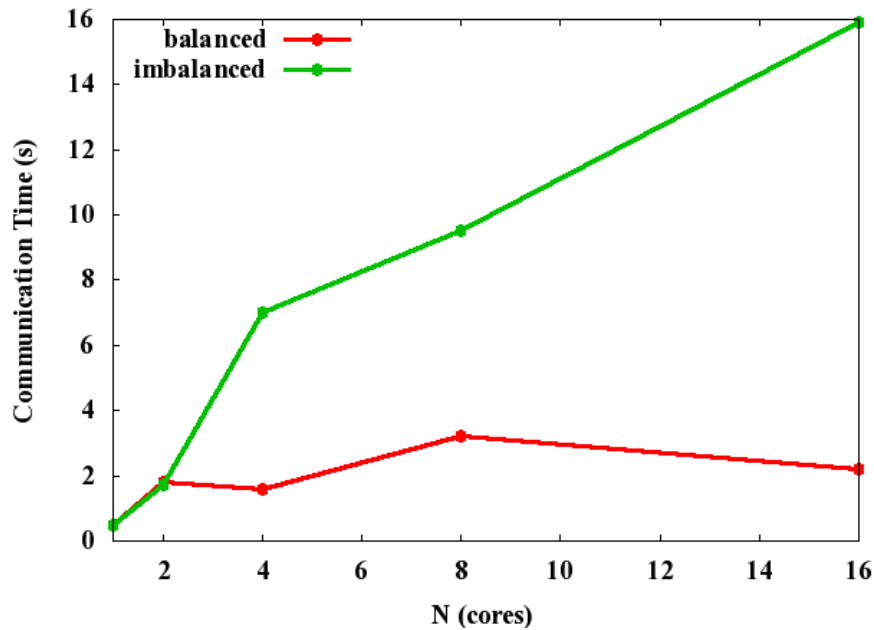


Figure 137. Communication time

Communication times should ideally reduce as the number of cores increases since the size of messages will reduce. However, competition for resources, network latency and imbalance actually result in the same order or even larger communication times.

5.13. Validation

Several cases have been studied in order to validate the code. Some of the cases were only checked for qualitative agreement and some cases for stricter quantitative agreement.

5.13.1. Cavity Flow in Cartesian Coordinate

The cavity flow is a well-known problem to test soundness of a CFD code. The problem consists of a square domain with stationary walls except for the top wall which is dragging the flow with certain speed. McCK works very well with all spectrums of Re

number and agrees with literature [249]. The development of corner vortices is adequately captured with a coarser grid (40×40) which is a characteristic of the code second order accuracy (See Figure 138 and Figure 139).

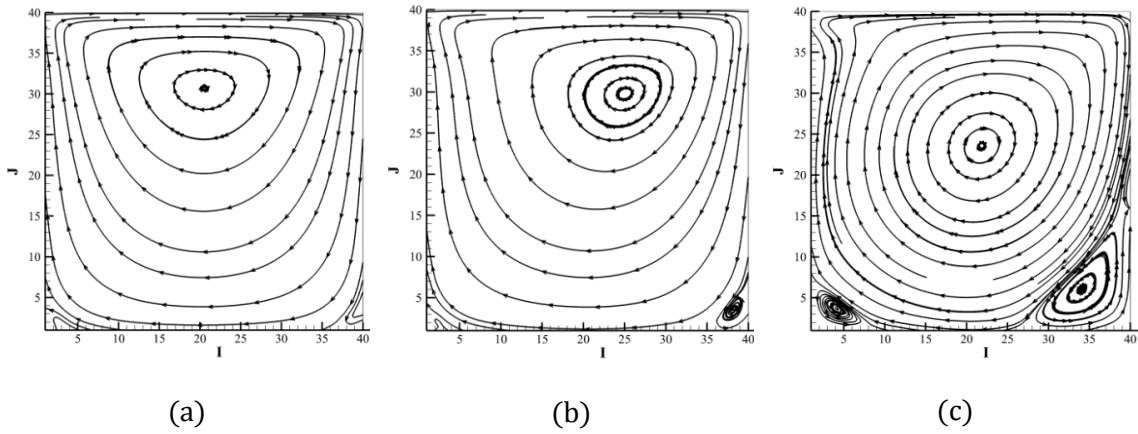


Figure 138. a) $Re=1 \beta=0.1$. b) $Re=100 \beta=100$.c) $Re=1000 \beta=10$

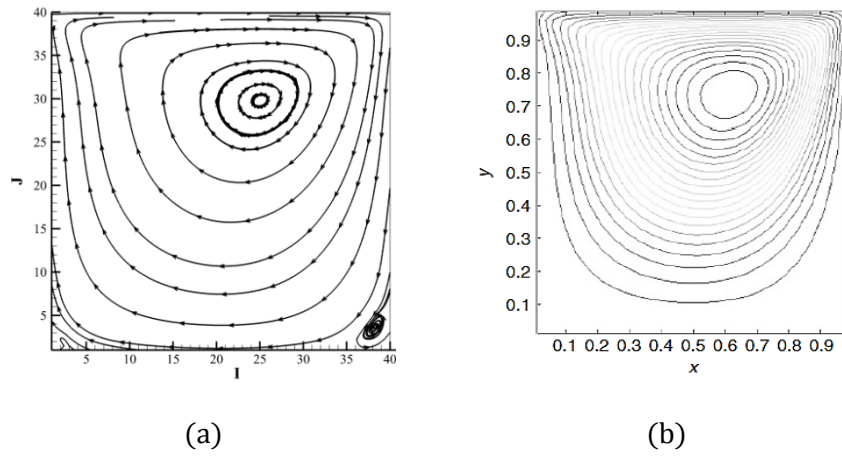


Figure 139. Cavity flow $Re=100$, (a) Current CFD code, (b) Hirsch (adapted from [249])

A comparison of pressure field between various methods test are given in Figure 140. Observe that the collocated grid in upwind method suffers from the checkerboard effect[250] and the staggered grid still suffers from large numerical diffusion:

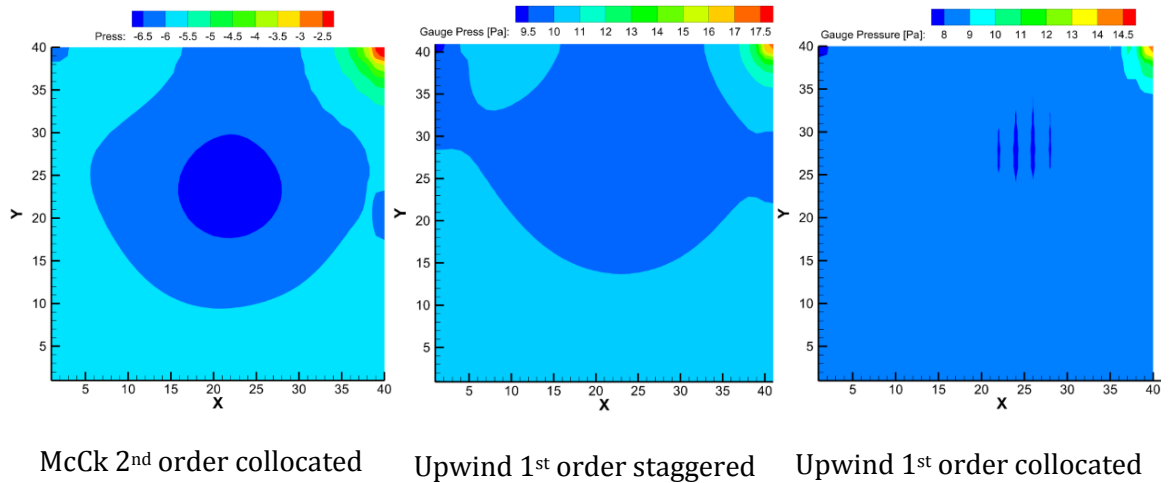


Figure 140. Pressure distribution $Re=10$

5.13.2. Taylor-Couette Flow in Stationary Frame

This case checks the code ability to model swirling flows and capturing secondary flows [251] (Taylor vortices). Governing equations are the same as general axisymmetric case. The schematic in Figure 141 shows the geometry. The inner cylinder rotates while the outer cylinder, the top and bottom walls are held fixed. This problem will from the vortices [252] inside the cavity while all three components of velocity are present. Figure 142 shows the secondary flow and vortex structure captured by the code. The streamlines refer to $\omega = 40 \text{ rad/s}$, $Re_{\theta} = 600$ and $C_r/L = 0.33$. High Re numbers with rotating inner wall cannot be simulated due to hydrodynamic stability.

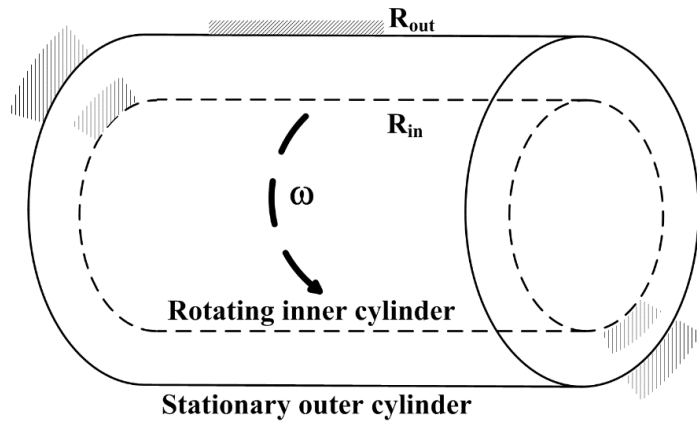


Figure 141. Confined flow in cylindrical coordinate

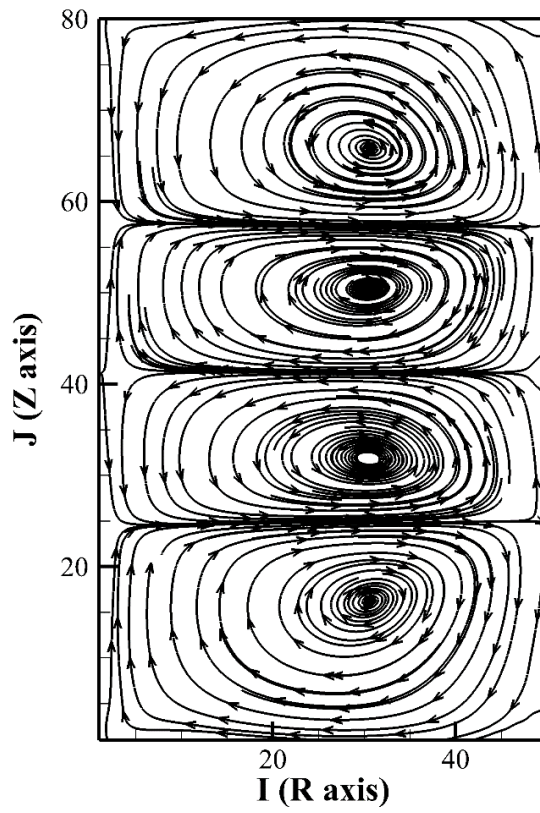


Figure 142 . Secondary flows in an annular cavity with rotating outer wall at $Re_{\theta}=600$

5.13.3. Fully Developed Steady Helical Flow Inside an Annulus

The exact solution will be derived for a steady coaxial pipe where the inner and outer walls rotate with speed of ω_{in} and ω_{out} , respectively. The flow is fully developed so the axial pressure gradient is a constant $\partial p/\partial z = G$ and other derivatives with respect to z cancel. The flow is axisymmetric, hence $\partial/\partial\theta = 0$. One can optionally introduce an axial drag flow by moving the outer wall axially by speed U . A schematic of the problem is sketched below:

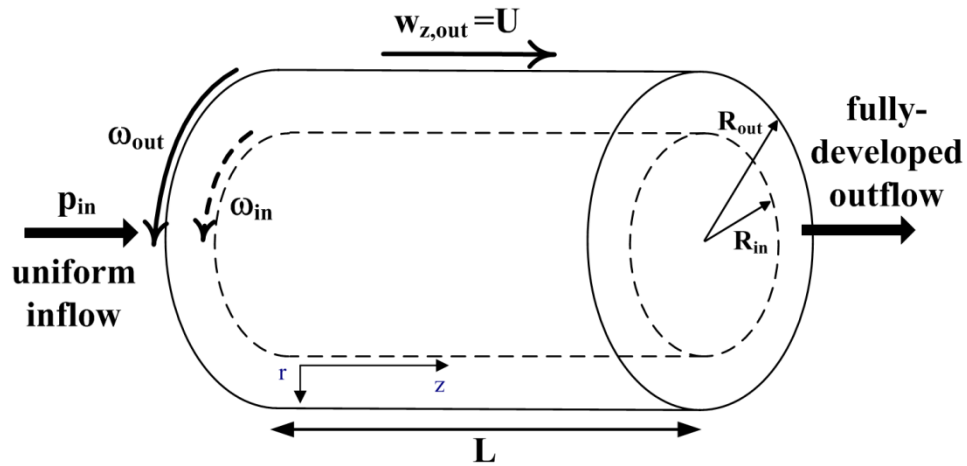


Figure 143. Schematic of helical flow geometry

with the BCs:

$$@r = R_{in}, \quad w_r = w_z = 0, \quad w_\theta = R_{in}\omega_{in} \quad (296)$$

$$@r = R_{out}, \quad w_r = 0, \quad w_z = U, \quad w_\theta = R_{out}\omega_{out} \quad (297)$$

The critical assumptions from the flow condition:

$$w_r = 0, \quad w_\theta = w_\theta(r), \quad w_z = w_z(r) \quad (298)$$

Then NS equations in cylindrical coordinate are simplified to:

$$\frac{w_\theta^2}{r} = \frac{1}{\rho} \frac{\partial p}{\partial r} \quad (299)$$

$$\frac{1}{r} \frac{\partial w_\theta}{\partial r} + \frac{\partial^2 w_\theta}{\partial r^2} - \frac{w_\theta}{r^2} = 0 \quad (300)$$

$$\mu \left(\frac{1}{r} \frac{\partial w_z}{\partial r} + \frac{\partial^2 w_z}{\partial r^2} \right) = \frac{\partial p}{\partial z} = -G \quad (301)$$

which decouples the θ and z momentum equations. Here G is the constant pressure gradient Then the exact solution will be [253]:

$$w_z = \frac{G}{4\mu} \left[R_{in}^2 - r^2 + \frac{(R_{out}^2 - R_{in}^2) \ln(r/R_{in})}{\ln(R_{out}/R_{in})} \right] + U \frac{\ln(r/R_{in})}{\ln(R_{out}/R_{in})} \quad (302)$$

$$w_\theta = \left(\frac{R_{out}^2 \omega_{out} - R_{in}^2 \omega_{in}}{R_{out}^2 - R_{in}^2} \right) r + \left(\frac{\omega_{in} - \omega_{out}}{R_{out}^2 - R_{in}^2} \right) \frac{R_{in}^2 R_{out}^2}{r} \quad (303)$$

$$p = C - Gz + \rho \int_{R_{in}}^r \frac{w_\theta^2}{r} dr \quad (304)$$

or,

$$\begin{aligned}
p = C - Gz + \rho & \left[\left(\frac{R_{out}^2 \omega_{out} - R_{in}^2 \omega_{in}}{R_{out}^2 - R_{in}^2} \right)^2 \left(\frac{r^2 - R_{in}^2}{2} \right) \right. \\
& + \left(\frac{\omega_{in} - \omega_{out}}{R_{out}^2 - R_{in}^2} R_{in}^2 R_{out}^2 \right)^2 \left(\frac{1}{2R_{in}^2} - \frac{1}{2r^2} \right) \\
& \left. + 2 \left(\frac{R_{out}^2 \omega_{out} - R_{in}^2 \omega_{in}}{R_{out}^2 - R_{in}^2} \right) \left(\frac{\omega_{in} - \omega_{out}}{R_{out}^2 - R_{in}^2} R_{in}^2 R_{out}^2 \right) \ln \frac{r}{R_{in}} \right]
\end{aligned} \tag{305}$$

where C is a constant for absolute pressure and can be dropped for gauge pressure. One can drop U in the solution to get coaxial pipe flow in z direction. The θ direction is the same as Taylor-Couette flow [251].

With a change of frame according to Figure 144 the problem can be solved in rotating frame:

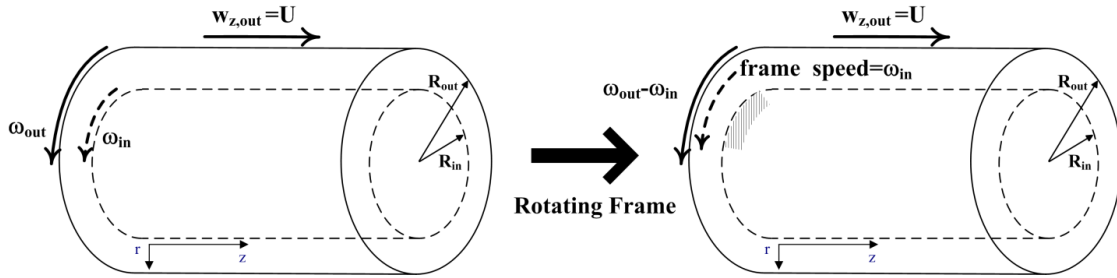


Figure 144. Change of frame

Pressure BCs at walls are found after dropping the vanishing terms,

$$\frac{\partial p}{\partial r} = \mu \left(\frac{\partial^2 w_r}{\partial r^2} \right) + \frac{\rho w_\theta^2}{r} + \text{ROT}(+2\rho\omega w_\theta + \rho r\omega^2) \tag{306}$$

which is discretized in backward second order at the outer wall and forward second order at inner wall. Both boundary conditions are independent of stationary/rotating frame and reduce to same expressions which means pressure is indifferent to frame change which is physical. Other boundary conditions are given in Table 27:

Table 27. Boundary conditions for helical flow inside an annulus

	$r = R_{in}$	$r = R_{out}$	$z = 0$	$z = Length$
p	Neumann forward	Neumann backward	Extrapolation	Constant gradient
w_z	No-slip	No-slip	Fixed/uniform	Fully developed
w_r	No-slip	No-slip	Fixed	Fully developed
w_θ	No-slip (non-rotating)	No-slip (rotating)	Pre-swirl/uniform	Fully developed

The results in Figure 145 and Figure 146 are obtained for $C_r = 0.01 m$, $L = 0.5m$, $\omega_{in} = 10 rad/s$, $\omega_{out} = 0 rad/s$, $U = 0.25 m/s$ $Re_\theta = 157.5$, $Re_z = 250$ and $Re_{tot} = 161$ and compared to the exact solution. The CFD solution closely matches the exact solution.

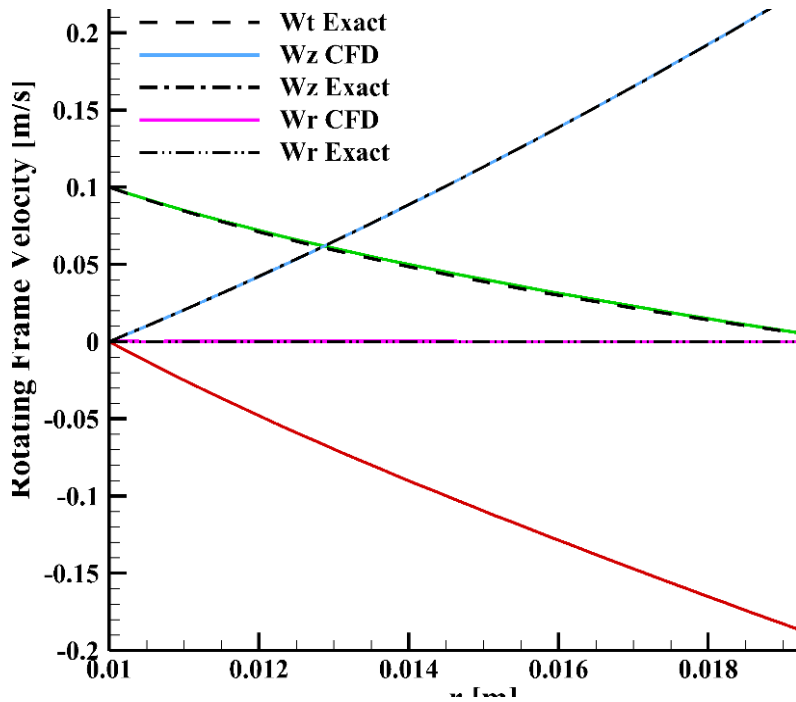


Figure 145. Helical flow, CFD vs exact solution

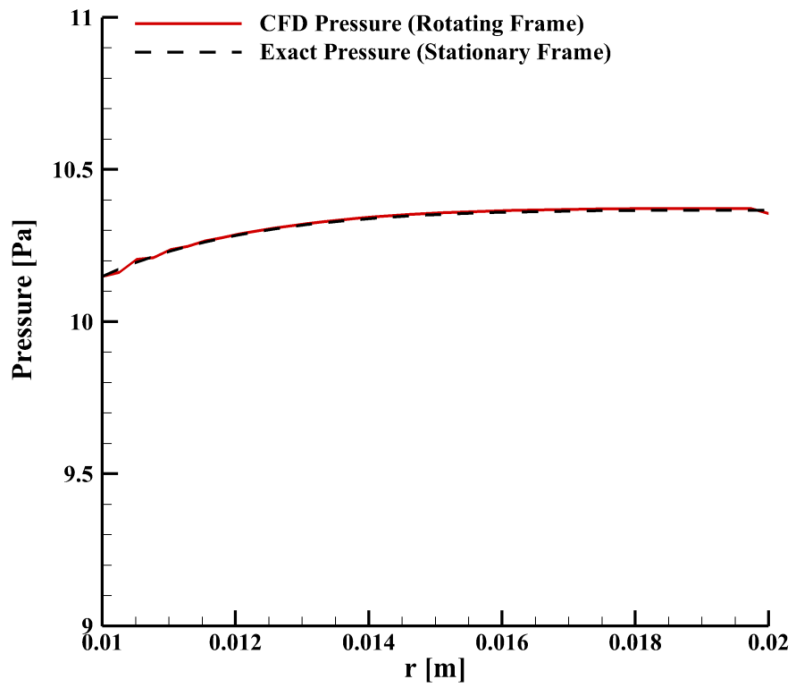


Figure 146. Helical flow pressure, CFD vs exact solution

5.13.4. Backward Facing Step Flow

In this case move to implementation of the more advanced problem with 2 blocks and an interface. Now the incoming flow has a uniform flow and at the interface the flow will become fully developed. There are two approaches to model multi-block flows.

One that is employed here is to put an interface and find the values at interface as by interpolation. Then using that values as new BCs for each block. This approach is tedious and requires introduction of 3 new BCs to a step-flow problem; in the current McCK approach, 6 new BCs should be introduced due to predictor and corrector steps. Also, new flux vectors should be implemented at new boundaries.

Second approach is to assign a very large viscosity μ_{∞} to the inactive block [218]. Then the very viscous fluid acts like a solid and suddenly the wall BCs surrounding the block will diffuse to the whole inactive block. As a result, the new boundaries will be the regions where there is a jump in viscosity. This procedure is much simpler to implement but wastes computational power (Not only because of the grid but also because of the numerical stiffness). In large problems, this method becomes impractical and therefore it is not practiced here.

Governing equations remain the same as axisymmetric flow for rotating frame. Although for these case, the rotation has been deactivated. BCs are given in Table 28:

Table 28. Boundary conditions for backward facing step

	$R_{in,1}, R_{in,2}$	R_{out}	Inlet	Step	Interface	Outlet
p	Neumann forward	Neumann backward	Extrapolation	Neumann forward	Interpolation	Constant gradient
w_z	No-slip	No-slip	Fixed/uniform	No-slip	Interpolation	Fully developed
w_r	No-slip	No-slip	Fixed/zero	No-slip	Interpolation	Fully developed
w_θ	No-slip	No-slip	Fixed/zero	No-slip	Interpolation	Fully developed

Figure 148 refers to $C_r = 0.04\text{ m}$, $L = 0.6\text{ m}$, with inlet opening of $0.5C_r$ and $Re = 120$.

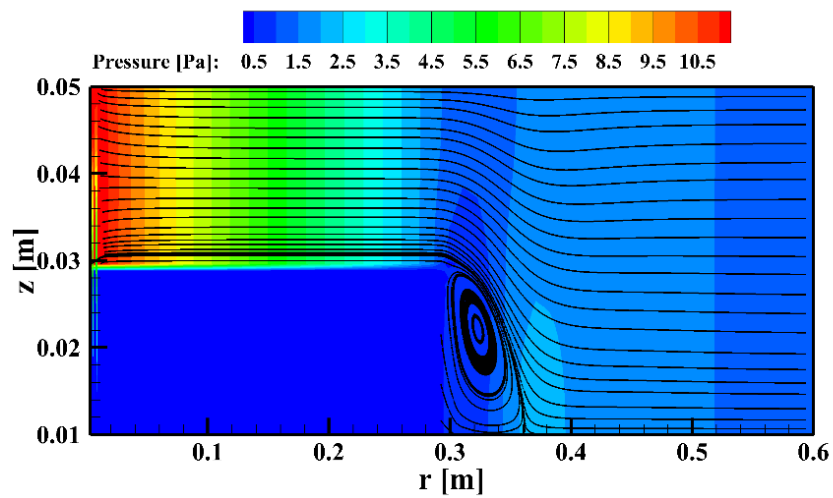


Figure 147. Backward facing step, pressure field

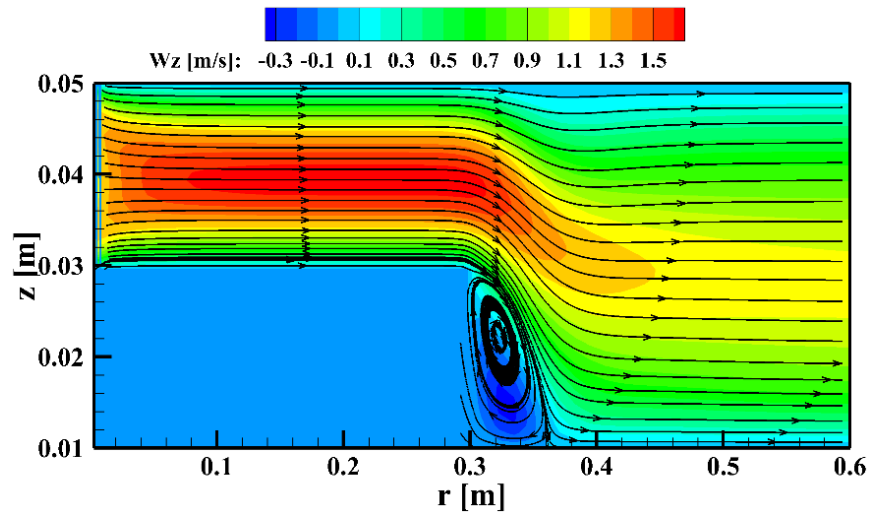


Figure 148. Backward facing step, axial velocity field

The significance of this flow lies in its similarity to grooved seals. The number of interfaces and BCs will be increased which calls for implementation of subroutines. Although there are numerous experimental measurements of backward facing step in channel geometry and in axisymmetric case with a symmetry line BC (not confined with inner-outer wall, instead symmetry line has been used either in place of inner wall or outer wall), similar case for an annular axisymmetric case is not available. Fortunately, there is a numerical study that provides reattachment length data and the results are compared with this study [254]. All the dimensions are set similar to those selected by validation case. The reattachment length z_r is illustrated in Figure 149.

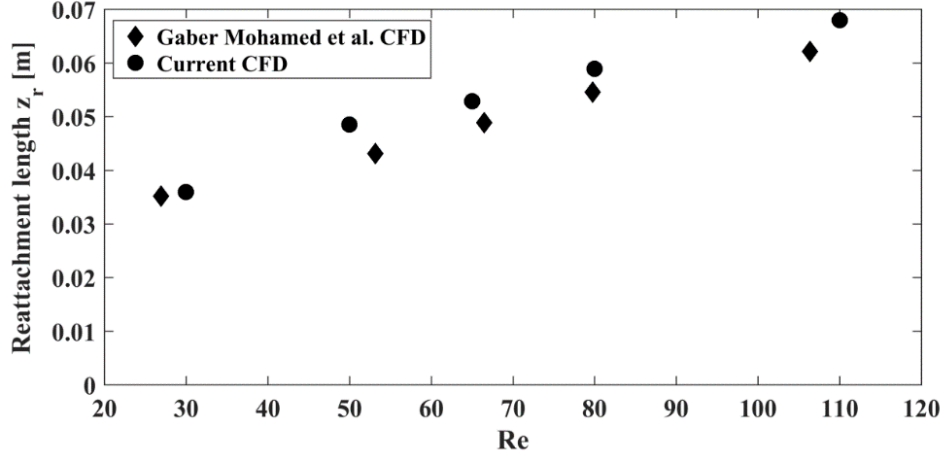


Figure 149. Current code prediction vs literature (validation adapted from [254])

The slight difference may be due to the fact that Gaber Mohamed et al. [254] used a fourth order method while current approach uses a second order discretization. Also, their outflow is closer to the step place (3 times the step size) while in current case outflow is further down the stream to ensure fully-developed condition.

It is preferred to provide static-pressure only at either inlet or outlet to have a better convergence. Nevertheless, it is possible to implement a pressure-pressure combination of BCs both at inlet and outlet. This BC goes well with zero-gradient inlet and outlet. However, one cannot use Dirichlet BC for all velocity terms and pressure at inlet [255]. Therefore, the inlet velocity condition preferably will be changed to zero-gradient (Neumann) for w_z to save the freedom to control inlet pre-swirl ratio through w_θ Dirichlet condition. The same problem can be solved in the rotating frame with an inner rotating wall (See Figure 150).

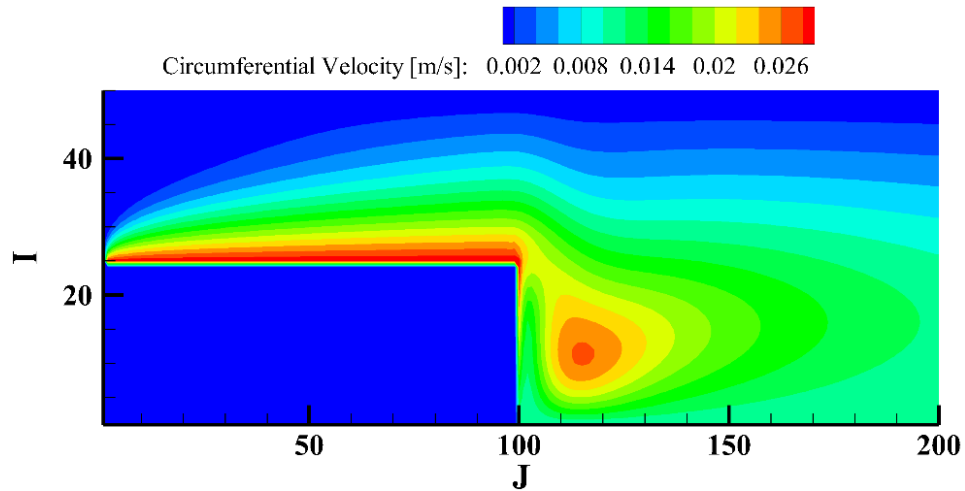


Figure 150. Pressure-pressure CFD solution of rotating BFS with PSR=0.0

5.13.5. Wall-function and Low-Re Predictions for Pipe Flow

The results correspond to the turbulent pipe flow at $Re = 6500$ with a uniform grid. The small number of cells in the case of wall-function greatly reduced computational cost and convergence time. Compared to the Low-Re results for the same Re number, wall-function grid size is 11 times smaller and convergence times almost 9 times faster. A summary of this comparison is given in Table 29:

Table 29. Low Re results vs High Re $k-\omega$ with wall-functions

Model	Grid size	Convergence	Run time (Single core)
Low Reynolds	252×27	4 orders	67 min
Wall-function	52×12	5 orders	9 min

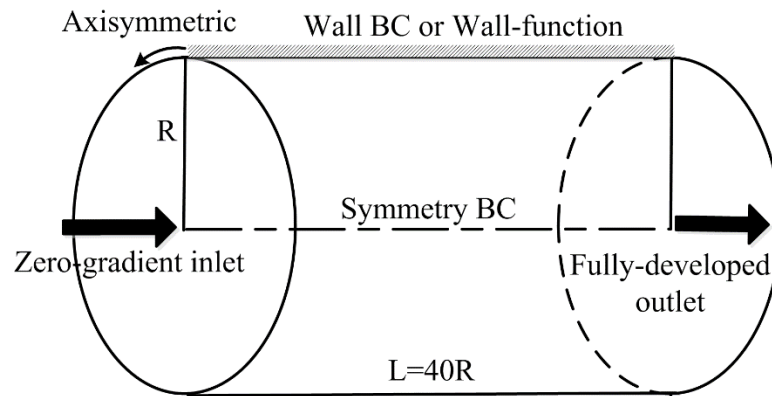


Figure 151. Fully developed turbulent pipe flow boundary conditions

Figure 151 shows the boundary conditions. For the inlet zero-gradient BC has been selected which is the most robust BC in turbulence modeling since there is no prior knowledge of turbulence parameter distribution at inlet. Zero-gradient BC removes this difficulty. At outlet fully developed condition has been implemented for the same reason. Also fully developed pipe flow allows to compare the simulation results to the well-known power-law profile. Pressure drop across the pipe is $\Delta p = 100 \text{ pa}$. Figure 152 shows the profile at outlet closely matches the power-law profile (for $Re = 6500$ the exponent is about 6). Note that the inner layer including viscous sublayer and buffer layer is not modelled with the benefit of wall-functions while low- Re version models the whole profile all the way to the wall. Since $Re = 6500$ is fairly low Re number for turbulent flows, the inner layer has a considerable thickness compared to the outer layer.

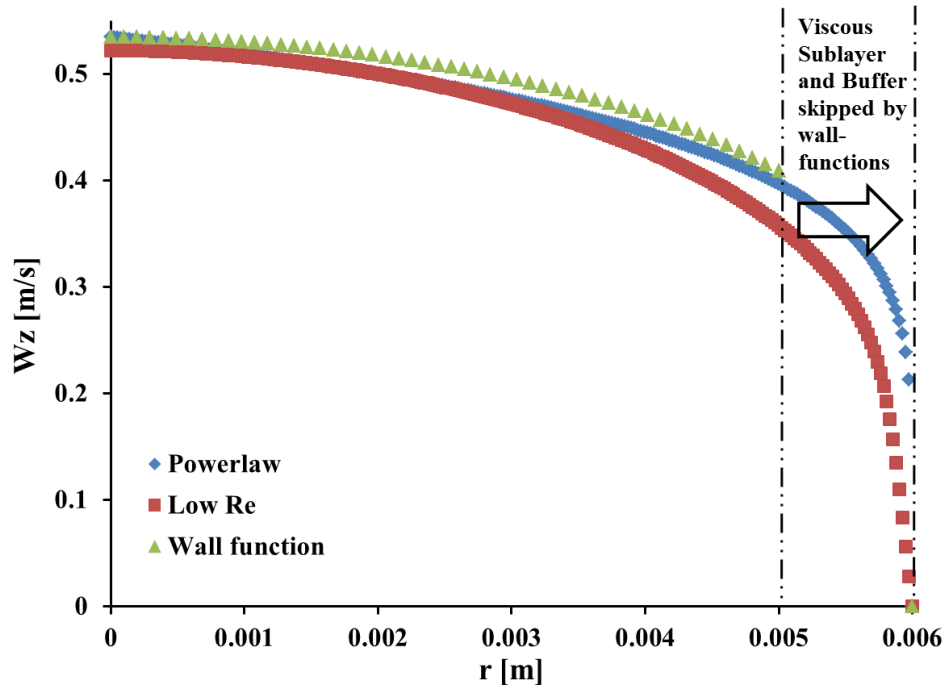


Figure 152. Velocity profile prediction of Low Re model, high Re with wall-function and power law

The skin friction predictions are compared with Moody chart [256] values in Table 30.

Table 30. Skin friction CFD versus Moody chart at Re=6500

	Moody	Low Re	Wall-Function
C_f	0.0087	0.0086	0.0076

Wilcox model could predict the turbulent pipe flow with zero-inlet BC successfully. The error associated with wall-functions grows smaller and smaller as the Re number increases and better convergence criteria is fulfilled.

5.13.6. Low Re Seal Leakage

The plain annular seal geometry in Table 31 has been selected for comparison:

Table 31. Plain annular seal dimensions and operational conditions

R_{in} [mm]	C_r [μm]	L [mm]	Fluid	Δp [Pa]	ω [rad/s]
50.8	203	50.8	ISO VG-2	807000	209.4

These settings mimic close operational conditions to Moreland and Childs[49]. Leakage rate of the seal is the metric selected for validation. Table 32 compares the Reynolds numbers from experiments and the current CFD code. In Moreland experiments Re_z is based on measured leakage, but Re_θ is not actually measured but calculated from simple 1D theoretical relations. The CFD Re_θ is based on average circumferential velocity across clearance.

$$\bar{v}_\theta = \frac{\int_{R_{in}}^{R_{out}} v_\theta 2\pi r dr}{\int_{R_{in}}^{R_{out}} 2\pi r dr}, \quad \bar{v}_z = W_0 = \frac{\int_{R_{in}}^{R_{out}} v_z 2\pi r dr}{\int_{R_{in}}^{R_{out}} 2\pi r dr} \quad (307)$$

Table 32. Leakage and Re validation (experimental data adapted from [49])

	Re_z	Re_θ	Re_{tot}
Moreland	2890	934	3037
CFD Laminar	3350	936	3478
CFD $k-\omega$ BSL	2784	932	2936

BSL version directly integrates to the wall and accounts for viscous effects because low Re number demands such provision. An inlet loss coefficient of 0.9 is assumed. A wall roughness of $1\mu\text{m}$ is implemented for better convergence of ω equation while still operating in hydraulically smooth region. Figure 153 compares the velocity profiles for this low Re turbulent seal flow. The laminar velocity profiles fail to reflect characteristics of turbulent flow both in z and θ direction, while the BSL model has slightly flattened profiles at the core.

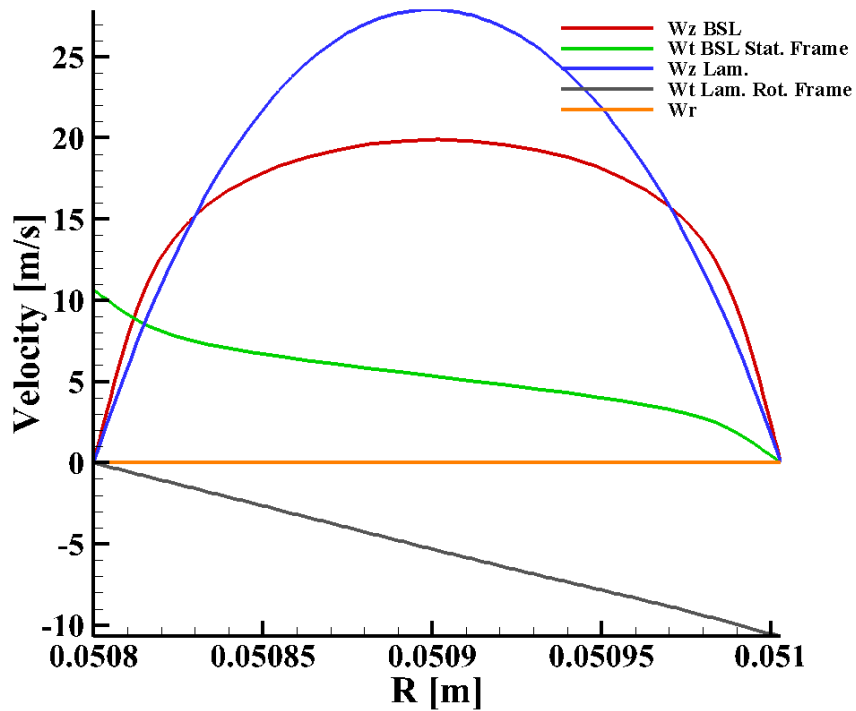


Figure 153. Velocity prediction of low Re and laminar versions of the code for an annular seal of $\text{Re}=3037$

5.13.7. High Re Seal Leakage

The study from Marquette et al. [50] has been chosen as the reference study. The operational condition and seal dimensions are given in Table 33:

Table 33. High Re plain annular seal dimensions and operational conditions (adapted from [50])

R_{in} [mm]	C_r [μm]	L [mm]	Fluid	Δp [Pa]	ω [rad/s]	Q [lit/s]
				4140000		0.83
38.145	110	34.93	water	5520000	1068.1	1.00
				6890000		1.09

In the case of Low Re models or High Re models with direct integration to the wall, the excessively large ω values close to the wall cause numerical difficulties in convergence and a very small time step has to be used. Experiments with roughness values show that this difficulty appears because of large ω values in order of 10^9 close to the wall. When a rough wall condition or a wall-function is used, this problem disappears and convergence is much smoother. Due to these difficulties the results have been obtained using wall-function approach. Figure 154 shows the convergence graphs. The velocity profiles for the $Re = 10300$ are plotted in Figure 155. The Reichardt's formula allowed to rebuilt the inner layers.

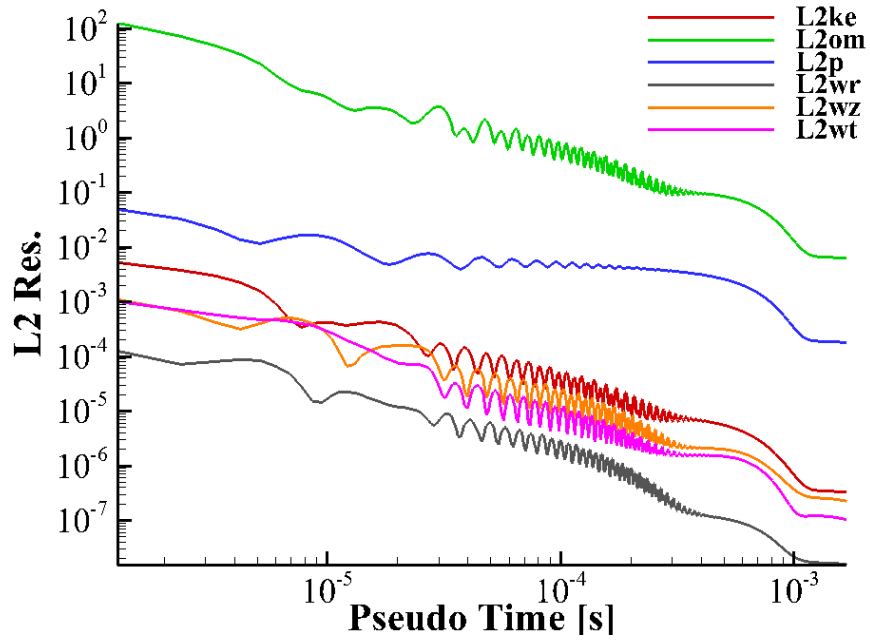


Figure 154. Convergence plot at $\Delta p=6.89$ MPa , $\omega=10200$ rpm, $Re=10300$

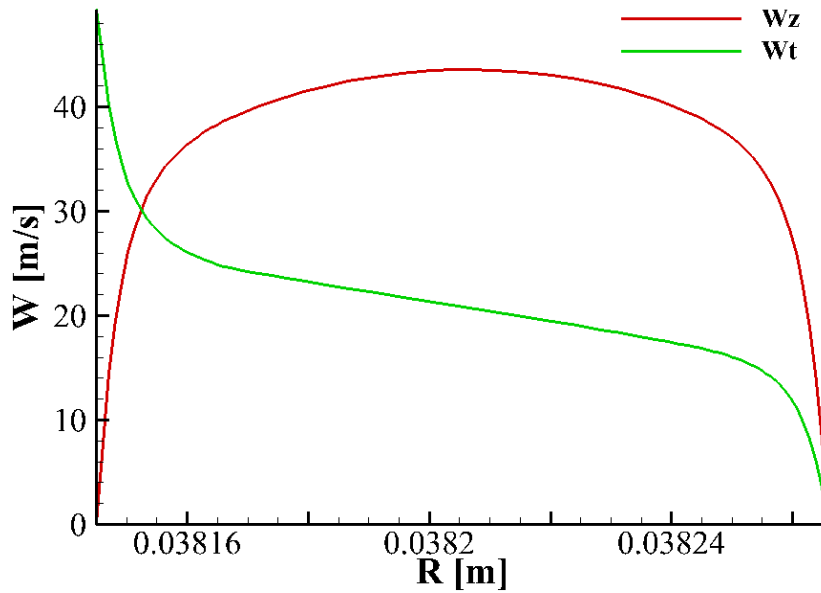


Figure 155. Axial and circumferential velocity profiles at $\Delta p=6.89$ MPa, $\omega=10200$ rpm, $Re_z=9000$, $Re_0=5000$

The developing nature of the flow is shown in Figure 156. The flow enters the seal with a uniform profile and achieves the fully developed condition approximately at $L/C_r = 140$. This entrance length can vary significantly with the shape of inlet profile. The figure also shows the selected non-uniform grid of the size 27×27 .

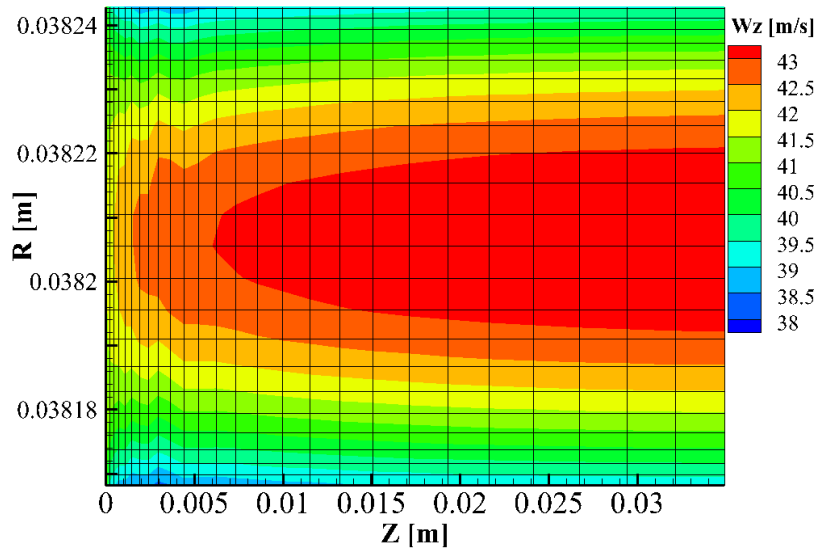


Figure 156. Developing flow and computational grid at $\Delta p=6.89$ MPa, $\omega=10200$ rpm and $Re=10300$

The pressure drop profile is almost linear which implies one can use a fully developed seal simulation instead of a developing seal simulation and get the same leakage results while the cost will be 10 times smaller (See Figure 157).

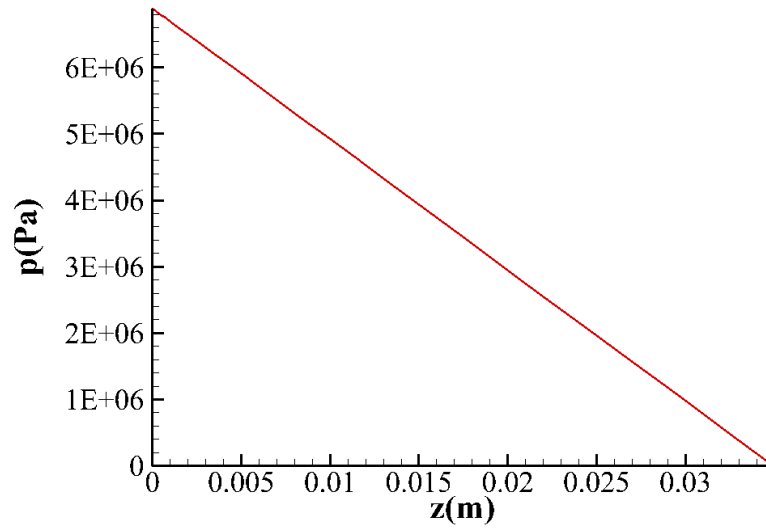


Figure 157. Pressure drop profile at $\Delta p=6.80$ MPa , $\omega=10200$ rpm and $Re=10300$

The Table 34 compares the leakage rates from CFD to experiments. The mean velocity is calculated from:

$$W_0 = \frac{Q}{1000\pi[(R_{in} + C_r)^2 - R_{in}^2]} \quad (308)$$

Table 34. Leakage rates vs pressure drop (experimental data adapted from [50])

		Δp [MPa]		
		4.14	5.52	6.89
Mean axial velocity W_0 [m/s]	Marquette et al. [50]	31.44	37.88	41.29
	CFD $k-\omega$	29.35	36.48	42.68
	CFD BSL	29.35	36.48	42.67

All the leakage rates are predicted reasonably well whether using Wilcox $k-\omega$ or Menter's BSL . In these simulations a smooth wall along with 10% pressure drop has been used (The authors declare the inlet loss coefficient of 0.1 which is replicated here). Leakage rate is slightly dependent on y^+ value unless the automatic wall-function option is used or integration to the wall is performed. When using a wall-function without automatic adjustment, the leakage rate generally reduces by increasing y^+ because the estimation of $\tau_p = \tau_w$ will slightly depart from reality. Therefore, for better accuracy one should use the lower end of y^+ (about 30-40) rather than the higher end (200-300). Figure 158 depicts the velocity profiles at the three operational conditions. The swirling component barely changes as Re_θ remains constant.

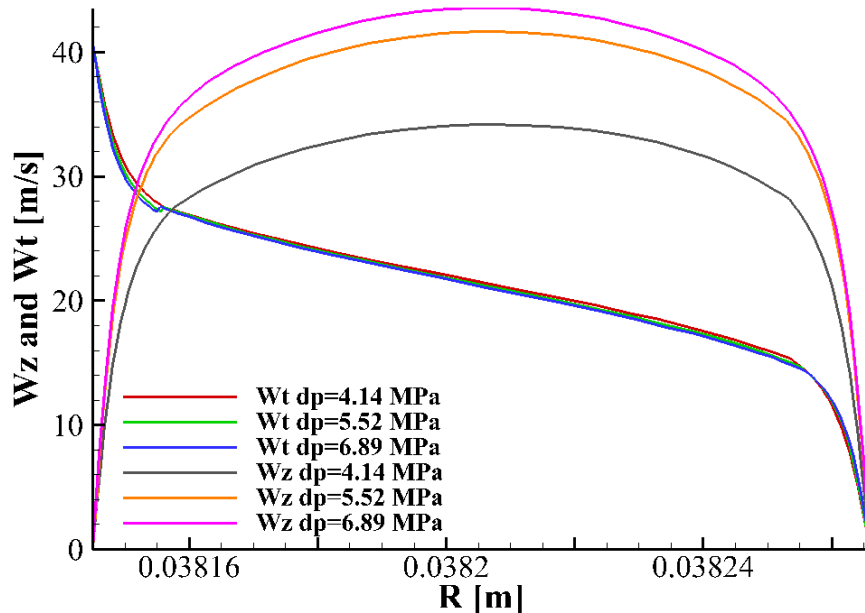


Figure 158. Axial and circumferential velocity profiles at $\Delta p=4.14$ MPa, 5.52 MPa, 6.89 MPa

5.13.8. 3D Seal Leakage

This problem presents the 3D version of the code in the cylindrical coordinates in turbulent mode. Also in this problem there are no side-walls; therefore, a periodic BC is required to close the domain. Figure 159 shows the periodicities. The 2π model also uses the same BCs.



Figure 159. Periodic BC schematic

The low Re seal results reported by Moreland [55] are used for validation of the 3D turbulent code. A standard Wilcox $k-\omega$ model without wall-functions is used to model the turbulent flow. The information about the seal is the same as Table 31. No inlet loss has been assumed. $1\mu m$ of roughness has been imposed to improve convergence of ω equation. The grid is stretched grid in r direction with $y^+ = 1$. Figure 160 shows the grid.

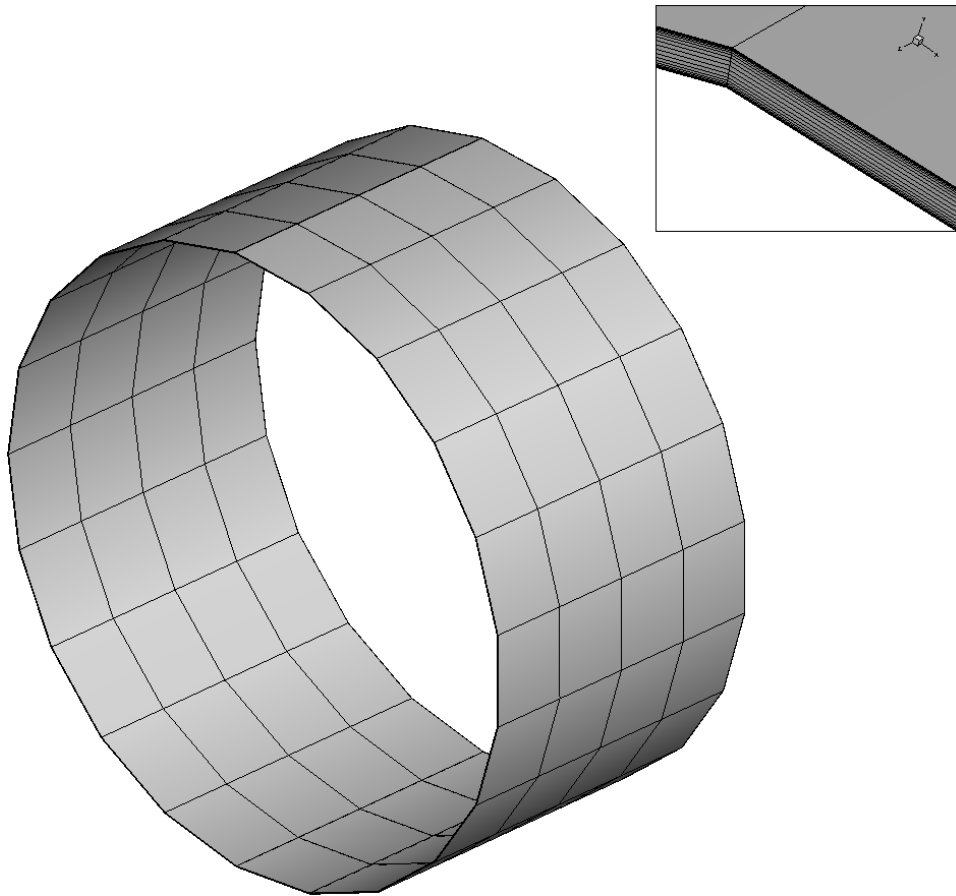


Figure 160. Annular seal 3D mesh (non-uniform)

The 3D nature of flow inside the clearance is depicted in Figure 161. The rotor causes the vectors to be mostly circumferential at inner radius, then the vectors gradually adopt an axial direction till they reach the stator.

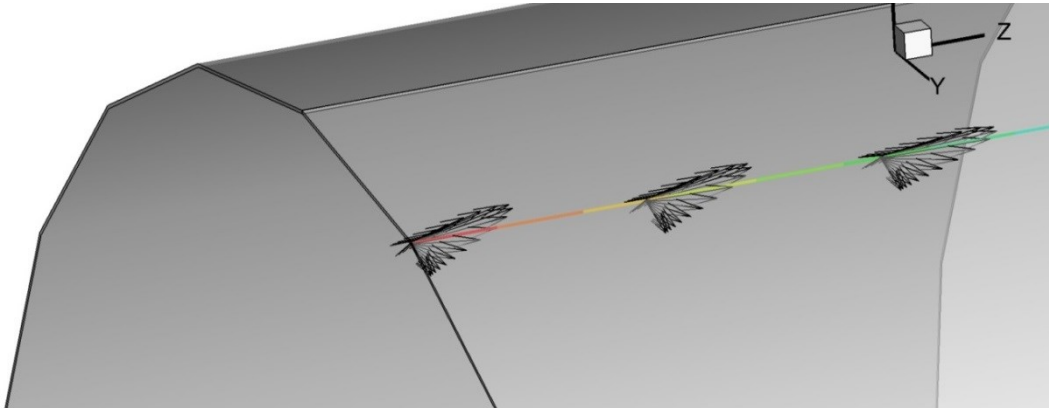


Figure 161. Velocity vectors inside the 3D laminar seal at $Re=1075$

Figure 162 shows the pressure drop inside the seal and the continuity of periodic BCs.

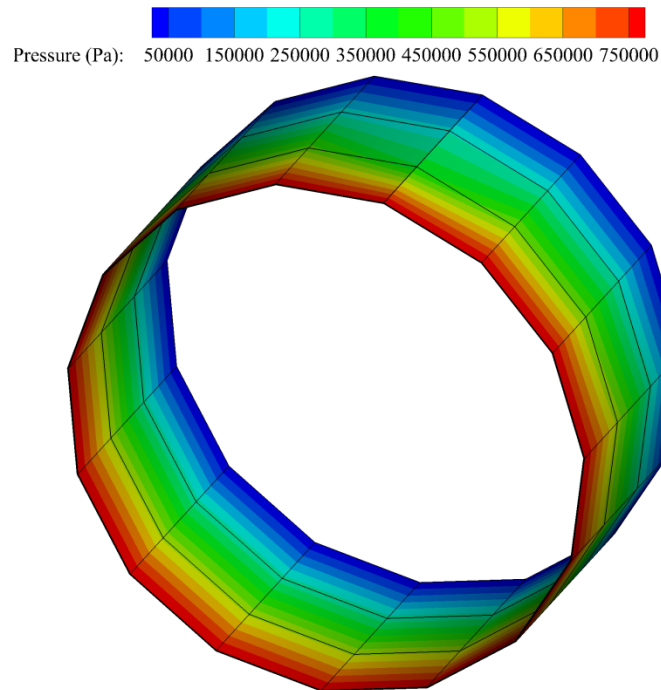


Figure 162. Pressure drop in the 2π model seal. Note that the discontinuity in periodics disappear upon convergence

The leakage predictions are in good agreement with experiments according to Table 35:

Table 35. Leakage prediction results in 3D turbulent mode

Case	Re_z	W_0 (m/s)
Moreland	2890	16.44
CFD $k-\omega$ Wilcox	2878	16.42

Despite the good agreement of the 3D code, the solution time is considerably higher than the 2D axisymmetric mode. Not only the computational domain is several times larger, but also the error in the 3D mode takes a long time to get damped and much larger iteration numbers are required to achieve the same level of convergence. For example for the above problem the 2D axisymmetric version gives the same results for 270x faster convergence (See Table 36):

Table 36. Computational cost of 2D and 3D modes for $L_2(w_z)=10^{-5}$

Case	Grid Size	Iterations	Sol. Time (min)
2D Axisymmetric	20×4	200,000	0.2
3D full 2π	$20 \times 4 \times 16$	3,000,000	53.8

It should be noted that seal problems by nature have slow convergence due to the small time step enforced by the tight clearance and sharp gradients in radial direction.

5.14. Conclusion

The McCk explicit scheme has been employed to solve the laminar and turbulent NS equations in the cylindrical coordinates. The equations were coupled with the continuity equation primarily through the PCM density based solver. The code has been validated against several experimental or theoretical results such as the exact solution to the laminar annular helical flow, cavity flow, cylindrical backward facing step, turbulent pipe flow and leakage results from low and high Re turbulent plain annular seals. Several BC subroutines are developed for various inlet-outlet conditions as well as interfaces to connect multiple domains. Periodic BCs allow to model slice 3D or full 3D seals. So far several features have been incorporated to the code including the turbulence models: low Re $k-\omega$ model, high Re $k-\omega$, Menter's BSL and SST. All the models can be integrated to the wall to model viscous effects.

The code allows for wall roughness modeling both with and without wall-functions. Several switch functions have been introduced to toggle between turbulent and laminar, stationary and rotating frame, full 3D and axisymmetric, etc. The code is capable to run on both uniform and non-uniform grids for speed-up. Other speed-up features include FAS-MG solver, SOR, and MPI parallel.

Current state of the code serves as a basis to accommodate features such as grooves to modify the seal type, add energy equation to adjust to gas seals, and to impose a small eccentricity on the 3D model to obtain the QS rotordynamic forces. Alternatively, a 2D perturbation model or hybrid Bulk-flow model can be appended to the code for rotordynamic forces.

6. CONCLUSION

The problem of fluid induced forces in whirling impellers and seals has been studied in this dissertation. It was shown through literature study and numerical investigation that the eccentric motion of turbomachinery components such as seals and impellers will induce forces proportional to the eccentricity also known as rotordynamic forces. Rotordynamic forces are detrimental to the machine's longevity and stability, and therefore should be evaluated prior to the operation in the design stage. Such predictive models are required by API level II stability analysis which has further motivated the current dissertation.

Considering the limitations of theoretical and experimental methods and the practicality of the demanded prediction model, CFD has emerged as the primary modern solution with a promising prospect. Specifically, commercial CFD codes are accessible, affordable and operable by a wide range of audience. In other words, a powerful yet easy-to-use tool better suits today's market demand. Current study benefits from both commercial CFD solvers for more advanced problems, and a freshly developed CFD code developed in FORTRAN as a long term goal.

6.1. Commercial CFD Approach

ANSYS CFX has been utilized in this dissertation as the primary commercial CFD solver. Several CFD approaches were studied in the current work. First a simpler model known as the quasi-steady (QS) model was applied to an axisymmetric seal problem and validated against experiments. Although the approach is steady-state and it

is computationally advantageous to transient methods; however, the eccentric mesh in orthogonal directions demands extra time in the pre-processing and post-processing stages. This approach is also (in theory) limited to axisymmetric geometries, yet it can be applied to non-axisymmetric geometries for certain problems with user's discretion. The QS model could successfully predict the rotordynamic forces and especially the negative stiffness behavior of groove-on-rotor seals. Furthermore, the results of this study revealed that the seal clearance and surface roughness are two decisive factors in rotordynamic characteristics of the seal that usually cannot be measured accurately and cause uncertainty in the prediction models.

An alternative transient CFD method was proposed to investigate the volute and diffuser rotordynamic forces problem. This approach was called for due to the asymmetric geometry of diffusers, volutes and impeller primary passage. Hence, this approach is more general than the QS approach. On the other hand, it is more computationally demanding as well. The transient approach works closely with the mesh deformation method. The transient data are post processed for the whirling component and a full impedance is extracted by simulating each frequency. The results were validated against experimental data. Several important lessons were learned from this study. First, volute and diffuser rotordynamic forces are in order of 25-30% of the impeller rotordynamic forces. Previously these components were ruled out of analysis as their contributions were perceived negligible. Second, it is the 2D spiral curve of the volute that most matters not the 3D design (cross-section shape). All volutes should be matched volutes otherwise flow rate effects contaminate the conclusions. Third, the

impeller front leakage path profile shape and clearance size is a key element in success of a quasi-steady model. A tight clearance means that QS performs well and a wide clearance reduces QS accuracy. Finally, it was that Gap A under whirling motion acts like a plain annular seal and tightening this gap (as is usual in hydraulic industry) has negative effect on the rotordynamic behavior of the impeller.

The previous transient method was further improved for computational cost by a new phase modulated multi-frequency approach. This approach allowed a speed-up of order 20 times compared to the single frequency approach. The downside with the multi-frequency method is its requirement for small individual eccentricity ratios of order $\epsilon = 0.005$. A small eccentricity reduces the errors from time-independent rotating frames and also nonlinear effects, but it is also susceptible to noise when a dominant mode such as stall appears.

The multi-frequency approach was applied to the problem of open impeller rotordynamic forces. Results of the multi-frequency method agreed well to experimental data and single frequency data. It was one again confirmed that some of the major jumps in impedance curves appear due to the phenomena such as rotating stall or rotating pressure patterns. Further investigation with closed impellers and Isolated Leakage Path Model (ILPM) disclosed modes known as whirl induced stall in the secondary path flow. These bumps and dips get stronger when the ILPM inlet swirl velocity increases, a condition that naturally appears in low flow rates.

The savings from the new approach allowed to experiment with several more geometrical aspects of impellers. It was found out that the contribution of the primary

flow path of a given closed impeller is in the same order as the secondary flow path contribution. This finding refutes the earlier notion that the majority of impeller forces stem from the secondary flow path. Furthermore, impellers of several various specific speeds were simulated in order to obtain dimensionless curves for a spectrum of impeller classes. Dimensional values for rotordynamic forces of impellers of similar class but different dimensions and operational conditions can be found extracted from these dimensionless curves.

6.2. Standalone CFD Code

As an independent long term goal, a FORTRAN CFD code was developed based on FDM to solve for seal leakage and rotordynamic forces. The code was validated against several laminar and turbulent test cases. Also, several schemes were used to accelerate the code including SOR, non-uniform grids, multigrid, MPI parallel, axisymmetric solution, and implementation of wall-functions. The underlying solver is a 2nd order in time and space McCk method. This predictor-corrector method allows solving the problem on a collocated grid without artificial viscosity. Some other features are supported including: Wilcox $k-\omega$ turbulence model, BSL and SST models, low Re models, surface roughness modeling, rotating frame solution, periodic BCs, PCM coupled solver, and SIMPLE decoupled solver in laminar mode.

6.3. Future Work

6.3.1. Linear Stability Analysis for Bumps and Dips

The experience gained through this dissertation opens the door to several fronts in the subject of impeller rotordynamics. A major unknown front is the originates of

bumps and dips. It is recommended to develop a linear hydrodynamic stability model for the ILPM Bulk-Flow model or an equivalent potential flow model. If the bumps and dips appear in Bulk-Flow [157], there is a good chance that a 2D potential flow model can predict the basic physics behind this phenomenon. Earlier experience with vaneless diffuser stall [106] has shown success of 2D inviscid models in predict of such instability patterns.

6.3.2. Phase Averaging for Concurrent Frequencies

It is further recommended to devise a computationally efficient procedure to perform CFD phase-averaging [80, 257, 258] for impeller rotordynamic forces. The phase-averaged data can subtract secondary frequencies such as stall from the impedance curves. It can also show the level of interaction between whirling modes and secondary modes. Other relevant question is how to distinguish between whirling forces, stall forces and whirl-induced stall forces. Currently there is no general metric to tell which modes scale with eccentricity and which modes come from the concentric solution. The only, not so much efficient, method is to do whirling and non-whirling simulations and compare for the stall forces.

6.3.3. Modified Alford Force Model

The axial impellers and compressors were not studied in current dissertation. Axial impellers, and especially axial compressors are prone to formation of Alford force [41, 87]. Current methodology can be further extended to axial impellers to further investigate the Alford force which is a concern in both power and aviation industries. Current Alford force models mostly use 2D actuator disk theory [42, 43, 112] which has

numerous limitations. Similar to the Alford force, the Propeller Whirl rotordynamic instability [259] with the pitch motion is a common problem in propellers which is noteworthy for future investigations with CFD-based impeller rotordynamics.

6.3.4. Impeller Rotordynamic Forces in Reverse Operation

Other interesting area concerns rotordynamic forces of impellers in reverse operation. Pump mode and turbine mode are only two modes out of 16 possible modes that an impeller can operate in [22]. There is a transition from the rotordynamic forces of the pump mode to the turbine mode. Such transition can be modeled and plotted to gain a so called full four quadrant operation data. A four quadrant rotordynamic curve is useful for reliability considerations, fault- scenario simulations and modern energy purposes such as Pump-As-Turbine (PAT) systems [260].

6.3.5. Potential Flow-Based Impeller Rotordynamic Forces

The theoretical impeller rotordynamic models based on potential flow theory [36, 102, 103, 105, 107, 261] have ceased development due to quick advances in CFD solutions. However, these methods are advantageous for quick estimates for Original Equipment Manufacturers, optimization purposes, stability analysis, and to give insight about the impeller design parameters influence on rotordynamic forces. The main issue with these codes is that they are too advanced for industrial users and they are developed as isolated modules. One approach only addresses primary flow path, and one method only solves the volute or the leakage path. If all these methods are integrated into a single piece of code, then a full theoretical model for the impeller rotordynamic forces will be achieved which can further advance this research topic.

6.3.6. High Fidelity Turbulence Modeling

Several limitations of the currently proposed transient multi-frequency method will be improved in future CFD solver generations. With more computational power, it will be possible to move toward more realistic turbulence models such as Reynolds Stress Models (RSM) and Large Eddy Simulation (LES). Moreover, currently CFD solvers do not support a time-dependent rotating frame which induced an error term in whirling simulations. In the current study, the eccentricities kept small to reduce this error. Perhaps in future generation this error can be removed by introduction of time-dependent rotating frames.

6.3.7. Novel 2D Axisymmetric Methods for Rotordynamic Forces

It is recommended that the standalone CFD code uses a 2D axisymmetric method for rotordynamic forces and to avoid a full 3D modeling. One simple approach is to use the 2D axisymmetric code to obtain the shear stress and leakage data and next input them in a Bulk-Flow solver to obtain the rotordynamic forces (Hybrid CFD-Bulk-Flow model [134]). The other approach is to use a perturbation model [117, 262] to solve for the rotordynamic forces using 2D axisymmetric domain. There newer perturbation models such as Homotopy method [263] that allow for finite amplitude perturbations. These approaches remove both time and the third dimension from the problem and results in fast solutions which are still much more accurate than a regular Bulk-Flow model. Furthermore, the energy equation can be easily appended to the current McCh-PCM solver to adapt the code to gas seals.

REFERENCES

- [1] Childs, D. W., 2013, Turbomachinery Rotordynamics with Case Studies, Minter Spring, Wellborn, Texas.
- [2] Massey, I., "Subsynchronous Vibration Problems in High-Speed Multistage Centrifugal Pumps," Proc. 14th Turbomachinery Symposium, Texas A&M University, Houston, TX, Oct, pp. 22-24.
- [3] Smith, D. R., Price, S. M., and Kunz, F., "Centrifugal Pump Vibration Caused by Supersynchronous Shaft Instability Use of Pumpout Vanes to Increase Pump Shaft Stability," Proc. Proceedings of the 13th International Pump Users Symposium, pp. 47-60.
- [4] Fowlie, D., and Miles, D., 1975, "Vibration Problems with High Pressure Centrifugal Compressors," ASME paper (75-PET), p. 28.
- [5] Millsaps, K. T., 1992, "The Impact of Unsteady Swirling Flow in a Single Gland Labyrinth Seal on Rotordynamic Stability: Theory and Experiment," Ph.D. dissertation, Massachusetts Institute of Technology, Cambridge, Massachusetts.
- [6] Childs, D. W., 1978, "The Space Shuttle Main Engine High-Pressure Fuel Turbopump Rotordynamic Instability Problem," Journal of Engineering for Power, 100(1), pp. 48-57.
- [7] Geary, C. H., Jr., Damratowski, L. P., and Seyer, C. H., 1976, "Design and Operation of the World's Highest Pressure Gas Injection Centrifugal Compressors," Offshore Technology Conference, Offshore Technology Conference, Houston, Texas, p. 12.
- [8] Frenning, L., 2001, Pump Life Cycle Costs: A Guide to LCC Analysis for Pumping Systems, Hydraulic Institute & Europump.
- [9] Szeri, A. Z., 2005, Fluid Film Lubrication: Theory and Design, Cambridge University Press, New York, New York.
- [10] Muszynska, A., 2005, Rotordynamics, CRC press, Boca Raton, Florida.
- [11] Childs, D. W., 1993, Turbomachinery Rotordynamics: Phenomena, Modeling, and Analysis, John Wiley & Sons, New York, New York.
- [12] Vance, J. M., Zeidan, F. Y., and Murphy, B., 2010, Machinery Vibration and Rotordynamics, John Wiley & Sons, Hoboken, New Jersey.

- [13] Tsujimoto, Y., 2017, "Rotordynamics of Turbopumps and Hydroturbines," Cavitation Instabilities and Rotordynamic Effects in Turbopumps and Hydroturbines, Springer, pp. 109-136.
- [14] Wachel, J. C., and von Nimitz, W. W., 1981, "Ensuring the Reliability of Offshore Gas Compression Systems," *Journal of Petroleum Technology*, 33(11), pp. 2252–2260.
- [15] API, 2002, "Axial and Centrifugal Compressors and Expander-Compressors for Petroleum, Chemical and Gas Industry Services," American Petroleum Institute, Washington, DC, Standard No. API 617.
- [16] API, 2006, "Centrifugal Pumps for General Refinery Service," American Petroleum Institute, Washington, DC, Standard No. API 610.
- [17] Nourbakhsh, S. A., 2005, *Turbomachinery*, University of Tehran Press, Tehran.
- [18] Nourbakhsh, A., Jaumotte, A., Hirsch, C., and Parizi, H. B., 2007, *Turbopumps and Pumping Systems*, Springer-Verlag, Berlin.
- [19] Eisenmann, R. C., and Eisenmann, R. C., 1998, *Machinery Malfunction Diagnosis and Correction: Vibration Analysis and Troubleshooting for the Process Industries*, Prentice Hall PTR, Upper Saddle River, New Jersey.
- [20] Black, H. F., "Effects of Fluid-Filled Clearance Spaces on Centrifugal Pump and Submerged Motor Vibrations," *Proc. 8th Turbomachinery Symposium*, Turbomachinery Laboratory, Texas A&M University, College Station, TX, pp. 29-34.
- [21] Stepanoff, A. J., 1957, *Centrifugal and Axial Flow Pumps Theory Design and Application*, 2nd ed., Wiley, New York.
- [22] Gülich, J. F., 2008, *Centrifugal Pumps*, 2nd ed., Springer-Verlag, Berlin.
- [23] Lobanoff, V. S., and Ross, R. R., 2013, *Centrifugal Pumps: Design and Application*, 2nd ed., Gulf Professional Publishing, Houston, TX.
- [24] Villasmil, L. A., Childs, D. W., and Chen, H.-C., 2005, "Understanding Friction Factor Behavior in Liquid Annular Seals with Deliberately Roughened Surfaces," *Journal of Tribology*, 127(1), pp. 213-222.
- [25] Childs, D. W., and Fayolle, P., 1999, "Test Results for Liquid “Damper” Seals Using a Round-Hole Roughness Pattern for the Stators," *Journal of Tribology*, 121(1), pp. 42-49.

- [26] Pletcher, R. H., Tannehill, J. C., and Anderson, D., 2012, *Computational Fluid Mechanics and Heat Transfer*, 3rd edition, CRC Press, Boca Raton, Florida.
- [27] Palazzolo, A., 2016, *Vibration Theory and Applications with Finite Elements and Active Vibration Control*, John Wiley & Sons, West Sussex.
- [28] Worster, R., 1963, "The Flow in Volute and Its Effect on Centrifugal Pump Performance," *Proceedings of the Institution of Mechanical Engineers*, 177(1), pp. 843-875.
- [29] Yoshida, Y., Tsujimoto, Y., Yokoyama, D., Ohashi, H., and Kano, F., 2001, "Rotordynamic Fluid Force Moments on an Open-Type Centrifugal Compressor Impeller in Precession Motion," *International Journal of Rotating Machinery*, 7(4), pp. 237-251.
- [30] Kim, E., and Palazzolo, A., 2017, "Rotordynamic Stability Effects of Shrouded Centrifugal Impellers With Combined Whirl and Precession," *Journal of Vibration and Acoustics*, 140(2), pp. 021007-021007-021012.
- [31] Williams, J. P., and Childs, D. W., 1991, "Influence of Impeller Shroud Forces on Turbopump Rotor Dynamics," *Journal of Vibration and Acoustics*, 113(4), pp. 508-515.
- [32] Childs, D. W., 1989, "Fluid-Structure Interaction Forces at Pump-Impeller-Shroud Surfaces for Rotordynamic Calculations," *Journal of Vibration, Acoustics, Stress, and Reliability in Design*, 111(3), pp. 216-225.
- [33] Pace, G., Valentini, D., Pasini, A., Torre, L., Hadavandi, R., and d'Agostino, L., 2017, "Inducer and Centrifugal Pump Contributions to the Rotordynamic Fluid Forces Acting on a Space Turbopump," *Journal of Fluids Engineering*, 140(2), pp. 021104-021104-021110.
- [34] Moore, J. J., and Palazzolo, A. B., 2001, "Rotordynamic Force Prediction of Whirling Centrifugal Impeller Shroud Passages Using Computational Fluid Dynamic Techniques," *Journal of Engineering for Gas Turbines and Power*, 123(4), pp. 910-918.
- [35] Kim, E., and Palazzolo, A., 2016, "Rotordynamic Force Prediction of a Shrouded Centrifugal Pump Impeller-Part I: Numerical Analysis," *Journal of Vibration and Acoustics, Transactions of the ASME*, 138(3), pp. 031014-031014-031010.
- [36] Shoji, H., and Ohashi, H., 1987, "Lateral Fluid Forces on Whirling Centrifugal Impeller (1st Report: Theory)," *Journal of Fluids Engineering, Transactions of the ASME*, 109(2), pp. 94-99.

- [37] Padavala, S., and Palazzolo, A., 1994, "Enhanced Simulation Software for Rocket Turbopump, Turbulent, Annular Liquid Seals," NASA technical paper 1994.
- [38] Brennen, C. E., 2011, *Hydrodynamics of pumps*, Cambridge University Press, New York, New York.
- [39] Ehrich, F., "Rotor Whirl Forces Induced by the Tip Clearance Effect in Axial Flow Compressors," *Proceedings of the 14th Biennial ASME Design Technical Conference on Mechanical Vibration and Noise*, September 19, 1993 - September 22, 1993, ASME, pp. 7-16.
- [40] Vance, J. M., and Laudadio, F. J., 1984, "Experimental Measurement of Alford's Force in Axial Flow Turbomachinery," *ASME Journal of Engineering for Gas Turbines and Power*, 106(3), pp. 585-590.
- [41] Thomas, H., 1958, "Unstable Natural Vibration of Turbine Rotors Induced by the Clearance Flow in Glands and Blading," *Bull. de l'AIM*, 71(11/12), pp. 1039-1063.
- [42] Colding-Jorgensen, J., 1992, "Prediction of Rotor Dynamic Destabilizing Forces in Axial Flow Compressors," *ASME Journal of Fluids Engineering*, 114(4), pp. 621-625.
- [43] Ehrich, F., 1993, "Rotor Whirl Forces Induced by the Tip Clearance Effect in Axial Flow Compressors," *ASME Journal of Vibration and Acoustics*, 115(4), pp. 509-515.
- [44] Lomakin, A., 1958, "Calculation of Critical Number of Revolutions and the Conditions Necessary for Dynamic Stability of Rotors in High-Pressure Hydraulic Machines When Taking Into Account Forces Originating in Sealings," *Power and Mechanical Engineering*, 4, pp. 1-5.
- [45] Norrbin, C. S., and Childs, D. W., 2018, "Lateral Equilibrium Position Analysis Program with Applications to Electric Submersible Pumps," *ASME Journal of Engineering for Gas Turbines and Power*, 140(6), pp. 062602-062602-062610.
- [46] Ohashi, H., and Shoji, H., 1984, "Lateral Fluid Forces Acting on a Whirling Centrifugal Impeller in Vaneless and Vaned Diffuser," *NASA. Lewis Research Center Rotordynamic Instability Problems in High-Performance Turbomachinery*, Document ID 19850005814, pp. 109-122.
- [47] Ehrich, F., and Childs, D., 1984, "Self-Excited Vibration in High-Performance Turbomachinery," *Mechanical Engineering*, 106(5), pp. 66-79.

- [48] Glienicke, J., 1966, "Experimental Investigation of Stiffness and Damping Coefficients of Turbine Bearings and Their Application to Instability Prediction," Institution of Mechanical Engineers, Proceedings of the Journal Bearings for Reciprocating and Turbo Machinery, 181(Part 3B), pp. 116-129.
- [49] Moreland, J. A., 2016, "Influence of Pre-Swirl and Eccentricity in Smooth Stator/Grooved Rotor Liquid Annular Seals, Measured Static and Rotordynamic Characteristics," Master of Science, Texas A&M University, College Station, Texas.
- [50] Marquette, O., Childs, D., and San Andres, L., 1997, "Eccentricity Effects on the Rotordynamic Coefficients of Plain Annular Seals: Theory versus Experiment," ASME Journal of Tribology, 119(3), pp. 443-447.
- [51] Childs, D. W., and Arthur, S. P., 2013, "Static Destabilizing Behavior for Gas Annular Seals at High Eccentricity Ratios," (55263), p. V07AT29A003.
- [52] Childs, D. W., Nolan, S. A., and Kilgore, J. J., 1990, "Test Results for Turbulent Annular Seals, Using Smooth Rotors and Helically Grooved Stators," ASME Journal of Tribology, 112(2), pp. 254-258.
- [53] Marquette, O. R., Childs, D. W., and Phillips, S. G., "Theory versus Experiment for Leakage and Rotordynamic Coefficients of Circumferentially-Grooved Liquid Annular Seals with L/D of 0.45," Proceedings of the 1997 ASME Fluids Engineering Division Summer Meeting, FEDSM. Part 16 (of 24), June 22, 1997 - June 26, 1997, ASME.
- [54] Iwatsubo, T., and Sheng, B., "Evaluation of Dynamic Characteristics of Parallel Grooved Seals by Theory and Experiment," Proceedings of the third IFToMM International Conference on Rotordynamics, Lyon, France, pp. 313-318.
- [55] Moreland, J. A., Childs, D. W., and Bullock, J. T., 2017, "Measured Static and Rotordynamic Characteristics of a Smooth-Stator/Grooved-Rotor Liquid Annular Seal," (58042), p. V01AT05A004.
- [56] Nagai, K., Kaneko, S., Taura, H., and Watanabe, Y., 2018, "Numerical and Experimental Analyses of Dynamic Characteristics for Liquid Annular Seals With Helical Grooves in Seal Stator," ASME Journal of Tribology, 140(5), pp. 052201-052201-052217.
- [57] Ertas, B. H., Delgado, A., and Vannini, G., 2012, "Rotordynamic Force Coefficients for Three Types of Annular Gas Seals with Inlet Preswirl and High Differential Pressure Ratio," ASME Journal of Engineering for Gas Turbines and Power, 134(4), p. 042503 (042512 pp.).

- [58] Vannini, G., Cioncolini, S., Vescovo, G. D., and Rovini, M., 2014, "Labyrinth Seal and Pocket Damper Seal High Pressure Rotordynamic Test Data," *ASME Journal of Engineering for Gas Turbines and Power*, 136(2):022501-022501-9. doi:10.1115/1.4025360.
- [59] Iwatsubo, T., Motooka, N., and Kawai, R., 1982, "Flow Induced Force of Labyrinth Seal," NASA technical paper 1982.
- [60] Vonpragenau, G. L., 1982, "Damping seals for Turbomachinery," NASA technical paper 1987.
- [61] Ha, T. W., and Childs, D. W., 1992, "Friction-Factor Data for Flat-Plate Tests of Smooth and Honeycomb Surfaces," *ASME Journal of Tribology*, 114(4), pp. 722-729.
- [62] Kleynhans, G. F., and Childs, D. W., 1997, "The Acoustic Influence of Cell Depth on the Rotordynamic Characteristics of Smooth-Rotor/Honeycomb-Stator Annular Gas Seals," *ASME Journal of Engineering for Gas Turbines and Power*, 119(4), pp. 949-956.
- [63] Vannini, G., Bertoneri, M., Nielsen, K. K., Iudiciani, P., and Stronach, R., 2016, "Experimental Results and Computational Fluid Dynamics Simulations of Labyrinth and Pocket Damper Seals for Wet Gas Compression," *ASME Journal of Engineering for Gas Turbines and Power*, 138(5):052501-052501-13. doi:10.1115/1.4031530.
- [64] Voigt, A. J., Mandrup-Poulsen, C., Nielsen, K. K., and Santos, I. F., 2017, "Design and Calibration of a Full Scale Active Magnetic Bearing Based Test Facility for Investigating Rotordynamic Properties of Turbomachinery Seals in Multiphase Flow," *ASME Journal of Engineering for Gas Turbines and Power*, 139(5), pp. 052505-052505-052510.
- [65] San Andrés, L., Lu, X., and Liu, Q., 2016, "Measurements of Flow Rate and Force Coefficients in a Short-Length Annular Seal Supplied with a Liquid/Gas Mixture (Stationary Journal)," *Tribology Transactions*, 59(4), pp. 758-767.
- [66] Yoshida, Y., Tsujimoto, Y., Ishii, N., Ohashi, H., and Kano, F., 1999, "Rotordynamic Forces on an Open-Type Centrifugal Compressor Impeller in Whirling Motion," *Journal of Fluids Engineering, Transactions of the ASME*, 121(2), pp. 259-265.
- [67] Hergt, P., and Krieger, P., 1969, "Radial Forces in Centrifugal Pumps with Guide Vanes," *Proceedings of the Institution of Mechanical Engineers, Conference Proceedings*, 184(14), pp. 101-107.

- [68] Ohashi, H., and Shoji, H., 1987, "Lateral Fluid Forces on Whirling Centrifugal Impeller (2nd Report: Experiment in Vaneless Diffuser)," *ASME Journal of Fluids Engineering*, 109(2), pp. 100-106.
- [69] Ohashi, H., Sakurai, A., and Nishihama, J., 1989, "Influence of Impeller and Diffuser Geometries on the Lateral Fluid Forces of Whirling Centrifugal Impeller," NASA, Lewis Research Center, *Rotordynamic Instability Problems in High-Performance Turbomachinery*, 1988; p 285-306.
- [70] Jery, B., Acosta, A., Brennen, C., and Caughey, T., 1984, "Hydrodynamic Impeller Stiffness, Damping, and Inertia in the Rotordynamics of Centrifugal Flow Pumps," NASA technical report 1984.
- [71] Franz, R., and Arndt, N., 1986, "Measurements of Hydrodynamic Forces on the Impeller of the HPOTP of the SSME," California Institute of Technology, Pasadena, California, Report No. E249.2.
- [72] Chamieh, D. S., Acosta, A. J., Brennen, C. E., and Caughey, T. K., 1985, "Experimental Measurements of Hydrodynamic Radial Forces and Stiffness Matrices for a Centrifugal Pump-Impeller," *Journal of Fluids Engineering, Transactions of the ASME*, 107(3), pp. 307-315.
- [73] Jery, B., 1987, "Experimental Study of Unsteady Hydrodynamic Force Matrices on Whirling Centrifugal Pump Impellers," Ph.D. Dissertation, California Institute of Technology, Pasadena, California.
- [74] Guinzburg, A., Brennen, C. E., Acosta, A. J., and Caughey, T. K., 1993, "The Effect of Inlet Swirl on the Rotordynamic Shroud Forces in a Centrifugal Pump," *ASME Journal of Engineering for Gas Turbines and Power*, 115(2), pp. 287-293.
- [75] Sivo, J. M., Acosta, A. J., Brennen, C. E., and Caughey, T. K., 1995, "The Influence of Swirl Brakes on the Rotordynamic Forces Generated by Discharge-to-Suction Leakage Flows in Centrifugal Pumps," *ASME Journal of Fluids Engineering*, 117(1), pp. 104-108.
- [76] Uy, R. V., and Brennen, C. E., 1999, "Experimental Measurements of Rotordynamic Forces Caused by Front Shroud Pump Leakage," *ASME Journal of Fluids Engineering*, 121(3), pp. 633-637.
- [77] Bhattacharyya, A., Acosta, A. J., Brennen, C. E., and Caughey, T. K., 1997, "Rotordynamic Forces in Cavitating Inducers," *ASME Journal of Fluids Engineering*, 119(4), pp. 768-774.

- [78] Bolleter, U., Wyss, A., Welte, I., and Stuerchler, R., 1987, "Measurement of Hydrodynamic Interaction Matrices of Boiler Feed Pump Impellers," *Journal of vibration, acoustics, stress, and reliability in design*, 109(2), pp. 144-151.
- [79] Tsujimoto, Y., Yoshida, Y., Ohashi, H., Teramoto, N., and Ishizaki, S., 1997, "Fluid Force Moment on a Centrifugal Impeller Shroud in Processing Motion," *Journal of Fluids Engineering, Transactions of the ASME*, 119(2), pp. 366-371.
- [80] Yoshida, Y., Tsujimoto, Y., Morimoto, G., Nishida, H., and Morii, S., 2003, "Effects of Seal Geometry on Dynamic Impeller Fluid Forces and Moments," *ASME Journal of Fluids Engineering*, 125(5), pp. 786-795.
- [81] Nagao, N., Eguchi, M., Uchiumi, M., and Yoshida, Y., "Rotordynamic Forces Acting on a Centrifugal Open Impeller in Whirling Motion by Using Active Magnetic Bearing," *Proc. Progress in Propulsion Physics, EDP Sciences*, pp. 445-456.
- [82] Song, B., Horiguchi, H., Ma, Z., and Tsujimoto, Y., 2010, "Rotordynamic Instabilities Caused by the Fluid Force Moments on the Backshroud of a Francis Turbine Runner," *International Journal of Fluid Machinery and Systems*, 3(1), pp. 67-79.
- [83] Childs, D. W., and Muhammed, A., 2014, "Comments on a Newly-Identified Destabilizing Rotordynamic Mechanism Arising in Vertical Hydraulic Turbines and the Back Shrouds of Centrifugal Impellers," *ASME Journal of Engineering for Gas Turbines and Power*, 136(4):042502-042502-7. doi:10.1115/1.4025889.
- [84] Valentini, D., Pace, G., Torre, L., Pasini, A., and D'Agostino, L., 2015, "Influences of the Operating Conditions on the Rotordynamic Forces Acting on a Three-Bladed Inducer Under Forced Whirl Motion," *ASME Journal of Fluids Engineering*, 137(7):071304-071304-10. doi:10.1115/1.4029887.
- [85] Fu, Y., Yuan, J., Yuan, S., Pace, G., D'Agostino, L., Huang, P., and Li, X., 2014, "Numerical and Experimental Analysis of Flow Phenomena in a Centrifugal Pump Operating under Low Flow Rates," *ASME Journal of Fluids Engineering*, 137(1):011102-011102-12. doi:10.1115/1.4027142.
- [86] Martinez-Sanchez, M., Jaroux, B., Song, S. J., and Yoo, S., 1995, "Measurement of Turbine Blade-Tip Rotordynamic Excitation Forces," *ASME Journal of Turbomachinery*, 117(3), pp. 384-392.
- [87] Alford, J. S., 1965, "Protecting Turbomachinery from Self-Excited Rotor Whirl," *American Society of Mechanical Engineers, Transactions, Journal of Engineering for Power*, 87(4), pp. 333-344.

- [88] Song, S. J., and Martinez-Sanchez, M., 1997, "Rotordynamic Forces Due to Turbine Tip Leakage: Part II—Radius Scale Effects and Experimental Verification," *ASME Journal of Turbomachinery*, 119(4), pp. 704-713.
- [89] Storace, A. F., Wisler, D. C., Shin, H. W., Beacher, B. F., Ehrich, F. F., Spakovszky, Z. S., Martinez-Sanchez, M., and Song, S. J., 2001, "Unsteady Flow and Whirl-Inducing Forces in Axial-Flow Compressors: Part I - Experiment," *ASME Journal of Turbomachinery*, 123(3), pp. 433-445.
- [90] Hirs, G. G., 1973, "A Bulk-Flow Theory for Turbulence in Lubricant Films," *Transactions of the ASME. Series F, Journal of Lubrication Technology*, 95(2), pp. 137-146.
- [91] Childs, D. W., 1983, "Dynamic Analysis of Turbulent Annular Seals Based on Hirs' Lubrication Equation," *Journal of Lubrication Technology*, 105(3), pp. 429-436.
- [92] Palazzolo, A., Bhattacharya, A., Athavale, M., Venkataraman, B., Ryan, S., and Funston, K., 1997, "Developments in Impeller/Seal Secondary Flow Path Modeling for Dynamic Force Coefficients and Leakage," NASA technical report 1997.
- [93] San Andrés, L., 1990, "Turbulent Hybrid Bearings with Fluid Inertia Effects," *ASME Journal of Tribology*, 112(4), pp. 699-707.
- [94] Scharrer, J. K., 1988, "Theory versus Experiment for the Rotordynamic Coefficients of Labyrinth Gas Seals: Part I—A Two Control Volume Model," *Journal of Vibration, Acoustics, Stress, and Reliability in Design*, 110(3), pp. 270-280.
- [95] Nordmann, R., and Weiser, P., 1991, "Evaluation of Rotordynamic Coefficients of Look-through Labyrinths by Means of a Three Volume Bulk Flow Model," NASA technical report 1991.
- [96] Venkataraman, B., and Palazzolo, A. B., 1996, "Effects of Wall Flexibility on the Rotordynamic Coefficients of Turbulent Cryogenic Annular Seals," *ASME Journal of Tribology*, 118(3), pp. 509-519.
- [97] Andrés, L. S., 2011, "Rotordynamic Force Coefficients of Bubbly Mixture Annular Pressure Seals," *ASME Journal of Engineering for Gas Turbines and Power*, 134(2), pp. 022503-022503-022508.
- [98] Hess, J. L., 1974, "The Problem of Three-Dimensional Lifting Potential Flow and Its Solution By Means of Surface Singularity Distribution," *Computer Methods in Applied Mechanics and Engineering*, 4(3), pp. 283-319.

- [99] Schobeiri, M. T., 2010, *Fluid Mechanics for Engineers*, Springer-Verlag, Berlin.
- [100] Csanady, G. T., 1962, "Radial Forces in a Pump Impeller Caused by a Volute Casing," *Journal of Engineering for Power*, 84(4), pp. 337-340.
- [101] Colding-Jorgensen, J., 1980, "Effect of Fluid Forces on Rotor Stability of Centrifugal Compressors and Pumps," NASA technical report 1980.
- [102] Adkins, D., and Brennen, C., 1988, "Analyses of Hydrodynamic Radial Forces on Centrifugal Pump Impellers," *ASME Journal of Fluids Engineering*, 110(1), pp. 20-28.
- [103] Tsujimoto, Y., Acosta, A. J., and Brennen, C. E., 1988, "Theoretical Study of Fluid Forces on a Centrifugal Impeller Rotating and Whirling in a Volute," *Journal of vibration, acoustics, stress, and reliability in design*, 110(3), pp. 263-269.
- [104] Tsujimoto, Y., Acosta, A. J., and Yoshida, Y., 1989, "A Theoretical Study of Fluid Forces on a Centrifugal Impeller Rotating and Whirling in a Vaned Diffuser," NASA technical paper 1989.
- [105] Yoshida, Y., Tsurusaki, H., Murakami, Y., and Tsujimoto, Y., 1990, "Rotating Stalls in Centrifugal Impeller/Vaned Diffuser Systems: 2nd Report, Comparison between Experiment and Theory," *Transactions of the Japan Society of Mechanical Engineers Series B*, 56(530), pp. 2999-3006.
- [106] Tsujimoto, Y., Yoshida, Y., and Mori, Y., 1996, "Study of Vaneless Diffuser Rotating Stall Based on Two-Dimensional Inviscid Flow Analysis," *ASME Journal of Fluids Engineering*, 118(1), pp. 123-127.
- [107] Hiwata, A., and Tsujimoto, Y., 2002, "Theoretical Analysis of Fluid Forces on an Open-Type Centrifugal Impeller in Whirling Motion," *ASME Journal of Fluids Engineering*, 124(2), pp. 342-347.
- [108] Semenov, Y. A., Fujii, A., and Tsujimoto, Y., 2004, "Rotating Choke in Cavitating Turbopump Inducer," *ASME Journal of Fluids Engineering*, 126(1), pp. 87-93.
- [109] Song, S. J., and Martinez-Sanchez, M., 1997, "Rotordynamic Forces Due to Turbine Tip Leakage: Part I - Blade Scale Effects," *ASME Journal of Turbomachinery*, 119(4), pp. 695-703.
- [110] Song, S. J., and Cho, S. H., 2000, "Nonuniform Flow in a Compressor Due to Asymmetric Tip Clearance," *ASME Journal of Turbomachinery*, 122(4), pp. 751-760.

- [111] Spakovszky, Z. S., 2000, "Analysis of Aerodynamically Induced Whirling Forces in Axial Flow Compressors," *ASME Journal of Turbomachinery*, 122(4), pp. 761-768.
- [112] Ehrich, F. F., Spakovszky, Z. S., Martinez-Sanchez, M., Song, S. J., Wisler, D. C., Storace, A. F., Shin, H. W., and Beacher, B. F., 2001, "Unsteady Flow and Whirl-Inducing Forces in Axial-Flow Compressors: Part II - Analysis," *ASME Journal of Turbomachinery*, 123(3), pp. 446-452.
- [113] Song, J., and Song, S. J., "An Analytical Model of Flow-Induced Rotordynamic Forces in Shrouded Centrifugal Pump Impellers," *Proc. ASME Turbo Expo 2016: Turbomachinery Technical Conference and Exposition*, American Society of Mechanical Engineers, pp. V07AT30A009-V007AT030A009.
- [114] Demko, J. A., Morrison, G. L., and Rhode, D. L., 1989, "The Prediction and Measurement of Incompressible Flow in a Labyrinth Seal," *ASME Journal of Engineering for Gas Turbines and Power*, 111(4), pp. 697-702.
- [115] Dietzen, F. J., and Nordmann, R., 1987, "Calculating Rotordynamic Coefficients of Seals by Finite-Difference Techniques," *ASME Journal of Tribology*, 109(3), pp. 388-394.
- [116] Arghir, M., and Frêne, J., 1997, "Rotordynamic Coefficients of Circumferentially-Grooved Liquid Seals Using the Averaged Navier-Stokes Equations," *ASME Journal of Tribology*, 119(3), pp. 556-567.
- [117] Arghir, M., and Frêne, J., 1999, "A Quasi-Two-Dimensional Method for the Rotordynamic Analysis of Centered Labyrinth Liquid Seals," *ASME Journal of Engineering for Gas Turbines and Power*, 121(1), pp. 144-152.
- [118] Rhode, D. L., and Nail, G. H., 1992, "Computation of Cavity-by-Cavity Flow Development in Generic Labyrinth Seals," *ASME Journal of Tribology*, 114(1), pp. 47-51.
- [119] Tam, L. T., Przekwas, A. J., Muszynska, A., Hendricks, R. C., Braun, M. J., and Mullen, R. L., 1988, "Numerical and Analytical Study of Fluid Dynamic Forces in Seals and Bearings," *Journal of vibration, acoustics, stress, and reliability in design*, 110(3), pp. 315-325.
- [120] Dietzen, F., and Nordmann, R., 1989, "A 3-Dimensional Finite-Difference Method for Calculating the Dynamic Coefficients of Seals," NASA technical report 1989.

- [121] Hendricks, R., Tam, L., and Muszynska, A., 2004, "Turbomachine Sealing and Secondary Flows. Part 2; Review of Rotordynamics Issues in Inherently Unsteady Flow Systems with Small Clearances," NASA technical report 2004.
- [122] Rhode, D. L., Hensel, S. J., and Guidry, M. J., 1992, "Labyrinth Seal Rotordynamic Forces Using a Three-Dimensional Navier-Stokes Code," ASME Journal of Tribology, 114(4), pp. 683-689.
- [123] Baskharone, E. A., and Hensel, S. J., 1991, "A Finite-Element Perturbation Approach to Fluid/Rotor Interaction in Turbomachinery Elements. Part 1: Theory," ASME Journal of Fluids Engineering, 113(3), pp. 353-361.
- [124] Baskharone, E. A., 1999, "Swirl Brake Effect on the Rotordynamic Stability of a Shrouded Impeller," ASME Journal of Turbomachinery, 121(1), pp. 127-133.
- [125] Moore, J. J., and Palazzolo, A. B., 1999, "CFD Comparison to 3D Laser Anemometer and Rotordynamic Force Measurements for Grooved Liquid Annular Seals," ASME Journal of Tribology, 121(2), pp. 306-314.
- [126] Moore, J. J., Ransom, D. L., and Viana, F., 2011, "Rotordynamic Force Prediction of Centrifugal Compressor Impellers Using Computational Fluid Dynamics," ASME Journal of Engineering for Gas Turbines and Power, 133(4), p. 042504.
- [127] Untaroiu, A., Wood, H. G., Migliorini, P., Allaire, P. E., and Kocur Jr, J. A., "Hole-Pattern Seals: a Three Dimensional CFD Approach for Computing Rotordynamic Coefficient and Leakage Characteristics," Proc. ASME 2009 International Mechanical Engineering Congress and Exposition, IMECE2009, November 13, 2009 - November 19, 2009, American Society of Mechanical Engineers (ASME), pp. 981-990.
- [128] Untaroiu, A., Hayrapetian, V., Untaroiu, C. D., Wood, H. G., Schiavello, B., and McGuire, J., 2013, "On the Dynamic Properties of Pump Liquid Seals," ASME Journal of Fluids Engineering, 135(5), p. 051104.
- [129] Untaroiu, A., Morgan, N., Hayrapetian, V., and Schiavello, B., 2017, "Dynamic Response Analysis of Balance Drum Labyrinth Seal Groove Geometries Optimized for Minimum Leakage," ASME Journal of Vibration and Acoustics, 139(2), pp. 021014-021014-021019.
- [130] Ha, T. W., and Choe, B. S., 2012, "Numerical Simulation of Rotordynamic Coefficients for Eccentric Annular-Type-Plain-Pump Seal Using CFD Analysis," Journal of Mechanical Science and Technology, 26(4), pp. 1043-1048.

- [131] Storteig, E., 2000, "Dynamic characteristics and leakage performance of liquid annular seals in centrifugal pumps." Ph.D. dissertation, Norwegian University of Science and Technology, Trondheim, Norway.
- [132] Moore, J. J., 2003, "Three-Dimensional CFD Rotordynamic Analysis of Gas Labyrinth Seals," *ASME Journal of Vibration and Acoustics*, 125(4), pp. 427-433.
- [133] Kim, E., and Palazzolo, A., 2016, "Rotordynamic Force Prediction of a Shrouded Centrifugal Pump Impeller-Part II: Stability Analysis," *ASME Journal of Vibration and Acoustics*, 138(3), pp. 031015-031015-031013.
- [134] Migliorini, P. J., Untaroiu, A., Wood, H. G., and Allaire, P. E., 2012, "A Computational Fluid Dynamics/Bulk-Flow Hybrid Method for Determining Rotordynamic Coefficients of Annular Gas Seals," *ASME Journal of Tribology*, 134(2):022202-022202-9. doi:10.1115/1.4006407.
- [135] Migliorini, P. J., Untaroiu, A., and Wood, H. G., 2014, "A Numerical Study on the Influence of Hole Depth on the Static and Dynamic Performance of Hole-Pattern Seals," *ASME Journal of Tribology*, 137(1):011702-011702-7. doi:10.1115/1.4028604.
- [136] San Andrés, L., Wu, T., Maeda, H., and Tomoki, O., 2017, "A Computational Fluid Dynamics Modified Bulk Flow Analysis for Circumferentially Shallow Grooved Liquid Seals," *ASME Journal of Engineering for Gas Turbines and Power*, 140(1), pp. 012504-012504-012509.
- [137] Chochua, G., and Soulas, T. A., 2007, "Numerical Modeling of Rotordynamic Coefficients for Deliberately Roughened Stator Gas Annular Seals," *ASME Journal of Tribology*, 129(2), pp. 424-429.
- [138] Nielsen, K. K., Jønck, K., and Underbakke, H., 2012, "Hole-Pattern and Honeycomb Seal Rotordynamic Forces: Validation of CFD-Based Prediction Techniques," *ASME Journal of Engineering for Gas Turbines and Power*, 134(12), pp. 122505-122505.
- [139] Yan, X., Li, J., and Feng, Z., 2011, "Investigations on the Rotordynamic Characteristics of a Hole-Pattern Seal Using Transient CFD and Periodic Circular Orbit Model," *ASME Journal of Vibration and Acoustics*, 133(4).
- [140] Li, Z., Li, J., and Yan, X., 2013, "Multiple Frequencies Elliptical Whirling Orbit Model and Transient RANS Solution Approach to Rotordynamic Coefficients of Annular Gas Seals Prediction," *ASME Journal of Vibration and Acoustics*, 135(3), pp. 031005-031005-031014.

- [141] Li, Z., Li, J., and Feng, Z., 2015, "Comparisons of Rotordynamic Characteristics Predictions for Annular Gas Seals Using the Transient Computational Fluid Dynamic Method Based on Different Single-Frequency and Multifrequency Rotor Whirling Models," *ASME Journal of Tribology*, 138(1), pp. 011701-011701-011718.
- [142] Li, Z., Li, J., and Feng, Z., 2016, "Comparisons of Rotordynamic Characteristics Predictions for Annular Gas Seals Using the Transient Computational Fluid Dynamic Method Based on Different Single-Frequency and Multifrequency Rotor Whirling Models," *ASME Journal of Tribology*, 138(1).
- [143] Marquette, O. R., and Childs, D. W., "An Extended Three-Control-Volume Theory for Circumferentially-Grooved Liquid Seals," *Proceedings of the 1995 Jt. ASME/STLE Tribology Conference*, October 8, 1995 - October 11, 1995, ASME, pp. 10pp-10pp.
- [144] Untaroiu, A., Untaroiu, C. D., Wood, H. G., and Allaire, P. E., 2013, "Numerical Modeling of Fluid-Induced Rotordynamic Forces in Seals with Large Aspect Ratios," *ASME Journal of Engineering for Gas Turbines and Power*, 135(1):012501-012501-7. doi:10.1115/1.4007341.
- [145] Meng, Z., Xiao-fang, W., Sheng-li, X., and Wei, W., 2013, "Numerical Simulation of the Flow Field in Circumferential Grooved Liquid Seals," *Advances in Mechanical Engineering*, p. 797201 (797210 pp.).
- [146] Kim, S. H., and Ha, T. W., 2016, "Prediction of Leakage and Rotordynamic Coefficients for the Circumferential-Groove-Pump Seal Using CFD Analysis," *Journal of Mechanical Science and Technology*, 30(5), pp. 2037-2043.
- [147] Childs, D., and Hale, K., 1994, "Test Apparatus and Facility to Identify the Rotordynamic Coefficients of High-Speed Hydrostatic Bearings," *ASME Journal of Tribology*, 116(2), pp. 337-344.
- [148] Smirnov, P. E., and Menter, F. R., 2009, "Sensitization of the SST Turbulence Model to Rotation and Curvature by Applying the Spalart-Shur Correction Term," *ASME Journal of Turbomachinery*, 131(4), p. 041010 (041018 pp.).
- [149] Balasubramanian, R., Barrows, S., and Chen, J. P., "Investigation of Shear-Stress Transport Turbulence Model for Turbomachinery Applications," *Proc. 46th AIAA Aerospace Sciences Meeting and Exhibit*, January 7, 2008 - January 10, 2008, American Institute of Aeronautics and Astronautics Inc, AIAA 2008-566.
- [150] Nikparto, A., and Schobeiri, M. T., "Investigation of Aerodynamics and Heat Transfer of a Highly Loaded Turbine Blade Using the Universal Intermittency

Function," Proc. International Gas Turbine Institute (IGTI) June 2017, American Society of Mechanical Engineers (ASME), GT2017-64988.

- [151] Schobeiri, M. T., and Nikparto, A., "A Comparative Numerical Study of Aerodynamics and Heat Transfer on Transitional Flow around a Highly Loaded Turbine Blade with Flow Separation Using RANS, URANS and LES," Proc. ASME Turbo Expo 2014: Turbine Technical Conference and Exposition, American Society of Mechanical Engineers, pp. V05CT17A001-V005CT017A001, GT2014-25828.
- [152] Jafari, M., Afshin, H., Farhanieh, B., and Bozorgasareh, H., 2016, "Experimental and Numerical Investigation of a 60cm Diameter Bladeless Fan," Journal of Applied Fluid Mechanics, 9(2).
- [153] Khalesi, J., Modaresahmadi, S., and Atefi, G., 2018, "SEM Gamma Prime Observation in a Thermal and Stress Analysis of a First-stage Rene'80H gas Turbine Blade: Numerical and Experimental Investigation," Iranian Journal of Science and Technology, Transactions of Mechanical Engineering, pp. 1-14.
- [154] Ansys-CFX, 2016, "ANSYS CFX-solver theory guide," ANSYS CFX Release 16.2.
- [155] Untaroiu, A., Throckmorton, A. L., Patel, S. M., Wood, H. G., Allaire, P. E., and Olsen, D. B., 2005, "Numerical and Experimental Analysis of an Axial Flow Left Ventricular Assist Device: The Influence of the Diffuser on Overall Pump Performance," Artificial Organs, 29(7), pp. 581-591.
- [156] Suzuki, T., Prunieres, R., Horiguchi, H., Tsukiya, T., Taenaka, Y., and Tsujimoto, Y., 2007, "Measurements of Rotordynamic Forces on an Artificial Heart Pump Impeller," ASME Journal of Fluids Engineering, 129(11), pp. 1422-1427.
- [157] Childs, D. W., 1991, "Centrifugal-Acceleration Modes for Incompressible Fluid in the Leakage Annulus between a Shrouded Pump Impeller and Its Housing," ASME Journal of Vibration and Acoustics, 113(2), pp. 209-218.
- [158] Hafezisefat, P., Nasr Esfahany, M., and Jafari, M., 2017, "An Experimental and Numerical Study of Heat Transfer in Jacketed Vessels by SiO₂ Nanofluid," Heat and Mass Transfer, 53(7), pp. 2395-2405.
- [159] Goodarzi, M., and Khalesi, J., 2012, "Experimental and Numerical Studies on Frequency and Damping of Liquid Oscillation in a Storage Tank." Journal of Aerospace Mechanics, 7(4), pp. 25-34.

- [160] Jafari, M., Babajani, A., Hafezisefat, P., Mirhosseini, M., Rezaia, A., and Rosendahl, L., 2018, "Numerical Simulation of a Novel Ocean Wave Energy Converter," *Energy Procedia*, 147, pp. 474-481.
- [161] Rahbari, I., and Scalo, C., "Quasi-Spectral Sparse Bi-Global Stability Analysis of Compressible Channel Flow over Complex Impedance," *Proc. 55th AIAA Aerospace Sciences Meeting*, p. 1879.
- [162] Schobeiri, M. T., and Ghoreyshi, S. M., 2015, "The Ultrahigh Efficiency Gas Turbine Engine with Stator Internal Combustion," *ASME Journal of Engineering for Gas Turbines and Power*, 138(2), pp. 021506-021506-021514.
- [163] Jafari, M. M., Atefi, G., Khalesi, J., and Soleymani, A., 2012, "A New Conjugate Heat Transfer Method to Analyze a 3D Steam Cooled Gas Turbine Blade with Temperature-Dependent Material Properties," *Proceedings of the Institution of Mechanical Engineers, Part C: Journal of Mechanical Engineering Science*, 226(5), pp. 1309-1320.
- [164] Jafari, M. M., Atefi, G. A., and Khalesi, J., 2012, "Advances in Nonlinear Stress Analysis of a Steam Cooled Gas Turbine Blade," *Latin American Applied Research*, 42(2), pp. 167-175.
- [165] Baskharone, E. A., and Hensel, S. J., 1991, "A Finite-Element Perturbation Approach to Fluid/Rotor Interaction in Turbomachinery Elements. Part 2: Application," *ASME Journal of Fluids Engineering*, 113(3), pp. 362-367.
- [166] Mortazavi, F., and Palazzolo, A., 2017, "Prediction of Rotordynamic Performance of Smooth Stator-Grooved Rotor Liquid Annular Seals Utilizing Computational Fluid Dynamics," *ASME Journal of Vibration and Acoustics*, 140(3), pp. 031002-031002-031009.
- [167] Posa, A., Lippolis, A., Verzicco, R., and Balaras, E., 2011, "Large-Eddy Simulations in Mixed-Flow Pumps Using an Immersed-Boundary Method," *Computers & Fluids*, 47(1), pp. 33-43.
- [168] Castilla, R., Gamez-Montero, P. J., Raush, G., and Codina, E., 2017, "Method for Fluid Flow Simulation of a Gerotor Pump Using OpenFOAM," *ASME Journal of Fluids Engineering*, 139(11), pp. 111101-111101-111109.
- [169] del Campo, D., Castilla, R., Raush, G. A., Gamez Montero, P. J., and Codina, E., 2012, "Numerical Analysis of External Gear Pumps Including Cavitation," *ASME Journal of Fluids Engineering*, 134(8), pp. 081105-081105-081112.
- [170] CFturbo, 2017, "CFturbo User Manual," CFturbo GmbH, Dresden - Munich, Germany.

- [171] Jery, B., Brennen, C. E., Caughey, T. K., and Acosta, A., 1985, "Forces on Centrifugal Pump Impellers," Second International Pump Symposium, College Station, TX, pp. 21–32.
- [172] Makay, E., and Barrett, J., "Changes in Hydraulic Component Geometries Greatly Increased Power Plant Availability and Reduced Maintenance Cost: Case Histories," Proc. Proceedings of the First International Pump Symposium, pp. 85-100.
- [173] Guelich, J. F., and Bolleter, U., 1992, "Pressure Pulsations in Centrifugal Pumps," Journal of vibration, acoustics, stress, and reliability in design, 114(2), pp. 272-279.
- [174] ANSYS, 2017, "ANSYS user manual," ANSYS, Inc., Canonsburg, PA.
- [175] Ghoreyshi, S. M., and Schobeiri, M. T., 2017, "Numerical Simulation of the Multistage Ultra-High Efficiency Gas Turbine Engine, UHEGT," (50831), p. V003T006A034.
- [176] Nikparto, A., and Schobeiri, M. T., 2018, "Combined Numerical and Experimental Investigations of Heat Transfer of a Highly Loaded Low-Pressure Turbine Blade under Periodic Inlet Flow Condition," Proceedings of the Institution of Mechanical Engineers, Part A: Journal of Power and Energy, 0(0), p. 0957650918758158.
- [177] DaqiqShirazi, M., Torabi, R., Riasi, A., and Nourbakhsh, S., 2017, "The Effect of Wear Ring Clearance on Flow Field in the Impeller Sidewall Gap and Efficiency of a Low Specific Speed Centrifugal Pump," Proceedings of the Institution of Mechanical Engineers, Part C: Journal of Mechanical Engineering Science, 0(0), p. 0954406217729420.
- [178] Berten, S., 2010, "Hydrodynamics of High Specific Power Pumps for Off-Design Operating Conditions," Ph.D. dissertation, École Polytechnique Fédérale de Lausanne, Switzerland.
- [179] Celik, I. B., Ghia, U., Roache, P. J., Freitas, C. J., and Coleman, H., 2008, "Procedure for Estimation and Reporting of Uncertainty Due to Discretization in CFD Applications," ASME Journal of Fluids Engineering, 130(7), pp. 078001-078001-078004.
- [180] Mortazavi, F., Riasi, A., and Nourbakhsh, A., 2017, "Numerical Investigation of Back Vane Design and Its Impact on Pump Performance," ASME Journal of Fluids Engineering, 139(12), pp. 121104-121104-121109.

- [181] Droege, A. R., Williams, R. W., and Garcia, R., 2000, "Unshrouded Impeller Technology Development Status," NASA report 2000.
- [182] Babajani, A., Jafari, M., Hafezisefat, P., Mirhosseini, M., Rezaia, A., and Rosendahl, L., 2018, "Parametric Study of a Wave Energy Converter (Searaser) for Caspian Sea," *Energy Procedia*, 147, pp. 334-342.
- [183] Jafari, M., Sojoudi, A., and Hafezisefat, P., 2017, "Numerical Study of Aeroacoustic Sound on Performance of Bladeless Fan," *Chinese Journal of Mechanical Engineering*, 30(2), pp. 483-494.
- [184] Nejat, A., Aryanaki, M., and Rahbari, I., 2014, "A Robust Engineering Approach for Wind Turbine Blade Profile Aeroelastic Computation," *Energy Equipment and Systems*, 2(2), pp. 121-128.
- [185] Mortazavi, F., and Palazzolo, A., 2018, "Rotordynamic Force Coefficients of Volutes and Diffusers for Prediction of Turbomachinery Vibration," *ASME Journal of Vibration and Acoustics*, 140(5), pp. 051015-051015-051012.
- [186] Schroeder, M., 1970, "Synthesis of Low-Peak-Factor Signals and Binary Sequences with Low Autocorrelation (Corresp.)," *IEEE Transactions on Information Theory*, 16(1), pp. 85-89.
- [187] Lakshminarayana, B., 1991, "An Assessment of Computational Fluid Dynamic Techniques in the Analysis and Design of Turbomachinery—the 1990 Freeman Scholar Lecture," *ASME Journal of Fluids Engineering*, 113(3), pp. 315-352.
- [188] Menter, F., Kuntz, M., and Langtry, R., 2003, "Ten Years of Industrial Experience with the SST Turbulence Model," *Turbulence, Heat and Mass Transfer*, 4(1), pp. 625-632.
- [189] Jafari, M., Afshin, H., Farhanieh, B., and Bozorgasareh, H., 2015, "Numerical Aerodynamic Evaluation and Noise Investigation of a Bladeless Fan," *Journal of Applied Fluid Mechanics*, 8(1), pp. 133-142.
- [190] Langtry, R. B., and Menter, F. R., 2009, "Correlation-Based Transition Modeling for Unstructured Parallelized Computational Fluid Dynamics Codes," *AIAA Journal*, 47(12), pp. 2894-2906.
- [191] Pasini, A., Torre, L., Cervone, A., and d'Agostino, L., 2011, "Continuous Spectrum of the Rotordynamic Forces on a Four Bladed Inducer," *ASME Journal of Fluids Engineering*, 133(12), pp. 121101-121101-121110.

- [192] Martinez-Sanchez, M., Jaroux, B., Song, S. J., and Yoo, S., 1993, "Measurement of Turbine Blade-Tip Rotordynamic Excitation Forces," (78880), p. V001T003A058.
- [193] Hussain, A. K. M. F., and Reynolds, W. C., 1970, "The Mechanics of an Organized Wave in Turbulent Shear Flow," *Journal of Fluid Mechanics*, 41(2), pp. 241-258.
- [194] Slotnick, J., Khodadoust, A., Alonso, J., Darmofal, D., Gropp, W., Lurie, E., and Mavriplis, D., 2014, "CFD Vision 2030 Study: a Path to Revolutionary Computational Aerosciences," NASA report 2014.
- [195] Wilcox, D. C., 2008, "Formulation of the k-w Turbulence Model Revisited," *AIAA Journal*, 46(11), pp. 2823-2838.
- [196] Boussinesq, J., 1877, "Théorie de l'écoulement tourbillant," *Mem. Présentés par Divers Savants Acad. Sci. Inst. Fr*, 23(46-50), p. 6.5.
- [197] Morinishi, Y., Vasilyev, O. V., and Ogi, T., 2004, "Fully Conservative Finite Difference Scheme in Cylindrical Coordinates for Incompressible Flow Simulations," *Journal of Computational Physics*, 197(2), pp. 686-710.
- [198] Currie, I. G., 2002, *Fundamental Mechanics of Fluids*, 3rd edition, Marcel Dekker, Inc., New York, New York.
- [199] Schobeiri, M., 2005, *Turbomachinery Flow Physics and Dynamic Performance*, 2nd edition, Springer-Verlag, Berlin.
- [200] Prandtl, L., and Wieghardt, K., 1947, Über ein neues Formelsystem für die ausgebildete Turbulenz, *Vandenhoeck & Ruprecht*.
- [201] Kolmogorov, A. N., "Equations of Turbulent Motion in an Incompressible Fluid," *Proc. Dokl. Akad. Nauk SSSR*, pp. 299-303.
- [202] Hellsten, A., Laine, S., Hellsten, A., and Laine, S., 1997, "Extension of the K-Omega-SST Turbulence Model for Flows over Rough Surfaces," 22nd Atmospheric Flight Mechanics Conference, American Institute of Aeronautics and Astronautics.
- [203] Menter, F. R., 1996, "Comparison of Some Recent Eddy-Viscosity Turbulence Models," *Journal of Fluids Engineering, Transactions of the ASME*, 118(3), pp. 514-519.
- [204] Wilcox, D. C., 1998, *Turbulence Modeling for CFD*, 2nd edition, DCW industries La Canada, California.

- [205] Lai, W. M., Rubin, D. H., Rubin, D., and Krempl, E., 2009, Introduction to Continuum Mechanics, 4th edition, Butterworth-Heinemann, Oxford.
- [206] Lakshminarayana, B., 1986, "Turbulence Modeling for Complex Shear Flows," AIAA journal, 24(12), pp. 1900-1917.
- [207] Dufour, G., Cazalbou, J.-B., Carbonneau, X., and Chassaing, P., 2008, "Assessing Rotation/Curvature Corrections to Eddy-Viscosity Models in the Calculations of Centrifugal-Compressor Flows," ASME Journal of Fluids Engineering, 130(9), p. 091401.
- [208] Menter, F. R., 1992, "Improved Two-Equation k-omega Turbulence Models for Aerodynamic Flows." NASA report 1992.
- [209] Jones, W., and Launder, B., 1972, "The Prediction of Laminarization with a Two-Equation Model of Turbulence," International Journal of Heat and Mass Transfer, 15(2), pp. 301-314.
- [210] Bradshaw, P., Ferriss, D., and Atwell, N., 1967, "Calculation of Boundary-Layer Development Using the Turbulent Energy Equation," Journal of Fluid Mechanics, 28(03), pp. 593-616.
- [211] Wilcox, D. C., 1993, "Comparison of Two-Equation Turbulence Models for Boundary Layers with Pressure Gradient," AIAA Journal, 31(8), pp. 1414-1421.
- [212] Chorin, A. J., 1968, "Numerical Solution of the Navier-Stokes Equations," Mathematics of Computation, 22(104), pp. 745-762.
- [213] Ferziger, J. H., and Peric, M., 2012, Computational Methods for Fluid Dynamics, 3rd edition, Springer-Verlag, Berlin.
- [214] MacCormack, R. W., "Numerical Solution of the Interaction of a Shock Wave with a Laminar Boundary Layer," Proceedings of the second international conference on numerical methods in fluid dynamics, Springer, pp. 151-163.
- [215] MacCormack, R. W., 1976, "An Efficient Numerical Method for Solving the Time-Dependent Compressible Navier-Stokes Equations at High Reynolds Number." NASA technical report 1976.
- [216] Maccormack, R., 1985, "Current status of numerical solutions of the Navier-Stokes equations," 23rd Aerospace Sciences Meeting, American Institute of Aeronautics and Astronautics.
- [217] Hoffmann, K. A., 1989, "Computational Fluid Dynamics for Engineers," Engineering Education System, Austin, Texas.

- [218] Patankar, S., 1980, Numerical Heat Transfer and Fluid Flow, CRC press.
- [219] Caretto, L. S., Gosman, A. D., Patankar, S. V., and Spalding, D. B., 1973, "Two Calculation Procedures for Steady, Three-Dimensional Flows with Recirculation," Proceedings of the Third International Conference on Numerical Methods in Fluid Mechanics: Vol. II Problems of Fluid Mechanics, H. Cabannes, and R. Temam, eds., Springer Berlin Heidelberg, Berlin, Heidelberg, pp. 60-68.
- [220] Spalding, D. B., 1972, "A Novel Finite Difference Formulation for Differential Expressions Involving both First and Second Derivatives," International Journal for Numerical Methods in Engineering, 4(4), pp. 551-559.
- [221] Rhie, C. M., and Chow, W. L., 1983, "Numerical Study of the Turbulent Flow Past an Airfoil with Trailing Edge Separation," AIAA Journal, 21(11), pp. 1525-1532.
- [222] Fornberg, B., 1988, "Generation of Finite Difference Formulas on Arbitrarily Spaced Grids," Mathematics of computation, 51(184), pp. 699-706.
- [223] Batterson, J., 2014, <http://fundamentalthinking.blogspot.com/2014/08/second-order-finite-difference-schemes.html>.
- [224] CFD-Online, 2012, http://www.cfd-online.com/Wiki/Structured_mesh_generation.
- [225] Vinokur, M., 1983, "On One-Dimensional Stretching Functions for Finite-Difference Calculations," Journal of Computational Physics, 50(2), pp. 215-234.
- [226] Burden, R. L., and Faires, J. D., 1993, "Numerical Analysis," PWS, Boston.
- [227] Launder, B. E., and Spalding, D. B., 1974, "The Numerical Computation of Turbulent Flows," Computer Methods in Applied Mechanics and Engineering, 3(2), pp. 269-289.
- [228] Williams, M., Chen, W. C., Baché, G., and Eastland, A., 1991, "An Analysis Methodology for Internal Swirling Flow Systems with a Rotating Wall," ASME Journal of Turbomachinery, 113(1), pp. 83-90.
- [229] Schlichting, H., Gersten, K., Krause, E., Oertel, H., and Mayes, K., 1960, Boundary-Layer Theory, Springer.
- [230] Reichardt, H., 1951, "Vollständige Darstellung der Turbulenten Geschwindigkeitsverteilung in Glatten Leitungen," ZAMM - Journal of Applied Mathematics and Mechanics / Zeitschrift für Angewandte Mathematik und Mechanik, 31(7), pp. 208-219.

- [231] Hachem, M. E., 2009, "Stabilized Finite Element Method for Heat Transfer and Turbulent Flows Inside Industrial Furnaces," Ph.D. dissertation, Ecole Nationale Supérieure des Mines de Paris, Paris, France.
- [232] Menter, F., and Esch, T., 2001, "Elements of Industrial Heat Transfer Predictions," Proc. 16th Brazilian Congress of Mechanical Engineering (COBEM), Nov 26 (Vol. 109).
- [233] Vieser, W., Esch, T., and Menter, F., 2002, "Heat Transfer Predictions Using Advanced Two-Equation Turbulence Models." NASA report 2002.
- [234] Patel, V. C., Rodi, W., and Scheuerer, G., 1985, "Turbulence Models for Near-Wall and Low Reynolds Number Flows - A Review," AIAA Journal, 23(9), pp. 1308-1319.
- [235] Derksen, R. W., and Azad, R. S., 1981, "Behavior of the Turbulent Energy Equation at a Fixed Boundary," AIAA Journal, 19(2), pp. 238-239.
- [236] Kreplin, H. P., and Eckelmann, H., 1979, "Behavior of the Three Fluctuating Velocity Components in the Wall Region of a Turbulent Channel Flow," The Physics of Fluids, 22(7), pp. 1233-1239.
- [237] Backshall, R., and Landis, F., 1969, "The Boundary-Layer Velocity Distribution in Turbulent Swirling Pipe Flow," Journal of Basic Engineering, 91(4), pp. 728-733.
- [238] Lilley, D., and Rhode, D., 1982, "A Computer Code for Swirling Turbulent Axisymmetric Recirculating Flows in Practical Isothermal Combustor Geometries," NASA report 1982.
- [239] Demko, J. A., 1986, "The Prediction and Measurement of Incompressible Flow in a Labyrinth Seal," Ph.D. Dissertation, Texas A&M University, College Station, Texas.
- [240] Trottenberg, U., Oosterlee, C. W., and Schuller, A., 2000, Multigrid, Academic Press, San Diego, California.
- [241] Anderson, D. A., Tannehill, J. C., and Pletcher, R. H., 1984, "Computational Fluid Mechanics and Heat Transfer," Hemisphere Publishing Corporation.
- [242] Brandt, A., 1977, "Multi-Level Adaptive Solutions to Boundary-Value Problems," Mathematics of Computation, 31(138), pp. 333-390.
- [243] Han, J.-C., 2016, Analytical Heat Transfer, CRC Press, Boca Raton, Florida.

- [244] Benton, E. R., and Platzman, G. W., 1972, "A Table of Solutions of the One-Dimensional Burgers Equation," *Quarterly of Applied Mathematics*, 30(2), pp. 195-212.
- [245] McCormick, S. F., 1987, *Multigrid Methods*, SIAM, Dexter, Michigan.
- [246] Roger Briley, W., 1974, "Numerical Method for Predicting Three-Dimensional Steady Viscous Flow in Ducts," *Journal of Computational Physics*, 14(1), pp. 8-28.
- [247] Amdahl, G. M., 2007, "Validity of the Single Processor Approach to Achieving Large Scale Computing Capabilities, Reprinted from the AFIPS Conference Proceedings, Vol. 30 (Atlantic City, N.J., Apr. 18–20), AFIPS Press, Reston, Va., 1967, pp. 483–485, when Dr. Amdahl was at International Business Machines Corporation, Sunnyvale, California," *IEEE Solid-State Circuits Society Newsletter*, 12(3), pp. 19-20.
- [248] Donzis, D., 2016, "High Performance CFD Class Notes," Texas A&M University, College Station, Texas.
- [249] Hirsch, C., 2007, *Numerical Computation of Internal and External Flows: The Fundamentals of Computational Fluid Dynamics*, Butterworth-Heinemann.
- [250] Harlow, F. H., and Welch, J. E., 1965, "Numerical Calculation of Time-Dependent Viscous Incompressible Flow of Fluid with Free Surface," *Physics of Fluids*, 8(12), p. 2182.
- [251] Panton, R. L., 2006, *Incompressible Flow*, John Wiley & Sons.
- [252] Drazin, P. G., and Reid, W. H., 2004, *Hydrodynamic Stability*, Cambridge University Press.
- [253] Langlois, W. E., and Deville, M. O., 1964, *Slow Viscous Flow*, Springer.
- [254] Mohamed, A. G., Valentine, D. T., and Hassel, R. E., 1991, "Numerical Study of Laminar Separation over an Annular Backstep," *Computers & Fluids*, 20(2), pp. 121-143.
- [255] Poinso, T. J., amp, and Lelef, S., 1992, "Boundary Conditions for Direct Simulations of Compressible Viscous Flows," *Journal of Computational Physics*, 101(1), pp. 104-129.
- [256] Moody, L. F., 1944, "Friction Factors for Pipe Flow," *Transactions of ASME*, 66(8), pp. 671-684.

- [257] Inoue, M., and Kurooumaru, M., 1989, "Structure of Tip Clearance Flow in an Isolated Axial Compressor Rotor," *ASME Journal of Turbomachinery*, 111(3), pp. 250-256.
- [258] Wu, S.-C., and Chen, Y.-M., 2003, "Phase-Averaged Method Applied to Periodic Flow Between Shrouded Corotating Disks," *International Journal of Rotating Machinery*, 9(4), pp. 293-301.
- [259] Hoover, C. B., Shen, J., and Kreshock, A. R., 2018, "Propeller Whirl Flutter Stability and Its Influence on X-57 Aircraft Design," *Journal of Aircraft*, pp. 1-7.
- [260] Derakhshan, S., and Nourbakhsh, A., 2008, "Theoretical, Numerical and Experimental Investigation of Centrifugal Pumps in Reverse Operation," *Experimental Thermal and Fluid Science*, 32(8), pp. 1620-1627.
- [261] Tsujimoto, Y., Imaichi, K., Tomohiro, T., and Gotoo, M., 1986, "A Two-Dimensional Analysis of Unsteady Torque on Mixed Flow Impellers," *ASME Journal of Fluids Engineering*, 108(1), pp. 26-33.
- [262] Arghir, M., and Frêne, J., 1997, "Analysis of a Test Case for Annular Seal Flows," *ASME Journal of Tribology*, 119(3), pp. 408-414.
- [263] Liao, S., 2012, *Homotopy Analysis Method in Nonlinear Differential Equations*, Higher Education press, Beijing.
- [264] Barth, T., and Jespersen, D., "The Design and Application of Upwind Schemes on Unstructured Meshes," *Proc. 27th Aerospace sciences meeting*, p. 366.
- [265] Spalart, P., and Shur, M., 1997, "On the Sensitization of Turbulence Models to Rotation and Curvature," *Aerospace Science and Technology*, 1(5), pp. 297-302.

APPENDIX A CFX SOLVER THEORY

In this section some of the salient features of ANSYS CFX solver theory are discussed in more detail. For further details, the reader is encouraged to consult ANSYS user manual documentations [174].

A.1. Discretization of Governing Equations

CFX benefits from an element based FVM discretization which is advantageous in conserving mass, momentum and energy. Integration of governing equations is done based on Gauss Theorem over a given control volume. This way the transport equation for a given variable ϕ reads,

$$\frac{d}{dt} \int_V \rho \phi dV + \int_s \rho U_j \phi dn_j = \int_s \Gamma_{eff} \left(\frac{\partial \phi}{\partial x_j} \right) dn_j + \int_V S_\phi dV \quad (309)$$

Here s, V refer to surface and volume integrals, ρ is density, Γ_{eff} is the effective diffusivity and S_i is the source term. dn_j is the Cartesian normal vector. CFX uses adjacent elements to form a central control volume though the element mid-planes, as is shown in Figure 163:

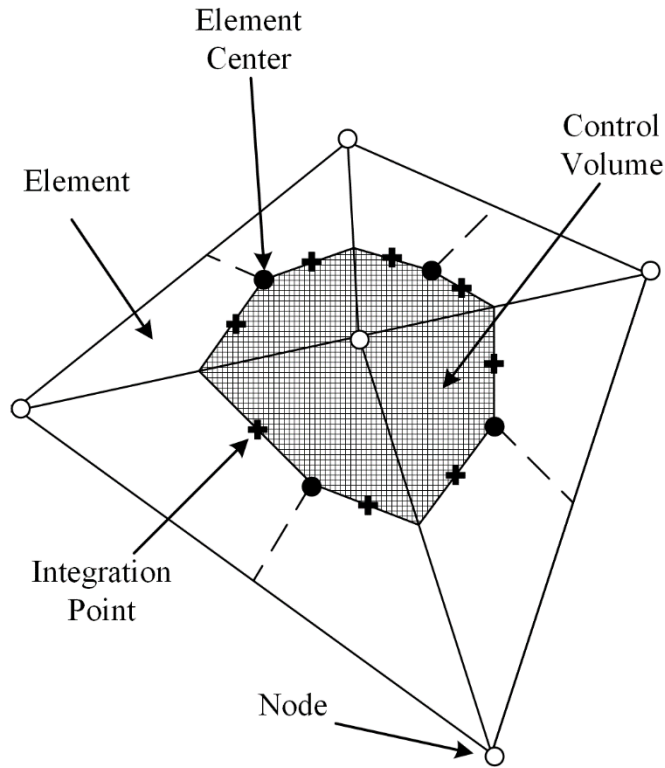


Figure 163. Element-based finite volume method, 2D representation

That is 24 surfaces in 3D to form the finite volume. The discrete form of the transport equation will be:

$$\Delta V \left(\frac{\rho\phi - \rho^0\phi^0}{\Delta t} \right) + \sum_{ip} \dot{m}_{ip} \phi_{ip} = \sum_{ip} \left[\Gamma_{eff} \frac{\partial\phi}{\partial x_j} \Delta n_j \right]_{ip} + \bar{S}_\phi \Delta V \quad (310)$$

For the sake of simplicity, a first order backward Euler was used in the equation. Here ip is short for integration point, \dot{m} is the mass flow rate, and \bar{S}_ϕ is averaged over the control volume. Since the solution is stored at nodes and fluxes are computed at integration points, based on the finite element approach the fluxes are found using shape functions N_n :

$$\frac{\partial \phi}{\partial x_i} |_{ip} = \sum_n \frac{\partial N_n}{\partial x_i} |_{ip} \phi_n \quad (311)$$

Since the CFX conservative formulation is based on Cartesian coordinates x, y, z , the shape function derivatives need to be transformed into the local coordinates s, t, u ($\in [0,1]$) using the Jacobian of transformation:

$$\begin{bmatrix} \frac{\partial N}{\partial x} \\ \frac{\partial N}{\partial y} \\ \frac{\partial N}{\partial z} \end{bmatrix} = \begin{bmatrix} \frac{\partial x}{\partial s} & \frac{\partial y}{\partial s} & \frac{\partial z}{\partial s} \\ \frac{\partial x}{\partial t} & \frac{\partial y}{\partial t} & \frac{\partial z}{\partial t} \\ \frac{\partial x}{\partial u} & \frac{\partial y}{\partial u} & \frac{\partial z}{\partial u} \end{bmatrix}^{-1} \begin{bmatrix} \frac{\partial N}{\partial s} \\ \frac{\partial N}{\partial t} \\ \frac{\partial N}{\partial u} \end{bmatrix} \quad (312)$$

The 8 tri-linear shape functions for the hexahedral element are defined as:

$$\begin{aligned} N_1 &= (1-s)(1-t)(1-u), & N_5 &= (1-s)(1-t)u \\ N_2 &= s(1-t)(1-u), & N_6 &= s(1-t)u \\ N_3 &= st(1-u), & N_7 &= stu \\ N_4 &= (1-s)t(1-u), & N_8 &= (1-s)tu \end{aligned} \quad (313)$$

The pressure gradient term is determined by the nodal values of pressure according to:

$$p_{ip} = \sum_n N_n(\xi_{ip}, \eta_{ip}, \zeta_{ip}) p_n \quad (314)$$

A.2. High Resolution Scheme

CFX allows setting the advection term accuracy from first order to second order.

In this study a High Resolution scheme has been used which tries to give the closes

form to the second order upwind unless there is an overshoot in presence of sharp gradients and shocks. The formulation:

$$\phi_{ip} = \phi_{up} + \beta \nabla \phi \cdot \Delta \vec{r} \quad (315)$$

finds β in such a way that that the solution does not under shoot or over shoot ϕ_{max} or ϕ_{min} bounds. These bounds are found from the limiter method of Barth and Jespersen [264] based on neighboring stencils. $\beta = 1$ is the limit for the second order upwind and $\beta = 0$ is the first order upwind limit. In the above formula ϕ_{up} is the value at the upwind node and $\Delta \vec{r}$ is the distance of the integration point from the upwind node.

A.3. Pressure-Velocity Coupling

CFX uses the Rhie-Chow [221] scheme in order to avoid a segregated solver, accelerate convergence, remove the checker board effect and enable utilization of collocated grids instead of staggered grids. The coupling is done through addition of a third order pressure term to the continuity equation, also known as the pressure-redistribution term (for a uniform grid):

$$\frac{\partial U_i}{\partial x_i} + \frac{\Delta x^3 A}{4\dot{m}} \left(\frac{\partial^4 p}{\partial x_i^4} \right) = 0 \quad (316)$$

where A is the cell surface area and \dot{m} is the mass flow rate to the cell. The fourth order derivative ensures that the last term vanish when the mesh is refined. CFX by default uses a 4th order derivative, but in vicinities of shocks on high speed flows, it automatically blends the term with a second order variation.

A.4. Mesh Deformation

The deformation in mesh volume equals to a time derivative source term which has to be conserved according to Leibnitz rule:

$$\frac{d}{dt} \int_{V(t)} \phi dV = \int_S \frac{\partial \phi}{\partial t} dV + \int_S \phi W_j dn_j \quad (317)$$

where W_j is the mesh cell boundary velocity. Therefore, with the mesh deformation solution, the transport equation is modified to:

$$\frac{d}{dt} \int_{V(t)} \rho \phi dV + \int_S \rho (U_j - W_j) \phi dn_j = \int_S \Gamma_{eff} \left(\frac{\partial \phi}{\partial x_j} \right) dn_j + \int_V S_\phi dV \quad (318)$$

A.5. Eddy Viscosity Turbulence Modeling

RANS equations are solved for turbulent flows which are governed by:

$$\begin{aligned} \frac{\partial \rho U_i}{\partial t} + \frac{\partial}{\partial x_j} (\rho U_i U_j) \\ = - \frac{\partial}{\partial x_i} \left(p + \frac{2}{3} \mu \frac{\partial U_k}{\partial x_k} \right) + \frac{\partial}{\partial x_j} \left[\mu \left(\frac{\partial U_i}{\partial x_j} + \frac{\partial U_j}{\partial x_i} \right) \right] \\ + \frac{\partial}{\partial x_j} (\rho \overline{u_i u_j}) + S_M \end{aligned} \quad (319)$$

here the total velocity is divided into an average velocity U_i and a fluctuating velocity u_i . Eddy viscosity models allow modeling the Reynolds stress term $\rho \overline{u_i u_j}$ in the RANS equations based on the diffusive nature of turbulence:

$$\rho \overline{u_i u_j} = \mu_t \left(\frac{\partial U_i}{\partial x_j} + \frac{\partial U_j}{\partial x_i} \right) - \frac{2}{3} \delta_{ij} \left(\rho k + \mu_t \frac{\partial U_k}{\partial x_k} \right) \quad (320)$$

δ_{ij} is the Kronecker delta. Then, the eddy viscosity RANS equations are governed by:

$$\frac{\partial \rho U_i}{\partial t} + \frac{\partial}{\partial x_j} (\rho U_i U_j) = -\frac{\partial p'}{\partial x_i} + \frac{\partial}{\partial x_j} \left[\mu_{eff} \left(\frac{\partial U_i}{\partial x_j} + \frac{\partial U_j}{\partial x_i} \right) \right] + S_M \quad (321)$$

where S_M shows the body forces, the effective viscosity is the sum of molecular and eddy viscosity:

$$\mu_{eff} = \mu + \mu_t \quad (322)$$

and p' is the modified form of pressure in general case:

$$p' = p + \frac{2}{3} \rho k + \frac{2}{3} \mu_{eff} \frac{\partial U_k}{\partial x_k} \quad (323)$$

The eddy viscosity model used in this work is SST model which gives an accurate prediction of separated flows. Details of this model were discussed in detail in the ‘‘Standalone CFD Code’’ section of the dissertation.

A.6. Curvature Correction

The SST model is further sensitized to rotation and curvature effects using Spalart and Shur [265] curvature correction multiplier of the production term f_r :

$$P_k \rightarrow P_k f_r \quad (324)$$

where

$$f_r = \max[0, 1 + C_{scale}(\tilde{f}_r - 1)]$$

$$\tilde{f}_r = \max\{\min[f_{rotation}, 1.25], 0\} \quad (325)$$

$$f_{rotation} = (1 + c_{r1}) \frac{2r^*}{1 + r^*} [1 - c_{r3} \tan^{-1}(c_{r2} \tilde{r}^*)] - c_{r1}$$

Here f_r is limited to 0 for strongly convex surfaces without turbulence production and 1.25 (empirical) for strongly concave surfaces with enhanced production. C_{sacate} is reserved for ad-hoc manipulations which in this study has a default value of 1.0. In this correction:

$$r^* = \frac{S}{\Omega} \quad (326)$$

$$\tilde{r} = 2\Omega_{ik}S_{jk} \left[\frac{DS_{ij}}{Dt} + (\epsilon_{imn}S_{jn} + \epsilon_{jmn}S_{in})\Omega_m^{Rot} \right] \frac{1}{\Omega D^3}$$

with the strain rate S_{ij} and rotation rate tensors Ω_{ij} :

$$S_{ij} = \frac{1}{2} \left(\frac{\partial U_i}{\partial x_j} + \frac{\partial U_j}{\partial x_i} \right), \quad S^2 = 2S_{ij}S_{ij}$$

$$\Omega_{ij} = \frac{1}{2} \left(\frac{\partial U_i}{\partial x_j} - \frac{\partial U_j}{\partial x_i} \right) + 2\epsilon_{mji}\Omega_m^{rot}, \quad \Omega^2 = 2\Omega_{ij}\Omega_{ij} \quad (327)$$

$$D^2 = \max(S^2, 0.09\omega^2)$$

and Ω_m^{rot} are the components of rotating frame vector. The constants $c_{r1} = 1, c_{r2} = 2$ and $c_{r3} = 1$ are empirical.

A.7. Automatic Near Wall Treatment

One of the advantages of ω based family of eddy viscosity models is that they can be directly integrated to the wall to model the near wall effects. However the Low Re variation requires very low y^+ values which limits the generality of the model. CFX does a transition between the wall-function formulation and low Re variation which supports a wide range of y^+ values. This procedure is called Automatic Near Wall

Treatment which is activated for ω based models. It is recommended to use at least 10 nodes inside the boundary layer to fully benefit from the blending function.

A.8. Transition Modeling

The transition from laminar to turbulence is modeled using a two equation $\gamma - \theta$ model which can predict standard bypass transition and low-free stream turbulence flows based on empirical relations. This transition model along with the SST model has been developed and tested for various cases including turbomachinery applications. However it has shortcomings such as not being Galilean invariant or being only accurate for wall boundary layer flows. The $\gamma - \theta$ model needs a y^+ value of order 1 for good predictions, and its accuracy drops if $y^+ > 5$. The equations are governed by:

$$\frac{\partial(\rho\gamma)}{\partial t} + \frac{\partial(\rho U_j \gamma)}{\partial x_j} = P_{\gamma 1} - E_{\gamma 1} + P_{\gamma 2} - E_{\gamma 2} + \frac{\partial}{\partial x_j} \left[\left(\mu + \frac{\mu_t}{\sigma_\gamma} \right) \frac{\partial \gamma}{\partial x_j} \right] \quad (328)$$

for the intermittency γ , and:

$$\frac{\partial(\rho \widetilde{Re}_{\theta t})}{\partial t} + \frac{\partial(\rho U_j \widetilde{Re}_{\theta t})}{\partial x_j} = P_{\theta t} + \frac{\partial}{\partial x_j} \left[\sigma_{\theta t} (\mu + \mu_t) \frac{\partial \widetilde{Re}_{\theta t}}{\partial x_j} \right] \quad (329)$$

for the transition momentum thickness Reynolds number $\widetilde{Re}_{\theta t}$. The source terms $P_{\gamma 1}, E_{\gamma 1}, P_{\theta t}$ and the destruction-relaminarization terms $P_{\gamma 2}, E_{\gamma 2}$ have empirical nature and are discussed in more detail in the solver theory guide.

The k equation in the SST model is revised to accommodate the transition model influence in the production and destruction terms:

$$\frac{\partial(\rho k)}{\partial t} + \frac{\partial(\rho U_j k)}{\partial x_j} = \tilde{P}_k - \tilde{D}_k + \frac{\partial}{\partial x_j} \left[(\mu + \sigma_k \mu_t) \frac{\partial k}{\partial x_j} \right] \quad (330)$$

where

$$\tilde{P}_k = \gamma_{eff} P_k, \quad \tilde{D}_k = \min(\max(\gamma_{eff}, 0.1), 1.0) D_k \quad (331)$$

the first blending function is also slightly modified. γ_{eff} accounts for effects of separation induced transition, according to an empirical relation supplied by CFX.

APPENDIX B CFTURBO DESIGN PROCEDURE

The design procedure start by selecting the machine type (See Figure 164):

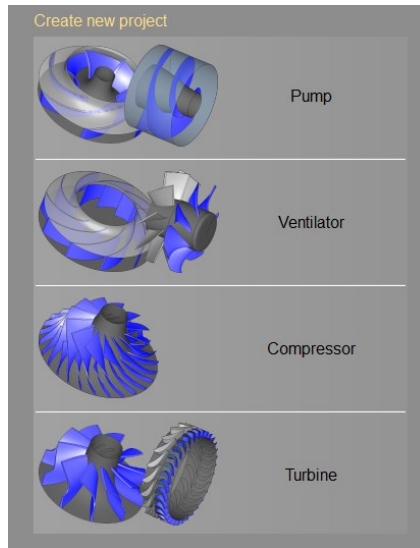
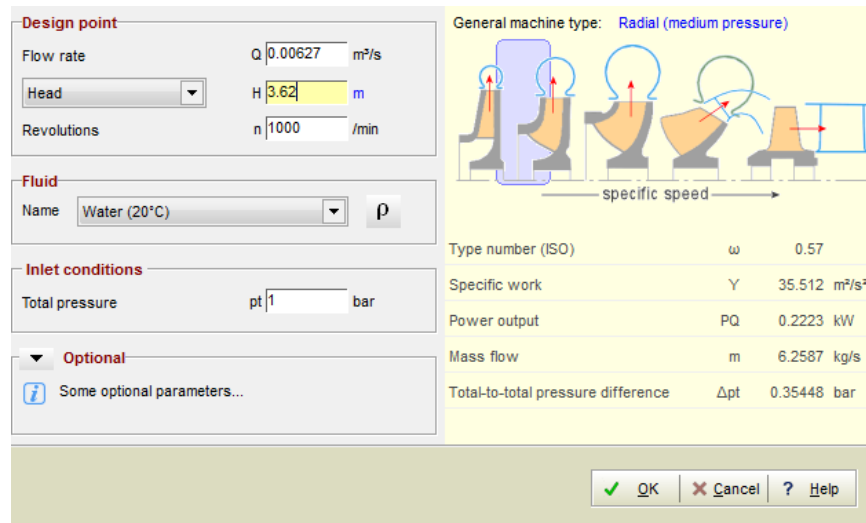


Figure 164. Select a pump project

The operational condition at BEP is inputted subsequently. The units can be changed to desirable ones as it is shown in Figure 165.



The image shows a software window for configuring design parameters. On the left, there are input fields for "Design point", "Fluid", and "Inlet conditions". On the right, there is a diagram of a pump and a table of calculated parameters.

Design point	
Flow rate	Q 0.00627 m ³ /s
Head	H 3.62 m
Revolutions	n 1000 /min

Fluid	
Name	Water (20°C) ρ

Inlet conditions	
Total pressure	pt 1 bar

Optional	
Some optional parameters...	

General machine type: Radial (medium pressure)

Type number (ISO)	ω	0.57
Specific work	Y	35.512 m ² /s ²
Power output	PQ	0.2223 kW
Mass flow	m	6.2587 kg/s
Total-to-total pressure difference	Δpt	0.35448 bar

Buttons: OK, Cancel, Help

Figure 165. Provide operational condition at BEP

Next, the meridional sketch tab pops up (Figure 166). Here select New Radial/Mixed flow impeller. Later other components can be added through this window.

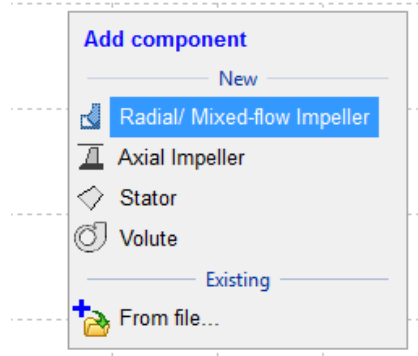


Figure 166. Select to create a new impeller

Consecutively, a new window pops up to define the main dimensions which is a critical step in design (Figure 167). Most of dimensions are calculated automatically either based of theoretical relations or well-known empirical relations. If an open impeller is desired, check the box fo “unshrouded” option in the “setup” tab. Otherwise go to the “Parameters” tab and activate “automatic” checkbox. Then move the third tab named “dimensions”. Here change the default values to your inverse design ones. Here Impeller X dimensions are input. Notice that CFturbo estimation of β_2 with the provided dimensions is quite close to Jery’s value of $\beta_2 = 23^\circ$.

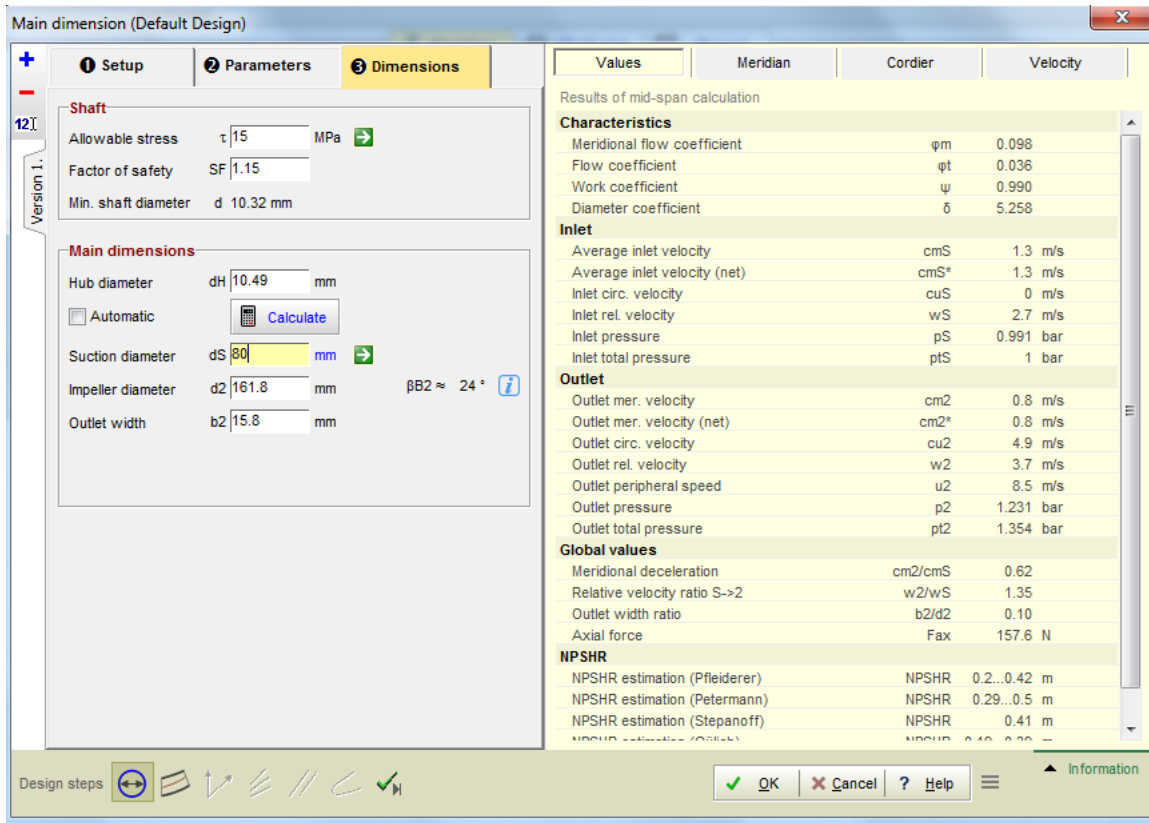


Figure 167. Provide the main dimensions

Going back to the meridional plane, it is noticed that the meridional sketch is still incomplete. The meridional profiles of the hub and shroud need to be set before moving forward. Select the “Meridional Contour” icon from the top left toolbar.

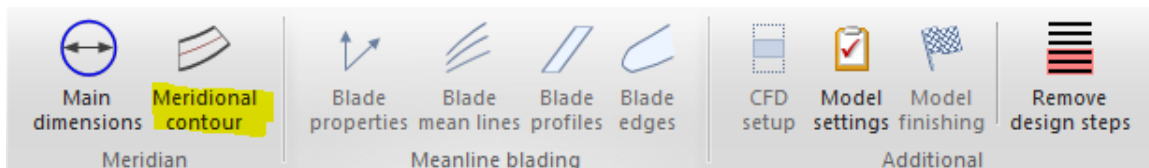


Figure 168. Select meridional contour

In the meridional contour window, if desired, one can alter the suggested hub and shroud contours for a modified design. Accept the default profiles shown in Figure 169.

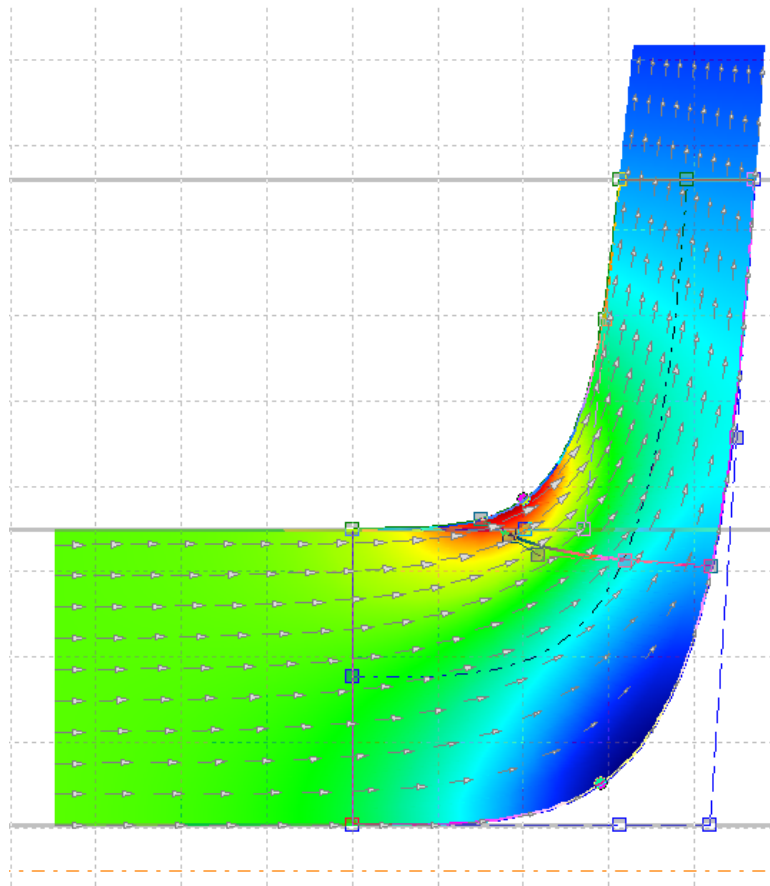


Figure 169. Accept or modify the hub and shroud profiles

The second tab “Hub/Shroud” Solids is selected to provide the shroud thickness. These curves are helpful because they have a direct influence on the dynamic coefficients. Check both Hub and Shroud options in Figure 172.

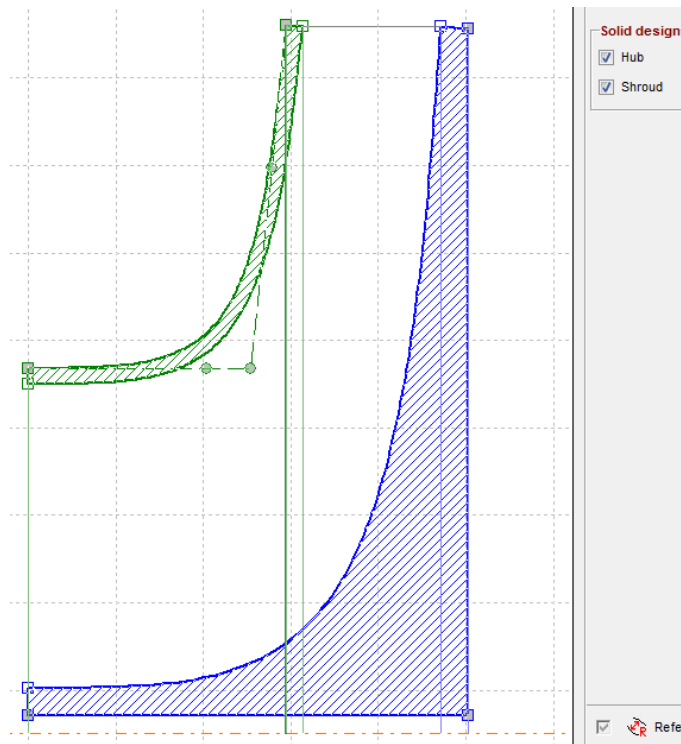


Figure 170. Add the hub and shroud thicknesses

Afterwards, in the down right corner click the arrows button named “Blade Properties” to be automatically transferred to the blade to blade plane design phase (Figure 171).

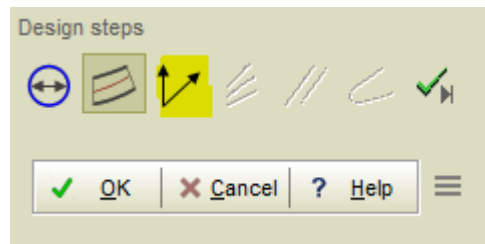


Figure 171. Select blade properties

In the blade properties tab, the critical values for blade angles, incidence angle, slip factor, and number of blades are defined. Alter the number of blades to 5 and leave the other options set as default in Figure 172.

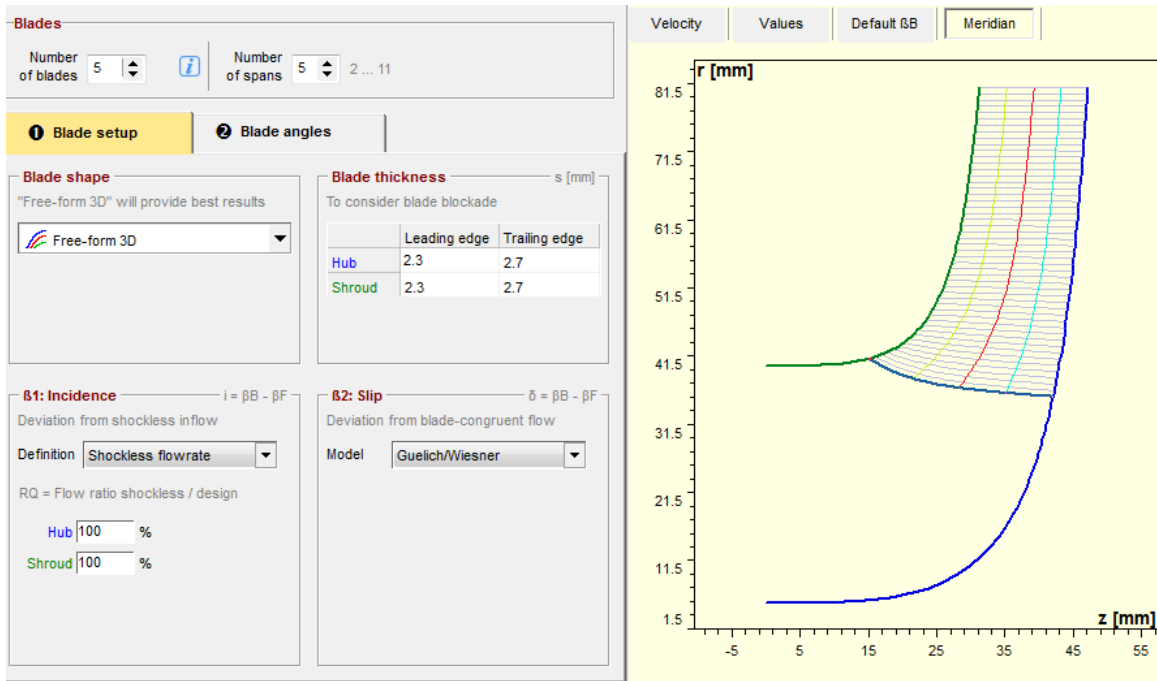


Figure 172. Set number of blades

The “Blades Angle” tab is shown in Figure 173 . Impeller X trailing edge angles is enforced by unchecking the automatic option and entering the 23° value.

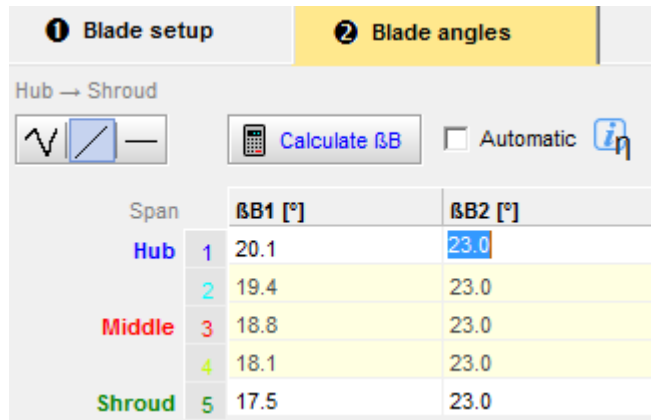


Figure 173. Set the blade angles

Select the “Blade Meanlines” icon from the navigation bar to move to the next step (Figure 174).



Figure 174. Select blade meanlines icon

In the blade meanlines window, the 2D meridional profile and 2D blade to blade profile are mapped into a 3D profile. The “Conformal Mapping” option is the modern approach compared to the beta progression method. Accept the default meanlines shown in Figure 175.

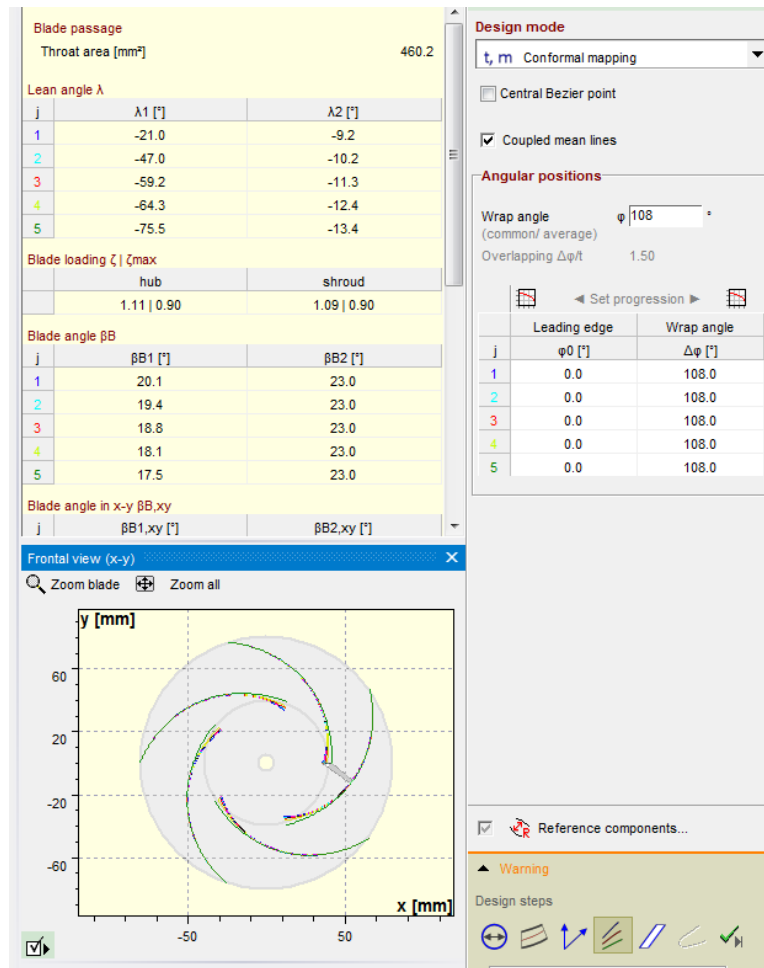


Figure 175. Design the meanlines

Move to the “Blade Profile” step in navigation bar (Figure 176).



Figure 176. Select blade profiles

In the blade profile window, the blade thickness distribution is input. Accept the default linear symmetric distribution similar to Figure 177. If one is interested, arbitrary predefined profiles like NACA profiles can be imported as polylines.

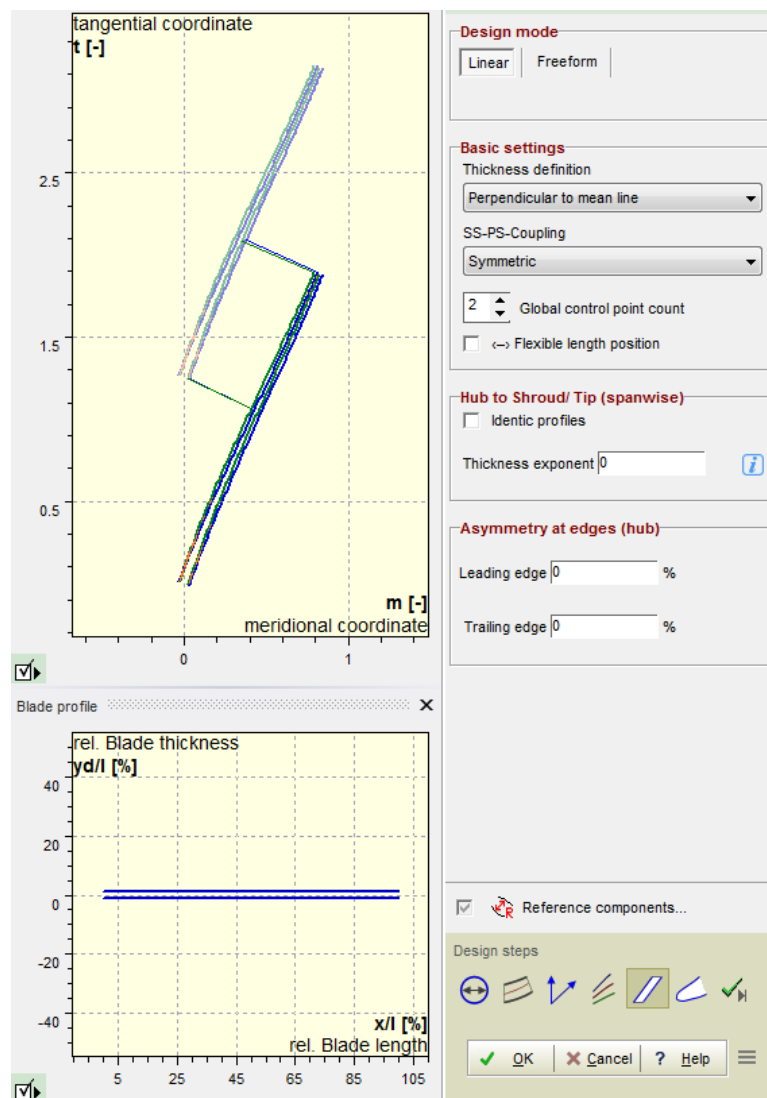


Figure 177. Input the desired blade thickness distribution

Once blade thickness is set, select “Blade Edges” icon (Figure 178).

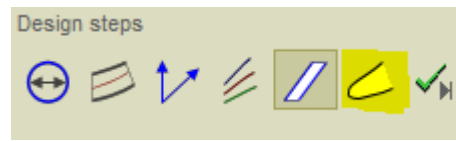


Figure 178. Select blade edges

In the blade edges window, various fillet operations for the leading and trailing edges of the blades are available. For the leading edge select an ellipse fillet and for the trailing edge select a simple trim option (See Figure 179). These are two of the most common fillets applied in industry.

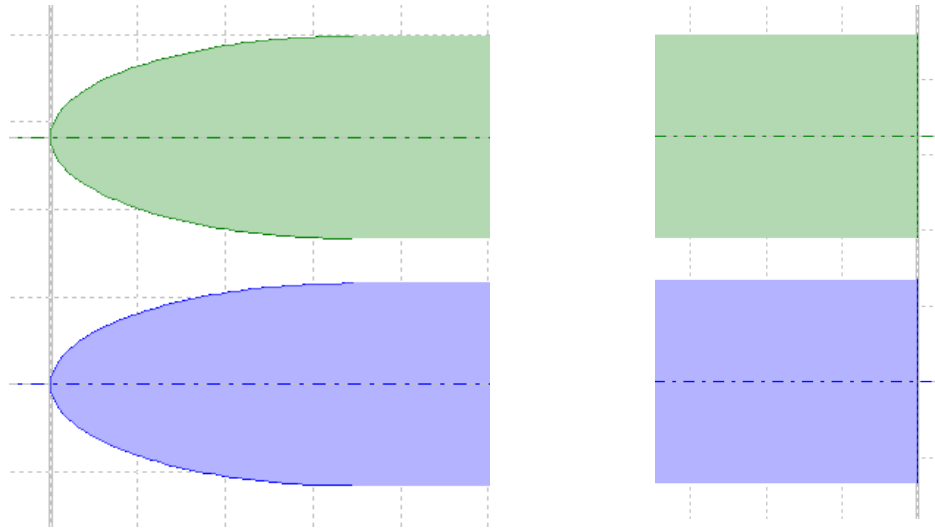


Figure 179. Fillet and trim the leading and trailing edges of the blades

The primary design for the impeller is done. One can do a quick check of the created impeller in 2D meridional view similar to Figure 180.

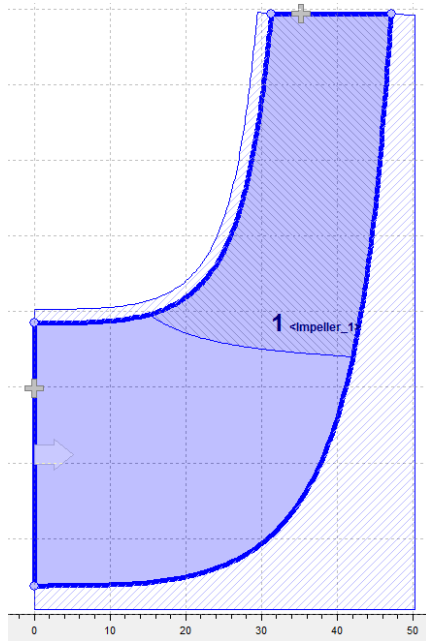


Figure 180. Select 3D model for inspection

And in 3D mode the impeller can be visualized for inspection (See Figure 181):

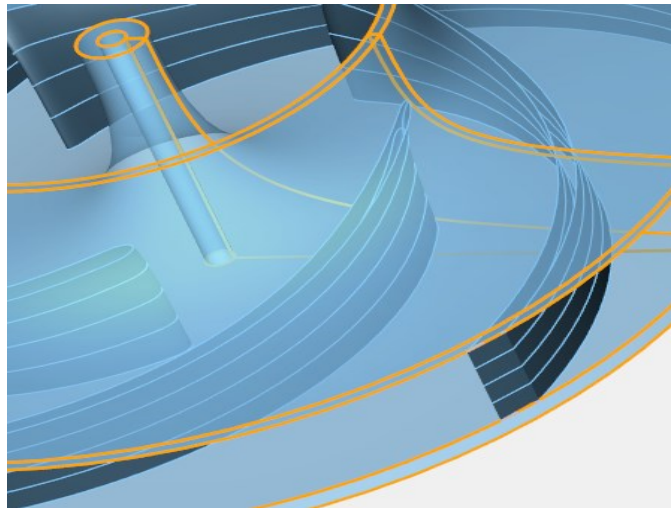


Figure 181. The 3D view of the created impeller

Before adding the diffuser, a small extension after the impeller is added help the meshing procedure. Select the “CFD setup” icon form the top toolbar. Then in the pop

up window select the “Extension” tab and from the “Direction” drop down list select the “Radial” option (See Figure 182). Check the “Extension at r=constant” box and accept the default extension value and click OK.

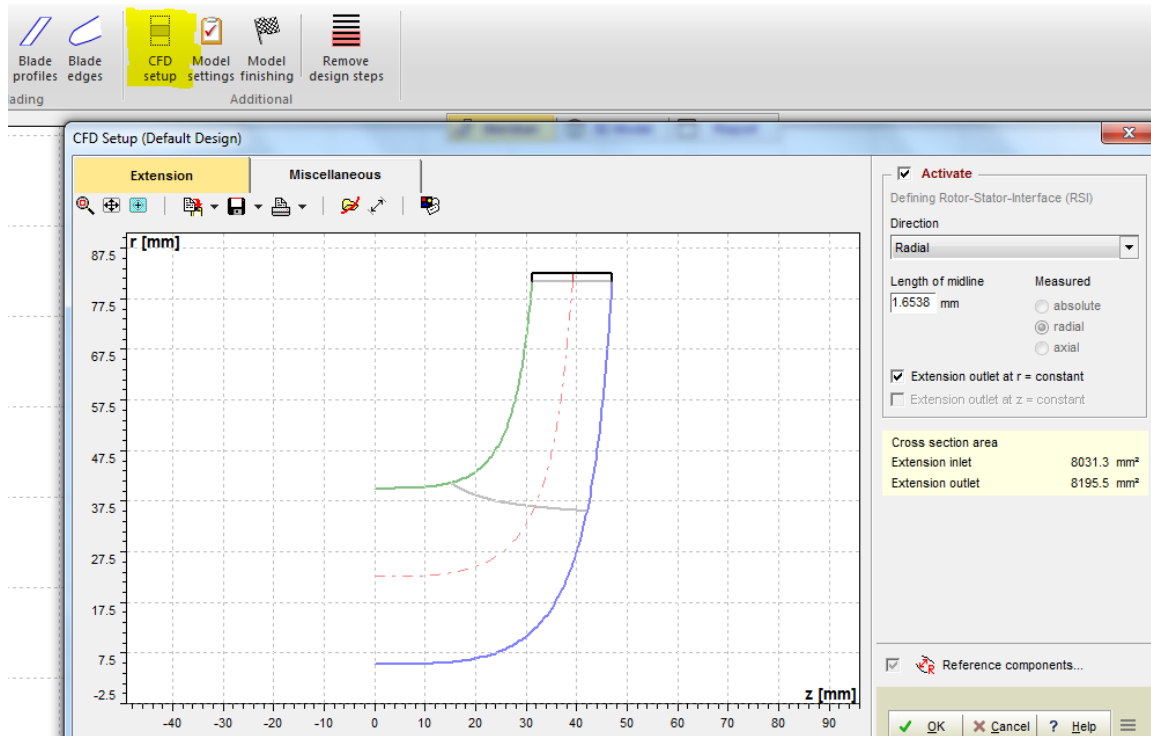


Figure 182. Add extension to the impeller

Next, add a diffuser to the impeller. Go back to the Meridian view and click the plus “+” button at the outlet of the impeller in Figure 183. In this way, several components can be coupled to each other in series. Select a “New Stator”.

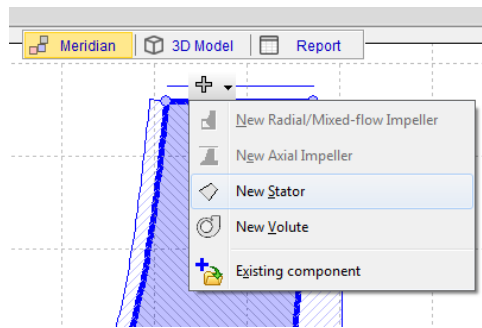


Figure 183. Add another component after impeller

In the popped up “Main Dimensions” window, select a radial diffuser and check the “Blades” box to add vanes to the diffuser according to Figure 184.

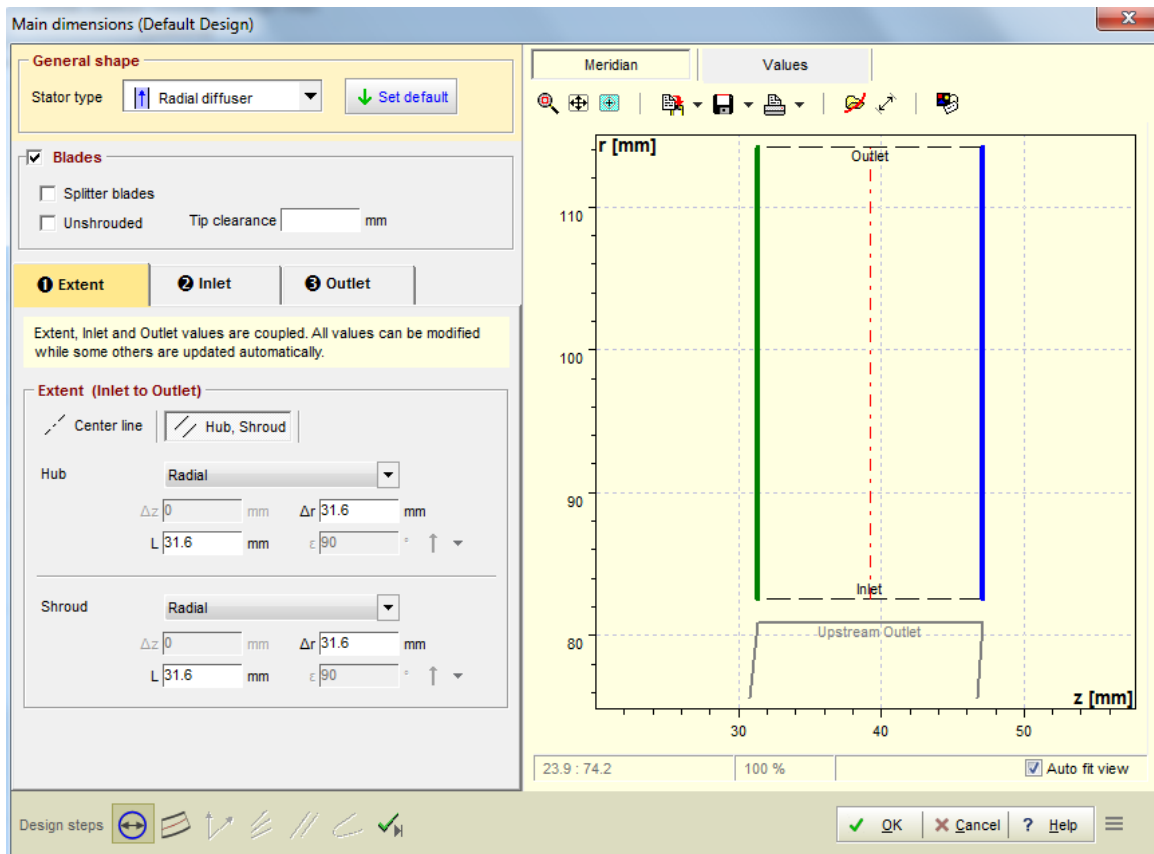


Figure 184. Set the diffuser dimensions

Select a radial hub and shroud profile. Different Gap A and overlap length settings can be inputted in this section. Also, to reduce the pressure pulsations one can increase the radial offset of the inlet as was adopted in the report.

When finished, select the “Meridional Contour” icon similar to what was done in the impeller step. There is no modification to the meridional profiles needed since the radial constraint has been selected.

Then select the “Blade Properties” to move to the next step. Here change the number of blades to 13 according to Figure 185. For the “Blade Shape” select the Log Spiral + Straight 2D option from the drop down list. Keep the number of spans.

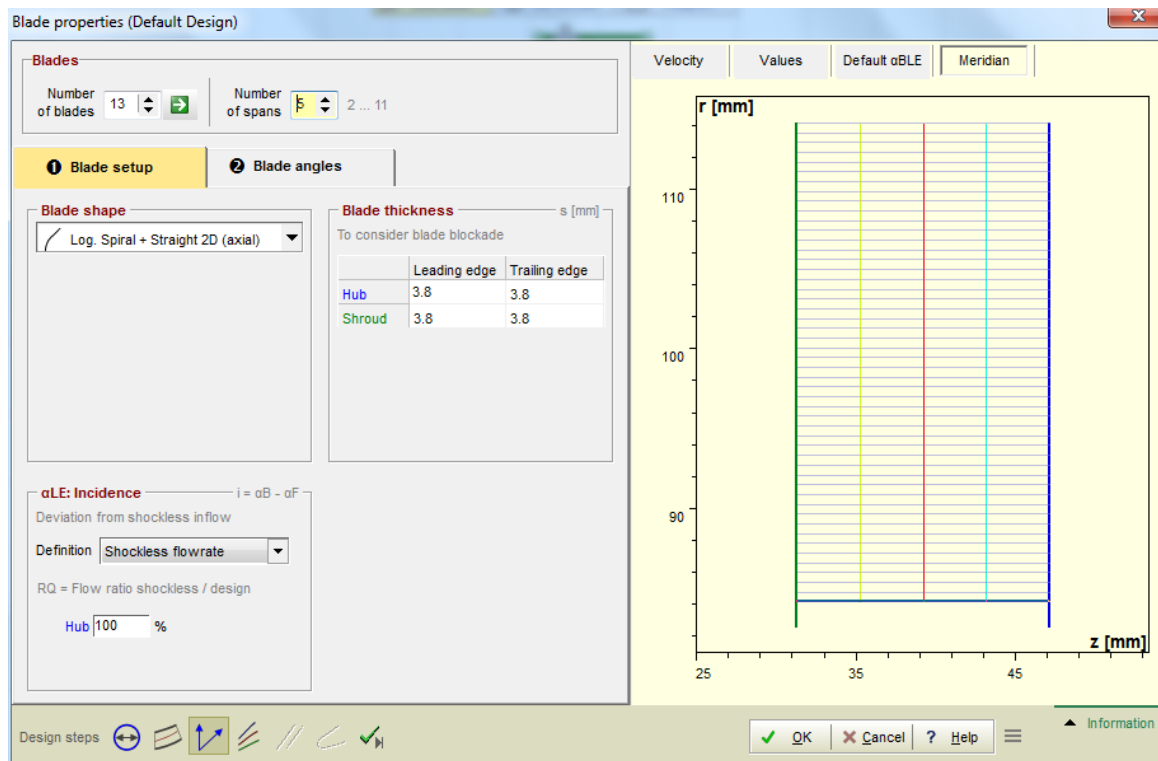


Figure 185. Set the diffuser vane properties

Move to the “Blade Meanline” step and accept default settings in Figure 186. If the pressure ratio is not satisfactory, one can go back to the main dimension step and change expansion rate of the diffuser to achieve higher pressure conversion values.

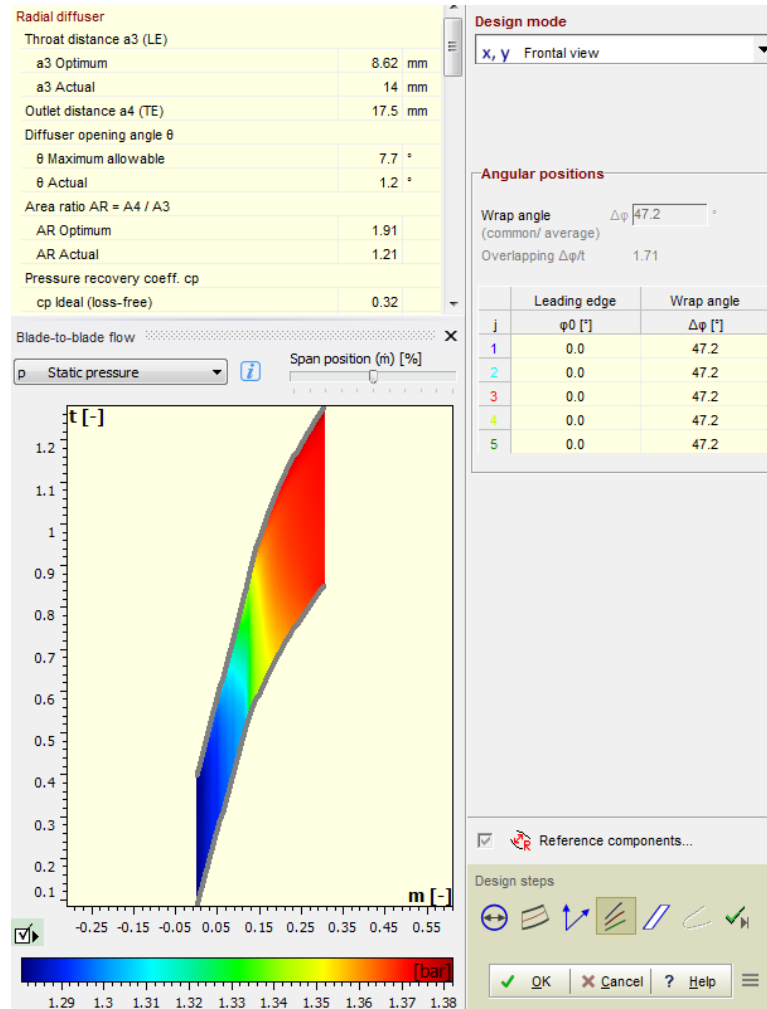


Figure 186. Define the meanline properties

Next, go the “Blade Profiles” step and select the desired thickness distribution. Accept the linear distribution. Finally, select the same ellipse and trim options as the impeller blades for the diffuser vanes in the “Blade Edges” step. Going back to the 3D model, the impeller and the diffuser can be visualized as in Figure 187.

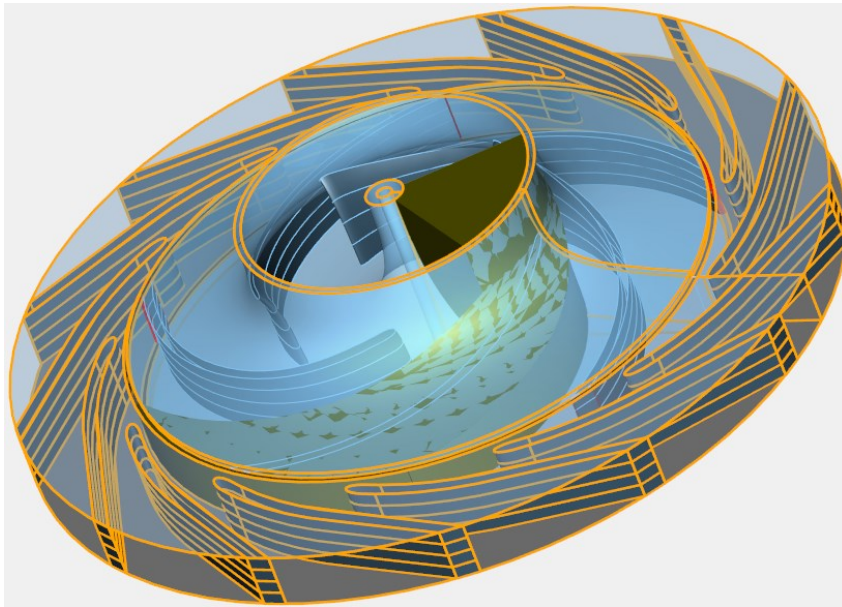


Figure 187. Impeller and diffuser 3D view

At this point one can add the volute. Go back to the Meridian view and push the “+” button at the outlet of the diffuser and select “New Volute” according to Figure 188.

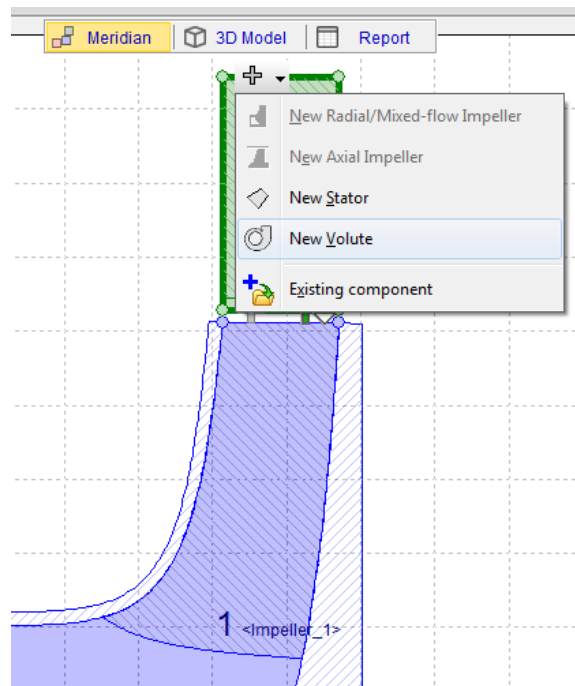


Figure 188. Add a volute

In the popped up “Inlet and Design” window select the single volute option and accept the default inlet dimensions that are coupled with the diffuser outlet and are automatically updated (See Figure 189).

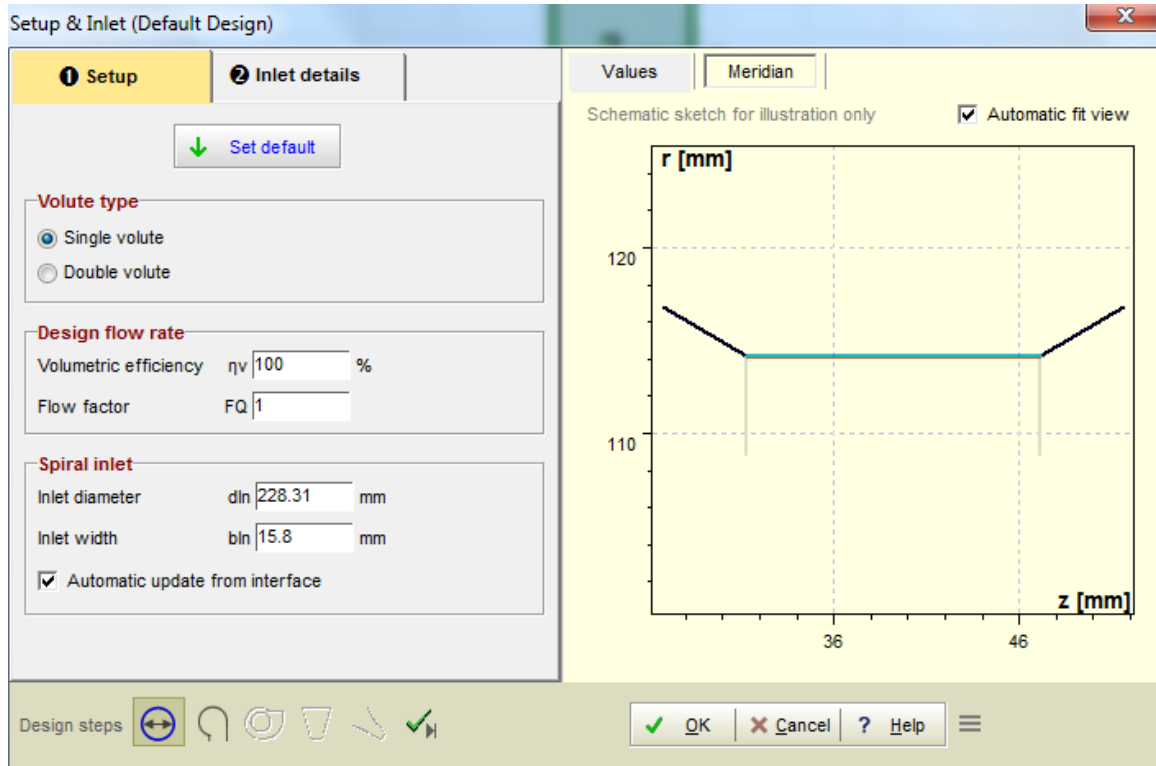


Figure 189. Set inlet dimensions of the volute

Select the “Cross Section” icon for the next step in Figure 190.



Figure 190. Select the cross section step

Select the cross section shape of the volute. Here a trapezoidal volute is desired. On the top right corner from the drop down list of the “Left (Shroud)” select the “Trapezoid” and leave the “Right (Hub)” option as “Symmetric”. Accept the default value of 25° for the cone angle according to Figure 191.

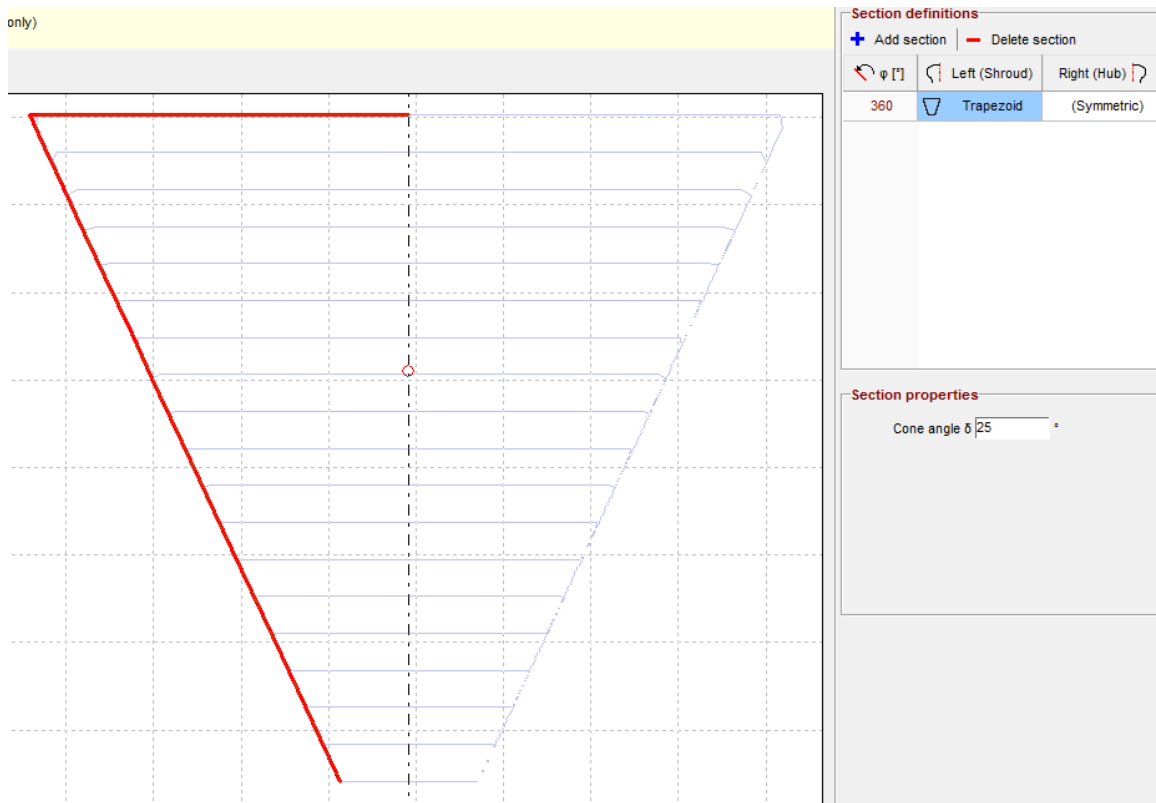


Figure 191. Select the volute cross section shape

Move to the “Spiral Areas” step (Figure 192).



Figure 192. Select spiral areas

In the Spiral Areas window, the progression of the volute area will be defined. Select the “Velocity Based” tab, and in the theory drop down list select “Stepanoff” accept the interpolated constant and check the “Cutwater Compensation” box according to Figure 193. One can alternatively import the area progression curve for inverse design.

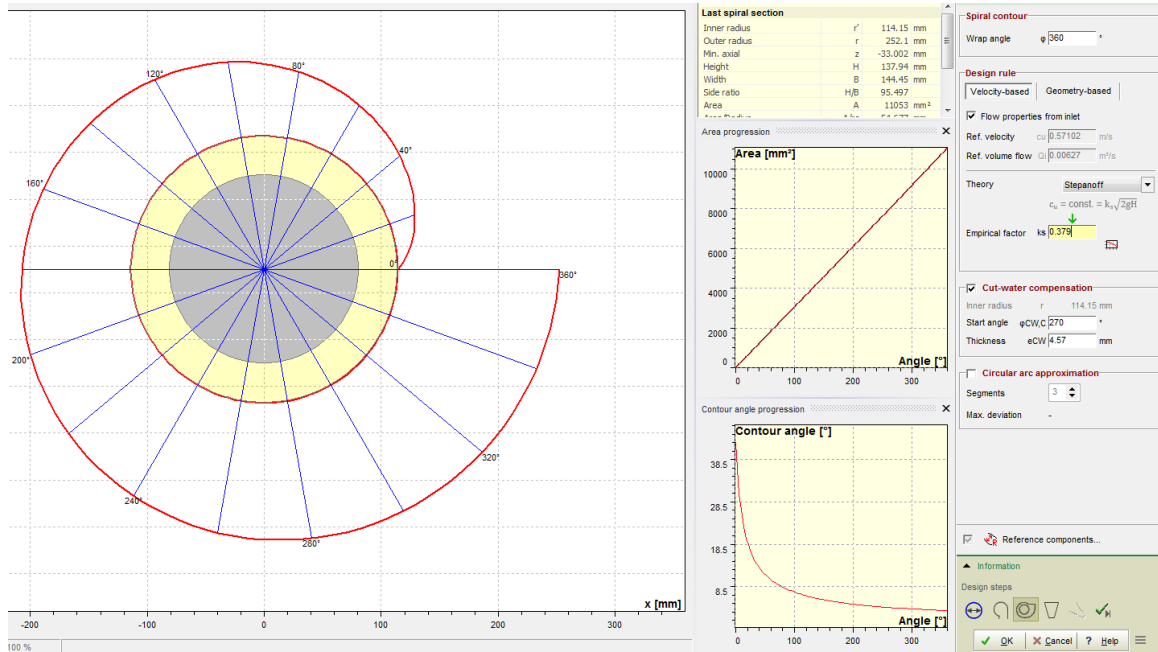


Figure 193. Set the area progression settings

Select the “Diffuser” icon to add a cone to the spiral casing.

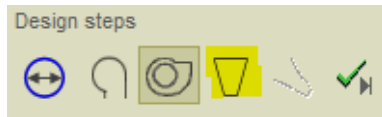


Figure 194. Select diffuser

Select a “Tangential” diffuser in “Concentric” mode. Change the “End Cross Section” to “Circle”. Increase the Height to 200 mm to avoid cutwater self-intersection and leave other settings as default in Figure 195.

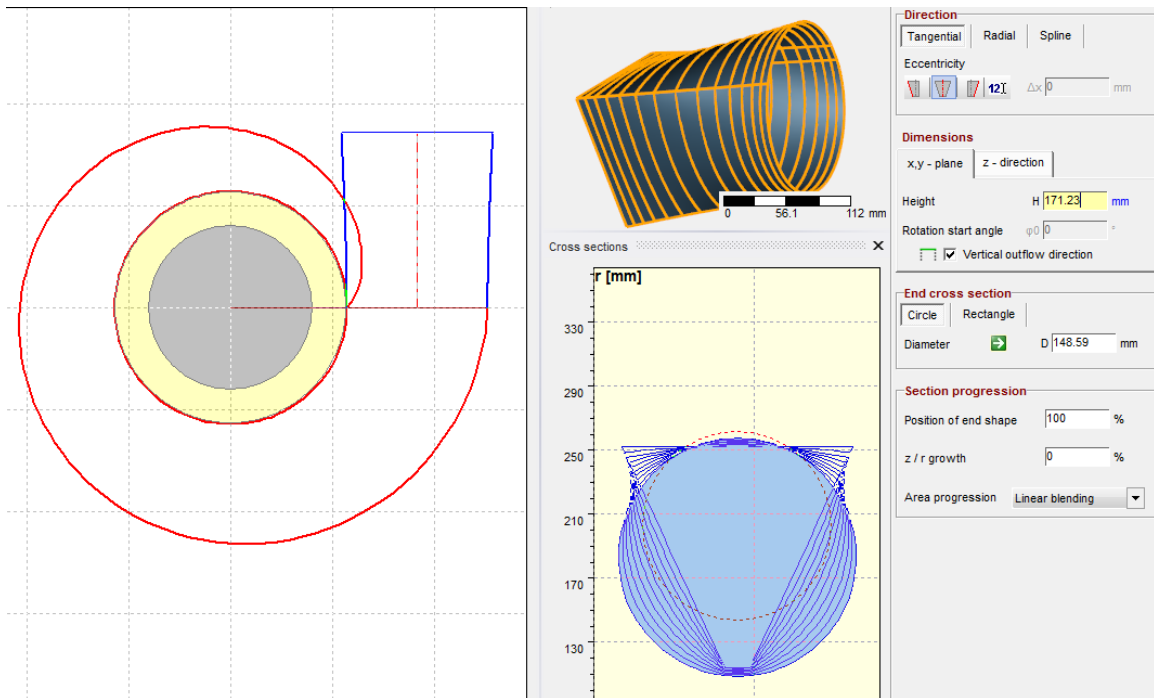


Figure 195. Add a diffuser to the volute

Select “Cutwater” step in Figure 196.



Figure 196. Select cutwater

In this window the fillet radius and circumferential position of the cutwater can be selected. The tongue angle and fillet radius cannot be too small otherwise problems occur in the meshing and CFD simulation steps. Accept the default values which consider these minimum constraints (See Figure 197).

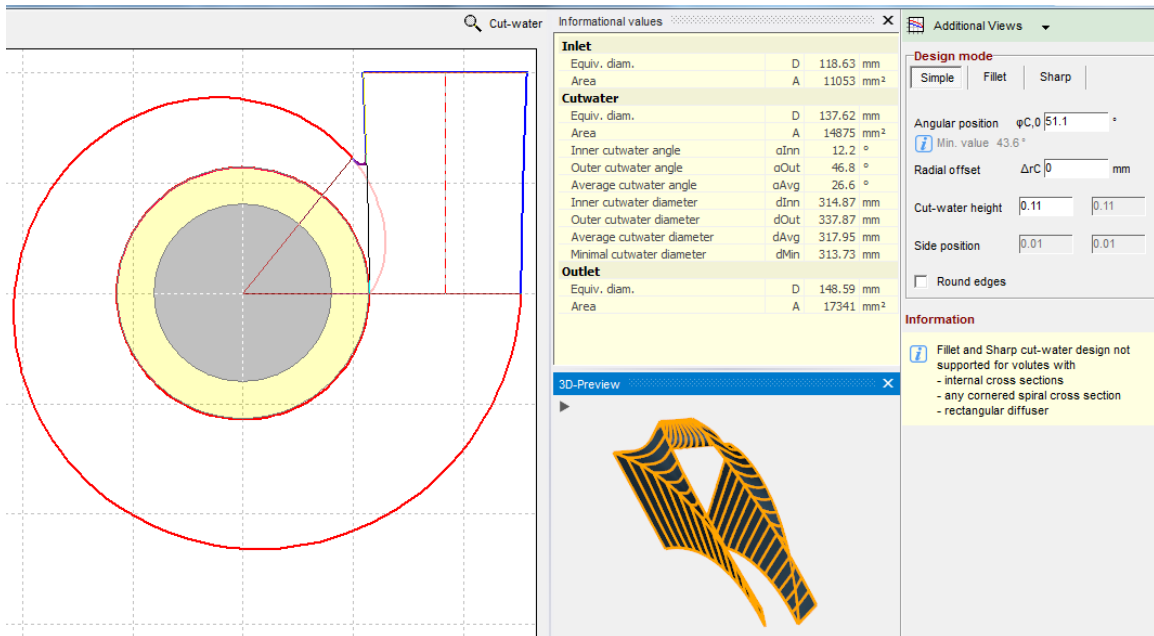


Figure 197. Set the cutwater angular position

Go to the 3D view and check the full model (See Figure 198).

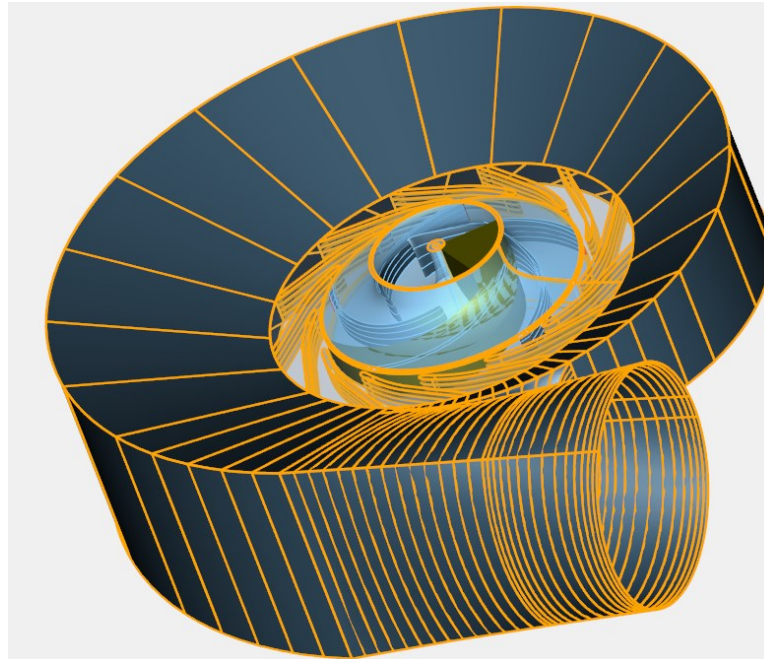


Figure 198. The 3D view of the impeller, diffuser and the volute

Before finishing, select the volute in Meridian view and click CFD setup in Figure 199.

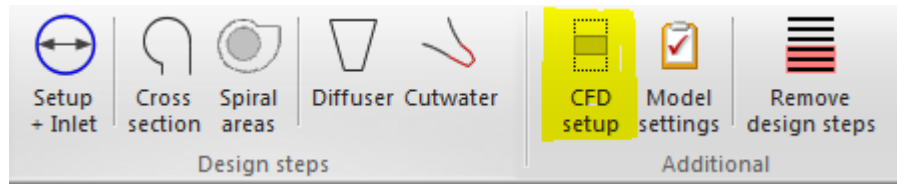


Figure 199. Go to the volute CFD setup

Add an extension pipe for better convergence in CFD solution according to Figure 200.

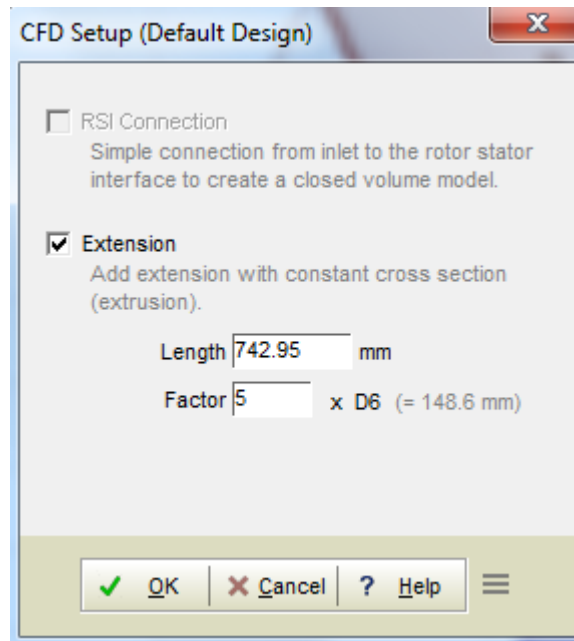


Figure 200. Add pipe extension

Return to the meridional view. Select the impeller and add a “New Stator” at inlet of the impeller according to Figure 201.

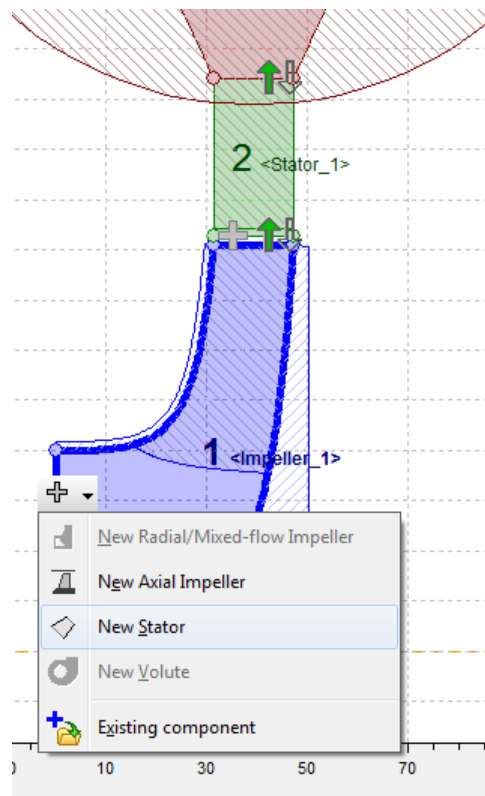


Figure 201. Add a new stator before the impeller

This stator is in fact the suction pipe before the impeller. Select the “Axial Diffuser” as the stator type similar to Figure 202. Check if the Hub and Shroud extents are set as “Axial”. The length can be changed for longer suction pipes. Suction pipe helps the convergence of CFD model when the zero gradient conditions are imposed at inlet BC.

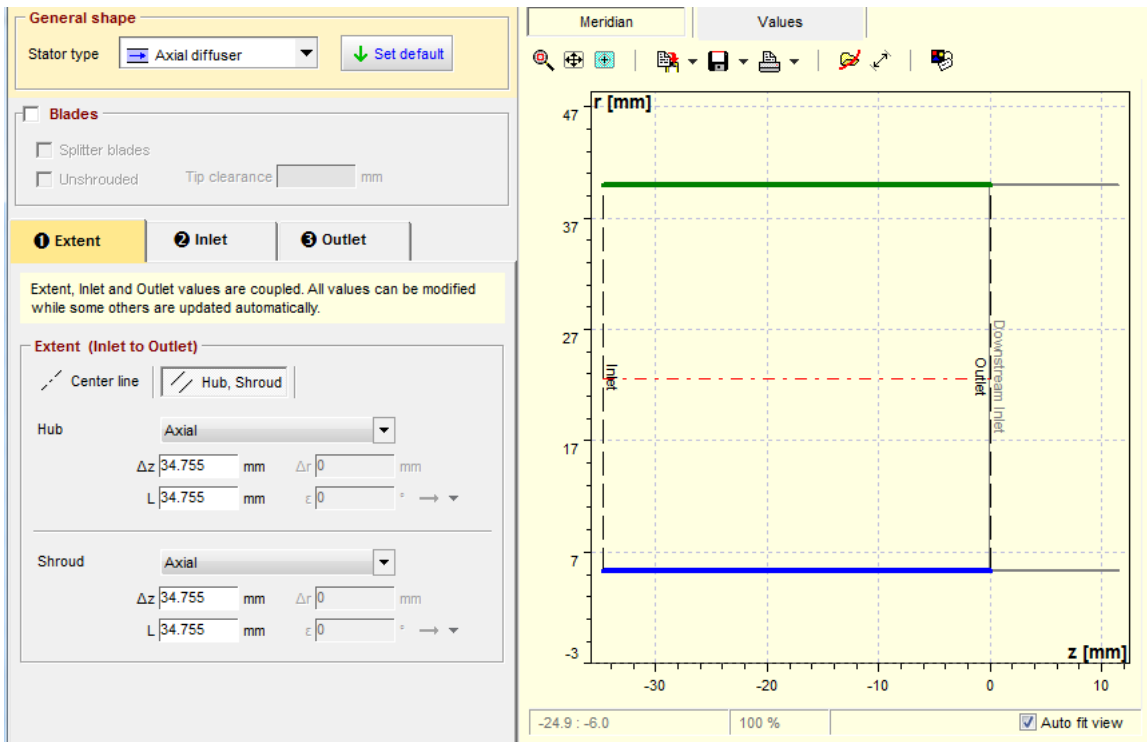


Figure 202. Define the suction pipe extent

The suction pipe is added to the model according to Figure 203.

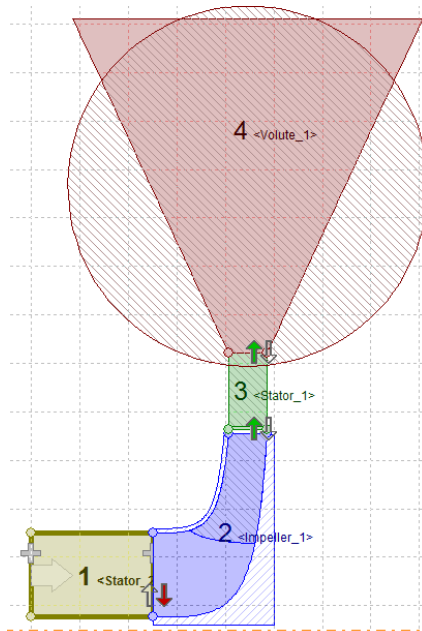


Figure 203. Model with suction pipe

Next, select the “Export” button in Meridian tab to get CAD file in Figure 204.

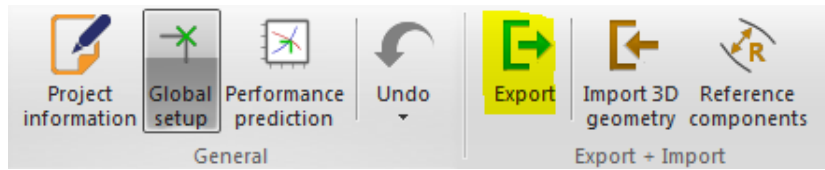


Figure 204. Go to export module

In the Export wizard, select the appropriate format of your choice (See Figure 205). Define the export path and click the “Set parameters” and choose “Default + CFD Setup” and export.

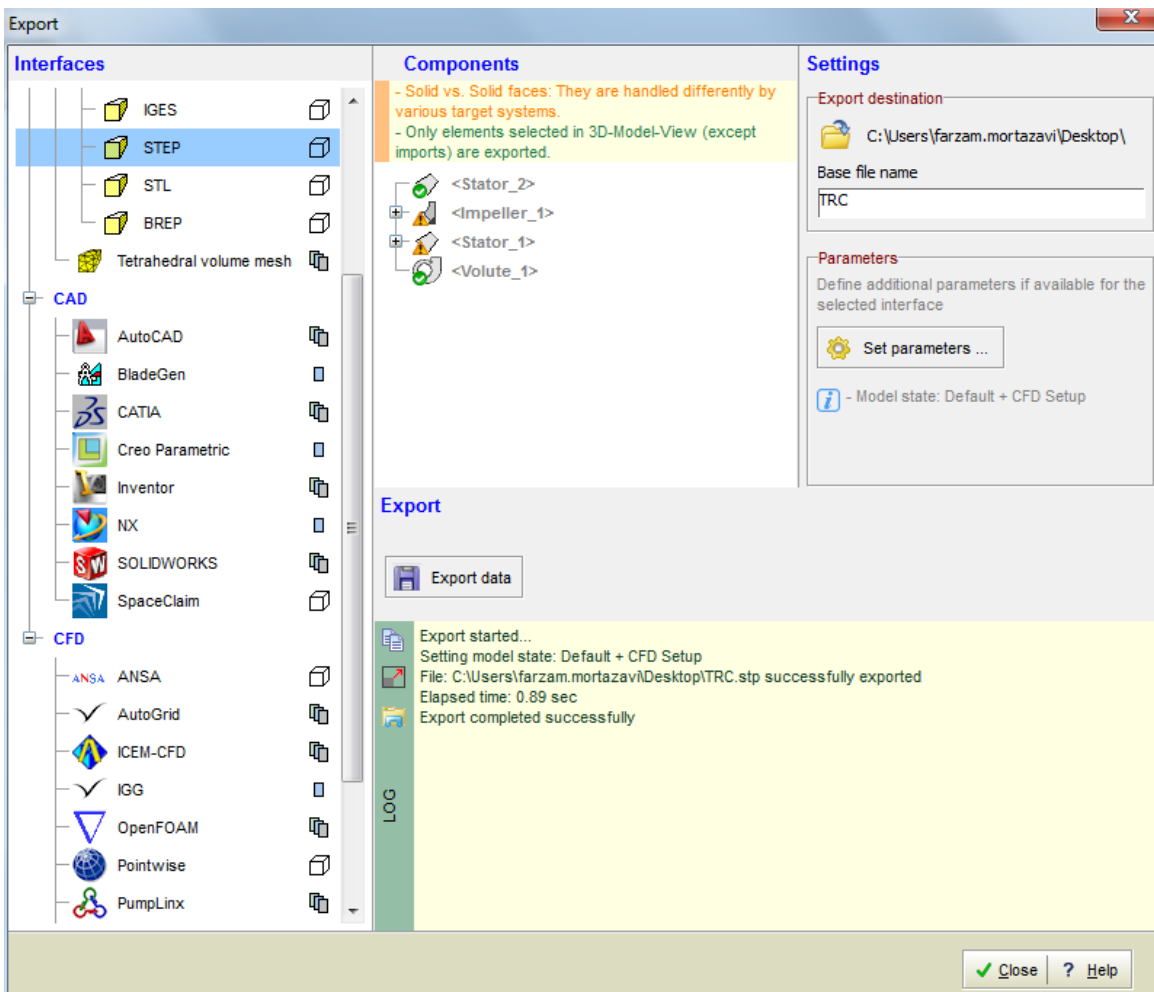


Figure 205. Export the CAD model

APPENDIX C CFX SAMPLE SET-UP FILE FOR A WHIRLING OPEN IMPELLER

In this section, it is demonstrated how to set-up a whirling open impeller pump using ANSYS CFX.

- Open ANSYS CFX.

- Import the mesh. If a periodic mesh is available, apply the turbo rotation to model all the passages. The whirling case requires the 2π model. This specific impeller has 6 blades.

-*Mesh>select impeller mesh>right click>select Transform Mesh>Transformation: Turbo Rotation* (See Figure 206)

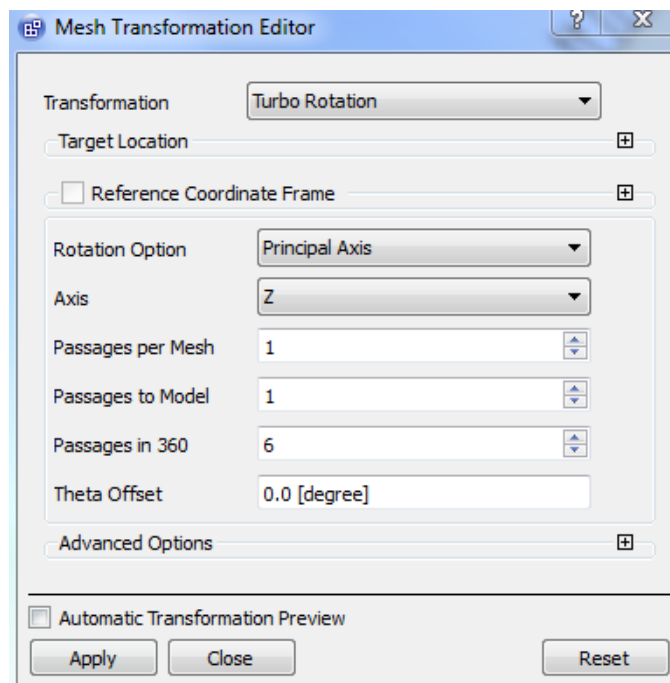


Figure 206. Apply turbo rotation for a full 360 degree model

Then the full domain will be loaded according to Figure 207.

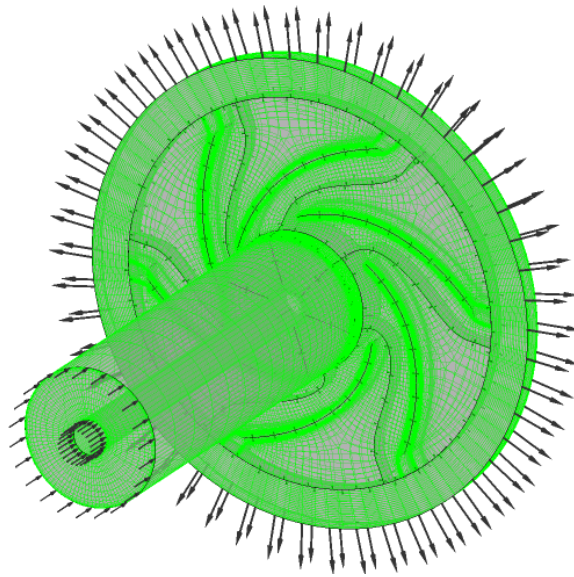


Figure 207. Import the computational domains

-Under *Analysis type*, enter the following settings. For the time step and total time of the simulation use the given expressions in Figure 208.

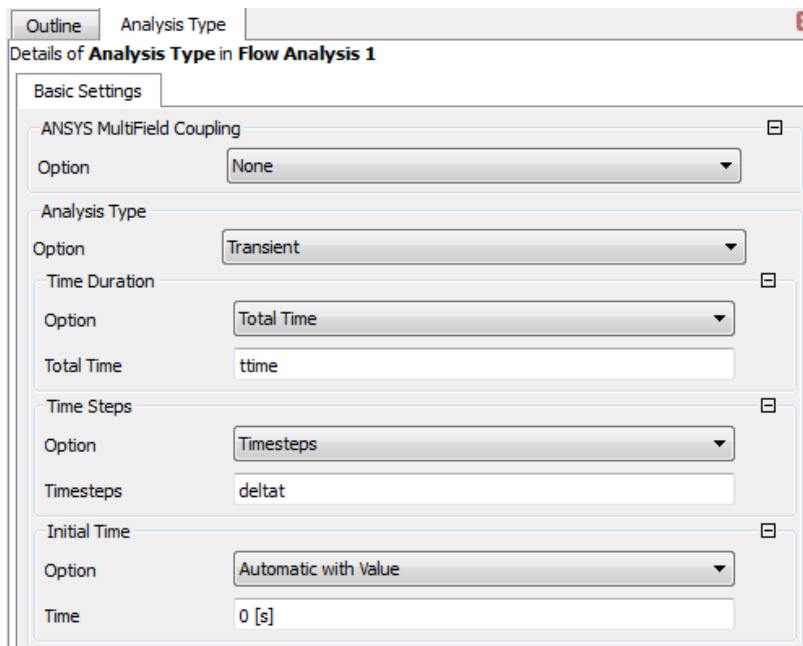


Figure 208. Transient analysis settings

-Create domains: *Open Simulation*>*Right click Flow analysis 1*>*Insert*>*Domain*.

-Name the domain impeller. Use Figure 209 settings under the tap *Basic Settings*:

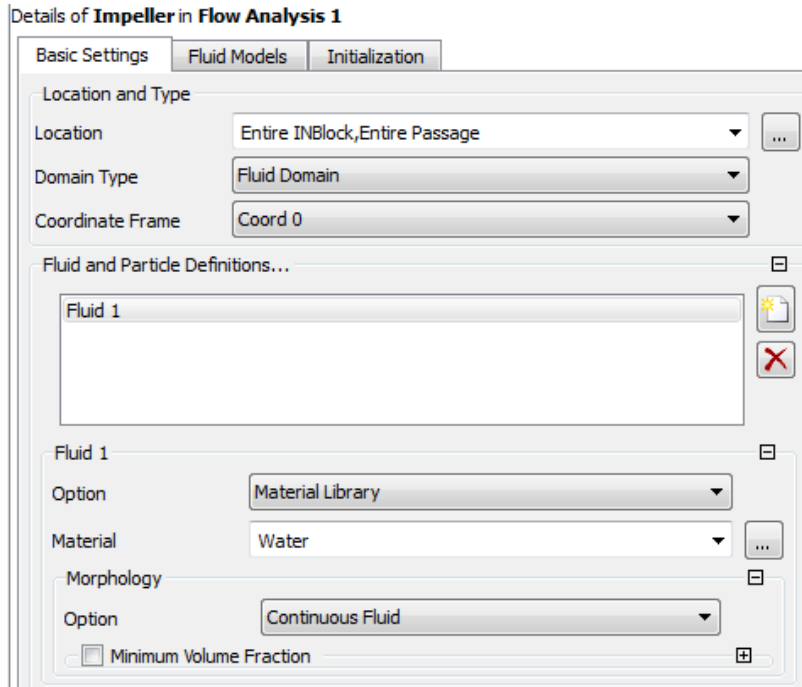


Figure 209. Select the mesh locations and the fluid type

-Here a *Rotating* domain with *Mesh Deformation* is selected. Do not activate the *Alternate Rotation Model* in the case of a centrifugal impeller. Select the *Regions of Motion Specified* as the option of *Mesh Deformation* to impose general mesh motion constraints. The *Mesh Motion Model* should be set to *Displacement Diffusion*. The *Mesh Stiffness* should not be too large, otherwise negative volume appears and solver fails. Please make sure that the displacement is relative to the *Previous Mesh* according to Figure 210.

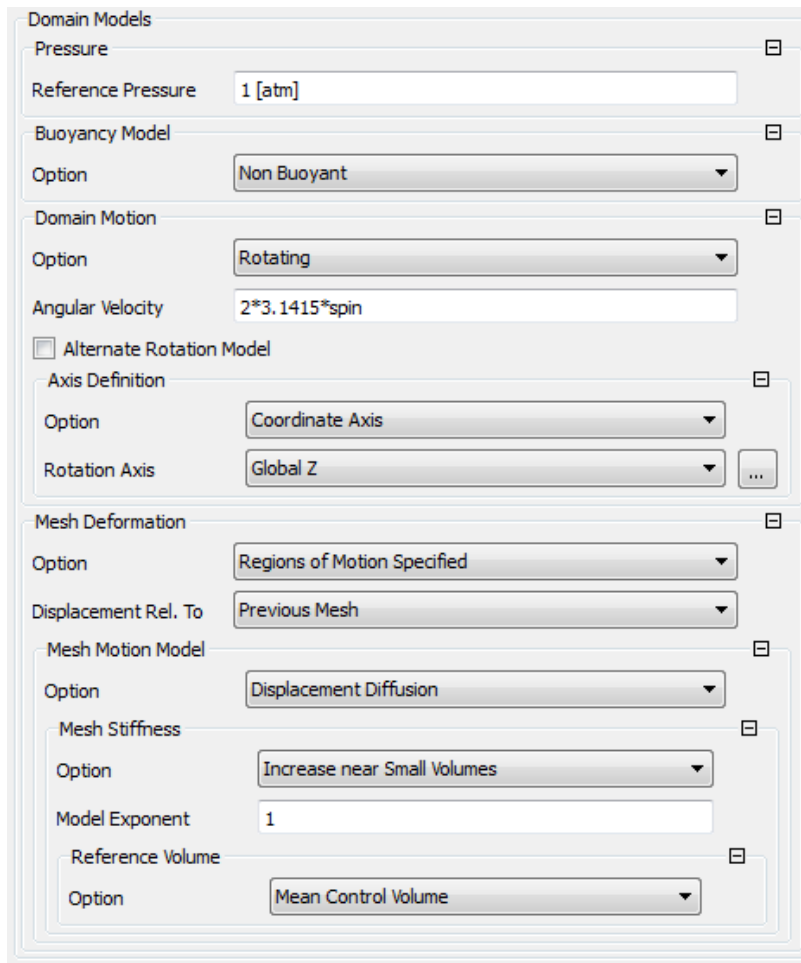


Figure 210. Mesh deformation settings

-Under the *Fluid Models* tab, enter the following settings shown in Figure 211. Use a *Shear Stress Transport* turbulence model and activate the *Transitional Turbulence* model. Select the *Gamma Theta Model*. Under *Advance Turbulence Control*, activate *Curvature Correction* with default coefficient of 1.

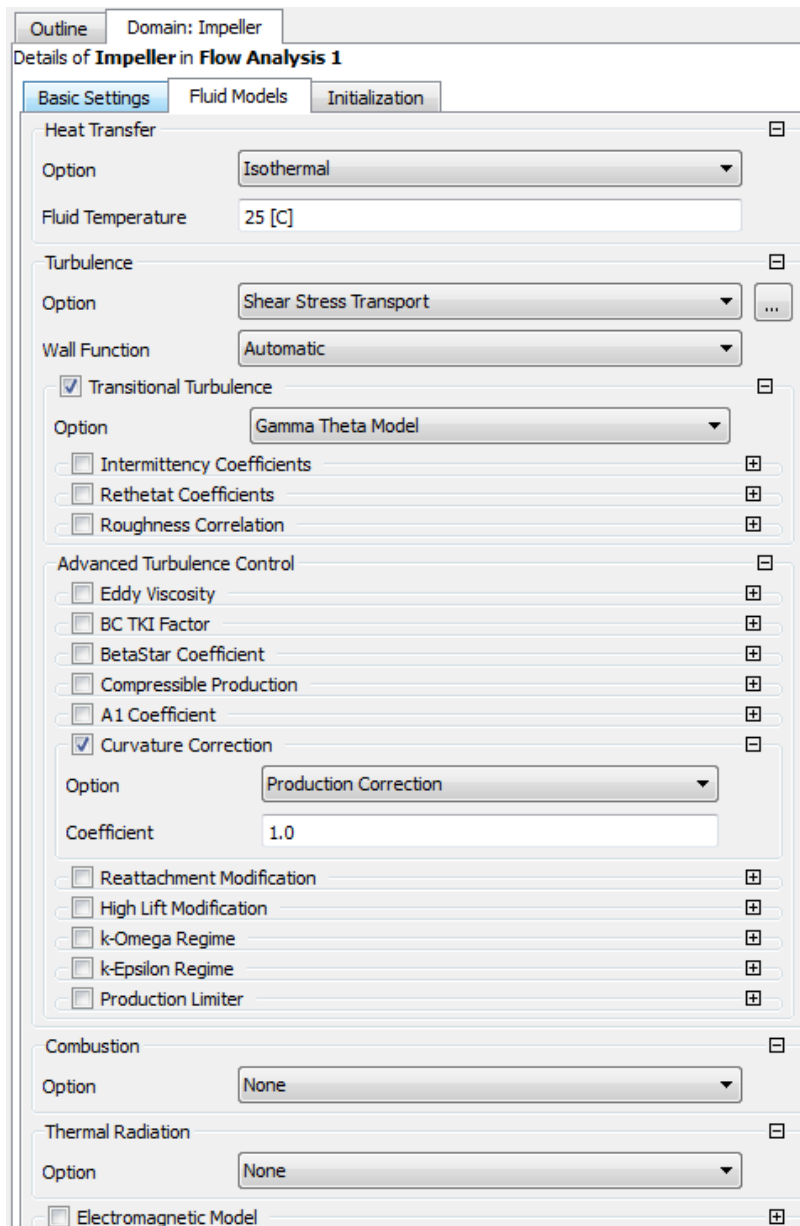


Figure 211. Turbulence settings

-Insert new domains and make a suction (pipe) domain and a diffuser domain. These are stationary domains and do not need mesh deformation settings.

- Create boundary conditions: *Right click Impeller>Insert>Boundary*

- Name the boundary “blade” and select the blade mesh under *Location*. The frame is *rotating* by default. Make sure that the blade tip surface is selected (See Figure 212).
- Use the following settings under the *Boundary Details* tab. Select a *Specified Displacement* and enter the expressions “eccx” and “eccy” for x and y components. The wall velocity should be relative to the *Mesh Motion*. If certain roughness is desired, it can be activated through *Rough Wall* option. Here the expression “eps” will be set to zero.

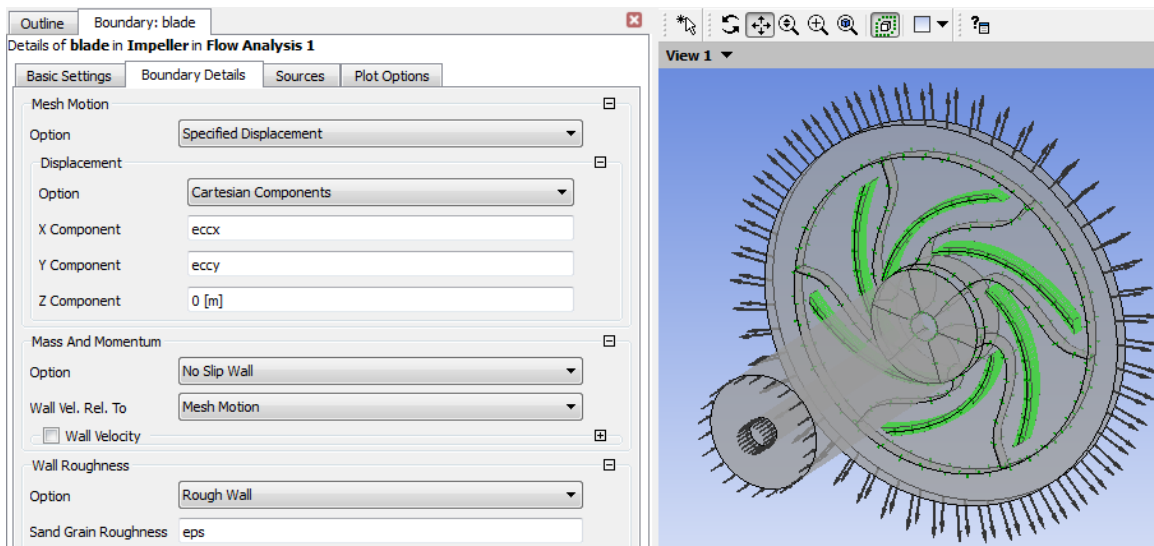


Figure 212. Blade boundary conditions

- Create a new boundary and name it “hub”. Use the exact settings as the blade.
- Create a new boundary and name it “shroud”. Use the following *Boundary Details*. The wall velocity should be relative to *Boundary Frame* and the *Mesh Motion* should be *Stationary*. Since the domain is rotating, the *Counter Rotating Wall* must be activated according to Figure 213.

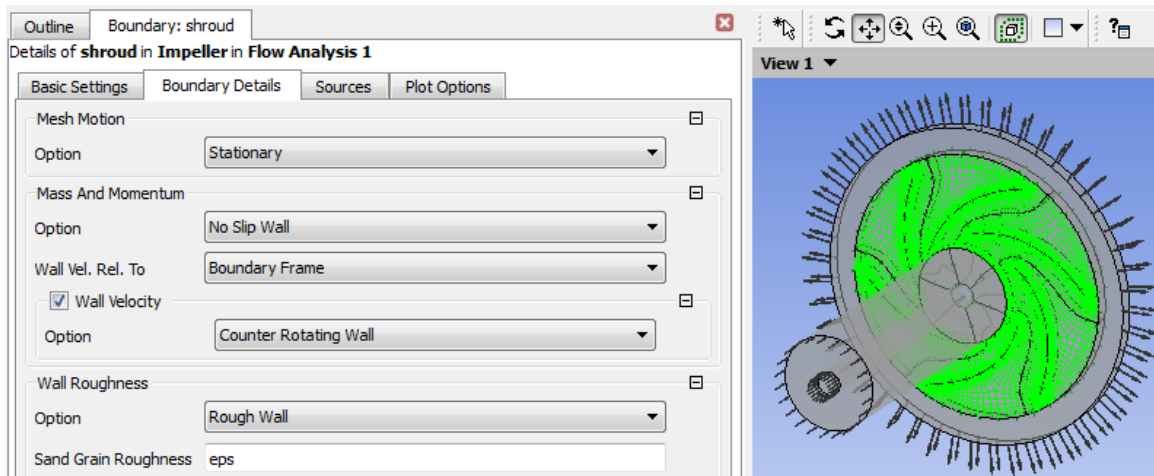


Figure 213. Shroud boundary conditions

- Create interfaces: *Right click Flow Analysis 1>Insert>Domain Interface*

-The first interface connects the pipe to the impeller. Use a *Transient Rotor Stator (TRS)* interface with a *GGI connection* according to Figure 214. Under *Mesh Connection*, check *Intersection Control* and activate the *Face Search Tolerance Factor* and *Face Intersection Depth Factor* according to Figure 215.

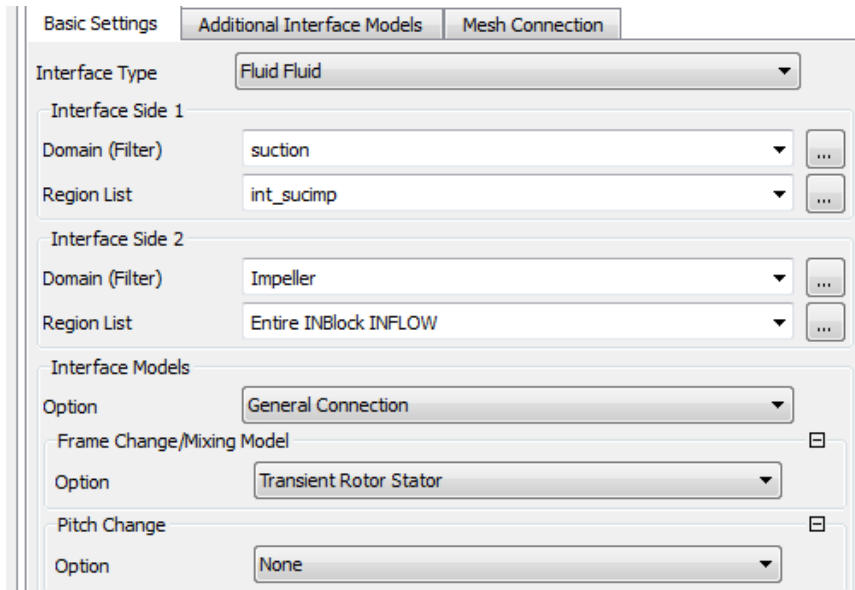


Figure 214. Interface location and frame settings

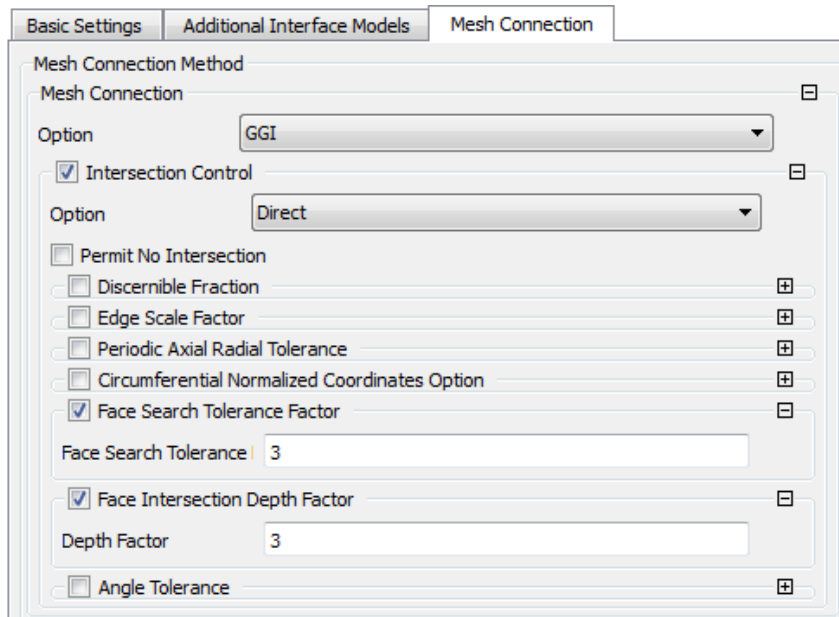


Figure 215. Interface connection settings

-Create another interface between the impeller and the diffuser. Use the same settings.

- If the impeller mesh is periodic similar to Figure 216, make sure that the internal interfaces use a *General Connection* without *Frame Change*.

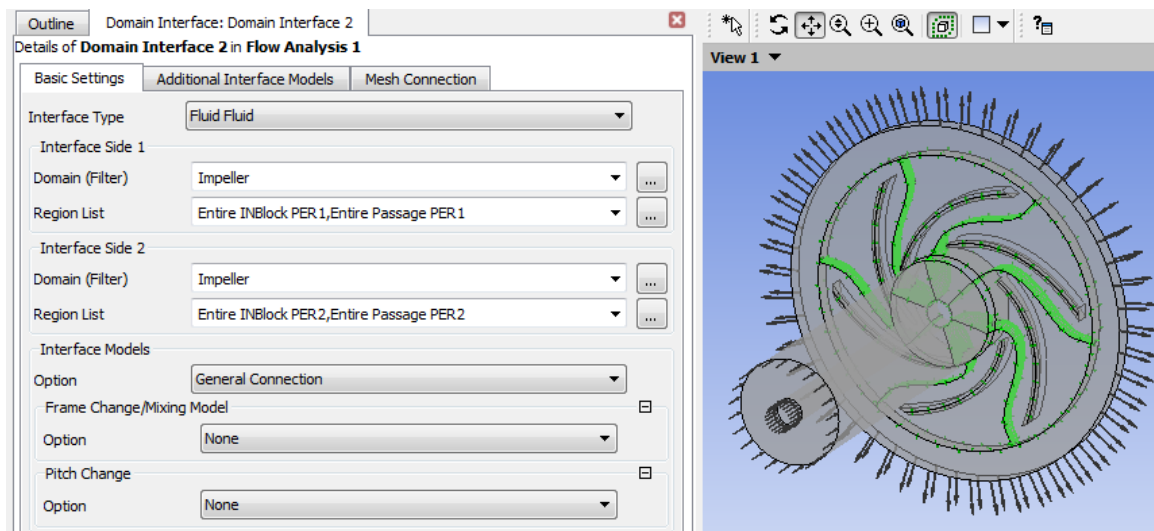


Figure 216. Internal interface settings

-Define the *Unspecified* boundary condition type of *Mesh Motion* for the impeller side of the two transient rotor-stator interfaces (See Figure 217). This ensures that the interface adjusts to the motions of the hub side and the shroud side.

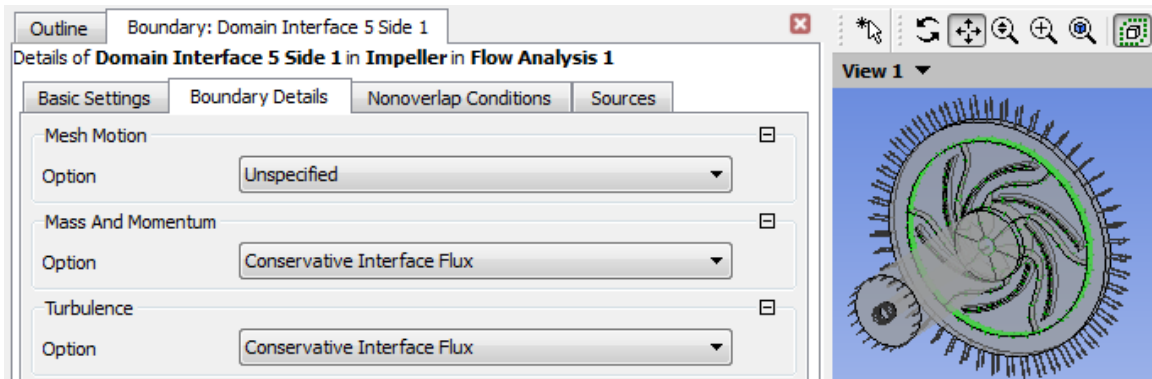


Figure 217. Interface mesh motion boundary condition

-Open: *Simulation>Solver>Solver Control*. And use the settings in Figure 218.

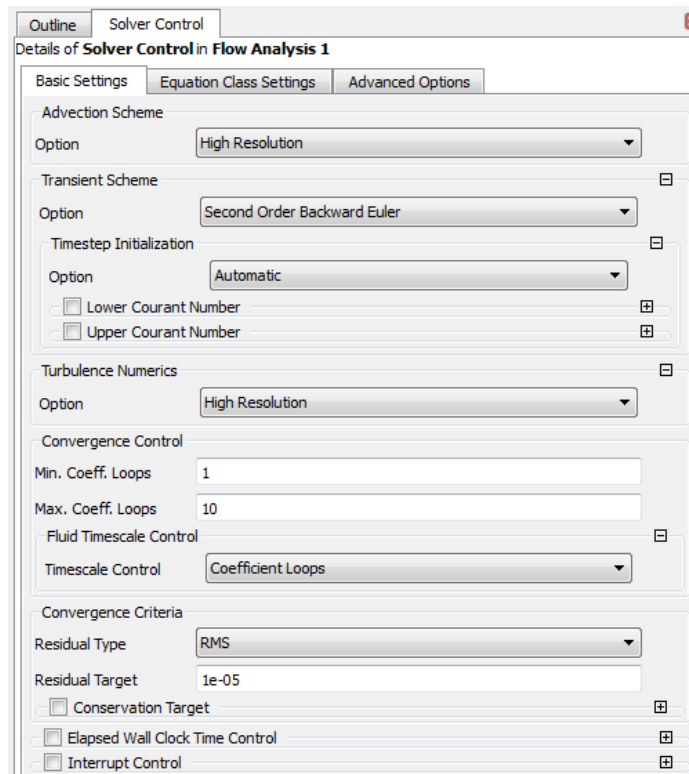


Figure 218. Solver settings

-Create expressions to define the mesh motion equations, input and output variables. Under *Simulation>Expressions, Functions and Variables>Right click Expressions>Insert>Expression*. The individual expression have been defined in the main body of the dissertation. Figure 219 shows a list of expressions used in this problem.

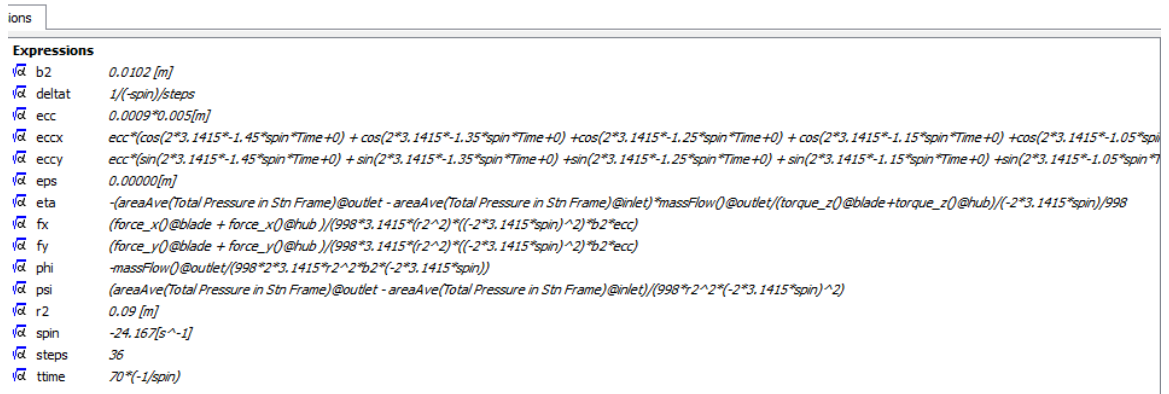


Figure 219. Define expressions

The array of phases introduced for each mode depends on what array of frequencies are being modeled and cannot be generalized. The closed form formula given in the dissertation has been used to generate the binary phases. For this case the array of frequencies and phases according to Figure 220 have been used. For the y motion, the $\cos(x)$ functions should be changed to $\sin(x)$.

```

Details of eccx
Definition Plot Evaluate
ecc*(cos(2*3.1415*-1.45*spin*Time+0) + cos(2*3.1415*-1.35*spin*Time+0)
+cos(2*3.1415*-1.25*spin*Time+0) + cos(2*3.1415*-1.15*spin*Time+0)
+cos(2*3.1415*-1.05*spin*Time+0) + cos(2*3.1415*-0.9*spin*Time+0)
+cos(2*3.1415*-0.8*spin*Time+0) + cos(2*3.1415*-0.7*spin*Time+3.1415)
+cos(2*3.1415*-0.6*spin*Time+3.1415) + cos(2*3.1415*-0.5*spin*Time+3.1415)
+cos(2*3.1415*-0.4*spin*Time+3.1415) + cos(2*3.1415*-0.3*spin*Time+0)
+cos(2*3.1415*-0.2*spin*Time+0) + cos(2*3.1415*-0.1*spin*Time+3.1415)
+cos(2*3.1415*0.15*spin*Time+3.1415) + cos(2*3.1415*0.25*spin*Time+0)
+cos(2*3.1415*0.35*spin*Time+0) + cos(2*3.1415*0.45*spin*Time+3.1415)
+cos(2*3.1415*0.55*spin*Time+0) + cos(2*3.1415*0.65*spin*Time+0)
+cos(2*3.1415*0.75*spin*Time+3.1415) + cos(2*3.1415*0.85*spin*Time+0)
+cos(2*3.1415*0.95*spin*Time+3.1415) + cos(2*3.1415*1.1*spin*Time+3.1415)
+cos(2*3.1415*1.2*spin*Time+0) + cos(2*3.1415*1.3*spin*Time+3.1415) +
cos(2*3.1415*1.4*spin*Time+0) + cos(2*3.1415*1.5*spin*Time+3.1415))

```

Figure 220. Array of frequencies and phases used in this case

-Define output variables to monitor the results. Open *Simulation>Solver>Output Control*. Under Monitor tab, activate Monitor Objects and define expressions to monitor the rotor motion, and stationary frame forces. The stationary frame forces F_x and F_y are critical for post processing (See Figure 221)

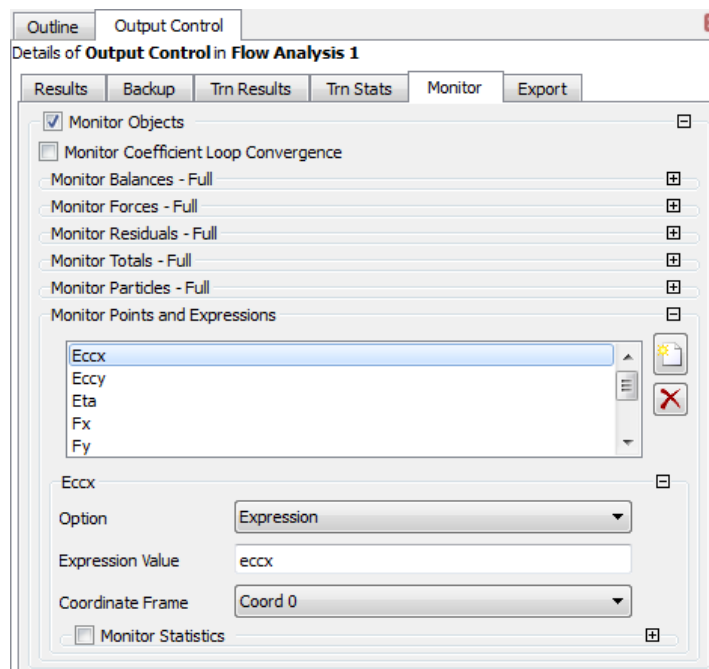


Figure 221. Define output monitors

In case that a single frequency model is desired, change the following steps:

-Change the *Mesh Deformation Option* to *Periodic Regions of Motion* and select the *Complex Displacement* as the *Periodic Model* in the impeller domain. Retain the other settings (See Figure 222).

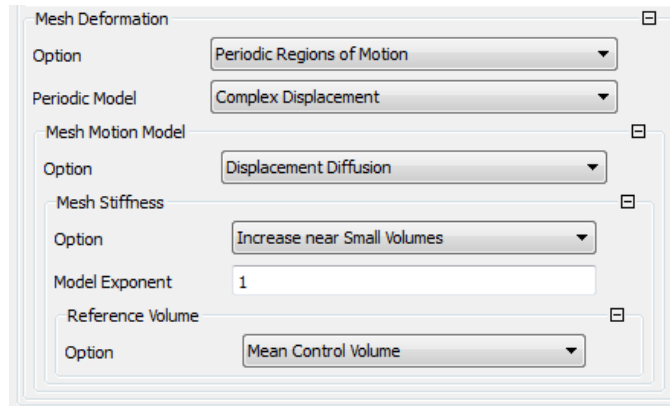


Figure 222. Single frequency complex displacement model

-Change the blade and hub Mesh Motion boundary condition settings as shown in Figure 223. Make sure the *Periodic Displacement* option is selected.

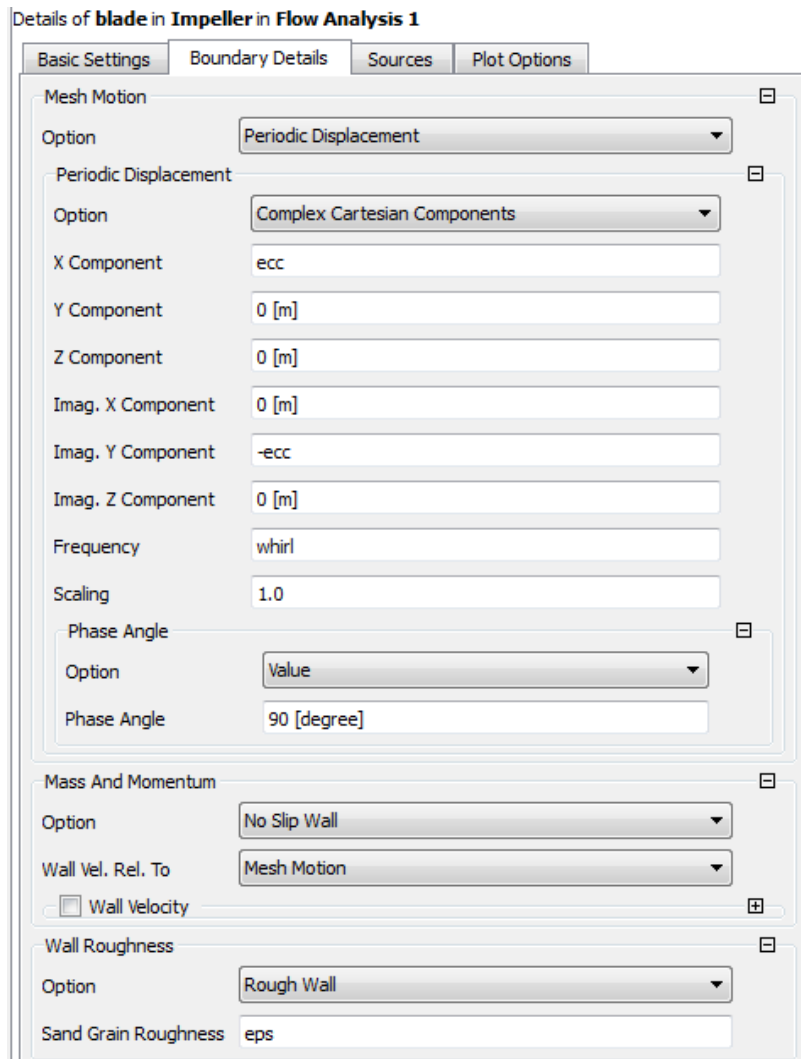


Figure 223. Periodic displacement BC on the blade and hub

- Insert a new Expression to define the whirling frequency as a fraction of the spin frequency according to Figure 224.

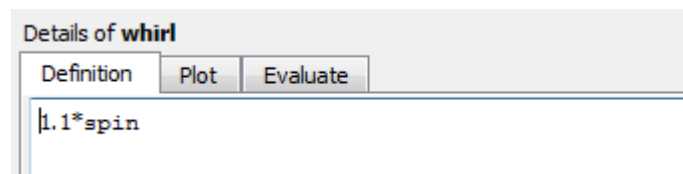


Figure 224. Define whirling frequency

**APPENDIX D MACCORMACK DISCRETIZATIONS FOR NON-UNIFORM
GRID**

The discretized predictor terms:

$$\begin{bmatrix} U_1^n \\ U_2^n \\ U_3^n \\ U_4^n \\ U_5^n \\ U_6^n \\ U_7^n \end{bmatrix}_{i,j,k} = \begin{bmatrix} p_{i,j,k}^n \\ w_r^n \\ w_\theta^n \\ w_z^n \\ \dots \text{energy} \dots \\ k_{i,j,k}^n \\ \omega_{i,j,k}^n \end{bmatrix} \quad (332)$$

$$\begin{bmatrix} E_1^n \\ E_2^n \\ E_3^n \\ E_4^n \\ E_5^n \\ E_6^n \\ E_7^n \end{bmatrix}_{i,j,k} = \begin{bmatrix} \frac{\rho w_r^n}{\hat{\beta}} \\ w_r^n w_r^n - 2(v + v_t^n) \frac{w_r^n - w_r^{n-1}}{\Delta r_i} + \frac{2}{3} k_{i,j,k}^n \\ w_r^n w_\theta^n - (v + v_t^n) \left[\frac{w_\theta^n - w_\theta^{n-1}}{\Delta r_i} - \frac{w_\theta^n}{r_i} + \frac{w_r^n - w_r^{n-1}}{r_i(\Delta\theta_j + \Delta\theta_{j+1})} \right] \\ w_r^n w_z^n - (v + v_t^n) \left[\frac{w_z^n - w_z^{n-1}}{(\Delta z_k + \Delta z_{k+1})} + \frac{w_z^n - w_z^{n-1}}{\Delta r_i} \right] \\ \dots \text{energy} \dots \\ w_r^n k_{i,j,k}^n - (v + \sigma_{k1} v_t^n) \frac{k_{i,j,k}^n - k_{i-1,j,k}^n}{\Delta r_i} \\ w_r^n \omega_{i,j,k}^n - (v + \sigma_{\omega 1} v_t^n) \frac{\omega_{i,j,k}^n - \omega_{i-1,j,k}^n}{\Delta r_i} \end{bmatrix} \quad (333)$$

$$\begin{bmatrix} F_{1,i,j,k}^n \\ F_{2,i,j,k}^n \\ F_{3,i,j,k}^n \\ F_{4,i,j,k}^n \\ F_{5,i,j,k}^n \\ F_{6,i,j,k}^n \\ F_{7,i,j,k}^n \end{bmatrix}$$

$$= \begin{bmatrix} \frac{\rho w_{\theta,i,j,k}^n}{\hat{\beta}} \\ w_{\theta,i,j,k}^n w_r^{\theta,i,j,k} - (\nu + \nu_t^{\theta,i,j,k}) \left[\frac{w_{\theta,i+1,j,k}^n - w_{\theta,i-1,j,k}^n}{(\Delta r_i + \Delta r_{i+1})} - \frac{w_{\theta,i,j,k}^n}{r_i} + \frac{w_r^{\theta,i,j,k} - w_r^{\theta,i,j-1,k}}{r_i \Delta \theta_j} \right] \\ w_{\theta,i,j,k}^n w_{\theta,i,j,k}^n - 2(\nu + \nu_t^{\theta,i,j,k}) \left(\frac{w_{\theta,i,j,k}^n - w_{\theta,i,j-1,k}^n}{r_i \Delta \theta_j} + \frac{w_r^{\theta,i,j,k}}{r_i} \right) + \frac{2}{3} k_{i,j,k}^n \\ w_{\theta,i,j,k}^n w_z^{\theta,i,j,k} - (\nu + \nu_t^{\theta,i,j,k}) \left[\frac{w_{\theta,i,j,k+1}^n - w_{\theta,i,j,k-1}^n}{(\Delta z_k + \Delta z_{k+1})} + \frac{w_z^{\theta,i,j,k} - w_z^{\theta,i,j-1,k}}{r_i \Delta \theta_j} \right] \\ \dots \text{energy} \dots \\ w_{\theta,i,j,k}^n k_{i,j,k}^n - (\nu + \sigma_{k1} \nu_t^{\theta,i,j,k}) \frac{k_{i,j,k}^n - k_{i,j-1,k}^n}{r_i \Delta \theta_j} \\ w_{\theta,i,j,k}^n \omega_{i,j,k}^n - (\nu + \sigma_{\omega 1} \nu_t^{\theta,i,j,k}) \frac{\omega_{i,j,k}^n - \omega_{i,j-1,k}^n}{r_i \Delta \theta_j} \end{bmatrix} \quad (334)$$

$$\begin{bmatrix} G_{1,i,j,k}^n \\ G_{2,i,j,k}^n \\ G_{3,i,j,k}^n \\ G_{4,i,j,k}^n \\ G_{5,i,j,k}^n \\ G_{6,i,j,k}^n \\ G_{7,i,j,k}^n \end{bmatrix} = \begin{bmatrix} \frac{\rho w_z^{\theta,i,j,k}}{\beta} \\ w_r^{\theta,i,j,k} w_z^{\theta,i,j,k} - (\nu + \nu_t^{\theta,i,j,k}) \left[\frac{w_r^{\theta,i,j,k} - w_r^{\theta,i,j,k-1}}{\Delta z_k} + \frac{w_z^{\theta,i+1,j,k} - w_z^{\theta,i-1,j,k}}{(\Delta r_i + \Delta r_{i+1})} \right] \\ w_z^{\theta,i,j,k} w_{\theta,i,j,k}^n - (\nu + \nu_t^{\theta,i,j,k}) \left[\frac{w_{\theta,i,j,k}^n - w_{\theta,i,j,k-1}^n}{\Delta z_k} + \frac{w_z^{\theta,i,j+1,k} - w_z^{\theta,i,j-1,k}}{r_i (\Delta \theta_j + \Delta \theta_{j+1})} \right] \\ w_z^{\theta,i,j,k} w_z^{\theta,i,j,k} - 2(\nu + \nu_t^{\theta,i,j,k}) \frac{w_z^{\theta,i,j,k} - w_z^{\theta,i,j,k-1}}{\Delta z_k} + \frac{2}{3} k_{i,j,k}^n \\ \dots \text{energy} \dots \\ w_z^{\theta,i,j,k} k_{i,j,k}^n - (\nu + \sigma_{k1} \nu_t^{\theta,i,j,k}) \frac{k_{i,j,k}^n - k_{i,j,k-1}^n}{\Delta z_k} \\ w_z^{\theta,i,j,k} \omega_{i,j,k}^n - (\nu + \sigma_{\omega 1} \nu_t^{\theta,i,j,k}) \frac{\omega_{i,j,k}^n - \omega_{i,j,k-1}^n}{\Delta z_k} \end{bmatrix} \quad (335)$$

$$\begin{bmatrix} H_{1,i,j,k}^n \\ H_{2,i,j,k}^n \\ H_{3,i,j,k}^n \\ H_{4,i,j,k}^n \\ H_{5,i,j,k}^n \\ H_{6,i,j,k}^n \\ H_{7,i,j,k}^n \end{bmatrix}$$

$$= \begin{bmatrix} \frac{p_{i+1,j,k}^n - p_{i,j,k}^n}{\rho \Delta r_{i+1}} + 2(v + v_t^n) \left(\frac{w_{\theta,i,j+1,k}^n - w_{\theta,i,j,k}^n}{r_i^2 \Delta \theta_{j+1}} + \frac{w_r^n}{r_i^2} \right) - \frac{2k_{i,j,k}^n}{3r_i} - \frac{w_{\theta,i,j,k}^n w_{\theta,i,j,k}^n}{r_i} + \text{ROT}(-2\omega w_{\theta,i,j,k}^n - r_i \omega^2) \\ \frac{p_{i,j+1,k}^n - p_{i,j,k}^n}{\rho r_i \Delta \theta_{j+1}} + \frac{w_r^n}{r_i} + \frac{w_{\theta,i,j,k}^n w_{\theta,i,j,k}^n}{r_i} - (v + v_t^n) \left(\frac{w_{\theta,i+1,j,k}^n - w_{\theta,i,j,k}^n}{r_i \Delta r_{i+1}} - \frac{w_{\theta,i,j,k}^n}{r_i^2} + \frac{w_r^n}{r_i^2 \Delta \theta_{j+1}} \right) + \text{ROT}(2\omega w_r^n) \\ \frac{p_{i,j,k+1}^n - p_{i,j,k}^n}{\rho \Delta z_{k+1}} \\ \dots \text{energy} \dots \\ -P_k^n + \beta^* k_{i,j,k}^n \omega_{i,j,k}^n \\ -\frac{\gamma_1}{v_t^n} P_k^n + \beta_1 \omega_{i,j,k}^n \omega_{i,j,k}^n \end{bmatrix} \quad (336)$$

where

$$P_k^n = v_t^n \left\{ 2 \left[\left(\frac{w_r^n}{\Delta r_{i+1}} \right)^2 + \left(\frac{w_z^n}{\Delta z_{k+1}} \right)^2 + \left(\frac{w_{\theta,i,j+1,k}^n - w_{\theta,i,j,k}^n}{r_i \Delta \theta_{j+1}} + \frac{w_r^n}{r_i} \right)^2 \right] \right. \\ \left. + \left(\frac{w_{\theta,i+1,j,k}^n - w_{\theta,i,j,k}^n}{\Delta r_{i+1}} - \frac{w_{\theta,i,j,k}^n}{r_i} + \frac{w_r^n}{r_i \Delta \theta_{j+1}} \right)^2 + \left(\frac{w_r^n}{\Delta z_{k+1}} + \frac{w_z^n}{\Delta r_{i+1}} \right)^2 \right. \\ \left. + \left(\frac{w_{\theta,i,j,k+1}^n - w_{\theta,i,j,k}^n}{\Delta z_{k+1}} + \frac{w_z^n}{r_i \Delta \theta_{j+1}} \right)^2 \right\}$$

For the corrector step:

$$\begin{array}{l}
 E_{1\ i,j,k}^* \\
 E_{2\ i,j,k}^* \\
 E_{3\ i,j,k}^* \\
 E_{4\ i,j,k}^* \\
 E_{5\ i,j,k}^* \\
 E_{6\ i,j,k}^* \\
 E_{7\ i,j,k}^*
 \end{array}
 \left[\begin{array}{l}
 \frac{\rho w_r^*{}_{i,j,k}}{\beta} \\
 w_r^*{}_{i,j,k} w_r^*{}_{i,j,k} - 2(v + v_t^*{}_{i,j,k}) \frac{w_r^*{}_{i+1,j,k} - w_r^*{}_{i,j,k}}{\Delta r_{i+1}} + \frac{2}{3} k_{i,j,k}^* \\
 w_r^*{}_{i,j,k} w_\theta^*{}_{i,j,k} - (v + v_t^*{}_{i,j,k}) \left[\frac{w_\theta^*{}_{i+1,j,k} - w_\theta^*{}_{i,j,k}}{\Delta r_{i+1}} - \frac{w_\theta^*{}_{i,j,k}}{r_i} + \frac{w_r^*{}_{i,j+1,k} - w_r^*{}_{i,j-1,k}}{r_i(\Delta\theta_j + \Delta\theta_{j+1})} \right] \\
 w_r^*{}_{i,j,k} w_z^*{}_{i,j,k} - (v + v_t^*{}_{i,j,k}) \left[\frac{w_r^*{}_{i,j,k+1} - w_r^*{}_{i,j,k-1}}{(\Delta z_k + \Delta z_{k+1})} + \frac{w_z^*{}_{i+1,j,k} - w_z^*{}_{i,j,k}}{\Delta r_{i+1}} \right] \\
 \dots \text{energy} \dots \\
 w_r^*{}_{i,j,k} k_{i,j,k}^* - (v + \sigma_{k1} v_t^*{}_{i,j,k}) \frac{k_{i+1,j,k}^* - k_{i,j,k}^*}{\Delta r_{i+1}} \\
 w_r^*{}_{i,j,k} \omega_{i,j,k}^* - (v + \sigma_{\omega 1} v_t^*{}_{i,j,k}) \frac{\omega_{i+1,j,k}^* - \omega_{i,j,k}^*}{\Delta r_{i+1}}
 \end{array} \right] \quad (337)$$

$$\begin{aligned}
& \begin{bmatrix} F_{1,i,j,k}^* \\ F_{2,i,j,k}^* \\ F_{3,i,j,k}^* \\ F_{4,i,j,k}^* \\ F_{5,i,j,k}^* \\ F_{6,i,j,k}^* \\ F_{7,i,j,k}^* \end{bmatrix} \\
& = \left[\begin{aligned} & \frac{\rho w_{\theta,i,j,k}^*}{\beta} \\ & w_{\theta,i,j,k}^* w_r^* w_{i,j,k} - (v + v_t^* w_{i,j,k}) \left[\frac{w_{\theta,i+1,j,k}^* - w_{\theta,i-1,j,k}^*}{(\Delta r_i + \Delta r_{i+1})} - \frac{w_{\theta,i,j,k}^*}{r_i} + \frac{w_r^* w_{i,j+1,k} - w_r^* w_{i,j,k}}{r_i \Delta \theta_{j+1}} \right] \\ & w_{\theta,i,j,k}^* w_{\theta,i,j,k}^* - 2(v + v_t^* w_{i,j,k}) \left(\frac{w_{\theta,i,j+1,k}^* - w_{\theta,i,j,k}^*}{r_i \Delta \theta_{j+1}} + \frac{w_r^* w_{i,j,k}}{r_i} \right) + \frac{2}{3} k_{i,j,k}^* \\ & w_{\theta,i,j,k}^* w_z^* w_{i,j,k} - (v + v_t^* w_{i,j,k}) \left[\frac{w_{\theta,i,j,k+1}^* - w_{\theta,i,j,k-1}^*}{(\Delta z_k + \Delta z_{k+1})} + \frac{w_z^* w_{i,j+1,k} - w_z^* w_{i,j,k}}{r_i \Delta \theta_{j+1}} \right] \\ & \dots \text{energy} \dots \\ & w_{\theta,i,j,k}^* k_{i,j,k}^* - (v + \sigma_{k1} v_t^* w_{i,j,k}) \frac{k_{i,j+1,k}^* - k_{i,j,k}^*}{r_i \Delta \theta_{j+1}} \\ & w_{\theta,i,j,k}^* \omega_{i,j,k}^* - (v + \sigma_{\omega 1} v_t^* w_{i,j,k}) \frac{\omega_{i,j+1,k}^* - \omega_{i,j,k}^*}{r_i \Delta \theta_{j+1}} \end{aligned} \right] \quad (338)
\end{aligned}$$

$$\begin{aligned}
& \begin{bmatrix} G_{1,i,j,k}^* \\ G_{2,i,j,k}^* \\ G_{3,i,j,k}^* \\ G_{4,i,j,k}^* \\ G_{5,i,j,k}^* \\ G_{6,i,j,k}^* \\ G_{7,i,j,k}^* \end{bmatrix} \\
& = \left[\begin{aligned} & \frac{\rho w_z^* w_{i,j,k}}{\beta} \\ & w_r^* w_{i,j,k} w_z^* w_{i,j,k} - (v + v_t^* w_{i,j,k}) \left[\frac{w_r^* w_{i,j,k+1} - w_r^* w_{i,j,k}}{\Delta z_{k+1}} + \frac{w_z^* w_{i+1,j,k} - w_z^* w_{i-1,j,k}}{(\Delta r_i + \Delta r_{i+1})} \right] \\ & w_z^* w_{i,j,k} w_{\theta,i,j,k}^* - (v + v_t^* w_{i,j,k}) \left[\frac{w_{\theta,i,j,k+1}^* - w_{\theta,i,j,k}^*}{\Delta z_{k+1}} + \frac{w_z^* w_{i,j+1,k} - w_z^* w_{i,j-1,k}}{r_i (\Delta \theta_j + \Delta \theta_{j+1})} \right] \\ & w_z^* w_{i,j,k} w_z^* w_{i,j,k} - 2(v + v_t^* w_{i,j,k}) \frac{w_z^* w_{i,j,k+1} - w_z^* w_{i,j,k}}{\Delta z_{k+1}} + \frac{2}{3} k_{i,j,k}^* \\ & \dots \text{energy} \dots \\ & w_z^* w_{i,j,k} k_{i,j,k}^* - (v + \sigma_{k1} v_t^* w_{i,j,k}) \frac{k_{i,j,k+1}^* - k_{i,j,k}^*}{\Delta z_{k+1}} \\ & w_z^* w_{i,j,k} \omega_{i,j,k}^* - (v + \sigma_{\omega 1} v_t^* w_{i,j,k}) \frac{\omega_{i,j,k+1}^* - \omega_{i,j,k}^*}{\Delta z_{k+1}} \end{aligned} \right] \quad (339)
\end{aligned}$$